Chair of Resource Mineralogy
Department Applied Geosciences and Geophysics
Montanuniversität Leoben

MASTER THESIS

W-Sn mineralisation in calc-silicate rocks of the Basal Amphibolite unit at Messelingscharte (Felbertauern area, Austria)

Alexander Ordosch

Supervisor: Johann G. Raith

Leoben, Austria, June 2017

Eidesstattliche Erklärung

Ich erkläre an Eides statt, dass ich diese Arbeit selbstständig verfasst, andere als die angegebenen Quellen und Hilfsmittel nicht benutzt und mich auch sonst keiner unerlaubten Hilfsmittel bedient habe.

Leoben, Juni 2017

Ort, Datum Vorname Zuname

Abstract

Wolfram Bergbau- und Hütten AG initiated this project with Montanuniversität Leoben to reinvestigate the previously known scheelite occurrence at Messelingscharte in the Felbertauern area where the company is currently holding the exploring permissions. The main aims of this project were to study the geological setting, the mineralogy and geochemistry of this unusual scheelite mineralisation in detail and to prospect for additional scheelite-bearing outcrops in this area.

Scheelite mineralisation at Messelingscharte is hosted in Early Palaeozoic amphibolites of the Basal Amphibolite unit of Tauern Window close to the contact with the Basal Schist unit. The Basal Amphibolite unit consists of various amphibolites, hornblende-biotite schist, hornblende fels and hornblende-biotite gneiss; the latter preserves intrusive contacts with the amphibolites but is co-magmatic. The amphibolites exhibit geochemical signatures comparable with enriched back-arc basalts. Intercalations of coarse-grained deformed orthogneiss at Messelingkogel were identified as equivalents of the Granatspitz Gneiss.

Four types of scheelite mineralisation are distinguished. (1) Scheelite-bearing calc-silicate pods, (2) Discordant, deformed scheelite-quartz veins, (3) Scheelite in concordant mylonitic quartz-amphibolite layers, (4) Scheelite on joint surfaces. Type 1 and 2 are assumed to be pre-Alpine (Variscan?) formations. The scheelite-bearing calc-silicate rocks occur as metre-sized irregular shaped pods. They are composed of major clinozoisite, quartz, and plagioclase with minor to accessory scheelite, titanite and chlorite. Bulk geochemistry reveals high concentrations of W (≤6.14 mass% WO_3), Sn (≤1254 ppm SnO_2), Be (≤41 ppm) and transition metals (Cu, Pb, Zn; ∑≤2500 ppm) in these rocks.

Three scheelite generations are distinguished based on micro-textures, zoning, Mo-content and luminescence colour. The first generation is coarse-grained and Mo-rich (0.82-1.7 mass% MoO_3) and normally preserved in the cores of large scheelite porphyroblasts. It is interpreted as primary pre-Alpine (Variscan?) scheelite. Scheelite generations 2 and 3 from Messelingscharte are Mo-poor/free and are interpreted as metamorphic mobilisations and recrystallization products formed during Variscan (?) and/or Young Alpine regional metamorphism. Hence, it is concluded that, similar to Felbertal scheelite deposit (Scheelite 1 and 2 there), pre-Alpine Mo-rich scheelite was overprinted by two stages of metamorphism. An unique feature of scheelite mineralisation at Messelingscharte is the association of W with Sn. Clinozoisite and titanite were identified as the main Sn-bearing phases (clinozoisite ≤3.00 mass% SnO_2, =0.09 apfu; titanite ≤6.48 mass% SnO_2). Sn-bearing clinozoisite (large anhedral grains with irregularly shaped Sn-rich lamella) was also affected by metamorphic recrystallization; the fine-grained, euhedral metamorphic clinozoisite is Sn-free. Substitution of $(Al,Fe)^{3+}$ by $(Sn,Ti)^{4+}$ is explained by simultaneous incorporation of divalent cations like Fe^{2+}. Titanite shows patchy irregular zoning defined by Sn-content and rarely hosts very small (<3µm), roundish cassiterite grains.

The mineralised calc-silicate rocks are the product of fluid rock interaction when W-Sn-bearing fluids interacted with the mafic Ca-bearing protoliths of the amphibolites. Clinozoisite-rich calc-silicate rocks from Felbertal mine exhibit different bulk geochemistry (e.g. Sn, Rb, Bi, As) and mineral chemistry of clinozoisite (e.g. Sn, Mn) compared to Messelingscharte reflecting different composition of the host rock and calc-silicate forming fluids. Moreover, the chemical signature clearly differs from

metamorphic clinozoisite segregations known in the Tauern Window and rather points to a magmatic hydrothermal source of these fluids (cf. skarn veins with Sn-bearing epidote in the St. Just aureole, Cornwall). Future exploration and research must test the hypothesis that Messelingscharte is a type of distal skarn associated with a so far unidentified granite (Felbertauern augengneiss?).

Zusammenfassung

Die Wolfram Bergbau- und Hütten AG führte in Kooperation mit der Montanuniversität Leoben (Österreich) ein Erkundungsprogramm auf bereits bekannte, ungewöhnlich Scheelit-reiche Gesteine nahe der Messelingscharte (Tauern Fenster, Österreich) durch. Ziel der Prospektion war die genaue mineralogische und geochemische Beschreibung der Scheelit-reichen Gesteine und Auffinden von weiteren Scheelit-führenden Aufschlüssen.

Scheelit-reiche Kalksilikatgesteine treten in früh-paläozoischen Amphiboliten (Basisamphibolit) nahe dem Kontakt zum Basisschiefer auf. Der Basisamphibolit besteht aus verschiedenen Amphiboliten, Hornblende-Biotit Schiefer, Hornblende Fels und Hornblende-Biotit Gneis. Letzterer besitzt intrusive Kontakte zum Amphibolit, ist jedoch co-magmatisch. Die Amphibolite zeigen geochemische Ähnlichkeiten zu angereicherten Backarc Basalten. Eine tektonische Schuppe aus deformierten Orthogneis am Messelingkogel konnte dem Granatspitz Gneis zugeordnet werden.

Das Vorkommen beinhaltet vier Typen von Scheelit-Vererzungen: (1) Scheelit-führende Kalksilikatlinsen, (2) Diskordante, verfaltete Quarz-Scheelit Gänge, (3) Scheelit in konkordanten mylonitischen Quarz-Amphibolit Lagen und (4) Scheelit auf Kluftflächen. Die ersten beiden Typen bildeten sich wahrscheinlich prä-alpidisch (variszisch?).

Wolfram-führende Kalksilikatgesteine treten als unregelmäßige Linsen im Meter-Bereich auf und bestehen hauptsächlich aus Klinozoisit, Quarz, Plagioklas mit Nebengemengteilen von Scheelit, Titanit und Chlorit. In der Gesamtgesteins-Geochemie dieser Gesteine wurden ungewöhnlich hohe Gehalte an W (≤6,14 Gew% WO_3), Sn (≤1254 ppm SnO_2), Be (≤41 ppm) und Buntmetallen (Cu, Pb, Zn; ∑≤2500 ppm) festgestellt.

Drei verschiedene Scheelit-Generationen können aufgrund von Mikrogefüge, Zonierung, Mo-Gehalt und Lumineszenzfarbe unterschieden werden. Die erste Generation befindet sich normalerweise im Kern von großen Scheelit Porphyroblasten, ist grobkörnig und Mo-reich (0,82-1,7 Gew% MoO_3). Dieser primäre Scheelit bildete sich wahrscheinlich prä-alpidisch (variszisch?). Die Scheelit-Generationen 2 und 3 sind Mo-arm bzw. -frei und bildeten sich durch metamorphe Mobilisierung und als Rekristallisationsprodukte während der variszischen (?) und/oder jung-alpidischen Regionalmetamorphose. Ähnlich wie in der W-Lagerstätte Felbertal (dort Scheelit 1 und 2) wurde prä-alpidischer Mo-reicher Scheelit im Zuge von zwei Metamorphose-Stadien überprägt.

Charakteristisch für das W-Vorkommen Messelingscharte ist das Auftreten von Silikat-gebundenem Zinn, welches durch Substitution in Klinozoisit und Titanit eingebaut wird (Klinozoisit ≤3,00 Gew% SnO_2, =0,09 apfu; Titanit ≤6,48 Gew% SnO_2). Durch die metamorphe Rekristallisation von Sn-reichem Klinozoisit (grobkörnige anhedrale Körner mit irregulären Sn-reichen Lamellen), entsteht feinkörniger, euhedraler Sn-freier Klinozoisit. Die Subsitution von $(Al,Fe)^{3+}$ durch $(Sn,Ti)^{4+}$ ist mit

gekoppelten Einbau von zweiwertigen Kationen, wie Fe^{2+}, verbunden. Titanit zeigt eine unregelmäßige Zonierung verursacht durch unterschiedliche Sn-Gehalte und führt selten rundliche, sehr feinkörnige (<3µm) Kassiterit-Einschlüsse.

Die W-führenden Kalksilikat-Gesteine entstanden metasomatisch als Reaktionsprodukt zwischen mafischen Ca-reichen Amphiboliten und W-Sn führenden Fluiden. Geochemisch unterscheiden sich die Klinozoisit-reichen Kalksilikatgesteine aus der Lagerstätten Felbertal von den untersuchten Kalksilikatgesteinen der Messelingscharte in ihrer Gesamtgesteins-Chemie (z.B. Sn, Rb, Bi, As) und der Mineralchemie von Klinozoisit (z.B. Sn, Mn). Des weiteren unterscheidet sich die geochemische Signatur metamorpher Klinozoisit-Segregationen aus dem Tauern Fenster stark von den Kalksilikatgesteinen der Messelingscharte. Diese Diskrepanzen deuten sowohl auf unterschiedliche Zusammensetzungen der Nebengesteine als auch der Kalksilikat-bildenden Fluide hin. Für letztere wird eine magmatisch-hydrothermale Quelle vermutet (vgl. Skarn Gänge mit Sn-führendem Epidot aus der St. Just Aureole, Cornwall). Künftige Untersuchungen müssen die Zuordnung der W-reichen Kalksilikat-Gesteine der Messelingscharte zum Typ „distale Skarn-Lagerstätten“ testen und deren Verbindung zu einem möglichen, zur Zeit unidentifizierten, assoziierten Granit (Felbertauern Augengneis?) klären.

Acknowledgments

Wolfram Bergbau und Hütten AG is thanked for making this project possible and for providing financial and logistic support. I am grateful to Steffen Schmid and Karsten Aupers from WBH AG for providing reports and analytical data as well as samples from Felbertal mine, accompanying me during field work and for fruitful discussion. Furthermore, I want to thank the team of the WBH's lab at the Felbertal mine for their help with XRF and XRD analyses. I also want to thank those who joined me during field work and assisted me with UV-lamping namely Prof. Frank Melcher, Martin Stern, Timotheus Steiner, Katharina Schneider and Werner Ordosch. The whole field work would not be possible without their great assistance. I am also grateful to Felbertal AG for permission to use the gravel road saving me extra 500 metres in altitude during each field visit. Moreover, I want to thank the team of St. Pöltener Hütte for their uncomplicated support and professional guidance in this rough field area. Federica Zaccerini and Maik Zimmermann, from the Chair for Resource Mineralogy, are thanked for sample preparation and help with the EPMA analyses. Prof. Thomas Meisel, from the Chair for Analytical Chemistry, offered helpful feedback to avoid potential traps in geochemical interpretation. Finally, I want to thank my academic advisor Prof. Johann Raith for all the support during this extensive project. I had a great time working at the Chair of Reslource Mineralogy working in cooperation with very supportive staff and colleagues. Moreover, I strongly appreciate the support of my parents. Studying in time would not be possible without their help financing me daily living.

Table of Contents

Units and abbreviations

n	number/quantity
apfu	atoms per formula unit
ppm	parts per million
µm	micrometer
mm	millimeter
cm	centimetre
m	meter
cf.	conferre (compare)
e.g.	exempli gratia (for example)
i.e.	id est (that is)
REE	rare earth elements
LREE	light rare earth elements
MREE	middle rare earth elements
HREE	heavy rare earth elements
HFSE	high field strength elements
LILE	large lithophile elements
BAB	back-arc basin
MORB	mid-oceanic-ridge basalt
MUL	Montanuniversität Leoben
WBH	Wolfram Bergbau- und Hütten AG
nd	not detected
bdl	below detection limit
np	not present
LOI	loss on ignition
BSE	back scattered electron
CL	cathodoluminescence
UV	ultra violet light
XRD	X-ray diffraction
XRF	X-ray flourescence spectroscopy
EMPA	electron probe microanalyzer

BA	Basal Amphibolite
BS	Basal Schist

Qz	quartz
Kfs	potassium feldspar
Plg	plagioclase
Bt	biotite
Chl	chlorite
Mus	muscovite
Phl	phlogopite
Czo	clinozoisite
Ep	epidote
Ap	apatite
Clc	calcite
Grt	garnet
And	andradite
Gro	grossular
Ttn	titanite
Mal	malayaite
Ilm	ilmenite
Rut	rutile
Sch	scheelite
Cpx	clinopyroxene
Dio	diopside
Hed	hedenbergite
Amp	amphibole
Hbl	hornblende
Cas	cassiterite
Tur	tourmaline
Mag	magnetite
PGM	platinum group metals

1. Introduction

In May 2016, Wolfram Bergbau- und Hütten AG (WBH) initiated a project in cooperation with Montanuniversität Leoben to re-explore the scheelite mineralisation at Messelingscharte (Eastern Tyrol, Austria) as part of ongoing exploration activities in the Eastern Alps. Scheelite-bearing rocks at Messelingschafrte were originally found in the 1960s and then were further explored in the 1970s. The study area is north of Matreier Tauernhaus close to the border of the provinces of Salzburg and Eastern Tyrol where WBH is currently holding the exploration licences (Freischurfe "Matreier Tauerntal"; BMWFJ-66.050/0015-IV/9/2014).

This area was also recently indicated as prospective for tungsten (Kozlik 2016) based on the detailed studies of the K1-K3 orthogneiss in the Felbertal mine and its chemical similarities and identical age with the Felbertal Augengneis, which is exposed in the exploration area. On the basis of new genetic concepts linking the genesis of the Felbertal tungsten deposit with Variscan granites a detailed re-investigation of scheelite showings to the south of the mine at Messelingscharte was recommended.

The main aims of this MSc project were (1) to review and compile current literature and exploration reports, (2) studying the known scheelite mineralisation in detail using geological, mineralogical and geochemical methods, and (3) prospecting for scheelite (UV lamping) in the vicinity of Messelingscharte.

For evaluating the exploration potential of the area it was was crucial to clarify whether scheelite mineralisation at Messelingscharte is comparable to Felbertal. This included questions like: Does Messelingscharte occur in the same geological formation? Is there any "old" pre-Alpine scheelite present or is it only a young metamorphic scheelite showing of Alpine age? Are there similar mineralisation styles and element associations of W (like Mo or Sn)? Is there any geological indication for a continuation of the known mineralisation that could be used for exploration?

Geological mapping and geochemical studies should clarify the exact geological position of mineralisation within the Tauern Window and constrain the geotectonic setting of the metabasites. Finally, petrographic and geochemical studies should assign an orthogneiss slice exposed on the eastern flank of Messelingkogel to Felbertauern Augengneiss or Granatspitz gneiss.

For better comparison to scheelite-bearing calc-silicate rocks from Messelingscharte, a few specimens of clinozoisite-rich rocks from Felbertal tungsten mine were included in this study.

2. Geological setting

2.1. Regional geology

The tungsten occurrence at Messelingscharte is located in the central Tauern Window (TW) in the Granatspitz Group in the Felber Tauern. The Tauern Window represents the largest of three tectonic windows in the Eastern Alps exposing European basement rocks with their Helvetic and Penninic cover units in an area of about 6500 km^2. The Tauern Window is the result of N-S shortening during Alpine orogeny, late Alpine escape tectonics followed by post Alpine exhumation during Miocene. It is boardered to the north by SEMP (Salzach-Ennstal-Marialzell-Puchberg) fault and to the south by the Mölltal strike-slip fault system. The Brenner and the Katschberg normal faults confine the Tauern Window in the west and east, respectively. These two normal faults represent ductile shear zones and are contemporaneous with N-S compression and E-W extension in the Eastern Alps (Schmid et al. 2004 and references therein).

The most prominent feature in the Tauern Window is the Vendiger Duplex. The Venediger Duplex is a folded stack of three nappes (Zillertal-Riffl Nappe, Tux- Granatspitz Nappe, Ahorn-Göss Nappe) arranged in a duplex structure during Alpine orogeny with distinct faults at the roof and the floor (Frisch 1977; Lammerer and Weger 1998; Schmid et al. 2013).

Subpenninic nappes in general are derived from the distal European margin. They comprise the Variscan basement, Permo-Carboniferous intrusions and post-Variscan cover units (Schmid et al. 2013). Those parts of the pre-Mesozoic metamorphic basement which were intruded by Variscan meta granitoids (“Zentralgneis”) conform to the established term “Altes Dach”, whereas pre-Carboniferous basement in general has been referred to as “Altkristallin” (Frasl 1958; Pestal et al. 2009; Schmid et al. 2013). Schmid et al. (2013) discriminates four different units in the Vendiger Duplex. (1) Ahorn and Göss nappes occur in the western and eastern Hohe Tauern and represent the lowermost nappe in the duplex. (2) Tux-Granatspitz and Hochalm nappes occupy and intermediate structural position. The Habach Complex belongs to structurally higher parts of these nappes. (3) Zillertal-Riffl Nappe represents the highest nappe in the duplex.

There are several Variscan to post-Variscan (?) unites incorporated in the Venediger Duplex in addition to the Variscan metagranitoids (Figure 1). They include supracrustal rocks of Upper Devonian to Triassic age. Two prominent units in the central Hohe Tauern are the so-called Basal Schist ("Basisschiefer", “Biotitporphyroblastenschiefer”, “Eiser sequence”) in the hanging wall and the Basal Amphibolite (“Basisamphibolit”, syn. Stubach Group; Frisch and Neubauer 1989) in the footwall. Other Subpenninic nappes (Eclogite Zone, “Glimmerschieferlamelle”, Wolfendorn Nappe, Geroldstein Mesozoic, Murtörl-Schrovin Unit) cover the Venediger Duplex.

Ophiolite-bearing Penninic units are the tectonically highest rocks in the Tauern Window. The Penninic units are derived from one of the two Alpine Tethys oceans (Valais Ocean or Piemont-Liguria Ocean) (discussions in Frisch 1980b; Kurz 2006) probably during Cretaceous age (Schmid et al. 2013). The most prominent unit of the Penninic units is the Glockner Nappe system. It contains mainly amphibolites and other meta-sediments (phyllite, rarely marble) (Pest et al. 2009). Other Penninic units are the Matrei Zone and the Reckner ophiolitic complex. The Matrei Zone is defines the northern

("Nordrahmenzone") and southern (Matrei Zone sens. str.) margin of the Tauern Window. It is composed of a mélange zone of other Penninic rocks and Permain to Jurassic meta-sediments (Schmid et al. 2013). The Reckner ophiolitic complex represents a piece of exhumed subcontinental mantle overlain by Jurrasic pelagic sediments (Koller and Pestal 2003).

2.1.1. Geology of the Central Tauern Window

The geology of the central Tauern Window is characterised by several Variscan meta-granites (Granatspitz gneiss, Felbertauern augengneiss, Knorrkogel gneiss, Hochweißenfeld gneiss), Pre-Variscan to Variscan metamorphic rocks of the Habach Complex (also "H. Serie", "H. Gruppe", "H. Formation") and Permo-Mesozoic cover rocks exposed in several tectonic nappes. All these rocks are derived palaeogeographically from the distal European margin and are therefore referred to Subpenninic nappes (Schmid et al. 2004; Schmid et al. 2013). Following the tectonic classification of Schmid et al. (2013), the Granatspitz meta-granite is part of the Tux-Granatspitz nappe, which itself is part of the Venediger Duplex. The Granatspitz meta-granite forms a dome structure covering an area of about 100 km^2. It represents the youngest post-Variscan puls of granitic magmatism (Kozlik and Raith 2017). Eichhorn et al. (2000) dated the granite-gneiss using $^{207}Pb/^{235}U$ to 271 ± 4 Ma. Kebede et al. (2005) and Kozlik (2016) argue for a Variscan age of 314 ± 1 Ma and 314 ± 18 Ma respectively. This orthogneiss is a high-K, peraluminous, leucocratic, mostly coarse-grained metagranite showing varying degrees of deformation (Frisch et al. 1993).

The Basal Amphibolite is widespread around the Granatspitz core (Höck 1993) and comprises of amphibolites and metagabbros showing geochemical signatures close to MOR-basalts (Höck 1993; von Quadt 1992) or back-arc basalts (Vavra and Frisch 1993). Its protolith age is debated. Whereas von Quadt (1992) and von Quadt et al. (1997) reported ages of 650 ± 10 Ma and 473 ± 8 Ma respectively assigning it to the pre-Variscan series. Eichhorn et al. (2001) also reports Early Paleozoic age of 551 ± 9 Ma for coarse-grained amphibolites. Kebede et al. (2005) on the other hand reported U-Pb zircon ages of 351-343 Ma and argued for a Variscan age.

The Basal Schist includes garnet-bearing micaschist and minor metavolcanic rocks and graphitic quartzite; in the recent geological map by Pestal et al. (2009) the Basal Schist is referred to as "Draxel-Komplex". Zircons from the Basal Schist yielded an U-Pb age 362 ± 6 Ma (Kebede et al. 2005) and were interpreted as age of detrital zircons. Hence, the zircons provide maximum sedimentation ages indicating that the sedimentary protoliths of the schist are Variscan to post-Variscan and younger than the magmatic series within the Habach Complex (Eichhorn et al. 1999, 2001; Kebede et al. 2005). Also, Pestal et al. (2009) and Schuster et al. (2006) argue for a Lower Carboniferous metamorphosed flysch sequence that is stratigraphically younger than the Early Palaeozoic igneous and sedimentary rocks of the lower parts of the Habach Complex although it is tectonically clearly positioned in its footwall. Around the Felbertal tungsten deposit the Basal Schist was interpreted to either overlie the Basal Amphibolite unconformably (Höck 1993 and references therein) or to be separated by a major Alpine thrust fault (Höll and Eichhorn 2002).

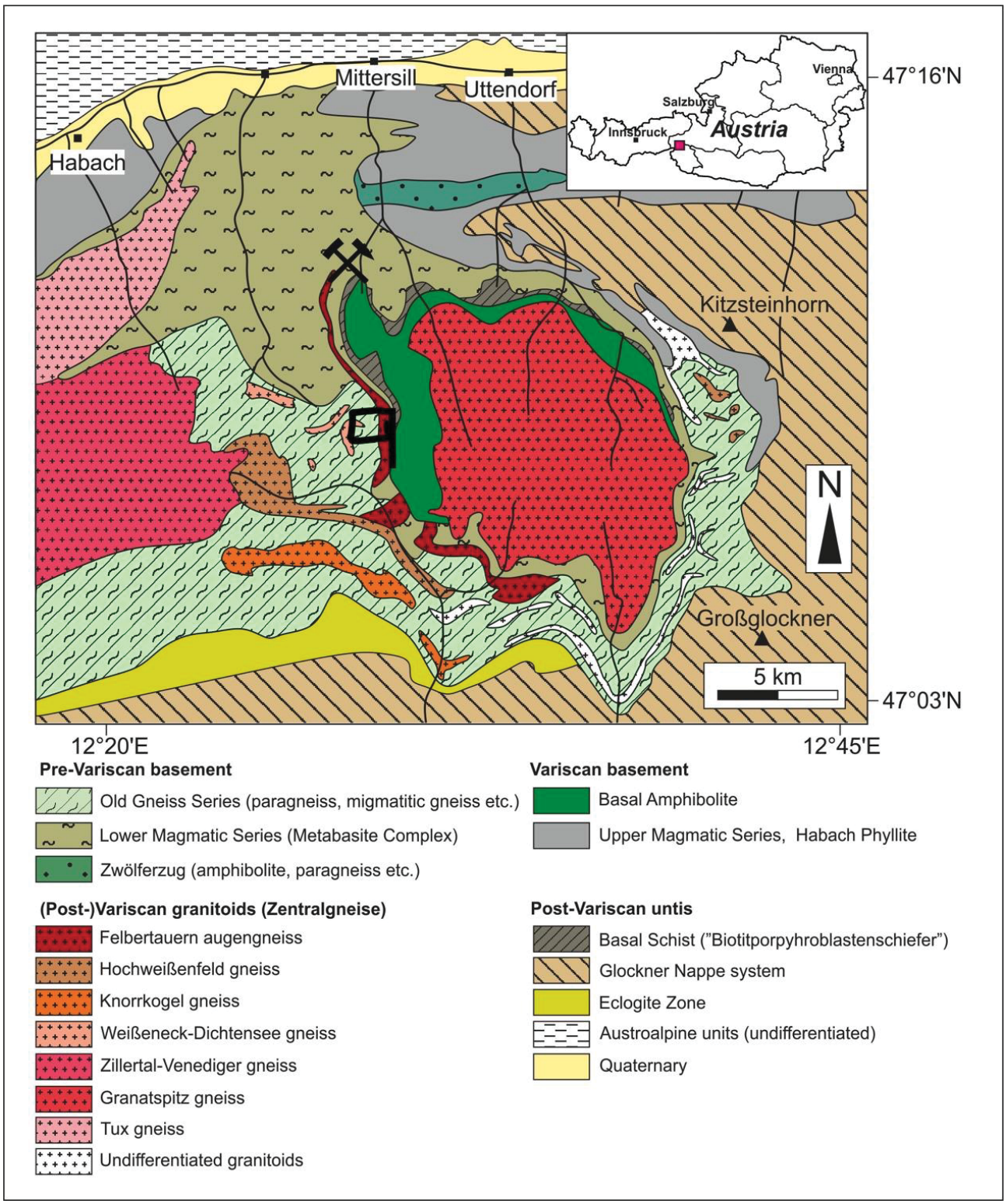

Figure 1: Geological map the central Tauern Window showing the of Granatspitz core and surrounding areas (modified from Kozlik and Raith 2017). Messelingscharte is marked by a black flag. The active Felbertal tungsten mine is marked with the hammer and chisel symbol.

2.1.2. Permomesozoic metasediments

Parautochthonous Mesozoic cover sequences (Figure 2) are recorded in many different successions in the Tauern Window (Hochstegen Group, Kaserer and Murtörl Group, Permian Wustkogel quartzite, and others). These cover sequences document the transition of a stable continental platform established after the Variscan orogeny to extension tectonics with development of a rift basin and an oceanic basin (Kurz et al. 1998). All these Permomesozoic metasedimentary units are now

incorporated in a nappe stack that was created during collision of the European continent and the Austroalpine units of the overriding Adriatic plate (Kurz et al. 1998). The most important rocks comprise calcite and dolomite marbles, calcareous mica schists, quartzites and meta-conglomerates (Kurz et al. 1998). Quartzites can occur either locally, or are missing completely within the Venediger nappe complex (Frisch 1980b; Lammerer 1986).

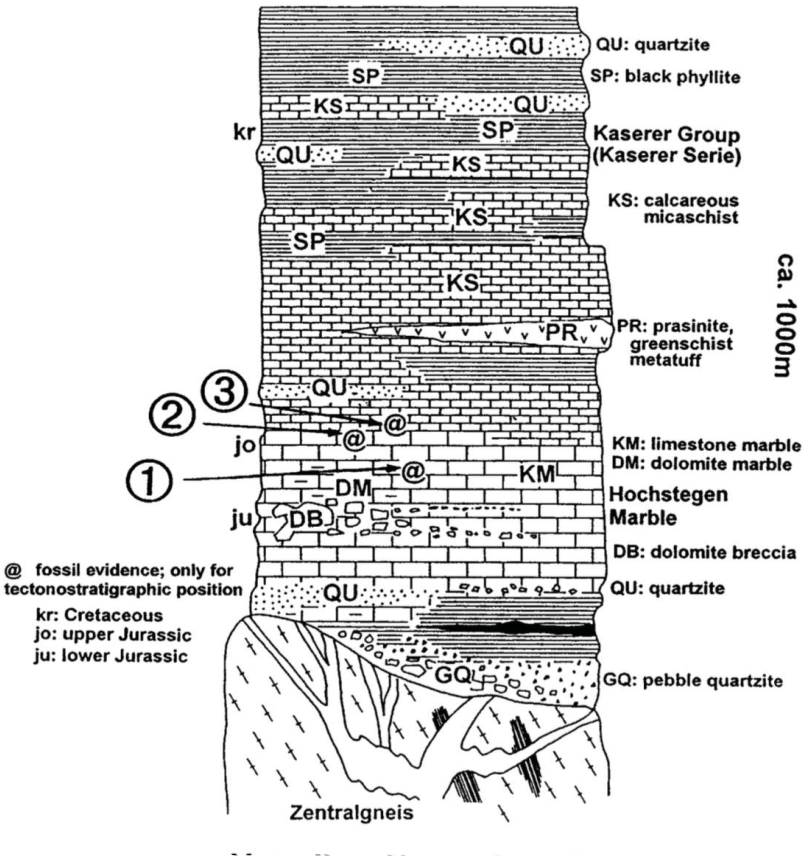

Figure 2: Sketch of a simplified column section of the lithofacies covering the Venediger Nappe (Steyrer 1987 (unpublished) in Kurz et al. 1998).

2.1.3. The Habach Complex

The Habach Complex represents the largest area of Pre-Mesozoic volcano-sedimentary basement rocks in the central Tauern Window. These rocks are among the oldest rocks in the Tauern Window (Schuster et al. 2004). The Habach Complex is poorly defined and has been subdivided differently by previous authors (Frasl 1958; Höll 1975; Höck 1993; Eichhorn et al. 2000, 2001; Kebede et al. 2005; Schmid et al. 2013). It represents a structurally higher part of the Tux-Granatspitz Nappe that is preserved in a larger syncline (Schmid et al. 2013). It is composed of pre-Variscan meta-igneous rocks (amphibolite, hornblende fels, metagabbro, intermediate to felsic orthogneiss) and clastic metasediments (phyllite, schist) and Variscan metagranitoids, and it records several stages of metamorphism (Höck 1993; Raith und Schmid 2010; Eichhorn et al. 2001).

Höll (1975) and Kraiger (1987) first divided the Habach Complex from the bottom to the top into the LMS (Lower Magmatic Series), UMS (Upper Magmatic Series) and the Habach Phyllite, a subdivision also later used by Eichhorn et al. (2000, 2001). Pestal et al. (2009) distinguished on their geological map the Habach Complex sens. str. comprising the UMS and the Habach Phyllite and separated the

LMS referring to as the Early Palaeozoic Metabasite Complex. Nevertheless, age data of the Habach Phyllite and the UMS contradicts this view, because Kebede et al. (2005) propose a Late Cambrian (506 ± 9 Ma) maximum sedimentation age for the Habach Phyllite. Eichhorn et al. (1999, 2000) and Kebede et al. (2005) determined an Early Carboniferous to Early Permian formation age of volcanic rocks of the UMS.

The LMS consists mainly of basic to ultrabasic meta-ophiolites and associated meta-sediments of Cambrian to Ordovician age (Höll 1975; von Quadt 1985; Pestal et al. 2009; Eichhorn et al. 2001; Höck 1993). Common lithologies are fine- to coarse grained amphibolites, hornblendites, serpentinites, various gneisses, schists and metavolcanics (Höck 1993; Raith and Schmid 2010). Eichhorn et al. (1999, 2001) dated the different amphibolites reporting ages of 547 ± 27 Ma for a fine-grained amphibolite and 482 ± 5 Ma for a coarse-grained amphibolite (meta-gabbro?), respectively. Some amphibolites showing MORB (modified by subduction processes) and volcanic arc basalt affinities indicate formation in an active continental margin setting (Thalhammer et al. 1989; Höll und Eichhorn, 2000 and references therein). During Early Cambrian volcanic arc related I-type granites were emplaced yielding ages of 529 ± 17 Ma (Eichhorn et al. 1999), 529 ± 17 Ma (EOZ gneiss) and 519 ± 14 Ma (Younger K2 gneiss) (Eichhorn et al. 2001). Höck (1993) interpreted the LMS as the subvolcanic part of an ophiolite sequence produced in a back-arc or marginal oceanic basin setting. Siliciclastic sediments accumulated in the back-arc basin contemporaneous to the magmatism and were transformed to paragneisses during the subsequent orogenies (Eichhorn et al. 2001). The LMS hosts the Felbertal scheelite ore deposit which will be given special consideration in Chapter 3.2.

The UMS of the Habach Group constitutes parts of the Variscan basement series (Kebede et al. 2005; Pestal et al. 2009). It developed in an island arc setting and consists of metamorphosed basaltic to rhyolitic volcanic rocks and overlaying siliciclastic sediments (Höck 1993). Common lithologies are amphibolites, prasinites, biotite-epidote gneisses, albite gneisses and micaschists (Höck 1993). Geochemical characteristics indicate a mature arc system, likely a continental arc (Höck et al. 1993). Ages for the UMS generally range from Lower Carboniferous to the early Permian (Eichhorn et al. 1999, 2000; Kebede et al. 2005).

The Habach Phyllite consists of dark grey to black phyllites, graphitic quarzites, mica schists and minor volcanic rocks (Frasl 1958; Pestal et al. 2009). Following Eichhorn et al. (1999, 2001) the Habach Phyllite represents an accretionary wedge of an active continental margin. Doubtful microfossil findings of Reitz and Höll (1988) were interpreted to indicate an upper Proterozoic age. Kebede et al. (2005) determined a maximum age for sedimentation of 509 ± 9 Ma.

2.2. Alpine tectonic evolution of the Tauern Window

Schmid et al. (2013) discriminates five different deformation events in the Hohe Tauern. Deformation stage 1 (D1) started in Turonian and accreted the Matrei Zone and Reckner ophiolitic complex, both belonging to the Piemont-Liguria Ocean, to the Austroalpine nappe stack (Schmid et al. 2013). This stage is followed by D2 that subducted the Glockner Nappe system and the most distal parts of the European margin beneath the Austroalpine upper plate including previously accreted units (Schmid et al. 2013). The D2 event produced very large-scale isoclinal folds that are only preserved in the central part of the Tauern Window (Schmid et al. 2013). During this event, high-pressure metamorphism took

place (Schmid et al. 2013). When the Valais Ocean was closed completely also parts of the European continent entered the subduction zone (Schmid et al. 2013). This event also caused isoclinal folding (D3) and a first stage of exhumation of the high-pressure units (Schmid et al. 2013). Kurz et al. (2008) argue for a time interval of 38-32 Ma for the decompression. Probably the most prominent deformation stage (D4) refers to the Venediger Duplex and is coeval with the Barrovian regional metamorphism ("Tauernkristallation") (Schmid et al. 2013). This event reached greenschist to amphibolite facies conditions. The last event D5 includes the indentation of the Southern Alpine crust into the Eastern Alps, slab break-off of the European slab and lateral orogenic extension (Schmid et al. 2013). Lateral escape, rapid doming and exhumation of the Tauern Window brought the nappe pile to the surface starting in Early Miocene (around 17 Ma ago) (Schmid et al. 2013).

2.3. Metamorphic evolution

There are several phases of metamorphism recorded in rocks of the Tauern Window ranging from Caledonian to Alpine age.

A Caledonian metamorphic event is indicated in zircons from the Habach Complex and the Basal Amphibolite (von Quadt et al. 1997; Eichhorn et al. 2001). Droop (1983) and von Quadt et al. (1987, 1989, 1997) report a Silurian (422-415 Ma) high-pressure metamorphic event (400-500°C, 8-12kbar; Zimmermann and Franz 1988) in the eclogitic amphibolites in the Lower Schist Cover located at the southern border of the Tauern Window. Eichhorn et al. (1995) couldn't find traces Silurian metamorphism in the Lower Schist Cover in the north of the Tauern Window. Eichhorn et al. (2001) reports an intense Silurian metamorphic event between 415-422 Ma (Sm-Nd garnet-whole rock, U-Pb zircon) in meta-sediments and amphibolites from the Habach Complex.

The Variscan metamorphic event heavily overprinted the rocks in the Tauern Window accompanied by intrusions of Variscan granites (Schuster et al. 2004). Several authors argue for several stages metamorphism (Droop 1983; Zimmermann 1992; Frisch et al. 1993). Von Quadt (1987) argues for a peak metamorphism around 320 Ma (Late Carboniferous). Droop (1983) and Frisch et al. (1993) argue for three different stages of pre-Hercynian/Variscan metamorphism. The first stage is a high pressure event followed by an amphibolite to granulite facies metamorphism (Variscan regional metamorphism) (Droop 1938; Frisch et al. 1993). Zimmermann (1992) determined PT conditions of 1.5 ± 0.2 Ga and 500 ± 50°C for the high-P event. Frisch et al. (1993) questions this view because the described localities from before-mentioned authors are very close to the Alpine eclogite zone. Also Eichhorn et al. (1995) could not find any traces of this high-P event in rocks located in the northern part of the Lower Schist Cover. Zimmermann (1992) argues for pT conditions of 0.7 ± 0.1 GPa, 600 ± 50°C for the regional metamorphism. The third stage is characterised by contact metamorphism due to intrusion of the precursors of the Central Gneisses (Droop 1983; Frisch et al. 1993). This event is also indicated by pseudomorphs after andalusite found by Cornelius (1944).

During the Alpine orogeny the Eastern Alps were affected by two stages of metamorphism. The Eo-Alpine metamorphic event during Cretaceous (peak at 100 Ma) is predominant in the Austroalpine units and didn't affect the Tauern Window (Schmid et al. 2004). The Neo-Alpine event is restricted to the Penninic Zone including underlying Subpenninic nappes (Schmid et al. 2004). Three phases of Alpine metamorphism are distinguished in the Tauern Window: (1) A first ecologite facies (1.9-2.2

GPa and 600-630°C) event (Hoschek 2001) is preserved in the "Eclogite Zone", which occupies a tectonic position above the Venediger Duplex and forms a narrow E-W striking zone at the southern margin of the TW (Schmid et al. 2013). Zimmermann et al. (1994) determined an age of 45-40 Ma for the high-P event. (2) Decompression to blueschist facies conditions occurred at around 32 Ma (Schmid et al. 2013). (3) Regional Barrovian-type metamorphism occurred at around 30-28 Ma reaching PT conditions of 500-600°C and around 1.0 GPa (Schmid et al. 2013 and references therein). This most important metamorphic event is often referred to "Tauernkristallation" because it transformed the prominent Variscan granitoids into gneisses (Central Gneisses).

2.4. Local geology of Messelingscharte

Messelingscharte is located in the Basal Amphibolite (Fuchs 1958; Frank et al. 1987), very close to the Basal Schist and the Granatspitz gneiss; the latter is exposed to the east of the study area. Another type of Variscan orthogneiss, the Felbertauern augengneiss, occurs as a N-S trending narrow sheet-like body that ends to the south next to Messelingscharte. The Messelingkogel is built by Basal Schist in the footwall and amphibolites, quartzites and gneisses of unclear assignment in the hanging wall (Fuchs 1958). There is also a prominent layer of leucocratic orthogneiss within the micaschists at the eastern flank of Messelingkogel (Fuchs 1958). On the east flank of the Messelingkogel also Triassic (?) marble and quartzite is exposed in an elongated folded band (Fuchs 1958).

3. Mineral deposits of tungsten worldwide and in Austria

Tungsten is a rare element in the Earth's crust. The average (Clark value) content of tungsten in the continental crust is between 1-1.5 ppm whereas it is significantly lower in the mantle (0.012 ppm) (Palme 2014). SiO_2-rich igneous rocks and shales are enriched in tungsten compared to mafic and ultramafic rocks (Parker 1967 and references therein). Tungsten is generally described to behave incompatible during the process of fractional crystallization. Furthermore, it displays a slight siderophile tendency.

Metallic tungsten is produced from two different minerals. First, wolframite $(Fe,Mn)WO_4$, (76 mass% WO_3) is a greyish-black heavy mineral that shows a perfect solid solution between the iron-rich ferberite and the manganese-rich hübnerite endmembers. Second, scheelite ($CaWO_4$, 80 mass% WO_3) is a translucent white to orange-brown mineral that shows very bright blue to yellow fluorescence under short wave UV-light. Other tungsten minerals of minor importance are tungstenite (WS_2) and stolzite ($PbWO_4$).

Tungsten is mainly used in the steel industry, for abrasive materials, in cars and weaponry. Metallic tungsten is used as ferroy-alloy metal to improve the hardness, thermal properties and ultimate tensile strength of iron-based alloys. Tungsten is also used in the form of ceramic material like WC (tungsten-carbide) to produce very hard abrasives and cutting tools.

The most important economically exploitable tungsten deposits are associated with magmatic-hydrothermal activity or medium- to high-grade metamorphic rocks (British Geological Survey 2011). Tungsten deposits are commonly associated with felsic intrusive rocks like granites. The largest tungsten provinces are located in Mesozoic Andean-type orogenic belts (British Geological Survey 2011). Important tungsten provinces are located e.g. in south-east Asia, Kasachstan (Altai-Sayan-Belt in Sibiria), North- and South American Cordillera (Canada, USA, Peru, Bolivia) and East Coast Fold Belt in Australia. Large tungsten resources on the European continent are located in the Variscan Fold Belt e.g. Erzgebirge (Germany), Massive Central (France), Cornwall (Great Britain) and the Iberian Peninsula. Minable grades of primary tungsten ore range from 0.7 mass% WO_3 for vein deposits, 0.3-0.1 mass% WO_3 for high-tonnage orebodies (Pohl 2011) and 0.3-1.4 mass% WO_3 for skarn deposits (British Geological Survey 2011).

Global tungsten production is strongly dominated by China (Reichl et al. 2016). 81% of the worldwide mined tungsten (about 70 kt W_{met}) is produced in China (British Geological Survey 2011). China holds also about 2/3 of the world's tungsten reserves (British Geological Survey 2011). Nevertheless, Europe has a high domestic production compared to other special metals.

Austria is currently the 8th largest tungsten producer in the world and an important import nation of tungsten concentrate and other intermediate tungsten products. The scheelite deposit Mittersill is the only active tungsten mine in Austria. The total tungsten production of Austria was 819 t of metallic tungsten (Reichl et al. 2016). This contributes about 1% to the worldwide mined tungsten (British Geological Survey 2011).

3.1. Tungsten occurrences in Austria – a brief overview

In addition to the world-class Felbertal scheelite deposit there are many sub-economic tungsten occurrences in the different tectonic units in Austria, which have all been classified as stratiform / stratabound scheelite mineralisations (see IRIS database). The only deposit from where minor scheelite was produced in the past is the magnesite-scheelite deposit Tux-Lanersbach (Wenger 1964; Höll and Maucher 1967; Raith et al. 1995). In the Tauern Window scheelite was reported from the gold deposits in the Schellgaden area (Wieser 2010). In the Lower Austroalpine Innsbruck quartzphyllite zone and equivalent units at the eastern margin of the Tauern Window stratabound scheelite occurrences were reported from e.g. Klamm Alm (Mühlbach/Neukirchen), Wagrein/Kleinarltal (Höll 1977). Similar scheelite mineralisation is known from the Thurnthaler Quartzphyllite Zone in Eastern Tyrol (see Portugaller 2010). Stratabound scheelite mineralisation in regional metamorphic calc-silicate rocks has been documented from the Austroalpine Crystalline Complex (Stub-, Kor-, Saualpe, Wölzer and Schladminger Tauern) (Raith 1991). The tungsten occurrence at Mallnock (Nockberge, Carinthia) in the Gurktaler nappe system is unique because of the very unusual paragenesis of iron-rich magnesite and wolframite (Neinavaie et al. 1989). Additionally, there is one stratabound scheelite occurrence in the Moldanubian zone in the Bohemian Massif (area around Obergrünbach, Lower Austria) hosted in calc-silicate rocks (Beran et al. 1985).

3.2. Scheelite deposit Felbertal

The scheelite deposit is located in the Felbertal about 8 km S of Mittersill. The ore deposit is separated in the (closed open pit) Eastern Ore Zone (EOZ) and the (active underground) Western Ore Zone (WOZ). It is hosted in the LMS (Lower Magmatic Series) of the Habach Complex in amphibolites, hornblendites and orthogneisses (Höll and Eichhorn 2000). The WOZ consists of two scheelite-mineralised metabasites sequences that are tectonically separated by a slice of barren Basal Schist (for details see e.g. Raith und Schmidt 2010). Several highly fractionated leucocratic granites (K1-K3 orthogneiss) intruded the Early Palaeozoic host rocks during the Early Carboniferous and are spatially and genetically related to the W mineralisation (Kozlik and Raith 2017). The orthogneisses occur generally as irregular and elongated lenses with a thickness of few dm to several 10 meters (Höll and Eichhorn 2000). Additionally, Cambrian orthogneisses are present in the WOZ and in the EOZ. The high grade ore zone in the EOZ included a quartz-scheelite stockwork and laminated scheelite-quartz ores (Höll and Eichhorn 2000; Raith and Schmid 2010). In the WOZ the mineralization consists of a stockwork of (deformed) quartz veins throughout different lithologies, mineralised shear and fault zones and disseminated scheelite mineralisation.

Several scheelite generations/stages have been distinguished in the deposit (for details see Höll and Eichhorn 2000). Scheelite 1 is fine-grained (up to 0.4 mm) and shows yellowish-white luminescence colours in short-wave UV light. It is further characterised by a Mo-content of ~1 mass% and a fine-scale oscillatory growth zoning (Höll and Eichhorn 2000; Raith and Stein 2006; Raith et al. 2011). Moreover, it contains several tens of ppm U and is most prominent in the eastern ore field in laminated scheelite-quartz ores (Höll and Eichhorn 2000). Eichhorn et al. (1999) postulated an Early Palaeozoic age of this scheelite. Raith et al. (2011) dated this scheelite generation with in-situ U-Pb dating by LA-SF-ICP-MS at 335.5 ± 4.6 Ma. This age is within the uncertainty of the age of the K1 gneiss

(336 ± 19 Ma Eichhorn et al. 1995; 341-336 Ma Kozlik 2016). This result strongly supports the Variscan granite-related genesis of the deposit.

Scheelite 2 is very common in the WOZ and is easily identified by its usually euhedral, large grain size and its grey colour (Höll and Eichhorn 2000). The Mo-content is similar to Scheelite 1 and ranges from 0.1-1.7 mass% Mo (Eichhorn et al. 1997; Raith and Stein 2006). Therefore, it also shows yellowish luminescence colours. Eichhorn et al. (1997) and Höll and Eichhorn (2000) argue for an Early Carboniferous age of Scheelite 2. Raith and Stein (2006) delivered Re-Os model ages for molybdenite associated with Scheelite 2 that range from 358 to 336 Ma. These ages support a genetic relationship to Early Carboniferous K1-K3 orthogneisses.

Scheelite 3 forms rims around Scheelite 1&2 and fills fractures within and replaces older scheelite generations. It is nearly Mo-free (around 100 ppm) and shows blue luminescence colours. Eichhorn et al. (1997) dated scheelite 3 at 319 ± 34 Ma. They interpreted Scheelite 3 to be the product of recrystallization of older scheelite during Variscan regional metamorphism. Fine-grained (metamorphic?) molybdenite is commonly associated with scheelite 3 (Raith and Stein 2006).

Scheelite 4 displays white to pale-blue luminescence colours (Mo-free, <0.05 mass% MoO_3) and occurs as coarse-grained porphyroblasts within Alpine metamorphic quartz veins. A Sm-Nd isochron age yielded an age of 29 ± 17 Ma that reflects local remobilization of Variscan scheelite during Neoalpine regional metamorphism (Eichhorn et al. 1997).

The genesis of the Felbertal tungsten deposit is still under discussion. There exist contrasting models: (1) The early syngenetic exhalative models argue that primary W mineralisation is stratiform to stratabound and unrelated to granites (cf. Sb-W-Hg formation; Höll 1971, 1975; Höll und Maucher 1976). (2) A purely Carboniferous granite related model (Briegleb 1987, 1991; Pestal 1983; Finger et al. 1985; Raith and Stein 2006; Kozlik 2016; Kozlik and Raith 2017). (3) Early Paleozoic and Variscan model (two independent tungsten inputs) proposed from Höll and Eichhorn (2000).

The most likely timing of magmatic-hydrothermal ore formation is Early Carboniferous because U-Pb dating of the K1-K3 gneiss and Scheelite 1 yielded ages around 340 Ma (Eichhorn et al. 1999; Raith et al. 2011). The K1-K3 gneisses seem to be highly fractionated subsidiaries of the Felbertauern augengneiss (Kozlik and Raith 2017; Kozlik et al. 2016). Kozlik and Raith (2017) point out several highly differentiated orthogneisses (K1-K3, aplite gneiss, othogneiss underneath the laminated ore) in both ore zones that indicate superior magmatic-hydrothermal system. Following Kozlik and Raith (2017) K1-K3 gneisses formed syn-temporal with the Felbertauern augengneiss in separate isolated melt batches with different composition.

However, the scheelite deposit has been overprinted by at least two regional metamorphic events; at about 320-330 Ma during the Variscan and at about 30 Ma during the Alpine orogeny. According to Raith and Schmid (2010) the Felbertal W deposit is best described as a “poly-metamorphosed granite-related stockwork type tungsten deposit” without any syngenetic component.

4. Methods and analytical techniques

4.1. Mapping and sampling

During fieldwork a detailed geological map on scale 1: 4000 was created (Figure 9; Appendix A.7). The corresponding profiles are shown in Figure 10 and Figure 11. The focus of the mapping was the area around Messelingscharte including Messelingkogel (2693 m), Hochgasser (2922 m) and the area around the three lakes (Grüner See, Grauer See, Schwarzer See). Additionally, the mountain Weinbichl (2545 m, 700 m ESE of St. Pöltener Hütte), the contact of the Felbertauern augengneiss to the Basal Amphibolite at St. Pöltener Hütte and the Weinbühl (Weinbühl is the old name for mountain Weinbichl) amphibolite were mapped in detail.

Special features considered were: quartz veins, quartz sheets, larger quartz nests and feldspar-chlorite alteration. Also shown on the map are several newly identified scheelite occurrences. Historical data is not included in this version of the map.

Sampling was performed during mapping. Samples were taken from all occurring lithologies for petrographic investigations. Additionally, representative samples were taken for geochemical analysis from the following lithologies.

- Orthogneiss at east-flank of Messelingkogel
- Amphibolites belonging to the Basal Amphibolite (all types including hornblende fels and deformed amphibolite) from several locations across the working area
- Biotite-hornblende gneiss intrusion in the Basal Amphibolite
- Calc-silicate rocks and associated lithologies containing scheelite

In total 97 samples were taken with a weight from 0.3 kg to 10 kg each. Figure 3 shows a map of sampling locations. GPS coordinates and other details are listed in Appendix A.1.

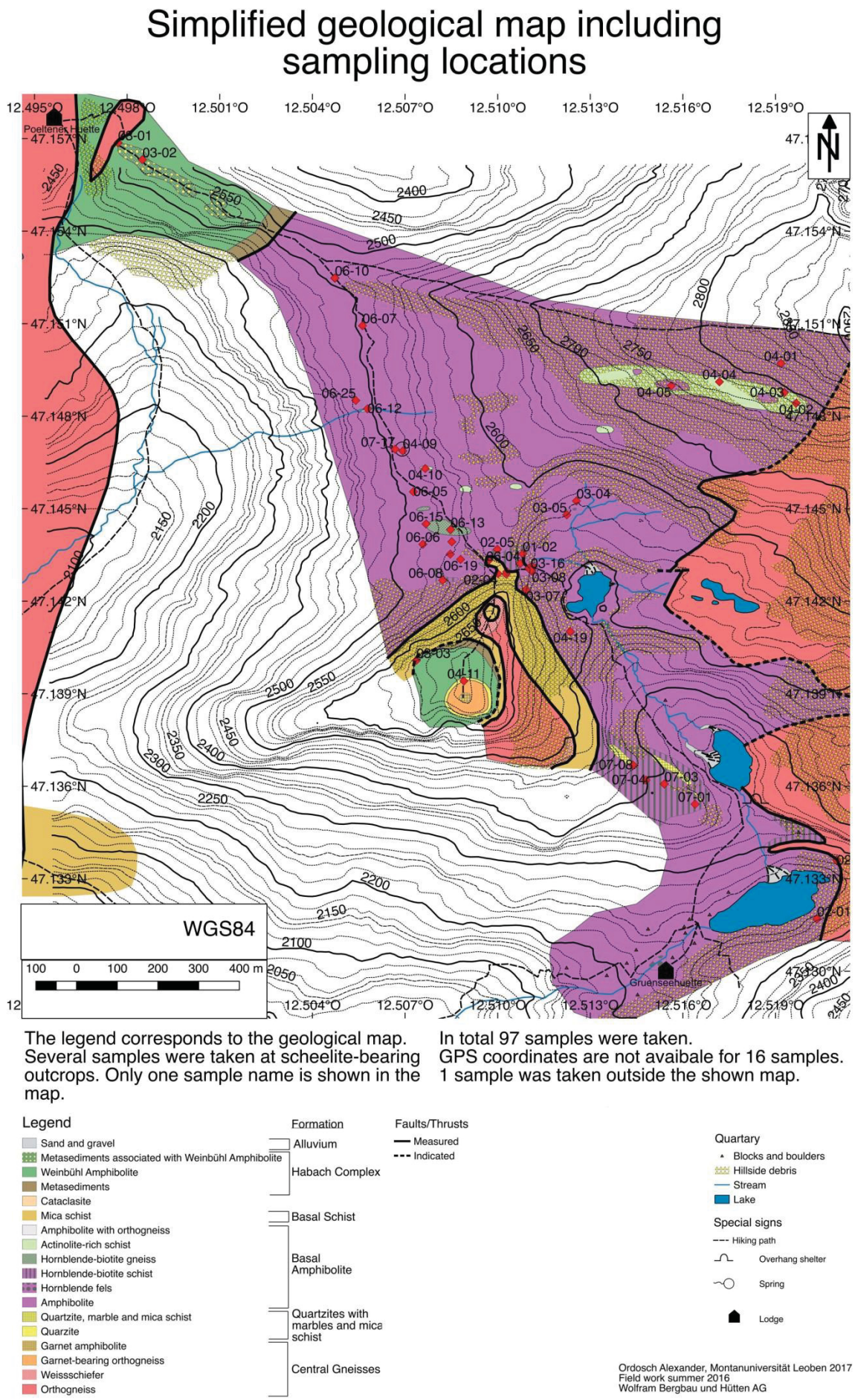

Figure 3: Map showing sampling locations.

Karsten Aupers (MSc), junior mine geologist at Mittersill tungsten mine, provided two samples of calc-silicate rocks from the underground Felbertal mine for comparison with calc-silicate rocks from Messelingscharte. The first sample (Figure 4; sample 08-01) originates from a drill core (drillcore_sample_UB437 1.33-1.66m). The second sample (Figure 5; sample 08-02) was taken from Teilsohle 650 / Hangendschiefer between K2' and SD-Gneis / Kammerbau 71 Ost.

Figure 4: Drill core with calc-silicate rocks within amphibolite, Felbertal WOZ. Sample 08-01 is from drill hole UB437, 1.33-1.66m.

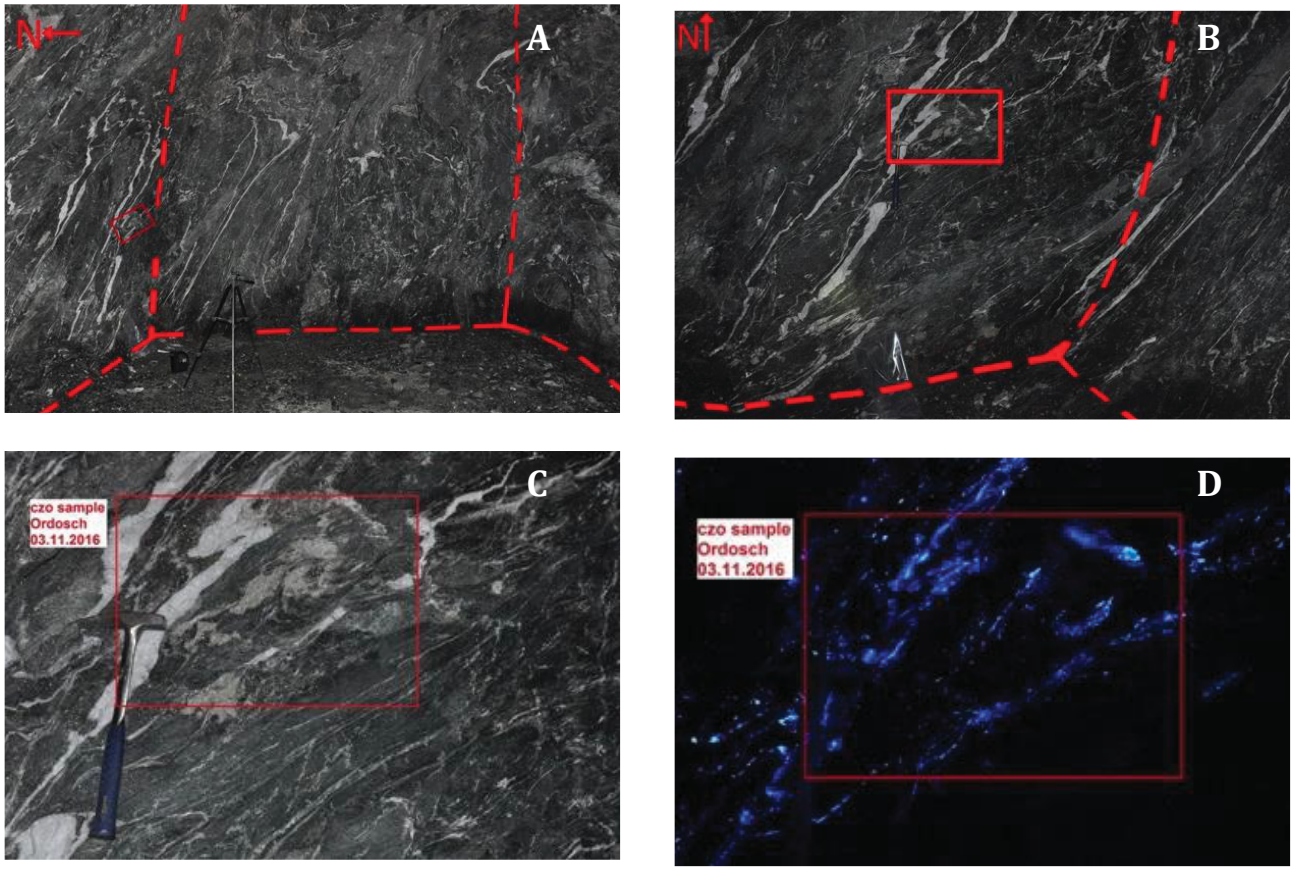

Figure 5: Photos of the sampling point of sample 08-02. **A,B** Overview of the sampling location at level 650 in the mine. Tripod is 1.5 m elevated. **C,D** Photos showing the same location of the calc-silicate patches occurring together with deformed quartz-veins within the amphibolite host rock. **D** Photo taken under short-wave UV light. Plenty of scheelite visible, also in the calc-silicate rock. Red dashed lines mark the edges of the excavation.

4.2. UV prospection

Overall, 10 nights were spent to prospect for scheelite during the field season in 2016 (Table 1). Additionally, UV lamping of selected outcrops was done during daytime using a large black cotton cloth. The following UV lamps were used:

- Two lamps UVG-47 (254nm, 6W)
- UV lamp (Raytech Industries R5-FLS-2) (254nm, 6W)

Table 1: List of all performed UV inspections.

	Date	Time	Area
2	19th July	20:15-22:30	Around Messelingscharte and adjacent area to the W
3	20th July	02:00-02:30	Around Messelingscharte and adjacent area to the E
4	28th July	20:00-23:00	Area NE of Messelingscharte and depression W of Messelingscharte
5	2nd August	20:00-22:30	W flank of Hochgasser
6	13th August	21:00-22:45	Messelingkogel eastern flank; from Messelingscharte to Grauer See
7	14th August	08:00-10:00	W of Messelingscharte
8	14th August	12:00-12:30	Between Grauer See and Schwarzer See
9	22nd August	19:00-21:30	W of Messelingscharte and direction towards St. Pöltener Hütte
10	26th July	14:00-16:00	E of Messelingscharte and up to Messelingkogel (no coordinates available)
11	27th July	20:45-21:30	Felbertauern augengneiss around St. Pöltener Hütte (no coordinates available)
12	1st August	21:00-22:00	Felbertauern augengneiss around St. Pöltener Hütte (no coordinates available)
13	2nd August	20:45-22:00	Felbertauern augengneiss around St. Pöltener Hütte (no coordinates available)

The goals of the UV prospection were to (1) relocate the scheelite-bearing outcrops reported in the literature (Gold Consultants 1978, 1979), (2) to discover more scheelite-bearing outcrops in the working area, and (3) to document the known and newly discovered scheelite mineralisation in detail.

4.3. Petrography

The petrographic description was performed in two steps. First, macroscopic description was done. Photos of rock specimens were taken using a Canon EOS 50D. Digital processing of the RAW pictures was done in Adobe Photoshop CS5 and Apple Aperture. Second, thin sections (polished sections, petrographic thin sections) were prepared from selected samples in the lab of the Chair of Resource Mineralogy and studied by optical microscopy. The microscopic study was performed using transmitted as well as reflected light microscopy. The microscopes used were Olympus BX40F4, and Zeiss AXIO Scope A.1, the latter equipped with a digital camera Zeiss AxioCam ERc 5s with the Software AxioVision Rel. 4.8.2.0.

4.4. Structural geology

Structural measurements were made in the field using a Freiberg Geologenkompass manufactured in the 1980s. Stereoplots and calculations were done using Stereonet for Apple OS X.

4.5. Geographic information system (GIS) and digital processing

The geological map was created in the open source software QGIS with several extensions (Contour plugin, Profile tool, Tile Map Scale Plugin). The used formats for the spatial data were CSV for point information, SQL for spatial information, and ESRI Shape Files for the polygons of formations. The contour lines were created using a public available DEM (digital elevation model) from the Austrian government (Geoland.at) with a spatial resolution of 10x10 m and a precision of several centimetres for the absolute height. The underground semi-transparent map in some map compilations is the Austrian Basemap (Basemap.at) that was imported into the GIS software using WMTS.

4.6. Major and trace element whole rock analyses

Geochemical data is plotted using R (v2.7.0) and GCDkit (v4.1; Janousek et al. 2006). Processing of the data was performed in Microsoft Excel 2013.

4.6.1. Sample preparation

It total, 32 samples of different lithologies were analysed for their major and trace element composition. Each sample taken had a mass between 1-5 kg, depending on the grain size of the sampled rock. The sample material was first cleaned by hand and then crushed in a jaw crusher at the Chair for Geology and Economic Geology, Montanuniversität Leoben. Afterwards, the crushed material was comminuted to a grain size <3 mm using a disc mill at the beneficiation plant of Wolfram Bergbau und Hütten AG. The used disks were made of stainless steel (ferrochrome; 83 mass% Fe, 14 mass% Cr, 1.7 mass% Si). The ground sample material was split in 3-4 representative subsamples of 200 to 400 g each using a riffle splitter. Two sub-samples were further processed for chemical analysis at Bureau Veritas Minerals Laboratiers (BVML) in Canada and at the laboratories of WBH AG in Mittersill. One sub-sample was archived and any remaining one was discarded.

Rock powders were prepared from two sub-samples using a vibrating cup mill with an agate grinding set at the Chair of Petroleum Geology, Montanuniversität Leoben. The sub-samples were first split using a riffle splitter with tight riffles to a mass between 50-100 g and then ground for 6.5 min to reduce the grain size to <63µm . Each final sub-sample had a weight between 60-80 g.

4.6.2. ICP-AES and ICP-MS analyses

The lithogeochemical analysis of the major and trace elements of all samples was performed by Bureau Veritas Minerals Laboratories (BVML) in Vancouver (Canada) using the analytical package LF202 (BVML 2016). In total 32 samples were sent to this laboratory.

Table 2: Detection limits for elements of analytical package LF202 as provided by Bureau Veritas Minerals Laboratories.

Element	Det. Lim.		Upper Lim.		Element	Det. Lim.		Upper Lim.	
SiO_2	0.01	%	100	%	Tb	0.01	ppm	1.000	ppm
Al_2O_3	0.01	%	100	%	Th	0.2	ppm	1.000	ppm
CaO	0.01	%	100	%	Tm	0.01	ppm	1.000	ppm
Cr_2O_3	0.002	%	100	%	U	0.1	ppm	1.000	ppm
Fe_2O_3	0.04	%	100	%	V	8	ppm	1.000	ppm
K_2O	0.01	%	100	%	W	0.5	ppm	1.000	ppm
MgO	0.01	%	100	%	Y	0.1	ppm	50.000	ppm
MnO	0.01	%	100	%	Yb	0.05	ppm	10.000	ppm
Na_2O	0.01	%	100	%	Zr	0.1	ppm	50.000	ppm
P_2O_5	0.01	%	100	%	Ag	0.1	ppm	100	ppm
TiO_2	0.01	%	100	%	As	0.5	ppm	1.000	ppm
Ba	5	ppm	5	%	Au	0.5	ppb	100.000	ppb
Nb	5	ppm	1.000	ppm	Bi	0.1	ppm	2.000	ppm
Ni	20	ppm	10.000	ppm	Cd	0.1	ppm	2.000	ppm
Sc	1	ppm	10.000	ppm	Cu	0.1	ppm	1.000	ppm
Sr	2	ppm	50.000	ppm	Hg	0.01	ppm	50	ppm
Y	3	ppm	50.000	ppm	Mo	0.1	ppm	2.000	ppm
Zr	5	ppm	50.000	ppm	Ni	0.1	ppm	10.000	ppm
LOI	0.1	%	100	%	Pb	0.1	ppm	10.000	ppm
Ce	30	ppm	50.000	ppm	Sb	0.1	ppm	2.000	ppm
Co	20	ppm	10.000	ppm	Se	0.5	ppm	100	ppm
Cu	5	ppm	10.000	ppm	Tl	0.1	ppm	1.000	ppm
Zn	5	ppm	10.000	ppm	Zn	1	ppm	10.000	ppm
Ba	1	ppm	50.000	ppm	C	0.02	%	100	%
Be	1	ppm	10.000	ppm	S	0.02	%	100	%
Ce	0.1	ppm	50.000	ppm					
Co	0.2	ppm	10.000	ppm					
Cs	0.1	ppm	1.000	ppm					
Dy	0.05	ppm	1.000	ppm					
Er	0.03	ppm	1.000	ppm					
Eu	0.02	ppm	1.000	ppm					
Ga	0.5	ppm	1.000	ppm					
Gd	0.05	ppm	1.000	ppm					
Hf	0.1	ppm	1.000	ppm					
Ho	0.02	ppm	1.000	ppm					
La	0.1	ppm	50.000	ppm					
Lu	0.01	ppm	1.000	ppm					
Nb	0.1	ppm	1.000	ppm					
Nd	0.3	ppm	1.000	ppm					
Pr	0.02	ppm	1.000	ppm					
Rb	0.1	ppm	10.000	ppm					
Sm	0.05	ppm	10	ppm					
Sn	1	ppm	10.000	ppm					
Sr	0.5	ppm	50.000	ppm					
Ta	0.1	ppm	1.000	ppm					

The package includes eleven major oxides and Sc determined by solution inductively coupled plasma – atomic emission spectrometry (ICP-AES). It is followed by lithium borate fusion and dilute acid digestion with hot aqua regia. Additionally, 45 trace elements were analysed by solution inductively coupled plasma – mass spectrometry (ICP-MS). Furthermore, the loss on ignition (LOI) is determined by sintering at 1000°C and Leco analysis for total carbon and sulphur is used. Iron is reported as total Fe_2O_3. Data quality and quality assurance was performed by the lab; no additional standards, duplicates or blanks were inserted.

4.6.3. XRF analyses

XRF analyses (Table 3) were performed at the laboratories of WBH AG in Mittersill on samples containing very high (>1 mass%) WO_3 concentrations. In total 8 samples were analysed for WO_3

content. Six of the samples were calc-silicate rocks containing scheelite from Messelingscharte. The remaining two calc-silicate rocks from the Habach Complex were taken in the underground mine Mittersill (see Chapter 4.1).

The WBH laboratory decided to further grind the samples to a not specified grain size because the delivered grain size did not match with the one the instrument is calibrated for.

Table 3: Conditions of XRF measurements

Device name	S4 Pioneer, Bruker
Anode material	Rhenium (4 kW)
Detector type	Scintillation counter or flow counter
Voltage and current	60 kW, 50 mA
Time for measurement	BPRESS ~3 min; EPRESS or 3-18% PRESS ~2 min
Calibration programs	BPRESS WO_3 0-0.2%, EPRESS 0.2-3%, PRESS 3-18%
Software	Spectra Plus, Bruker Topas

4.7. XRD analyses

XRD analyses of the scheelite-bearing calc-silicate rocks were also performed at the laboratory of WBH in Mittersill. Overall, 8 samples were analysed: 6 samples of calc-silicate rocks from Messelingscharte, 2 samples from calc-silicate rocks from Habach Complex. The aims of the XRD analysis was to verify the petrographic phase identification done by optical mineralogy and perform a qualitative as well as a quantitative phase analysis. Qualitative and quantitative (Rietveld refinement) XRD analysis were performed by the WBH's mine geologist Karsten Aupers (MSc).

Table 4: Conditions of XRD measurements

Device name	D4 Endeavour, Bruker
Cathode material	KFL-Cu-2K
Detector type	LynxEye, 1D-detector
Voltage and current	35 kV, 45 mA
Aperture	defined, 0.6 mm, no monochromator
Time for measurement	2 s / step
Measured 2Θ values, step size	5-90°, 0.2°
Geometry	Locked Coupled in continuous mode
Software	Diffrac Suite EVA, TOPAS V5

4.8. Electron probe microanalysis

A JEOL JXA 8200 superprobe operated by UZAG Steiermark installed at the Chair of Resource Mineralogy, Montanuniversität Leoben, was used to measure major and trace element composition of main and accessory phases in four polished thin sections. Quantitative measurements were performed using a wavelength-dispersive system (WDS). The exact measurement conditions are summarised Table 5,

Table 6 and Table 7. The beam diameter was set in focused mode to a diameter of around 1 µm. Analysis data was corrected for matrix effects by the ZAF-method.

Table 5: EMPA measurement conditions and standards for scheelite analyses. "-": no detection limit calculated because no response of the specific element was measured.

Scheelite		Acceleration voltage: 20 kV			Beam current: 10 nA	
Element	Crystal	Line	Counting time peak [s]	Counting time background [s]	Standard	Detection limit (ppm)
Ca	PETJ	Lα	20	10	Apatite	169
W	LIFH	Lα	20	10	pure W (100%)	700
Sn	PETH	Lα	40	20	PtSn alloy	-
Sr	PETH	Lα	40	20	Stronzianite	-
Mo	PETH	Lα	40	20	pure Mo (100%)	178

Table 6: EMPA measurement conditions and standards for clinozoisite analyses. "-": no detection limit calculated because no response of the specific element was measured.

Clinozoisite		Acceleration voltage: 15 kV			Beam current: 10 nA	
Element	Crystal	Line	Counting time peak [s]	Counting time background [s]	Standard	Detection limit (ppm)
Na	TAP	Kα	20	10	Albite	143
Si	PETJ	Kα	20	10	Diopside	365
Mn	LIFH	Kα	20	10	Rhodonite	193
Ca	PETH	Kα	20	10	Diopside	85
F	LDE1	Kα	20	10	F-phlogopite	-
Mg	TAP	Kα	20	10	F-phlogopite	110
Fe	LIFH	Kα	20	10	Magnetite	218
K	PETH	Kα	20	10	Sanidine	68
Al	TAP	Kα	20	10	Sanidine	108
Sn	PETH	Lα	40	20	PtSn alloy	127
Ti	PETH	Kα	20	10	Benitoite	5011

Table 7: EMPA measurement conditions and standards for titanite analyses. "-": no detection limit calculated because no response of the specific element was measured.

Titanite		Acceleration voltage: 20 kV			Beam current: 10 nA	
Element	Crystal	Line	Counting time peak [s]	Counting time background [s]	Standard	Detection limit (ppm)
F	LDE1	Kα	20	10	F-phlogopite	382
Al	TAP	Kα	20	10	REE glass	123
Fe	LIFH	Kα	20	10	Rhodonite	131
Si	PETH	Kα	20	10	Zircon	118
Zr	PETJ	Lα	40	20	Zircon	-
Ta	LIFH	Lα	40	20	pure Ta (100%)	-
Ti	PETH	Kα	20	10	Rutile	3190
Nb	PETJ	Lα	40	20	pure Nb (100%)	-
W	LIFH	Lα	40	20	pure W (100%)	-
Ca	PETH	Kα	20	10	Wollaston.	64
Sn	PETH	Lα	40	20	PtSn alloy	131

4.9. Raman spectroscopy

Raman measurements were performed using an ISA JobinYvon LABRAM confocal Raman spectrometer. A 100mW Nd-YAG Laser with an excitation wavelength of 532 nm was used. The instrument is combined with an Olympus BX40 microscope. The measurement time per spectrum was 25 s, repeated 4 times. Data was collected between 100 and 1600 cm^{-1}. A poly-ethylene standard was used for calibration. Crystal Sleuth software including the RRUFF database (Lafuente et al. 2015) was used for processing.

5. Local mapping and prospecting

5.1. Historic maps and drillings

The first detailed geological map of the study area was drawn by Fuchs (1958). This map was an integral part in the compilation of the official geological map of the area by Geologische Bundesanstalt (map Matrei in Osttirol, number 152).

In 1978 and 1979 Gold Consultants performed an exploration program including geological mapping and two drillings. The original Gold Consultants map has been digitised and is shown in Figure 6. Two exploration core drillings, each about 70 m long, were drilled by a sub-contractor in 1979. The digitised core logs of these drillings are shown in the Appendix A.6.

The geological map (Figure 6) shows several features that were not confirmed during this study:

- The discrimination between violet coloured "Hornblendefelse und Grobkornamphibolite" and brown coloured "Hornblendeprasinite, Hornblendeschiefer" was not reproducible. All four lithologies occur in intimate relationship and vary on a very small scale; i.e. they could not be mapped separately.
- The marble and quartzite unit observed on the eastern flank and on top of Messelingkogel is completely missing in the Gold Consultant's map.
- The garnet-bearing orthogneiss and garnet-amphibolite unit on top of Messelingkogel has also not been mapped although Fuchs (1958) already recognised this lithologies.
- The large E-W trending fault cutting the whole area north of Messelingscharte was not confirmed in this study. Also, other faults (e.g. south of Messelingkogel) were not confirmed.
- Finally, Gold Consultant's interpretation that the whole metabasite sequence belongs to the Habach Group is wrong. All other studies, including this one, clearly group the metabasites to the Basal Amphibolite because of field relations, lithology, geochemistry, and age data (see also Chapter 8.1, 10.1.2 and 10.1.3).

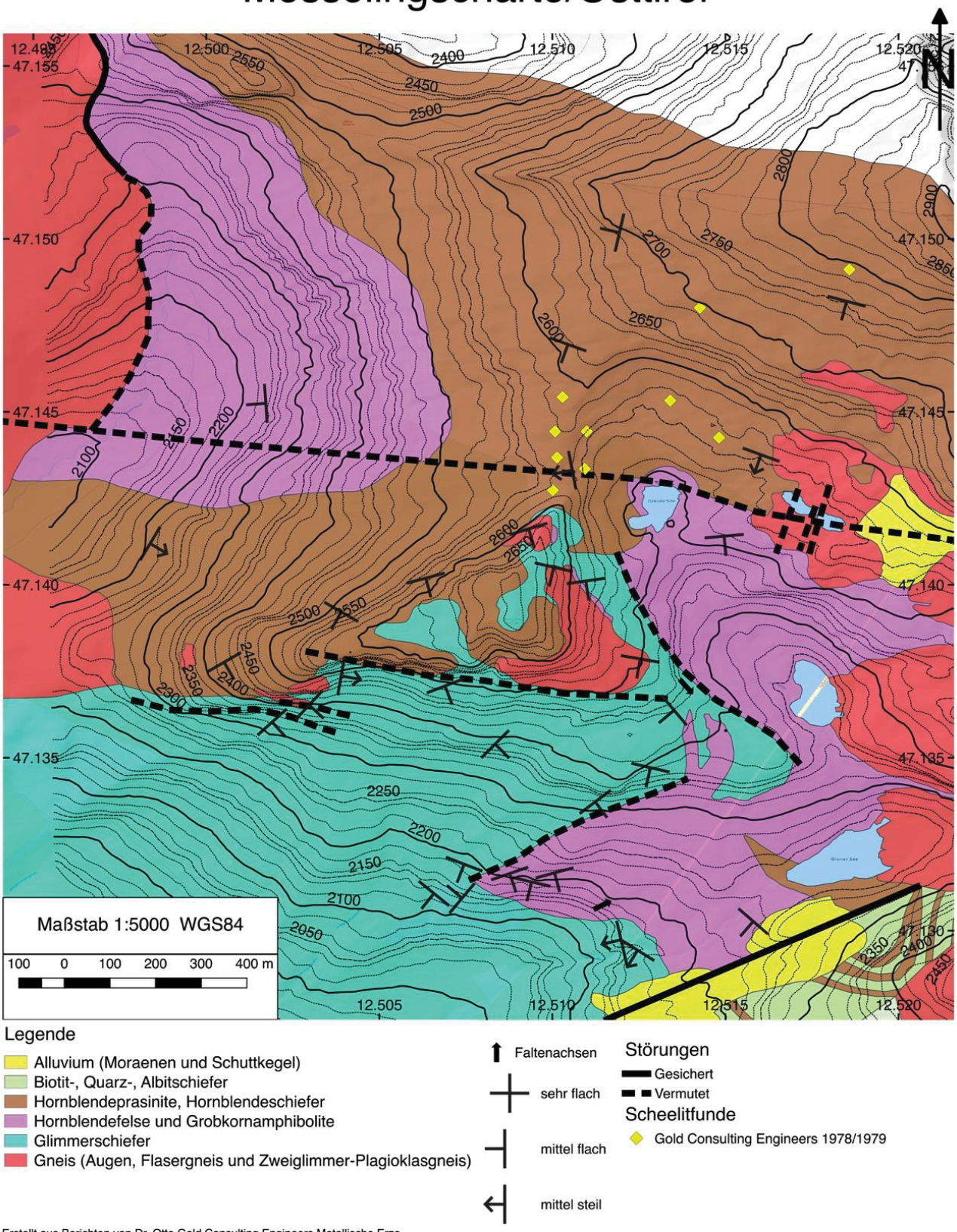

Figure 6: Digitised version of geological map from Gold Consultants (in German). The map was compiled from the geological and tectonic map and the map showing previous scheelite findings (yellow diamond symbols) by Gold Consultants (1978, 1979). The topographic background map is from geoland (basemap.at).

Exploration by Gold Consultants focussed around Messelingscharte although several high-grade scheelite-bearing outcrops/blocks were reported in the surrounding area. Two mineralised outcrops (SP5, SP6), located SW of mountain Hochgasser, yielded grades of 2-4 mass% WO_3 (with lots of sulphides). Directly at Messelingscharte an outcrop was reported with 3.05 mass% WO_3. The latter grade is an average of 7 sub-samples from a 6x2 m ore lens. However, Gold Consultants were not able to identify a larger high-grade ore body. Figure 7 shows a detail of the geological map by Gold Consultants (1978) with all then known scheelite occurrences and the locations of the two drilling sites.

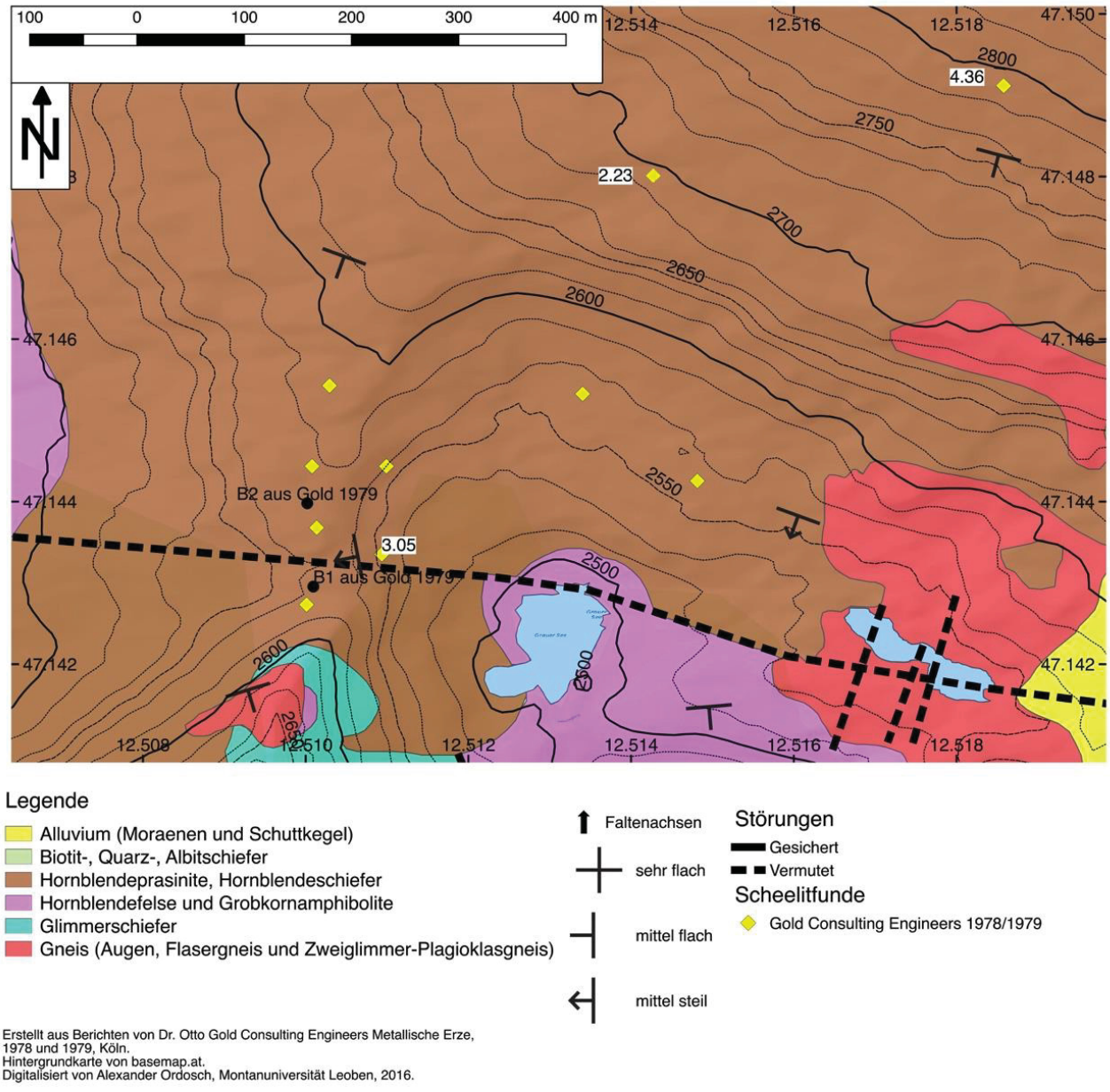

Figure 7: Scheelite findings (yellow diamonds) compiled from Gold Consultants (1978, 1979) reports. There are two high-grade ore lenses in the NE of Messelingscharte. They are marked with their grades as numbers next to the position (in mass% WO_3). The scheelite-bearing outcrop east of Messelingscharte shows a WO_3 content of 3.05 mass%. The two black spots mark the positions of the former drilling sites. The coordinate system used is WGS84.

Gold Consultants (1978, 1979) also reported two scheelite findings (together with powellite) in the Basal Schist unit although these occurrences were not marked on their map. If true, this would be interesting because the Basal Schist is known to be not mineralized in the Felbertal tungsten deposit. All the other scheelite mineralisations are bound to metabasites, especially to hornblende-prasinites (Gold Consultants 1978).

Two 70 m deep core drillings were performed in 1979 at Messelingscharte (detailed core log in the Appendix A.6). Both drill holes are situated very close to Messelingscharte (Figure 7). Amphibolites are the most common rocks with minor intercalations of gneisses and quartzites. Gold Consultants argue that the scheelite occurrence in drilling B1 between 43.8 and 44.0 m corresponds to the larger scheelite-bearing outcrop east of Messelingscharte. If correct, this scheelite-bearing zone would dramatically thin out to the west where it has a reduced thickness of only 20 cm. Then it gets terminated by an E-W trending fault. There was only minor scheelite mineralisation present in core B2, between 0.75-0.85 m, 0.9-1.0 m and 18.7-18.75 m. The WO_3 contents of the mineralised sections are very low ranging from 0.003-0.22 mass% WO_3. Gold Consultants expected a continuous scheelite-bearing horizon (similar to a stratiform syngenetic ore layer) but found it only in one drill hole at the expected depth of 0.4 m. The overall WO_3 grades of both cores were mostly below 0.1 mass% WO_3. At the end of Gold Consultants exploration campaign in 1979 it was still unknown if the mineralization continues underneath Messelingkogel; several scheelite-bearing boulders found to the west and south of Messelingkogel could indicate a larger mineralized structure.

5.2. Remarks on mapping and field work

During fieldwork, a detailed geological map on scale 1: 4000 was created (Figure 9; Appendix A.7). Corresponding geological profiles are shown in Figure 10 and Figure 11. The focus of the mapping done in 2016 was the area around Messelingscharte including Messelingkogel, Hochgasser and the area around the three lakes (Grüner See, Grauer See, Schwarzer See). Additionally, the mountain Weinbichl, the contact of the Felbertauern augengneiss to the Basal Amphibolite at St. Pöltener Hütte and the Weinbühl (Weinbühl is the old name for mountain Weinbichl) amphibolite were mapped.

During field work special attention was paid to quartz veins, quartz sheets, larger quartz nests and any type of alteration such as feldspar-chlorite alteration. Also shown on the map are all newly identified scheelite occurrences. "Historical" findings (cf. Figure 7) are not included in this map.

All major scheelite-bearing outcrops identified by Gold Consultants were re-visited, especially the two locations at Hochgasser from where high-grade scheelite-mineralization was reported. Only point SP5 was successfully relocated. This marked outcrop (Figure 8) turned out to have nearly no scheelite although Gold Consultants reported a grade of 4.36 mass% WO_3 for one sample. The coordinates of this location were given as N47.149119, E012.518582 (WGS84; recalculated from the original geographic coordinates) but no outcrop was found there or in the direct vicinity. The new coordinates of SP5, recorded by GPS, are N47.148150, E012.518512. The distance between the two positions is about 600 m in WSW direction.

The second important location (SP6) has not been found. Gold Consultants described an outcrop with a WO_3 grade of 2.23 mass%. Actually, the outcrop labelled as “5” on Figure 8 is close to SP6 (about 100

m SW). Therefore, it is assumed that coordinates were swapped by mistake. Hence, SP5 should be located at an altitude of about 2700 m and SP6 even higher towards the top of the mountain.

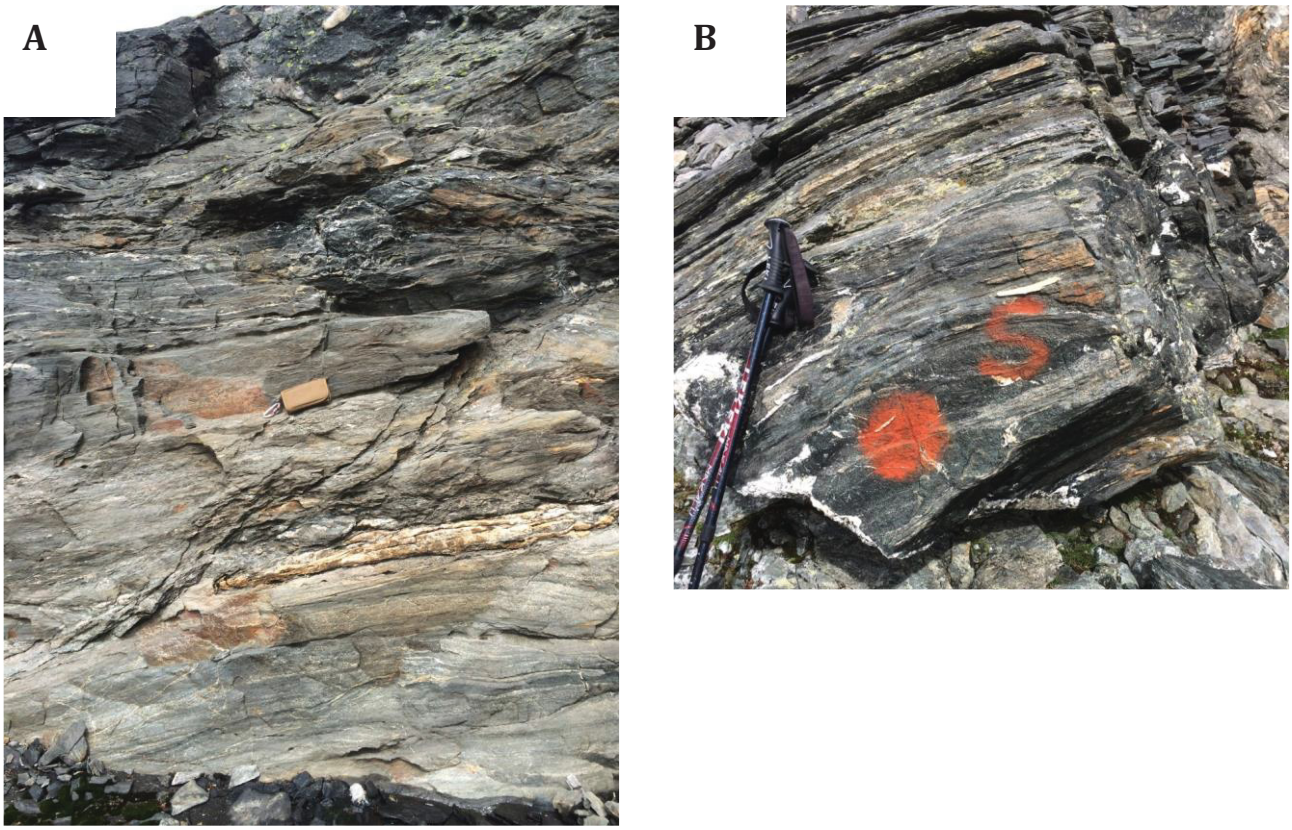

Figure 8: A Southern rock wall at outcrop SP5 (GPS #329) with the characteristic red label 5 as described in the report of Gold Consultants (1978). **B** Southern rock wall of outcrop SP5. The red labelled rock (**Figure 8**B) is directly located on the top of the outcrop. The outcrop exposes strongly deformed amphibolite with deformed quartz veins in actinolite-rich schist. Local zones of intense shear deformation are to be seen in A. There is some minor scheelite associated with epidote and quartz in thin layers (parallel to the foliation) but no significant W mineralization was identified.

The large scheelite-rich outcrop east of Messelingscharte, which is a main target of this study, was mentioned only briefly in the previous report. This outcrop is described in detail in Chapter 5.3.1.

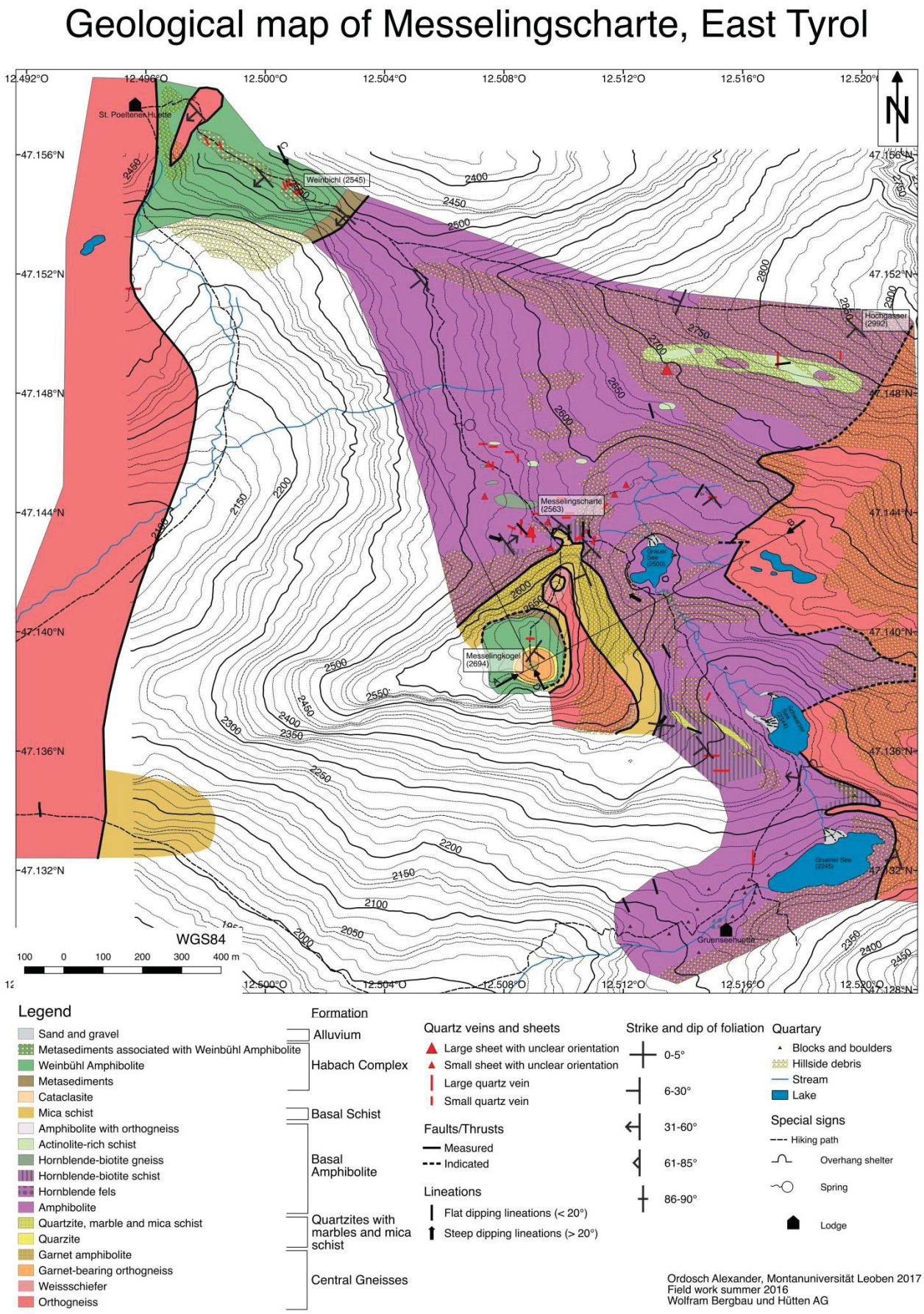

Figure 9: Geological map of Messelingscharte. The dip signs are selected signs that are representative for a larger area around the position of the sign (also statistically analysed). Veins, sheets and large nests of quartz shown are not to scale. Black arrows labelled with A-B, C-D indicate the profile lines (see **Figure 10**, **Figure 11**). Original map scale is 1:4000 (for full-scale map see Appendix A.7). The coordinate system used is WGS84.

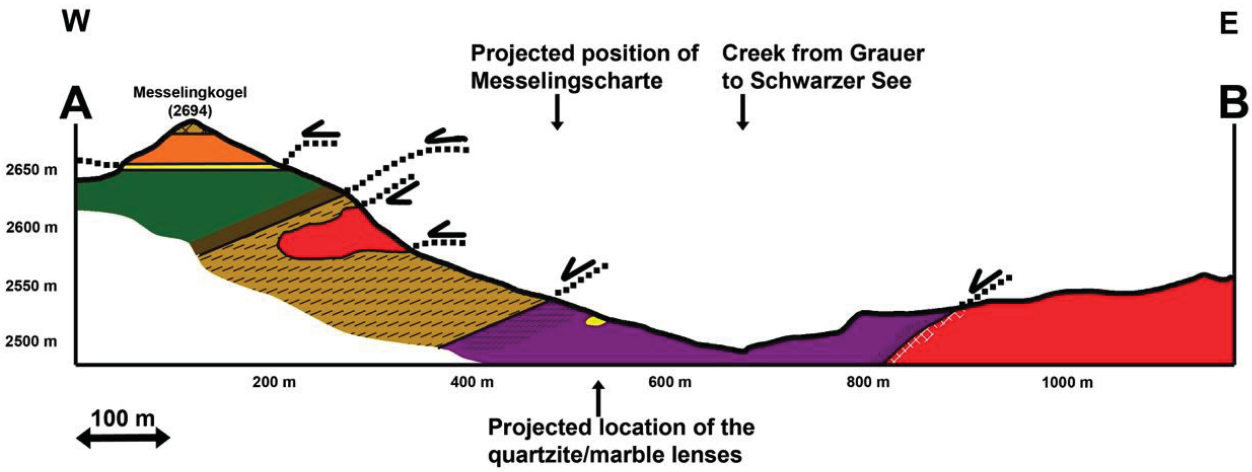

Figure 10: Geological cross section A-B. For exact location and legend see geological map (**Figure 9**).

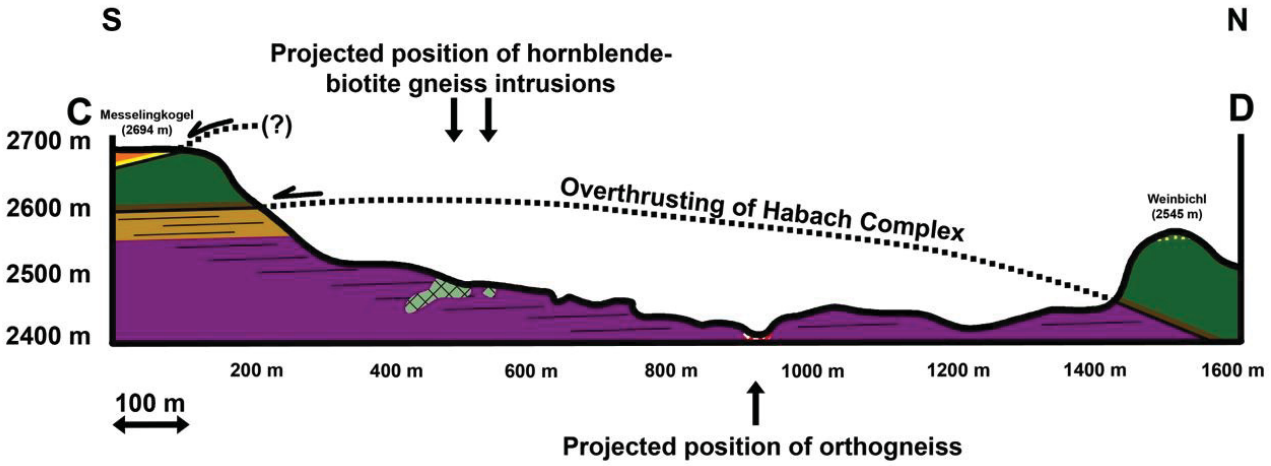

Figure 11: Geological cross section C-D. For exact location and legend see geological map (**Figure 9**). The metasediment-amphibolite sequence at Weinbichl is correlated with that above the Basal Schist at Messelingkogel and assigned to the Habach Complex. The contact to the underlying Basal Schist / Basal Amphibolite is interpreted as a thrust plane.

5.3. Scheelite occurrences

The scheelite mineralization at Messelingscharte is known since the 1970-ies and has already been described by Neinavaie (1979) when it was explored by Gold Consultants (1978, 1979) (see also Neinavaie et al. 1983). Neinavaie (1979) described the scheelite mineralisation as a stratabound, laterally extensive, 30 cm thick horizon that "continues 5 km to the south to Haupmeralm". However, the current fieldwork has not shown any significant lateral extension of this postulated scheelite-bearing horizon.

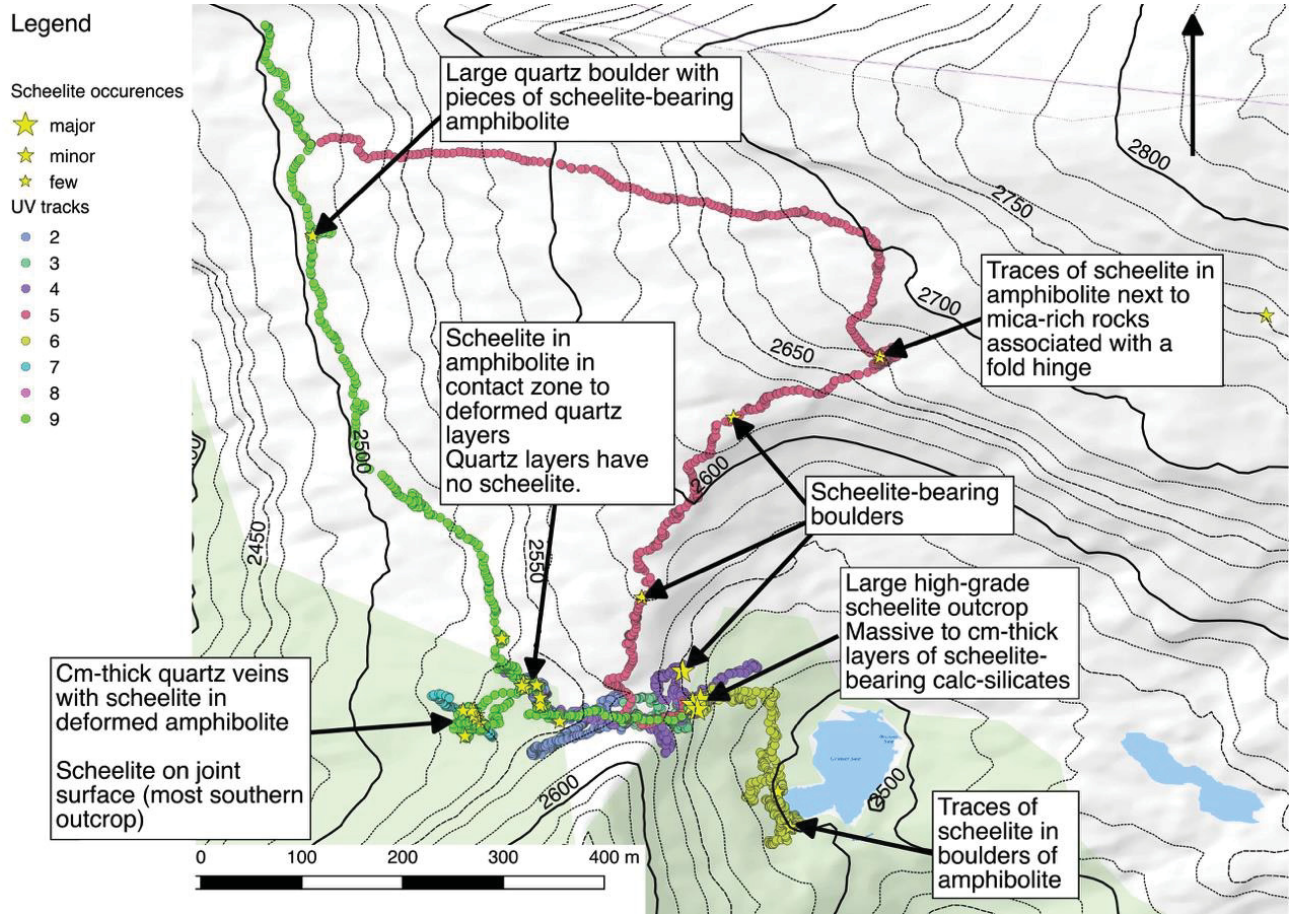

Figure 12: Map of the tracks covered during night prospecting with the UV lamp. Also, two short tracks of UV prospecting during daytime are included; they were revisited during night again because in both cases significant amounts of scheelite were identified.

The focus for further exploration for scheelite was the vicinity around Messelingscharte because of known scheelite-rich outcrops (description in Chapter 5.3.1).

Kozlik (2016) already took a sample of Felbertauern augengneiss (SP-25/34) on the south-west flank of Messelingkogel and reported traces of scheelite from this orthogneiss. Therefore, the Felbertauern augengneiss around St. Pöltener Hütte was also searched intensively three times during night for scheelite. Only two small occurrences of fine-grained blue luminescent scheelite were identified. In both cases scheelite occurs in quartz patches in deformed leucocratic gneiss. One location is located 70 m south of the lodge in a roundish quartz cluster. The second finding is located north of the lodge in a several metres long quartz layer inside the deformed gneiss. Both times no coordinates were recorded because of lacking precision (poor GPS signal).

5.3.1. Types of scheelite mineralization

All previous studies referred to W mineralization at Messelingscharte as stratabound; i.e. the lateral continuation of the scheelite-bearing horizon (Neinavaie 1979; Gold Consultants 1978, 1979). This study confirmed that scheelite is very common in the whole area around Messelingscharte. It occurs in different lithologies and the four different types of mineralization are described below.

Beside described mineralization types below, scheelite occurs regularly disseminated in amphibolite. Most identified boulders away from Messelingscharte show this type of scheelite occurrence (e.g. boulders on west flank of Hochgasser). Scheelite is exclusively blue, fine-grained and occurs in small scheelite accumulations. They are interpreted to be Alpine metamorphic mobilizations.

Scheelite-bearing clinozoisite-plagioclase-calc-silicate fels

There is one larger outcrop of massive- to semi-massive scheelite-bearing calc-silicate rocks only few metres east of Messelingscharte (N47.143067, E012.511009, WGS84). Scheelite occurs in massive non-foliated, bright clinozoisite-rich calc-silicate rocks together with green, tightly foliated amphibole schists. The calc-silicate rocks are hosted in amphibole schist and amphibolites, the latter partly strongly deformed. Just one single outcrop (GPS #301) exposing such high-grade scheelite-bearing calc-silicate rocks were found in the whole area. A sketch of the location of scheelite-bearing rocks and the geologic situation of the area is shown in Figure 13.

Figure 14 shows an UV photographs taken in-situ of scheelite-bearing calc-silicate rock and amphibole schist during night (more pictures are shown later in Figure 19, Figure 20, Figure 21).

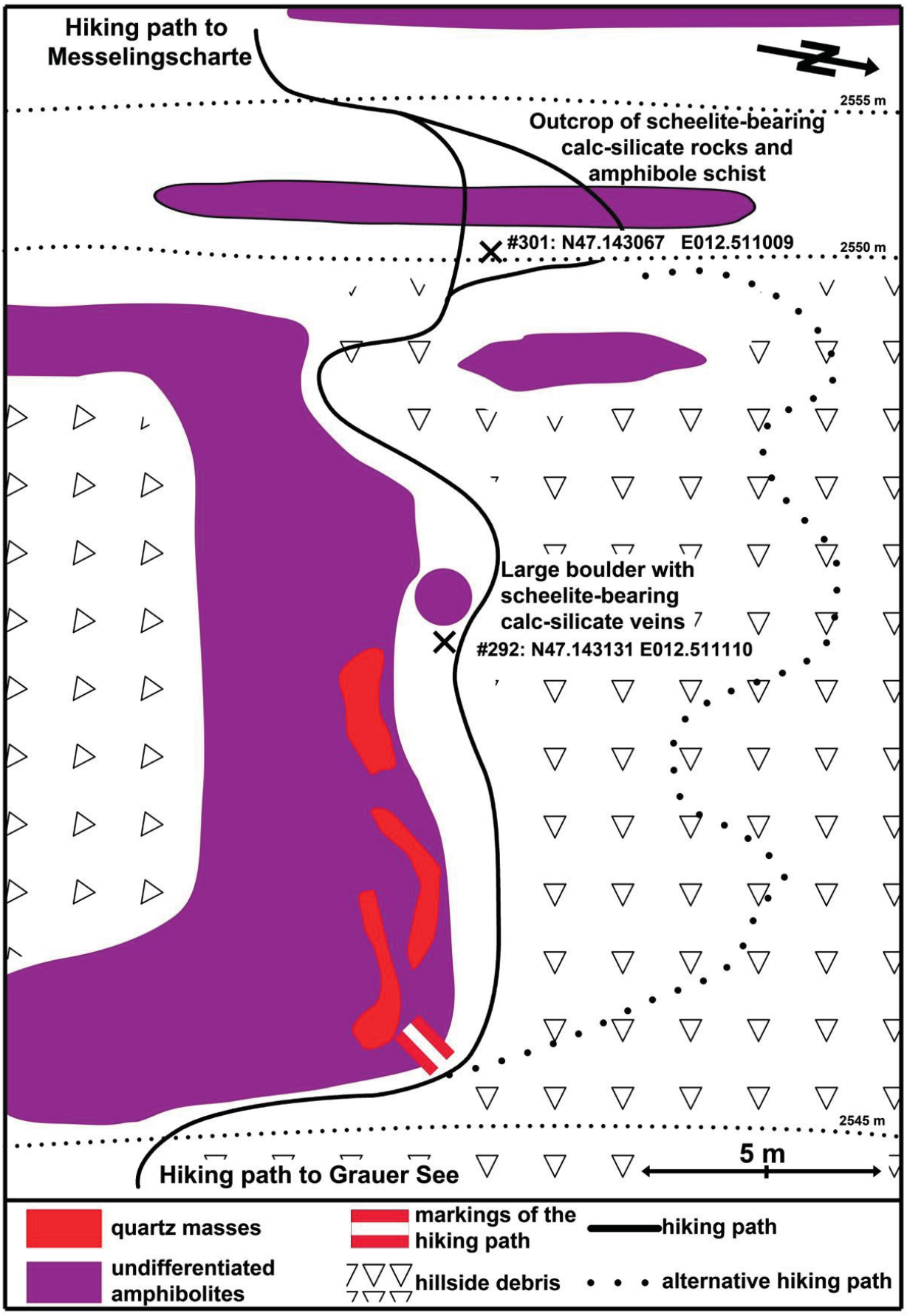

Figure 13: Sketch map (plan view) showing the position and surrounding outcrops of the main scheelite-bearing outcrop of calc-silicate rocks at Messelingscharte.

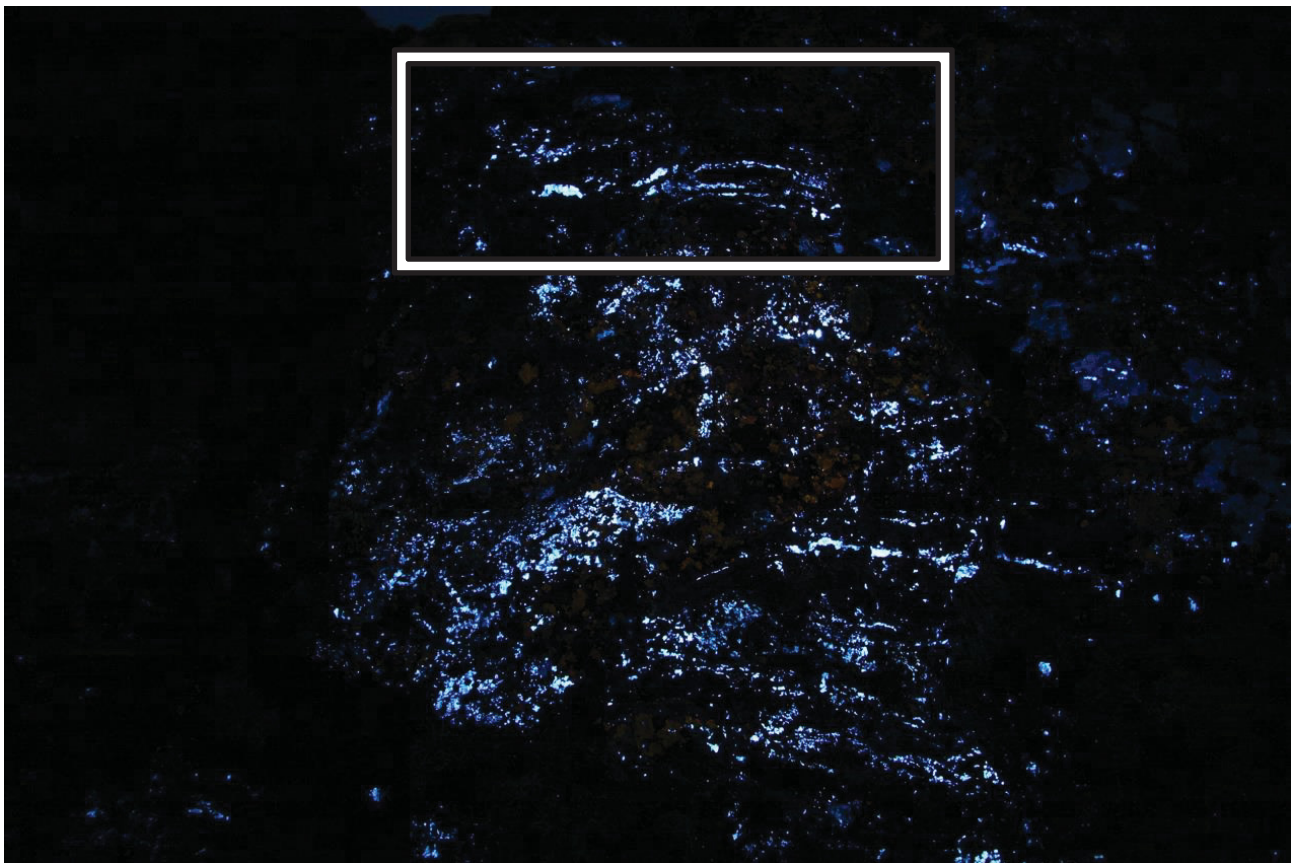

Figure 14: High- grade scheelite ore at Messelingscharte. The white rectangle marks the part which is enlarged in **Figure 19**. The length of the photo is about 2 m. The total area of the high-grade ore "pod" is c. 1.5x1.0 m. Field photo taken with short-waved UV-light.

Calc-silicate rocks are a subordinate lithology in the study area. They occur as roundish pods/nests exposed close to Messelingscharte. There the calc-silicate pods are exposed in an about 5 m long zone with a dimension of about 1x1 m on the southern side of the outcrop and 1.5x1.0 m on the northern side. The calc-silicate rock cuts the dominant foliation of the host rocks sharply although locally scheelite is aligned in individual layers (Figure 14, Figure 19).

Figure 16, Figure 17 and Figure 18 document the detailed field relationships of the scheelite-rich calc-silicate outcrop at Messelingscharte. The legend of those figures is shown in Figure 15.

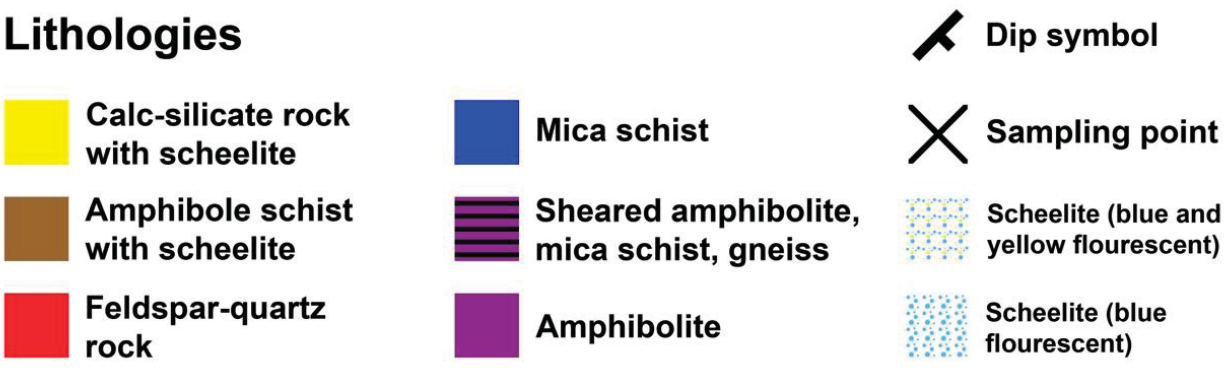

Figure 15: Legend for the different lithologies and other used symbols for **Figure 16**, **Figure 17** and **Figure 18**.

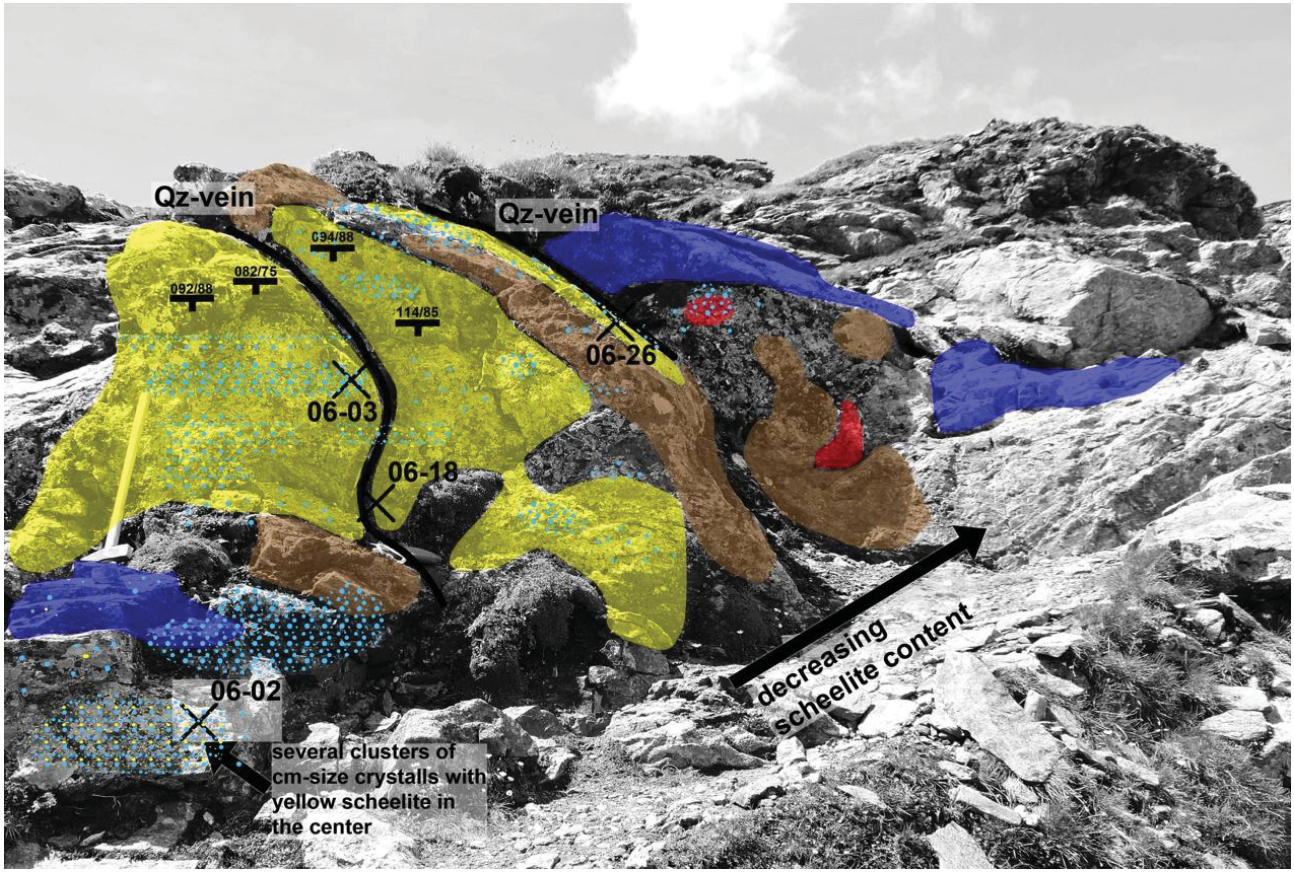

Figure 16: Illustration of the lithologies, sampling points (crosses), dip directions and further information of the outcrop of scheelite-bearing calc-silicate rock. The figure shows the right (northern) side of the outcrop.

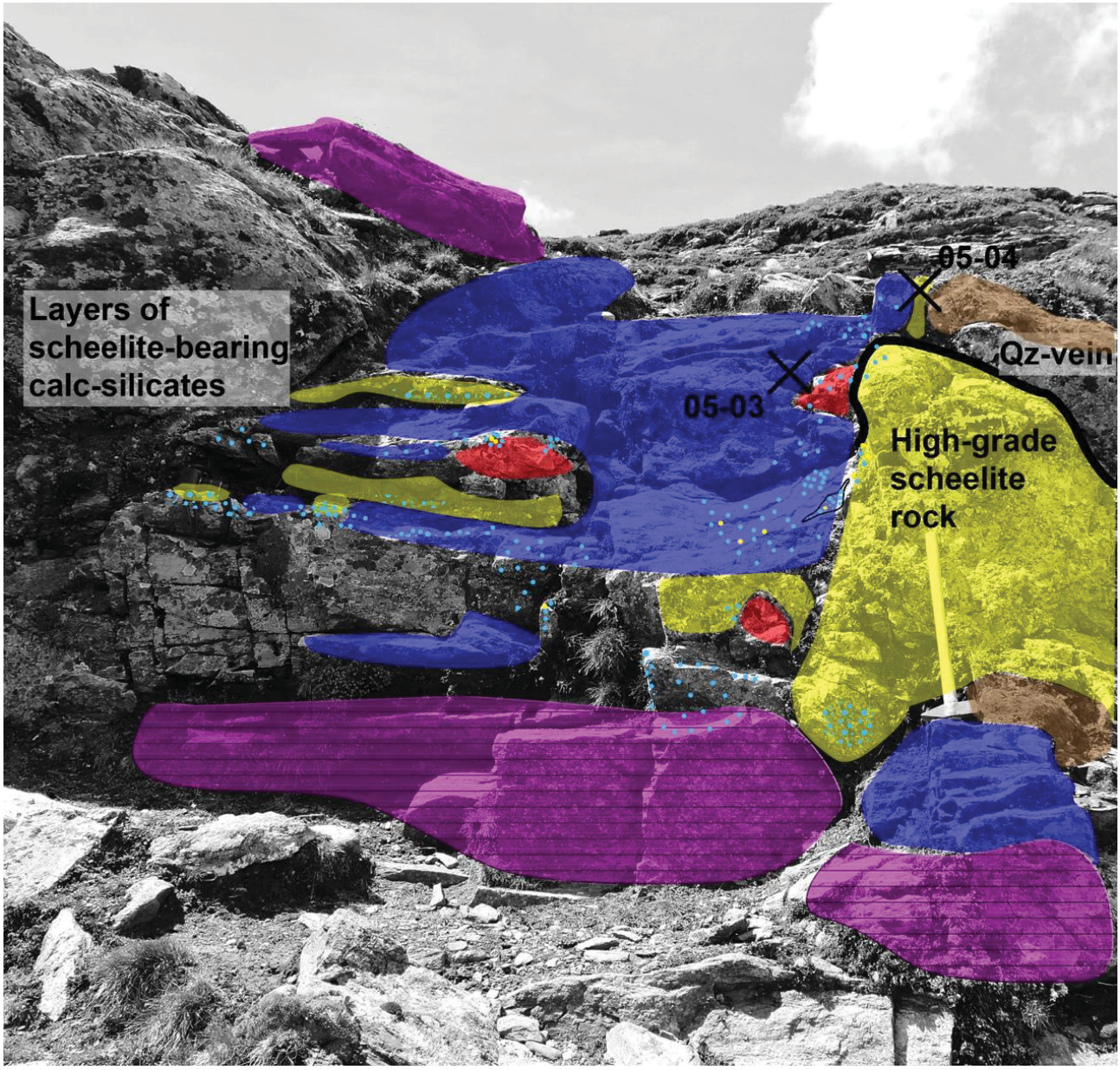

Figure 17: Illustration of the lithologies, sampling points (crosses), dip directions and further information of the outcrop of scheelite-bearing calc-silicate rock. The figure shows the middle part of the outcrop.

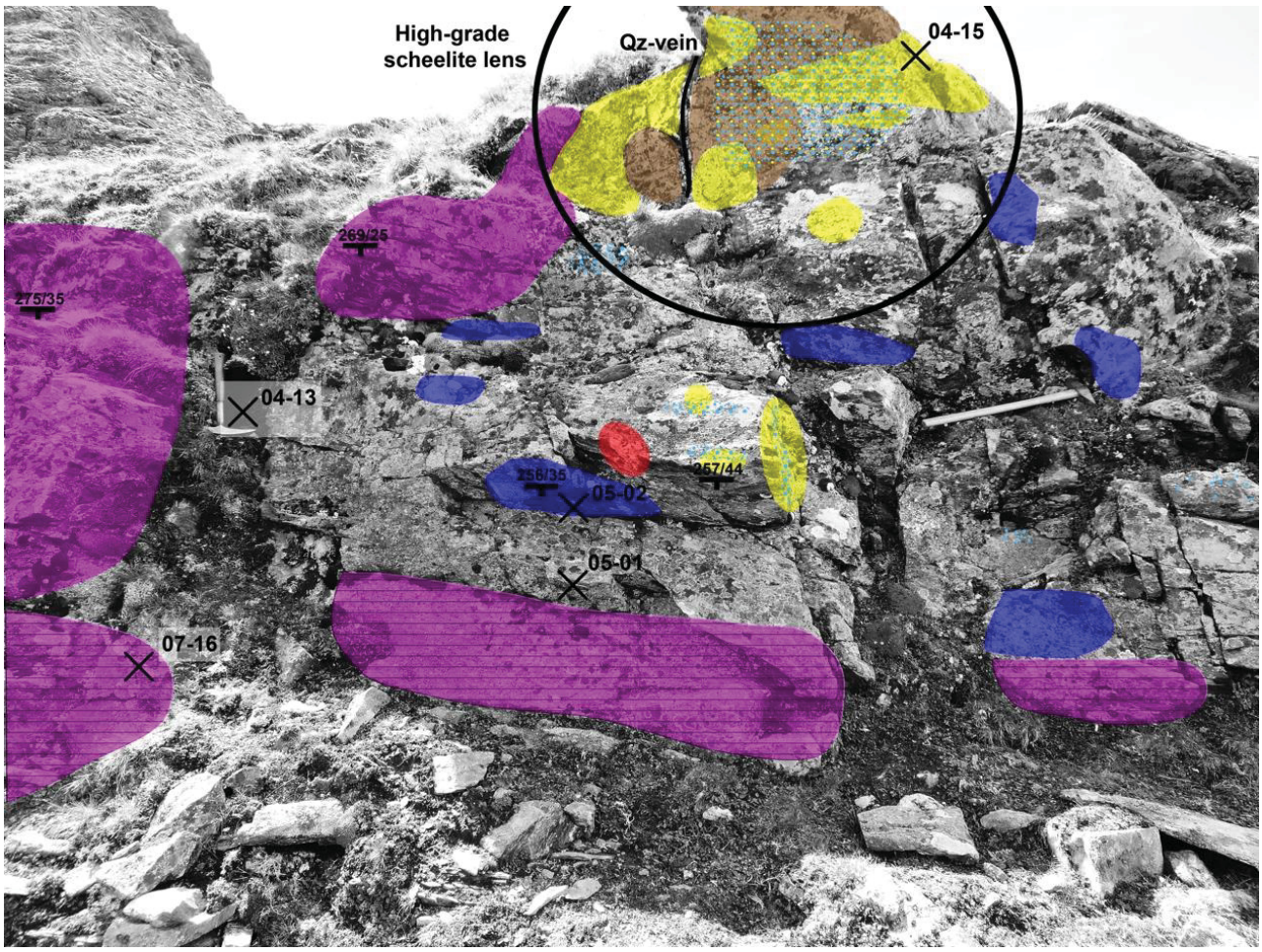

Figure 18: Illustration of the lithologies, sampling points, dip directions and further information of the outcrop of scheelite-bearing calc-silicate rock. The figure shows the left (southern) part of the outcrop.

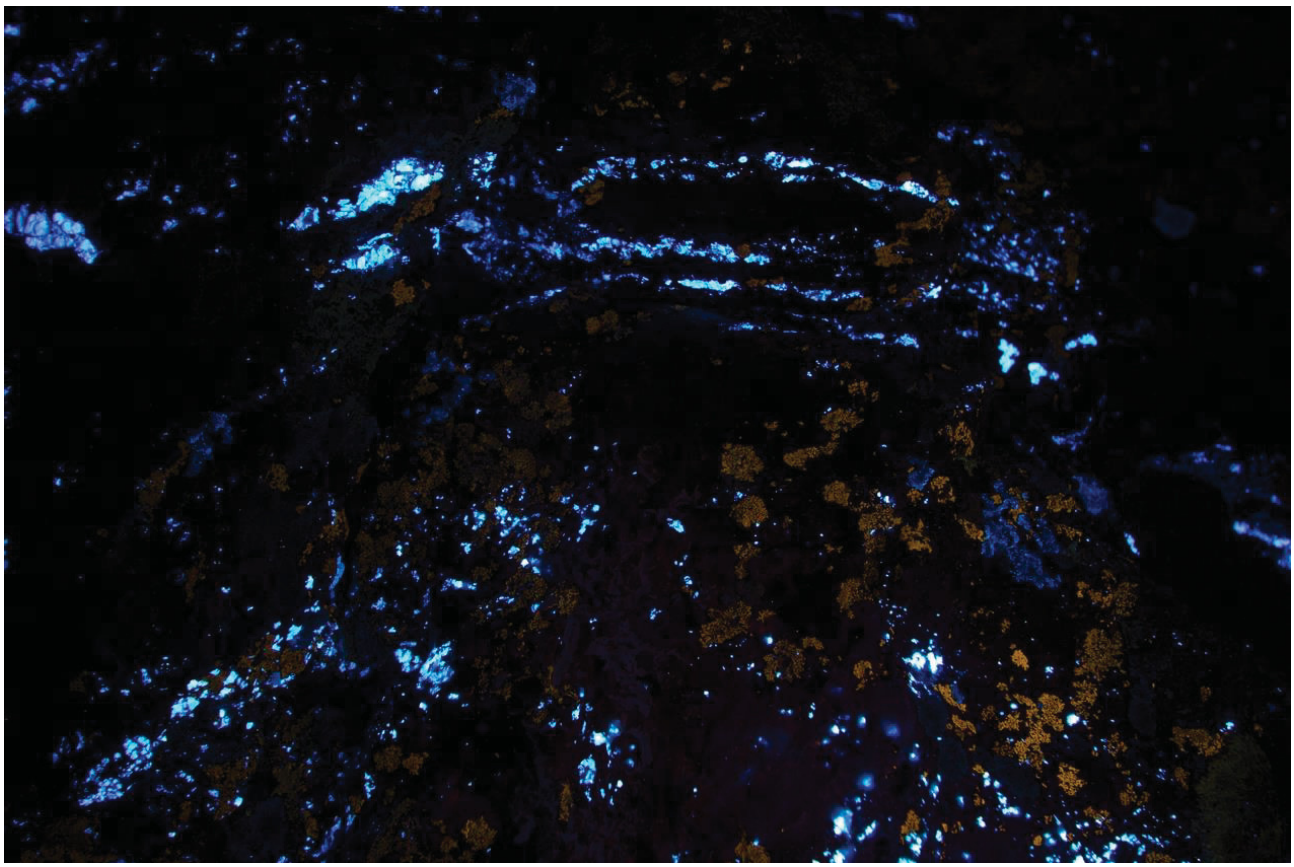

Figure 19: Enlarged area shown in **Figure 14**. Scheelite occurs in layers roughly showing the same orientation as the foliation in the host rocks. On this picture, also orange fluorescent lichens are visible. UV light with 254 nm wavelength. Length of photo is about 80 cm.

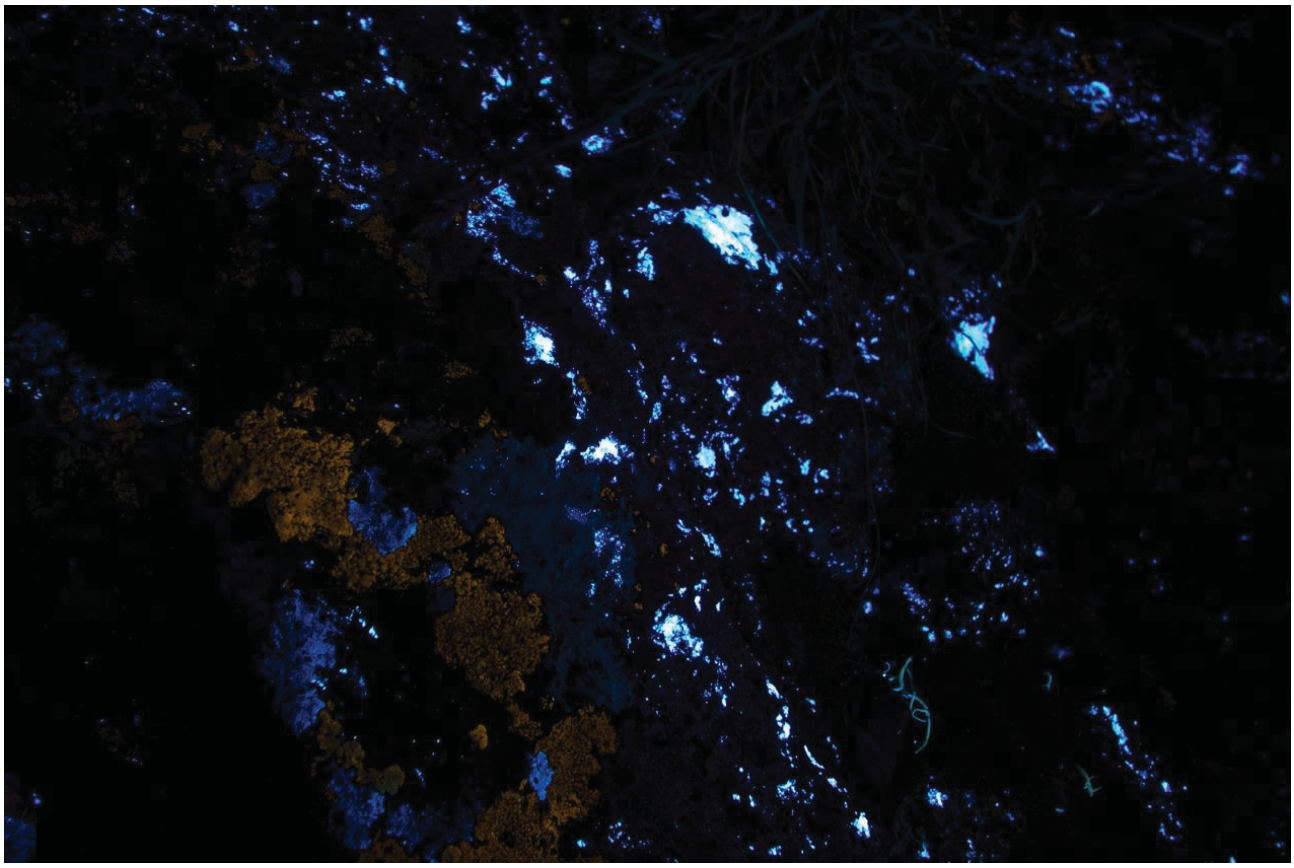

Figure 20: Scheelite mineralization in the central part of the scheelite outcrop. The long side of the picture is about 1 m.

Near to the main scheelite outcrop there is a single large boulder containing cm-thick discordant scheelite-bearing quartz veins (GPS #292 in Figure 13). This type of scheelite was not identified in any other outcrop. The quartz veins have an irregular shape. Scheelite occurs especially in areas where the vein widens becoming up to 5 cm thick. The host rock of these veins, an amphibole-micaschist, is not strongly mineralized. It consists of biotite (40%), amphiboles (20%), chlorite (10%), quartz (10%), plagioclase (10%), clinozoisite/epidote (10%), and accessory rutile, weathered pyrite and scheelite. Feldspar is intensively altered to epidote/clinozoisite. There is blue as well as yellow luminescent scheelite present.

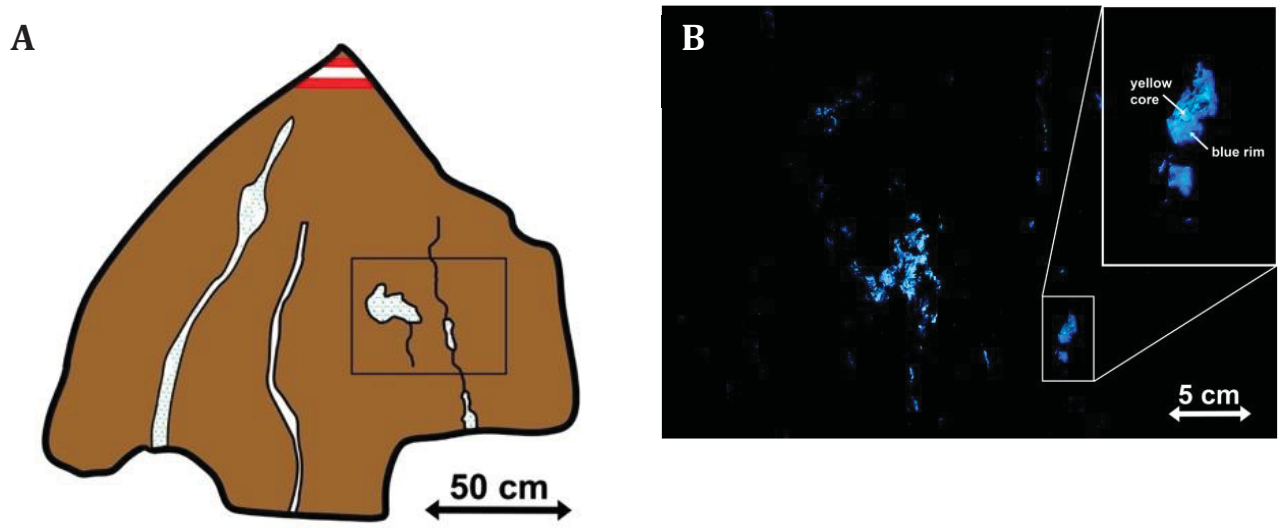

Figure 21: A Sketch of a single large boulder at outcrop #292 (N47.143131, E012.511110, WGS84). Boulder contains scheelite-bearing quartz veins and smaller patches of clinozoisite-plagioclase-calc-silicate rock in amphibole schist. The calc-silicate minerals are mainly found where the quartz vein widens. The black rectangle shows photograph area shown in B. This boulder can be identified easily by a hiking path sign (Austrian flag) on top of the boulder. **B** UV-photograph showing large scheelite crystals in quartz veins. In the larger scheelite crystals a yellow core and a blue rim can be distinguished.

Scheelite in deformed quartz veins

Scheelite was found in deformed quartz veins hosted in strongly deformed amphibolite about 150 m to the west of Messelingscharte (N47.142878, E12.508177, WGS84). It was possible to identify several different scheelite-bearing quartz veins (Figure 22) with a thickness ranging from few mm up to few centimetres. The veins are deformed; e.g. they show pinch-and-swell structures, but they are discordant to the main foliation of the host rock (Figure 22). The dip direction of the veins is roughly 045/80.

The originally discordant veins were affected by deformation. Depending on the orientation of the veins they are either rotated into the dominant foliation or become folded.

Figure 22: Deformed scheelite-bearing quartz veins in amphibolite. Discordant scheelite-quartz veins are rotated into the foliation. Scheelite-quartz vein showing ptygmatic folding. The carabiner has a length of 8 cm.

Additionally, there are also sheared and deformed layers and patches of calc-silicate rocks present in these outcrops but without visible scheelite. The surrounding hornblende fels also displays pinch-and-swell structures. There are several shear bands present with different orientations (032/45, 220/26).

Scheelite crystals in the quartz veins are up to 8 mm in size. Their luminescence colour is blue to pale blue for the smaller scheelite crystals. Larger scheelite crystals show mostly a yellowish core surrounded sharply by a blue rim (Figure 23).

Figure 23: Blue luminescent scheelite crystal with a size of 8 mm for the large crystal. The very bright centre of the large grain is the yellow luminescing core. The quartz vein trends from left to right in the picture.

Scheelite in amphibolite next to mylonitic quartz veins

This type of scheelite mineralization occurs in the depression about 100 m to the west of Messelingscharte (N47.143064, E12.509047, WGS84). This mineralized area is more than 100 m long in north-south direction and about 50 m in east-west direction. It ends sharply to the north due to topography but it could continue underneath Messelingkogel towards south. The mineralized rock package seems to taper out to the east; i.e. it is not exposed on the eastern side of Messelingscharte. The boundary to the west is defined by the morphology that goes downhill. The whole mineralized rock package has a thickness of about 5-10 m. It is characterized by strongly deformed layers of quartz that have a thickness of 1-50 cm and are hosted by fine- to coarse-grained deformed amphibolites and

hornblende felses (Figure 24). The quartz layers are aligned in the main foliation and show mylonitic texture. They likely represent strongly deformed quartz veins. Quartz layers and host amphibolite have a prominent nearly sub-horizontal penetrative foliation with local (isoclinal) folds. Locally, irregular massive quartz nests are to be seen.

The quartz layers are normally scheelite-free but scheelite occurs in the strongly foliated contact zone between quartz and amphibolite. Only sparse, fine-grained, blue luminescent scheelite was found. Despite the low scheelite content, this area is of potential interest because it has by far the largest spatial dimension of all mineralization types.

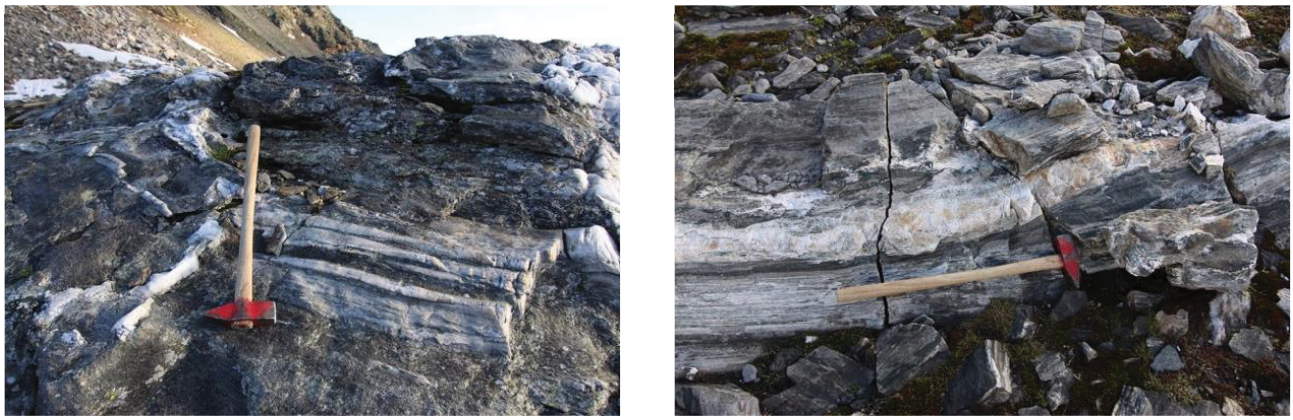

Figure 24: Outcrops of fine-grained blue scheelite in mylonitic quartz layers. Scheelite is present at the contacts within foliated amphibolite. Outcrops located ~100 m W of Messelingscharte.

Scheelite in joints in amphibolite

There is one location of scheelite-bearing amphibolite that shows a rich scheelite mineralization on a joint surface. It is located to the south of the scheelite-bearing quartz-veins (GPS #315, N47.142651, E012.508032, WGS84; Figure 12). The host rock is a dark, medium-grained, biotite-rich amphibolite that locally shows chlorite-feldspar alteration. The scheelite-rich joint surface is about 70x40 cm. There are several hundreds of (pale) blue as well as yellow luminescent scheelite grains with a grain size of <1 mm to few millimetres. The scheelite mineralization ends sharply at the chlorite-feldspar alteration front; i.e. it is predating alteration.

6. Petrography

6.1. Central gneisses

Central gneisses comprise a group of different orthogneisses that are assigned to Permo-Carboniferous intrusions or to the Variscan basement (Schmid et al. 2013). Three different central gneisses occur in the mapped area.

6.1.1. Granatspitz gneiss and Weissschiefer

Samples: 04-18 (thin section), 04-19, 04-20, 07-10, 07-18

Granatspitz gneiss occurs in the easternmost of the mapping area as part of the large Granatspitz core and as a tectonic slice in Basal Schist (later referred as "Messeling gneiss") on the eastern flank of Messelingkogel. The Granatspitz gneiss is a two-mica, medium- to coarse-grained, leucocratic orthogneiss (Figure 25; Table 8). Additionally, muscovite-rich orthogneiss and quartz-rich orthogneiss occur. The grain-size varies strongly but is normally coarse-grained to very-coarse grained. K-feldspar forms large porphyritic crystals (regularly >5 cm) and gives the rock the characteristic augengneiss fabric. The degree of deformation ranges from intensively deformed strongly foliated rock to rocks showing an undeformed fabric like a granite.

Figure 25: Sample (04-18) of leucocratic Granatspitz gneiss and the orthogneiss occurring at Messelingkogel characterized by cm-sized feldspar. The magnifier has a diameter of 2.5 cm.

Table 8: Rock forming minerals of Granatspitz gneiss.

Mineral	Remarks	Abundance
Quartz	medium- to coarse-grained, anhedral roundish grains, builds qz-layers parallel to foliation	40%
K-Feldspar	very coarse-grained, anhedral, plagioclase and muscovite inclusions, porphyric crystals, Karlsbader twins, perthitic exsolution	30%
Muscovite	medium- to coarse grained, subhedral platy, perfectly aligned in thin layers into the foliation, also alteration mineral of feldspar	20%
Plagioclase	medium-grained, altered, anhedral, also occurs as inclusions in K-feldspar, albite law twinning with narrow-spaced polysynthetic twin lamellae	8%
Biotite	medium-grained, euhedral, shows reaction to chlorite	2%

Accessory minerals are apatite, epidote/clinozoisite and chlorite. Fine-grained epidote/clinozoisite occurs in altered plagioclase grains. Chlorite occurs as alteration product of biotite.

The fabric is gneissose with large porphyroclastic K-feldspars (Figure 26). Mica is perfectly aligned in foliation planes. K-feldspar is wrapped by mica and quartz layers.

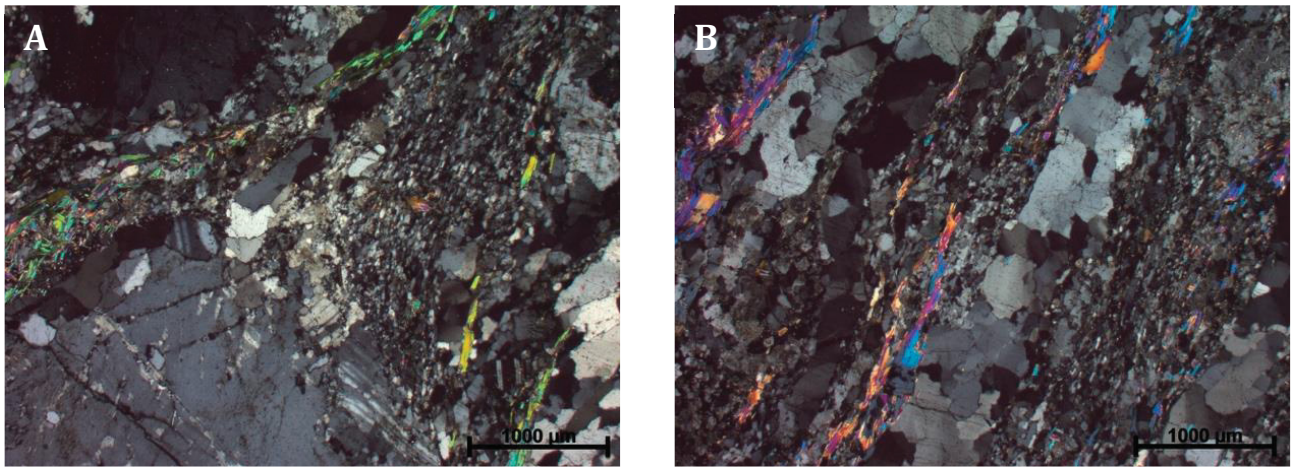

Figure 26: Photomicrographs of thin sections, sample 04-18. **A** Large porphyric K-feldspar with muscovite and quartz wrapping around it. **B** Quartz-rich and muscovite-rich layers defining the foliation in the gneiss. Quartz is partly recrystallized to a fine matrix. Crossed nicols.

Weissschiefer is a local term for strongly tectonized and altered Central Gneiss that contains nearly exclusively muscovite. The rock is purely white and grain size varies strongly from fine- to coarse-grained. The fabric is strongly foliated (S-tectonite). Weissschiefer typically develops in shear zones in orthogneiss. The transition from sheared orthogneiss to Weissschiefer is gradual. Weisschiefer is prominent on the northern ridge of Messelingkogel, about 200 m uphill from Messelingscharte, or in the east of the working area at the contact between Granatspitz gneiss and Basal Amphibolite. Furthermore, there are large faults in Felbertauern augengneiss indicated by Weisschiefer outcropping at the road from Venedigerblick towards St. Pöltener Hütte.

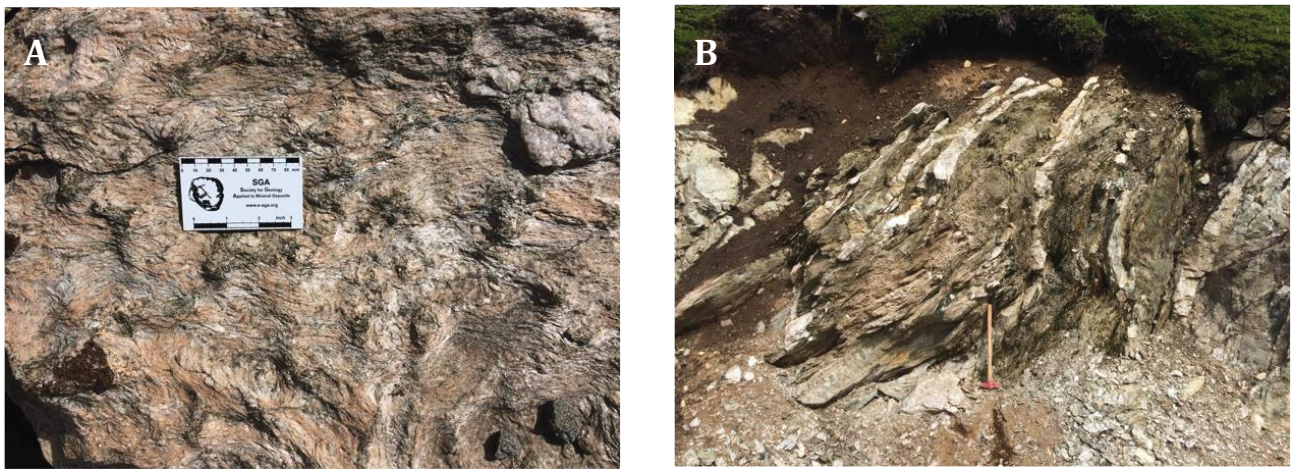

Figure 27: A Photo of a Weissschiefer boulder on the east flank of Messelingkogel. Rock contains only white muscovite and quartz. **B** Fault zone in Felbertauern augengneiss at the S-W flank of Messelingkogel. Fault zone about 4 m in width. Fault completely filled with Weissschiefer and bright quartz layers.

6.1.2. Felbertauern Augengneiss

The Felbertauern augengneiss occurs in the westernmost part of the working area. It is a leucocratic orthogneiss, commonly with a strongly foliated mylonitic fabric. The gneiss contains strongly deformed, medium- to coarse-grained, bright feldspar in addition to quartz and biotite. Quartz is also present in cm-thick layers, nests that can reach several dm in diameter and smaller cm-large deformed

spots. Biotite shows perfect plate-like habitus and is generally more fine-grained than feldspar and quartz. Blue luminescent, fine-grained scheelite occurs in quartz sheets, nests and spots at two locations near St. Pöltener Hütte. For a detailed petrographic description see Kozlik (2016).

6.1.3. Orthogneiss and amphibolite

Samples: 04-06 (thin section), 04-07 (thin section), 04-08

On the top of Messelingkogel occur garnet-bearing orthogneiss and garnet-amphibolite of unknown assignment. They are underlain by a sharply defined quartzite layer that is present in other locations upon the Central Gneisses as metamorphic equivalent of transgressive sandstone dominated cover sediments (Kurz et al. 1998). The orthogneiss is assigned to the Variscian basement ("Altes Dach") but is called "paragneiss" in the official geological map (Frank et al. 1987).

The orthogneiss is a mesocratic, small-grained, garnet-bearing two-mica gneiss (Figure 28A; Figure 29; Table 9). Brownish secondary limonite occurs along the foliation planes and as small dots in the rock. The fabric is slightly foliated shows a slight banding produced by higher content of biotite.

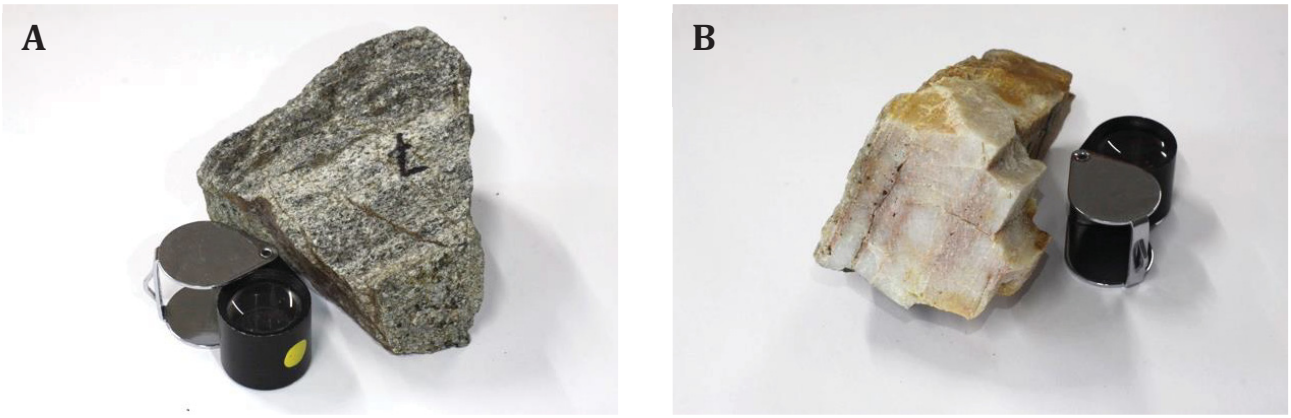

Figure 28: Photographes of hand specimen of rocks from the peak of Messelingkogel. **A** Typical greyish appearance of the garnet-bearing orthogneiss (sample 04-07). **B** Quartzite (sample 04-11) that underlies the orthogneiss at Messelingkogel. The petrography of this rock is shown in the Chapter 6.5.

Table 9: Rock forming minerals of garnet-bearing orthogneiss. Sample 04-07.

Mineral	Remarks	Abundance
K-feldspar	medium- to coarse-grained porphyroclastic (subhedral roundish grains), twins after Karlsbad law, growth zonation, perfect cleavage	55%
Biotite	brown pleochroism, medium-grained, platy, subhedral, wraps K-feldspar	20%
Quartz	medium-grained, anhedral roundish grains, recrystallized; concentrated in deformed layers, wraps K-feldspar	10%
Muscovite	medium-grained, platy, subhedral, also inclusions in feldspar	5%
Garnet	small- to coarse-grained garnet porphyroblasts, lots of inclusions, roundish grains	5%
Plagioclase	medium-grained, small sigmoidal grain shape, tightly spaced	5%

Plagioclase is rare compared to K-feldspar. Accessory medium-grained subhedral titanite occurs. Epidote/clinozoisite, chlorite and muscovite are common as inclusions of feldspar. Furthermore, fine-grained pyrite and limonite are present. Roundish, fine-grained apatite is rare.

The fabric is foliated and shows porphyritic K-feldspar grains.

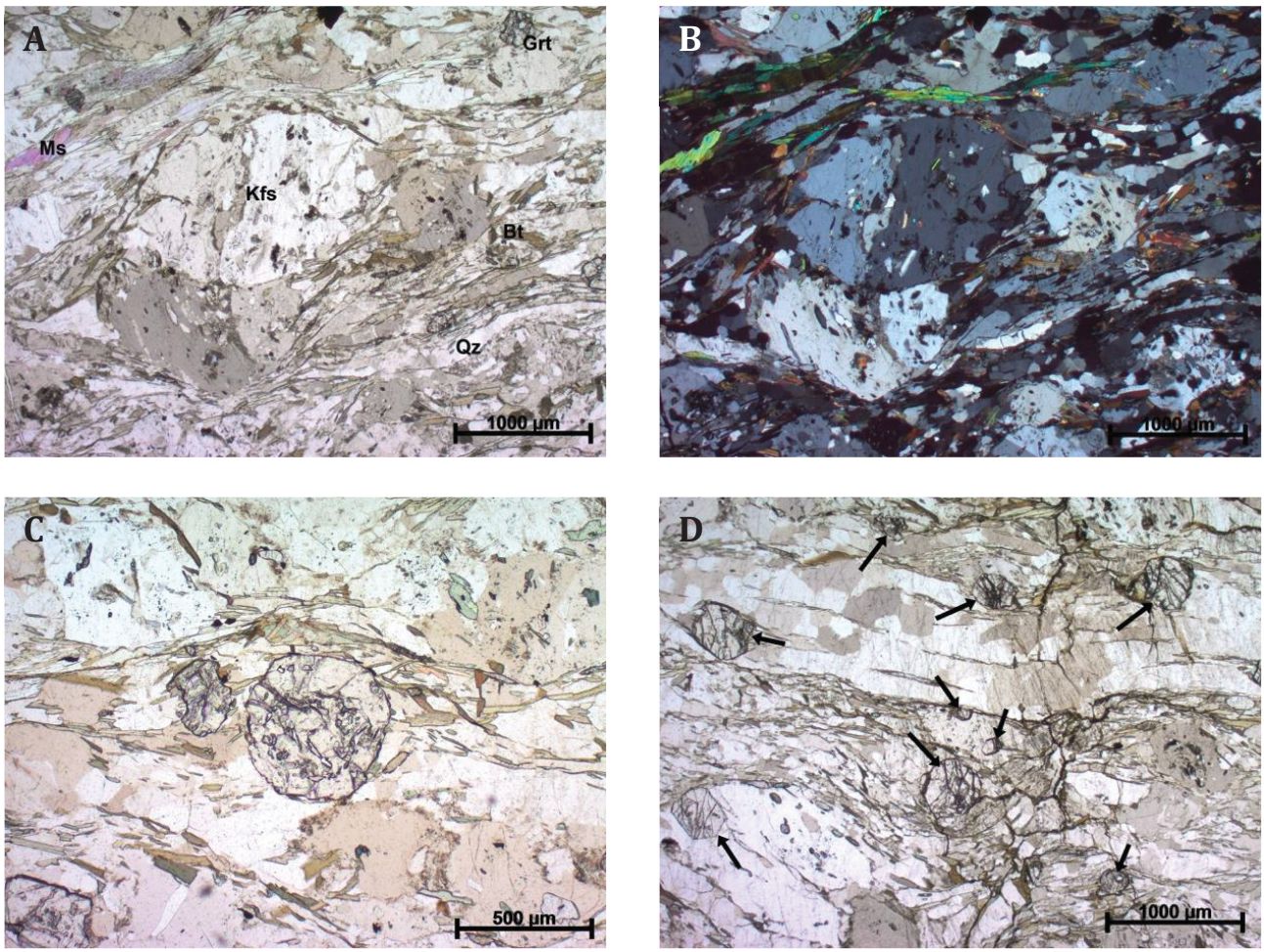

Figure 29: Photomicrographs of a thin section 04-07 from garnet-bearing orthogneiss. **A** Overview about the characteristic fabric. Coarse-grained k-feldspar grain is wrapped by muscovite, quartz and biotite. **B** Same view with crossed nicols. **C** Large round garnet porphyroblast. **D** View with an exceptional amount of garnet (marked with black arrows).

The garnet-bearing orthogneiss overlays a thin layer of a rock that was described as mica schist in the field. The microscopic investigation reveals that it is a garnet-amphibolite (Figure 30; Table 10).

Table 10: Rock forming minerals of garnet-amphibolite. Sample 04-06.

Mineral	Remarks	Abundance
Plagioclase	medium- to coarse-grained porphyroblastic, albite twins, subhedral roundish grains, weakly altered to chlorite (?) and epidote/clinozoisite	40%
Hornblende	medium-grained, euhedral, stalky, intense green-bluish pleochroism	40%
Quartz	medium-grained, anhedral roundish grains, concentrated in certain layers	10%
Chlorite	accumulation of fine-grained, platy, euhedral crystals, aligned in the foliation	5%
Garnet	small- to coarse-grained garnet porphyroblasts, inclusion-rich	5%

Accessory medium-grained euhedral weathered pyrite occurs regularly. Furthermore, epidote/clinozoisite can be found in altered feldspar grains.

The fabric is foliated and weakly porphyroblastic and very similar to garnet-bearing orthogneiss described before.

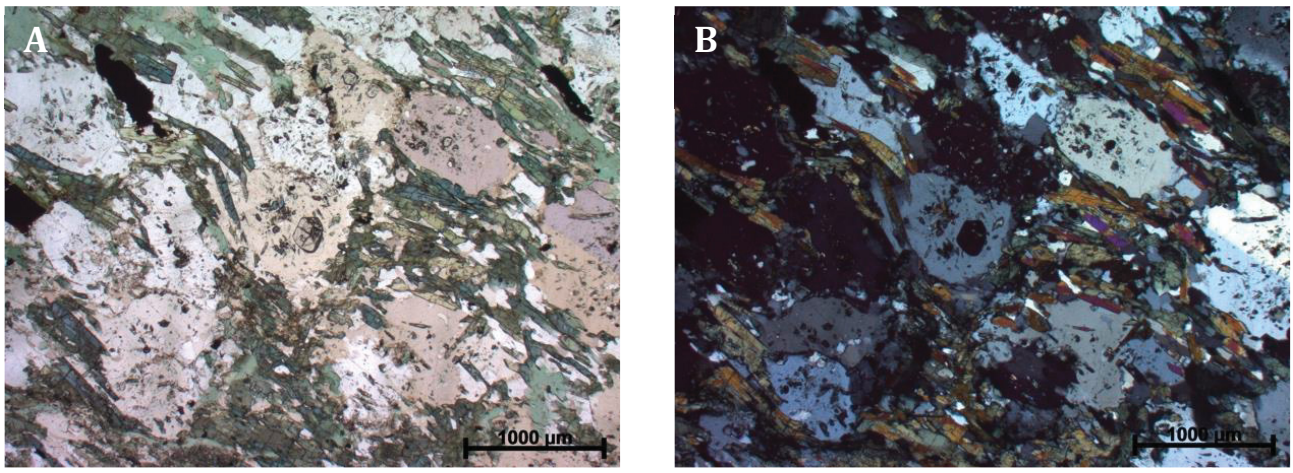

Figure 30: Photomicrographs of thin section, sample 04-06. **A** Typical foliated texture of the rock. Green stalky hornblende with minor chlorite and porphyroblastic feldspar and accessory opaque phase (weathered pyrite); small garnet is located in the centre of the picture; //N. **B** as A under crossed nicols.

6.2. Basal Amphibolite

The Basal Amphibolite unit is the most prominent unit in the working area. It covers the Granatspitz gneiss and shares a tectonic contact to the footwall as well as to the hanging wall to the Basal Schist. The Basal Amphibolite unit includes various metabasites and intermediate volcanic rocks. Calc-silicate rocks in the Basal Amphibolite are described separately in Chapter 6.6.

6.2.1. Massive to slightly foliated amphibolite

Samples: 02-10 (thin section), 06-16, 06-22, 06-23, 06-25

Massive amphibolite is a black to dark-green amphibolite containing coarse-grained, subhedral hornblende and coarse-grained, anhedral, altered plagioclase as major phases (Figure 31; Figure 32). Epidote/clinozoisite and quartz occur as inclusions in plagioclase. Epidote/clinozoisite crystals are stalky and fine-grained. Quartz forms roundish, irregular grains. Chlorite forms medium-grained, platy accumulations. Accessory phases are biotite, apatite, rutile and zircon. The accessory opaque phase was identified as weathered pyrite in reflected light.

The rock shows weak penetrative deformation seen as vague alignment of hornblende. There is no distinct foliation.

Figure 31: Hand specimen (sample 02-10) of a typical slightly foliated, coarse-grained amphibolite. The rock shows a weak foliation in cross-section. The hand lens has a diameter of 2.5 cm.

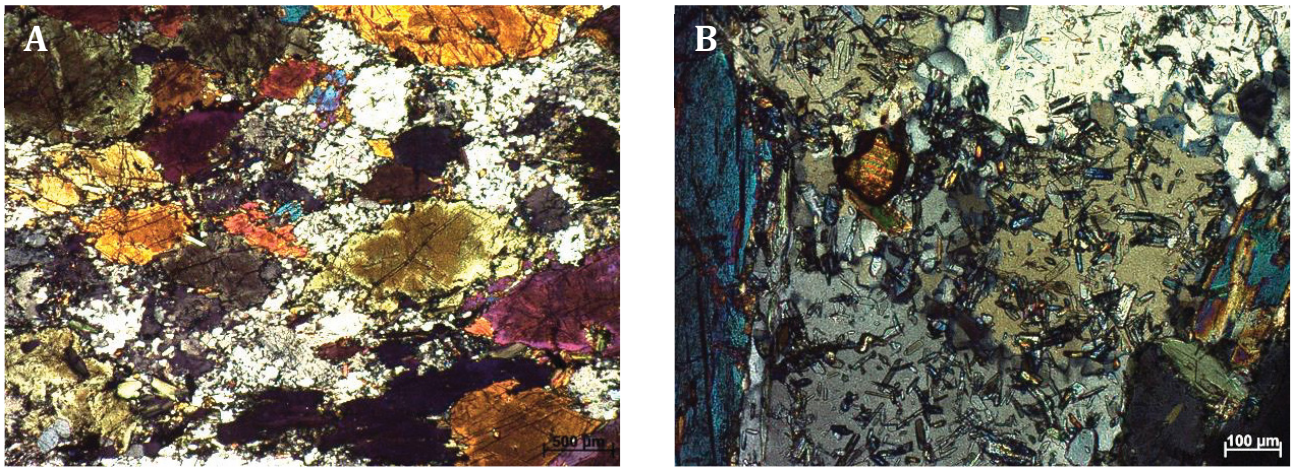

Figure 32: Photomicrographs of sample 02-10. **A** Typical non-foliated fabric with coarse-grained hornblende and altered plagioclase. **B** Elongate inclusions of epidote/clinozoisite formed by alteration in plagioclase; rutile (brown, dark rim) is also visible.

6.2.2. Banded amphibolite

Samples: 04-01, 06-24

Amphibolites show sometimes a gradual and alternating banding of hornblende-rich and plagioclase-rich layers (Figure 33). The layered texture is interpreted as remnant of a primary igneous cumulate texture (e.g. layered gabbro) that got probably enhanced during metamorphism. The thickness of each band ranges from 0.3-10 cm. The grain size of hornblende and plagioclase varies strongly (fine- to coarse-grained). Commonly, hornblende is much coarse-grained in thick hornblende-rich layers than in thin layers. Plagioclase is commonly fine-grained, especially in tight plagioclase-rich bands.

Figure 33: Hand specimen (sample 04-01) of banded amphibolite. The grain size of hornblende varies strongly between different bands. The thick hornblende-rich layer display a coarser grain size of hornblende compared to thin plagioclase-rich layers. The sample was taken closely to the northern end of Grauer See. The magnifier has a diameter of 2.5 cm.

6.2.3. Hornblende-biotite schist and hornblende schist

Samples: 02-01, 02-02, 02-05, 02-07 (thin section), 05-02 (section), 07-02, 07-03, 07-04, 06-17, 06-21, 07-13, 07-17

Hornblende-biotite schist and hornblende schist occur very regularly in the Basal Amphibolite. Areas mapped as hornblende-biotite schist display a content of more than around 75% of this rock. Hornblende-biotite schist occurs for example round the quartzite and marble unit on the east flank of Messelingkogel, or at the contact between Granatspitz gneiss and Basal Amphibolite. The fabric of hornblende-biotite schist is strongly schistose closely to the contact and gets weaker schistose with distance.

Hornblende-biotite schist is a mesocratic, tightly foliated schistose rock (Figure 34; Figure 35) occurring together with hornblende schist and mylonitic gneisses. Rock forming minerals are mainly biotite, quartz and hornblende (Table 11).

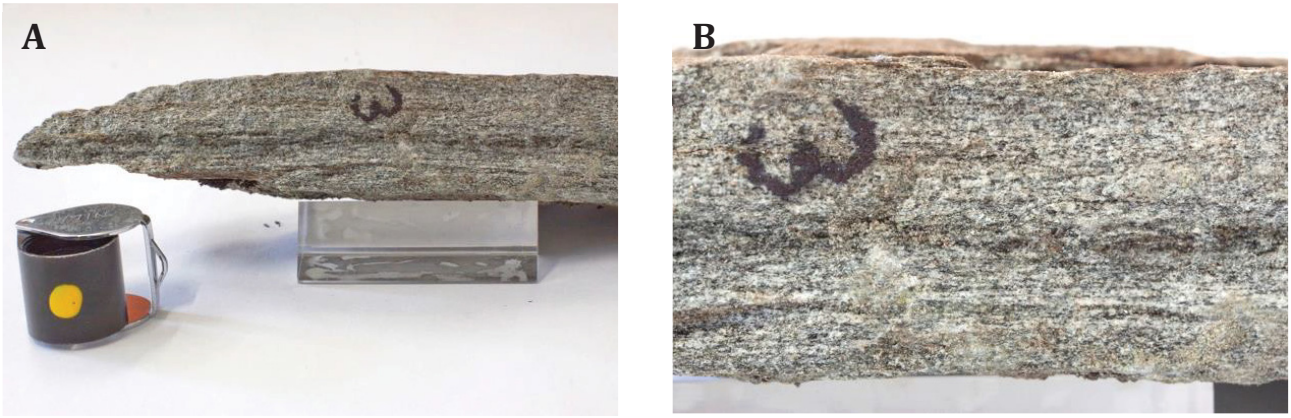

Figure 34: Photographs hand specimen from hornblende-biotite schist. **A** Sheared amphibolite (sample 07-03). The foliation is visible and enlarged in picture **B**. The magnifier has a diameter of 2.5 cm.

Table 11: Rock forming minerals of hornblende-biotite schist.

Mineral	Remarks	Abundance
Biotite	medium- to coarse-grained, subhedral, two generations of biotite: (1) medium- to coarse-grained, aligned in foliation (2) coarse-grained, porphyroblasts oblique to foliation	30%
Quartz	fine- to medium-grained, anhedral, roundish	30%
Hornblende	medium-grained, subhedral relict coarse-grained hornblende crystals may be present, wrapped in biotite-rich foliation planes; monomineralic deformed layers with coarse-grained hornblende	25%
Epidote/ Clinozoisite	fine- to medium-grained, anhedral, in mm-large accumulations	5%
Chlorite	medium-grained, shows reaction with biotite, aligned in the foliation	5%
Titanite	fine- to medium-grained, sub- to euhedral, not well aligned in the foliation, often close to biotite or inside biotite	5%

Accessory minerals are apatite, rutile and opaque minerals.

The fabric is dominated by a distinct schistosity. The tightly spaced foliation is mainly caused by alignment of biotite.

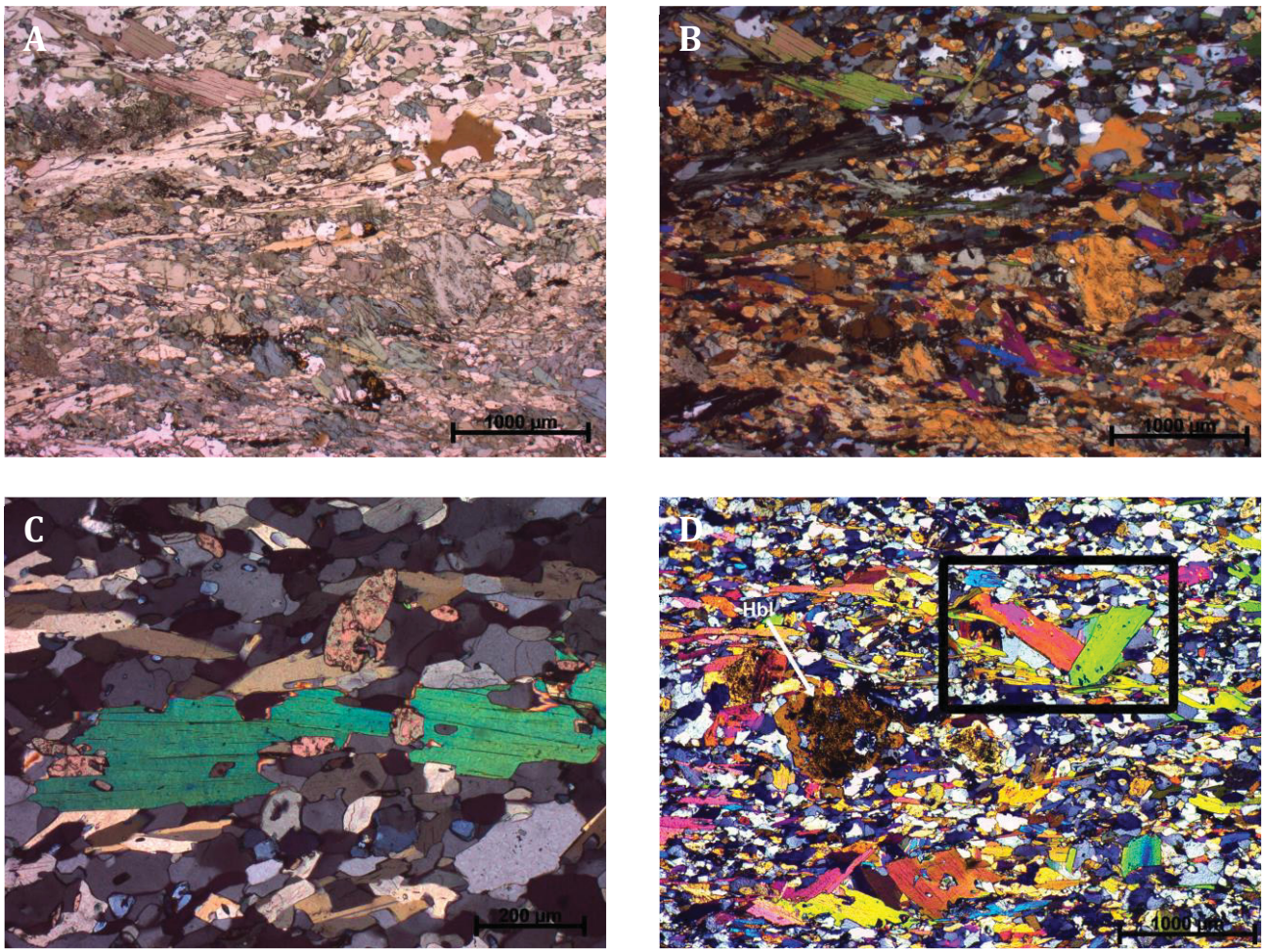

Figure 35: Photomicrographs of samples 05-02 (A-C) and 02-07 (D). **A** Typical fabric of hornblende-biotite schist. There is also porphyroblastic biotite visible growing oblique to the main foliation; IIN. **B** as A under crossed nicols. **C** Several titanite grains close to or in contact with biotite in matrix of quartz and tiny clinozoisite (light blue). **D** Non-oriented porphyroblastic biotite (marked rectangle). This second generation biotite forms larger crystals than the first generation biotite.Coarse-grained porphyroblastic hornblende is also present.

The main petrographic difference to the Basal Schist is the presence of coarse-grained hornblende. Furthermore, the hornblende-biotite schist contains titanite, the Basal Schist does not.

"Mylonitic rocks" were also observed in many outcrops in the Basal Amphibolite. These rocks occur in thin, discontinuous and strongly deformed horizons and are very irregularly distributed. Figure 36 shows pictures of a thin section prepared from a mylonitic garnet-biotite gneiss. The rock is generally fine-grained and shows a well-foliated fabric. It consists of fine-grained quartz and feldspar (70%), medium-grained biotite (20%) and medium-grained garnet (10%). Feldspar is partly altered to epidote/clinozoisite. Apatite and opaque phases occur as accessories. Biotite is partly altered to chlorite

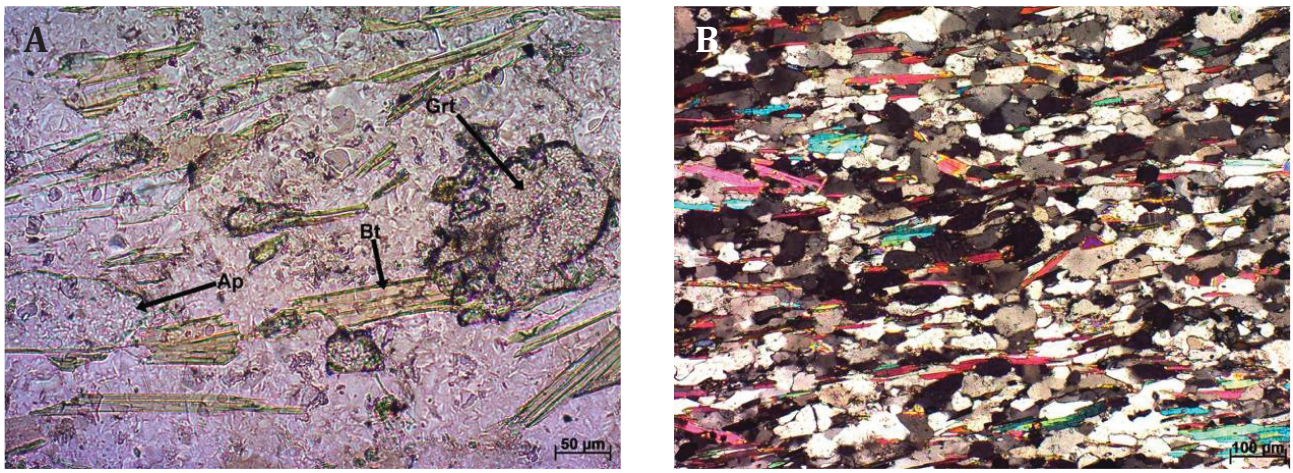

Figure 36: Photomicrographs of thin section of sample 04-09. The rock contains a significant amount of garnet. **A** Garnet, biotite and a roundish apatite grain in quartz-feldpar matrix; IIN. **B** Typical fabric of this rock under crossed nicols. Biotite is perfectly aligned in the foliation. Most black grains are isotropic garnet.

6.2.4. Hornblende fels

Samples: 06-04, 06-09, 06-10, 07-09

Hornblende fels has been observed at several places intercalated with other metabasites. It forms dark lens-shaped competent bodies/layers of dm- to m-size and pinch-and-swell structures (e.g. east of Messelingscharte). In areas mapped as hornblende fels this lithology is the most prominent one. A second important occurrence is located south-west of Grünsee Hütte directly on the hiking path. There is a several metre large black rock body that shows intense rusty brown weathering colours. It is embedded in common banded to massive amphibolite.

Hornblende fels (Figure 37) is dense, massive, dark green to black rock. It is composed from coarse-grained (3-7 mm) hornblende (80-95%) with minor amounts of plagioclase and quartz (5-20%). Medium-grained pyrite can occur as accessory mineral. Pyrite is regularly distributed in the rock and gives the rock a characteristic brownish weathered surface. Hornblende shows perfect cleavage. White feldspar is fine-grained and is irregularly distributed but may be accumulated in micro-areas. The fabric is massive and undeformed.

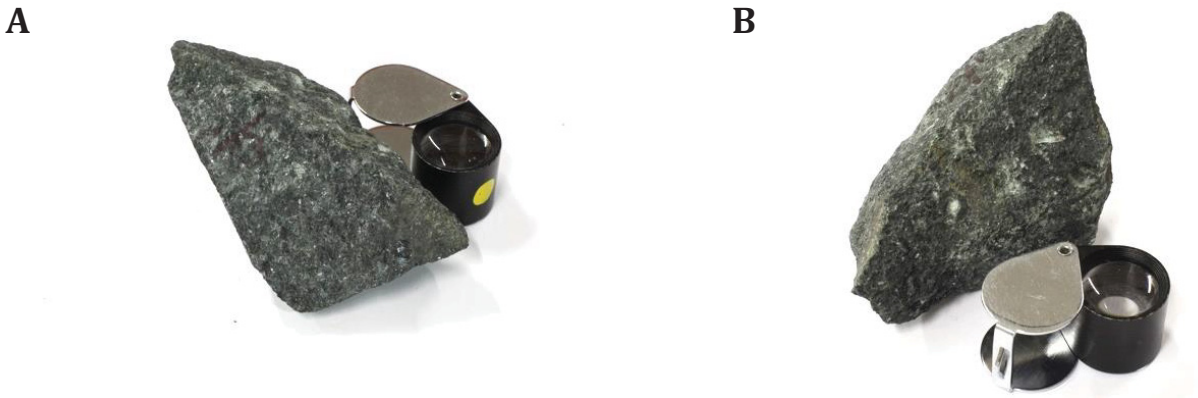

Figure 37: Photographs of green hornblende fels hand specimen. **A** Sample 04-04. **B** Sample 06-09. The magnifier has a diameter of 2.5 cm.

6.2.5. Hornblende-biotite gneiss

Samples: 02-09 (thin section), 06-13 (thin section), 03-10, 03-11, 06-13

Hornblende-biotite gneiss occurs as irregular bodies and discordant dykes with the amphibolites (Figure 38). At least four separate bodies of hornblende-biotite gneiss were mapped W to NW of Messelingscharte. The largest body (150x50 m) is located 200 m NW of Messelingscharte (see map in Figure 9). This lithology has also been observed in boulders at the western flank of Hochgasser. So-far no outcrop of hornblende-biotite gneiss has been found there.

Figure 38: Intrusive contact between light hornblende-biotite gneiss and banded amphibolite. Location of the block is N47.143012, E012.506974 (around 350 m W of Messelingscharte).

Hornblende-biotite gneiss is generally a fine-grained ilmenite-bearing foliated gneiss with altered larger plagioclase grains (Figure 39; Figure 40). The modal mineralogical composition is listed in Table 11.

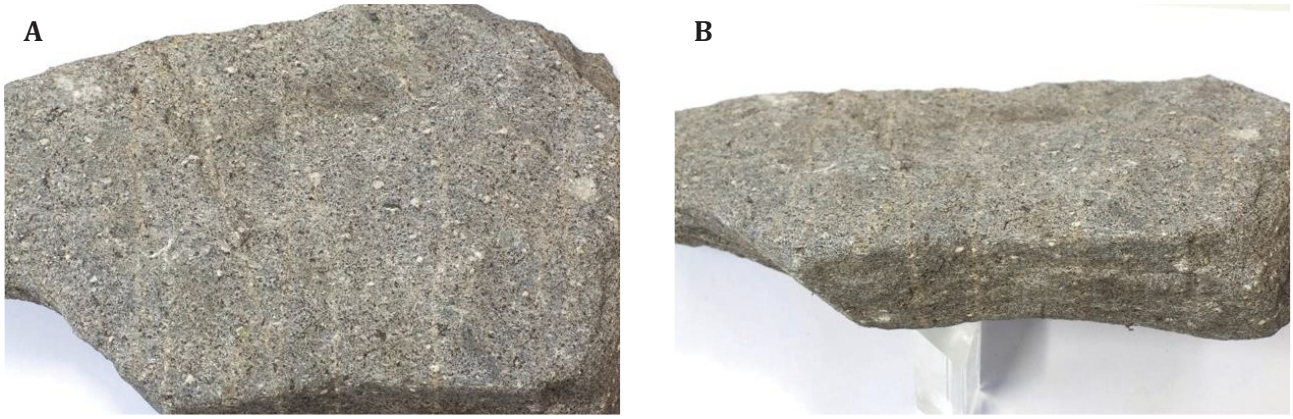

Figure 39: A,B Hand specimen of hornblende-biotite gneiss (sample 06-13). The shown pieces are 18 cm long.

Table 12: Rock forming minerals of hornblende-biotite gneiss.

Mineral	Remarks	Abundance
Plagioclase	variable grain size, strongly altered porphyric grains	35%
Hornblende	medium- to coarse-grained, sub- and anhedral, two types: (1) anhedral grains that are partly aligned into foliation (2) coarse-grained porphyroblastic, aligned into foliation	25%
Biotite	platy, strongly pleochroic, two generations: (1) fine- to medium-grained, aligned into foliation, (2) medium-grained, shows reaction with hornblende	20%
Quartz	fine-grained, recrystallised, forms the matrix together with fine-grained plagioclase	12%
Epidote/ Clinozoisite	fine-grained, anhedral, occurs as alteration mineral in plagioclase or as independent grains	5%
Ilmenite/ magnetite	fine-grained, platy very thin grains, aligned in the foliation, often next to biotite and biotite that reacts to chlorite	3%
Chlorite	medium-grained, forms mm-large accumulations together with Ep/Czo in completely altered feldspar	accessory

Accessory opaque phases were identified as fine-grained pyrite and chalcopyrite (2-40µm).

The rock shows a foliated fabric. Especially, biotite (generation 1) is perfectly aligned in the foliation planes. Feldspar and quartz are also aligned, larger plagioclase grains evidence alteration. Thin discordant quartz veinlets are common. This vein quartz is much coarser-grained than that in the matrix of the host rock.

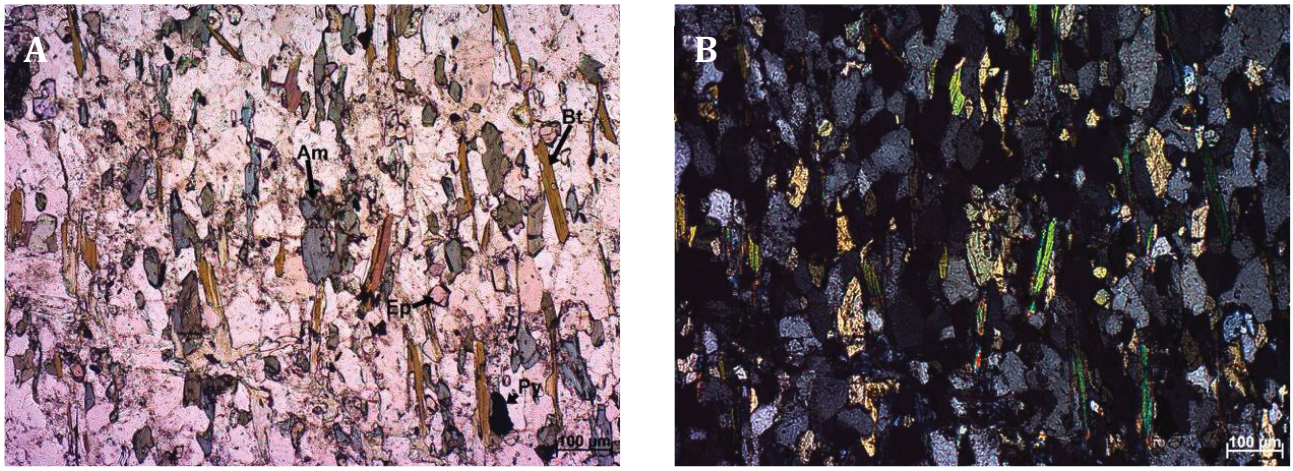

Figure 40: Photomicrographs of thin sections from hornblende-biotite gneiss (sample 02-09). **A** Overview showing greenish hornblende, elongated biotite and minor epidote in a light feldspar-quartz matrix. Biotite is perfectly aligned in the foliation **B** Same view under crossed nicols.

6.2.6. Actinolite-rich schist

Sample: 04-04

At mountain Hochgasser actinolite-biotite-chlorite schist occurs in high-strain zones within amphibolites and in fold hinges; they are locally associated with actinolite-talc schist ("Strahlstein"). This rock shows a retrograde greenschist facies mineral assemblage. Both rocks either show primarily intense foliation or rarely a massive fabric (Figure 41).

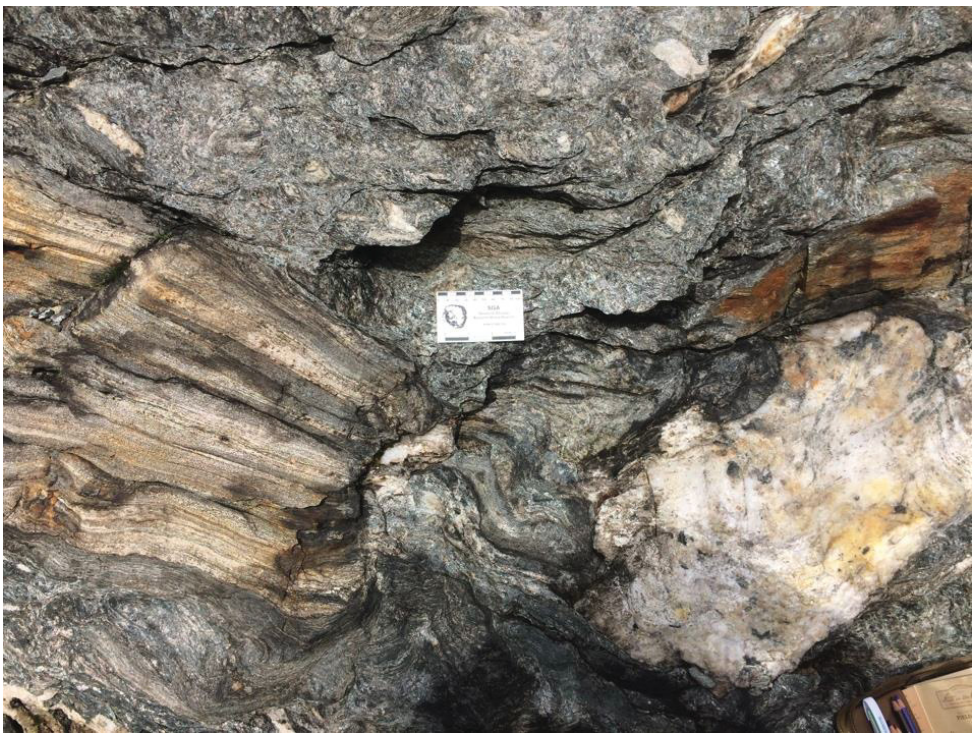

Figure 41: Banded amphibolite and irregular quartz mass with foliated actinolite-rich schist in-between. The rock is strongly deformed and cuts the amphibolite sharply and discordantly. Outcrop located SE of the top of mountain Hochgasser at 2760 m elevation.

Actinolite-rich schist (Figure 42) is commonly of (light) green colour and coarse-grained (Table 13).

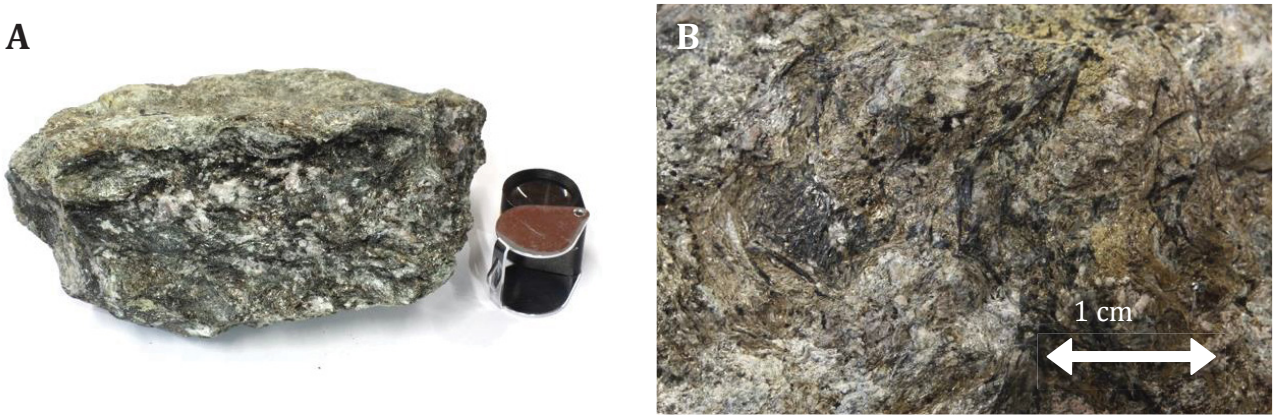

Figure 42: Hand specimen of actinolite-rich schist from west-flank of Hochgasser (sample 04-04). **A** Dark green actinolite schist with mm-size irregular quartz masses. **B** Stalky actinolite crystals with length of more than 1 cm.

Table 13: Rock forming minerals of actinolite-rich schist.

Mineral	Remarks	Abundance
Biotite	coarse-grained, brown to black, platy, aligned in deformed foliation, occurs always together with chlorite	30%
Actinolite	medium- to very coarse grained (1-50 mm), green, stalky, aligned in foliation	30%
Chlorite	coarse-grained, light to dark green, platy	20%
Feldspar and quartz	fine-grained, build isolated 2-10 mm large accumulations with irregular shape and layers parallel to foliation	20%

The mm-scale foliation is defined by aligned stalky actinolite and phyllosilicates. The foliated minerals show irregular deformation that is clearly visible in the outcrop but not well visible in the hand specimen. Quartz can also occur in 1-3 mm thick layers that are parallel to the foliation.

6.2.7. Orthogneiss in amphibolite

One small outcrop NNW of Messelingscharte reveals deformed dikes of leucocratic orthogneisses in amphibolite exposed in a temporary creek (Figure 43). The dikes are folded, rotated into the foliation and pinch out after a few dm. A similar occurrence is located at mountain Hochgasser. Cm-thick aplitic dykes crosscut amphibolites there.

Figure 43: Outcrop of leucocratic deformed irregular orthogneiss bands inside of dark amphibolite and hornblende fels.

6.3. Basal Schist

Samples: 02-04 (thin section), 02-06, 02-07

Basal Schist is located in the hanging wall of the Basal Amphibolite and is only present at Messelingkogel. The (tectonic?) contact to the Basal Amphibolite is located directly at Messelingscharte where the hiking track crosses the saddle. The unit has a thickness of nearly 100 m at Messelingkogel. A deformed gneiss slice is tectonically inserted in the Basal Schist at the east flank of Messelingkogel. The thickness of this gneiss slice is about 40-50 m in the north becoming slightly thicker to the south.

The most prominent rock of the Basal Schist is a grey schist with characteristic larger biotite porphyroblasts (Figure 44). Lepidoblastic biotite builds between 30-50% of the rock. Varieties with higher feldspar content grade into paragneisses. Sometimes the rock contains a significant amount of chlorite. Furthermore, hornblende occurs (Table 14; Figure 45). The rock is tightly foliated with intercalated quartz-rich layers. Biotite is perfectly aligned and builds the foliation.

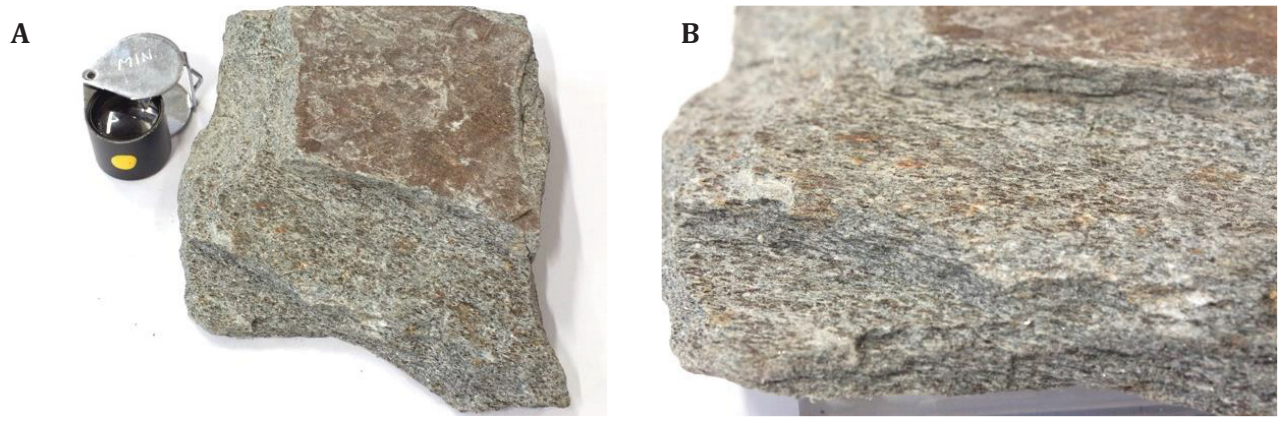

Figure 44: Photographs of representative sample of a schist from the Basal Schist. **A** Grey micaschist (sample 02-05) of the Basal Schist Formation from the footwall closely to Messelingscharte. Large brown biotite crystals aligned in the foliation planes. The magnifier has a diameter of 2.5 cm. **B** Close up view of the same sample. The foliation is very tightly spaced. The length of the picture is 3 cm.

Table 14: Rock forming minerals of schist.

Mineral	Remarks	Abundance
Biotite	medium- to coarse-grained, suhedral Two generations: (1) medium- to coarse-grained, aligned in the foliation (2) coarse-grained, porphyroblastic crystals	35%
Quartz	fine- to medium-grained, anhedral, concentrated in layers between biotite	25%
Hornblende	medium-grained, subhedral, irregular stalky grains, aligned in foliation	15%
Plagioclase	fine- to medium-grained, anhedral altered grains	10%
Epidote/ Clinozoisite	fine- to medium-grained, anhedral, in mm-large accumulations	10%
Chlorite	medium-grained, shows reaction with biotite	5%

Fine-grained to medium-grained, elongated rutile occurs as accessory mineral.

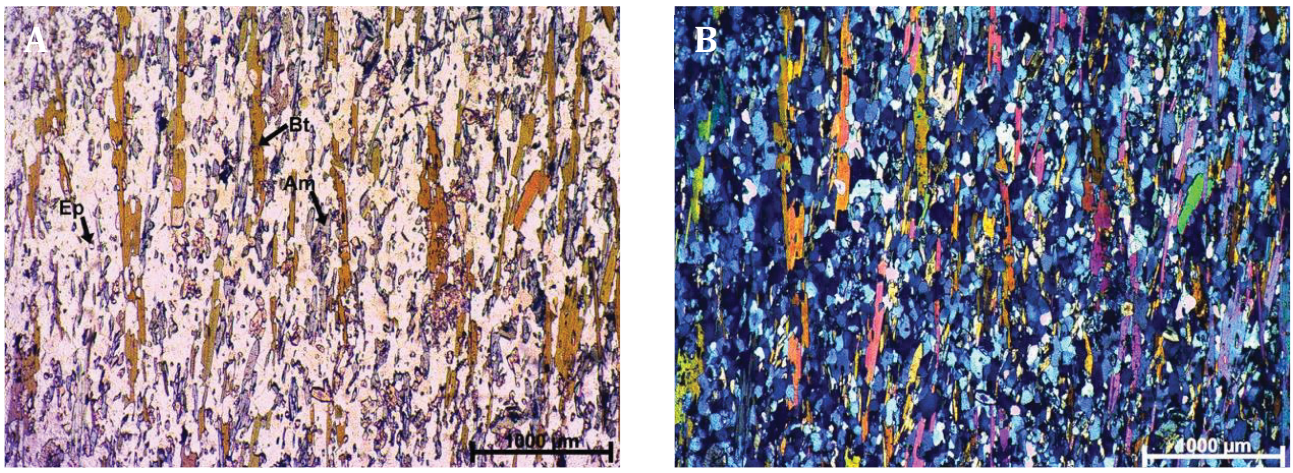

Figure 45: Photomicrographs of thin sections of sample 02-04. **A** Typical foliated fabric of schist. Larger biotite crystals are aligned in the foliation. Greenish subhedral mineral is hornblende. Small round grains are mostly epidote; TL IIN. **B** as A under crossed nicols. It reveals the quite large content of quartz (grey minerals).

6.4. Habach Complex

The Habach Complex consists of two major subunits in the working area: (1) A metasedimentary sequence in the footwall at the contact to the Basal Schist unit, (2) Amphibolite (Weinbühl amphibolite) in the hanging wall (cf. Fuchs 1958).

There are two areas in the working area where the Habach Complex occurs. First, it is located in an intermediate position at Messelingkogel between the Basal Schist in the footwall and orthogneiss with garnet-amphibolite hanging wall. The Habach Complex starts with an about 10-20 m thick metasedimentary sequence (Figure 46; Figure 47) followed by few tens of metres thick Weinbühl amphibolite. The contact in the footwall is tectonic. The second area is the mountain Weinbichl in the east of St. Pöltener Hütte. This ridge is built by metasediments (paragneiss, micaschist and quartzite) of the Habach Group in the east and a succession of Weinbühl amphibolite and metasediments in the west. The meta-sedimentary sequence overlies the Basal Amphibolite without any Basal Schist in-between (see also Fuchs 1958).

6.4.1. Metasediments

Samples: no samples taken

The metasedimentary sequence consists of graphitic schist, paragneiss that are locally quartzitic and micaschist. The footwall contact to the Basal Schist is a shear zone (Figure 46). The metasedimentary sequence starts witch graphitic schists.

Figure 46: Eastern ridge of the Weinbichl. In the lower part of the picture are strongly sheared graphitic schists followed by gneisses, amphibolites and mica schists. The yellow line marks the measuring tape for the detailed profile shown in **Figure 47**. The hiking path follows the ridge uphill. The person on the picture is 1.9 m tall.

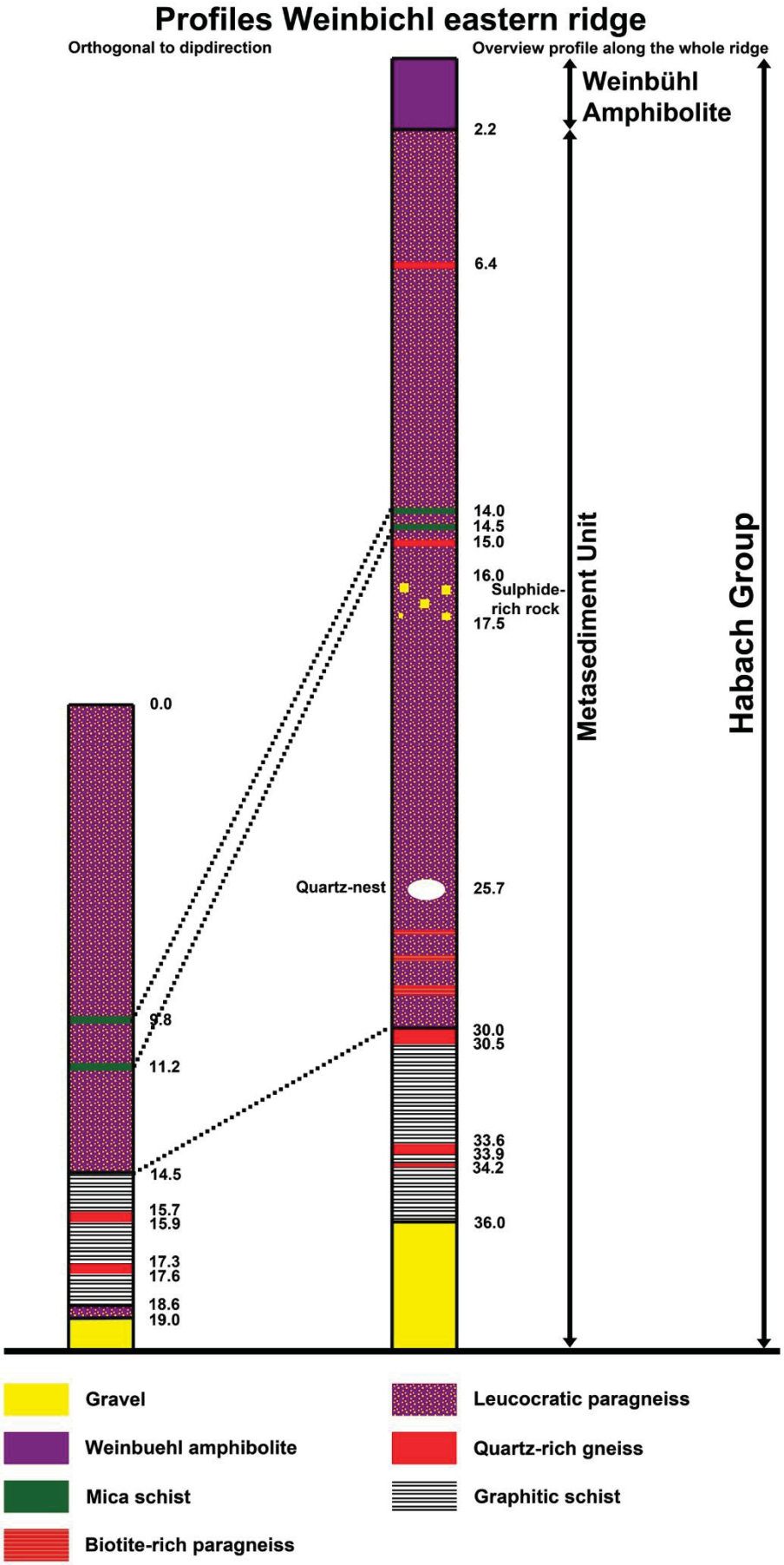

Figure 47: Profiles along the eastern ridge of Weinbichl mountain. Profile 1 (left) is orthogonal to the dip direction, therefore showing the true thickness of the different rock unites. Profile 2 (right) shows the whole ridge from bottom to nearly the top of Weinbichl peak. The starting point of both profiles has the coordinates N47.154188, E012.502395. The end point of profile 2 has the coordinates N47.154037, E012.502798.

6.4.2. Weinbühl amphibolite and associated metasediments

Samples: 03-01, 03-02, 03-03 (thin section)

The Weinbühl amphibolite is a mesocratic, medium-grained amphibolite with a porphyroblastic fabric (Figure 48; Figure 49; Table 15).

Figure 48: Hand specimen of Weinbühl amphibolite from mountain Weinbichl. The diameter of the magnifier is 2.5 cm.

Table 15: Rock forming minerals of Weinbühl amphibolite.

Mineral	Remarks	Abundance
Hornblende	medium-grained, euhedral, stalky, intense pleochroism	40%
Plagioclase	coarse-grained, anhedral roundish grains, polysynthetic twins, strongly altered	40%
Quartz	medium-grained, roundish anhedral grains, lots of fluid inclusions	10%
Chlorite	medium-grained, alteration product of hornblende and plagioclase, not aligned in foliation	5%
Epidote, Clinozoisite	fine- to medium grained, anhedral, alteration product of large feldspar grains, rarely euhedral stalky medium-grained crystals together with accumulation of quartz	5%

Accessory minerals are rutile and opaque phases. Limonite occurs regularly in irregular thin coatings of grains. Larger inclusion-rich plagioclase crystals are surrounded by perfectly aligned hornblende and chlorite (Figure 49). Plagioclase shows beginning alteration to epidote/clinozoisite and chlorite. Chlorite also grows oblique to the foliation. Quartz forms several mm-large micro-areas.

The fabric is porphyroblastic with nematoblastic hornblende defining the foliation.

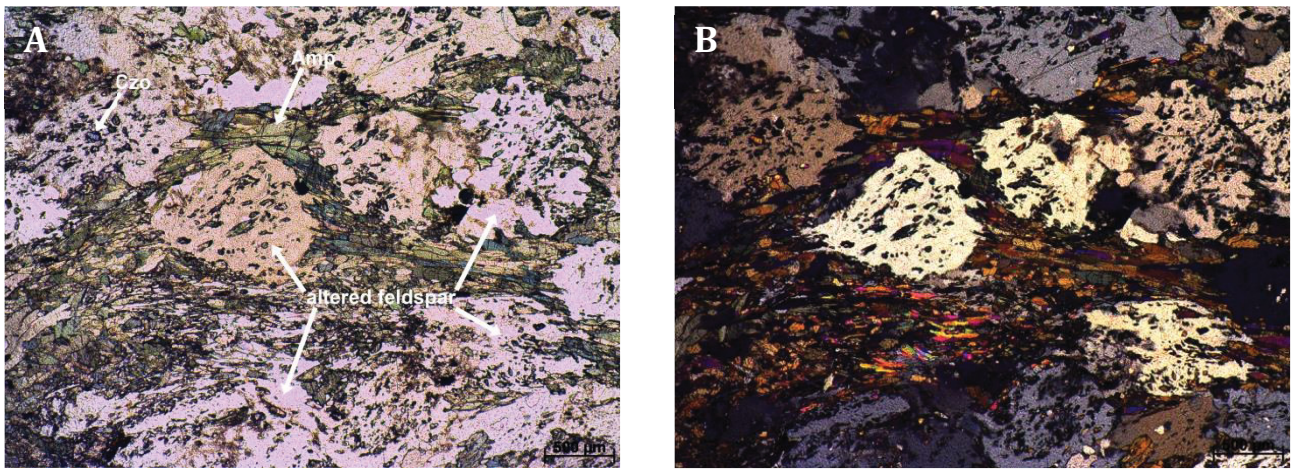

Figure 49: Photographs of Weinbühl amphibolite (sample 03-03). Large plagioclase is wrapped by amphiboles. Plagioclase is partly altered to clinozoisite. **A** Parallel nicols, **B** Crossed nicols.

6.5. Quartzite and marble

Quartzites and marbles occur as deformed lenses or undeformed concordant layers in two different tectonic positions. First, a quartzite layer crops out on top of Messelingkogel. Secondly, intensely folded quartzite builds together with marble parts of the east flank of Messelingkogel. Following Kurz et al. (1998) coarse grained quartzites and other meta-sediments occur directly upon Central Gneisses beas Permo-Mesozoic cover units.

6.5.1. Quartzite

Sample: 04-11 (thin section)

On top of Messelingkogel between amphibolites of the Habach Complex and paragneisses occurs a 5 m thick quartzite layer. The impure quartzite is bright yellowish in colour showing rusty staining (Figure 28B). The rock is predominantly composed of quartz (>90%) (Figure 50). Quartz forms a medium-grained mosaic fabric typical for metamorphic recrystallisation. Biotite and plagioclase are minor phases. Pyrite is a common accessory phase and reaches a size of several millimetres (normally <1 mm). Rutile and zircon are other accessories.

Sometimes there are small cavities present (around 1 mm in diameter). The rock is weakly foliated due to preferred orientation of biotite. The fabric of the quartzite is equigranular, granoblastic with a distinct lineation.

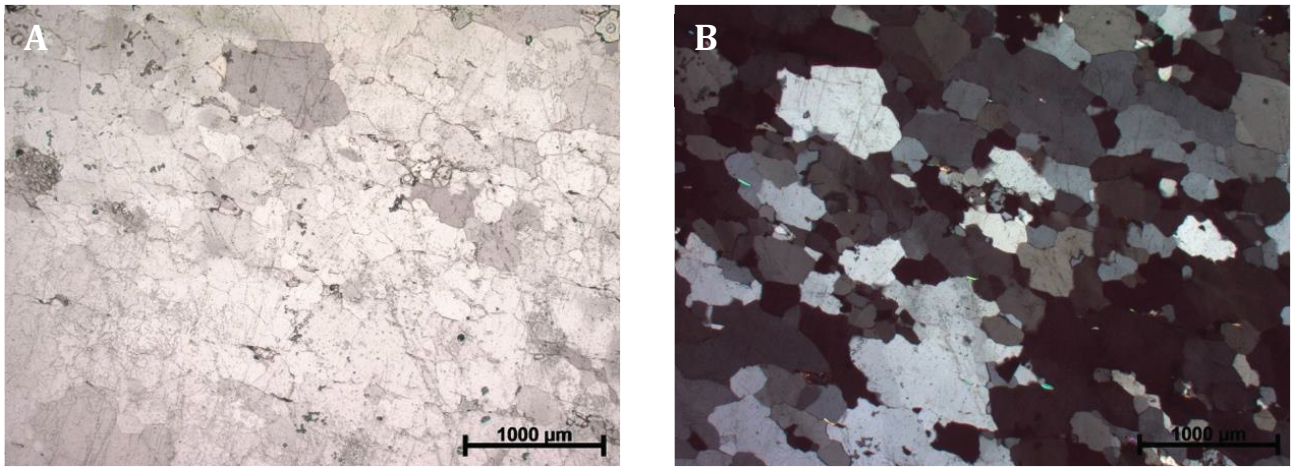

Figure 50: Photomicrographs of a thin section of sample 04-11. **A** Medium-grained recrystallised quartz defining in granoblastic fabric; TL IIN. **B** as A under crossed nicols.

6.5.2. Calcite marble, quartzite and mica schist

Samples: 07-06, 07-07, 07-08

Quartzites associated with marble and micaschists from the eastern flank of Messelingkogel are very different from quartzites from top of Messelingkogel. Quartzites from the flank (Figure 51A) are strongly deformed, coarser-grained and closely intercalated with white calcite marbles. The thickness of single quartzite layers can reach several metres but are normally few decimetres. The fabric is dominated by distinct lineation (L-tectonite) and open to tight folds.

Intercalated marbles are very coarse-grained, pure white when fresh, and exhibit a text-book like granoblastic fabric (Figure 51B). Calcite is the only mineral that was identified macroscopically. The

rocks display minor linear fabric or folds (s-type folds, open folds) because there are no minerals present that could align perfectly in the direction of the linear.

Additionally, dark-grey, fine- to medium-grained biotite schist (Figure 51C) is to be found between the quartzite and marble in thin layers that have a thickness between few mm and few cm. Beside biotite only minor medium-grained quartz and feldspar build the rock. The rock is not homogenous because there are parts that are richer in feldspar and quartz and parts that are nearly solely built by biotite. The rock weathers very fast and is very weakly cohesive. The fabric is strongly foliated and shows partly crenulation cleavage.

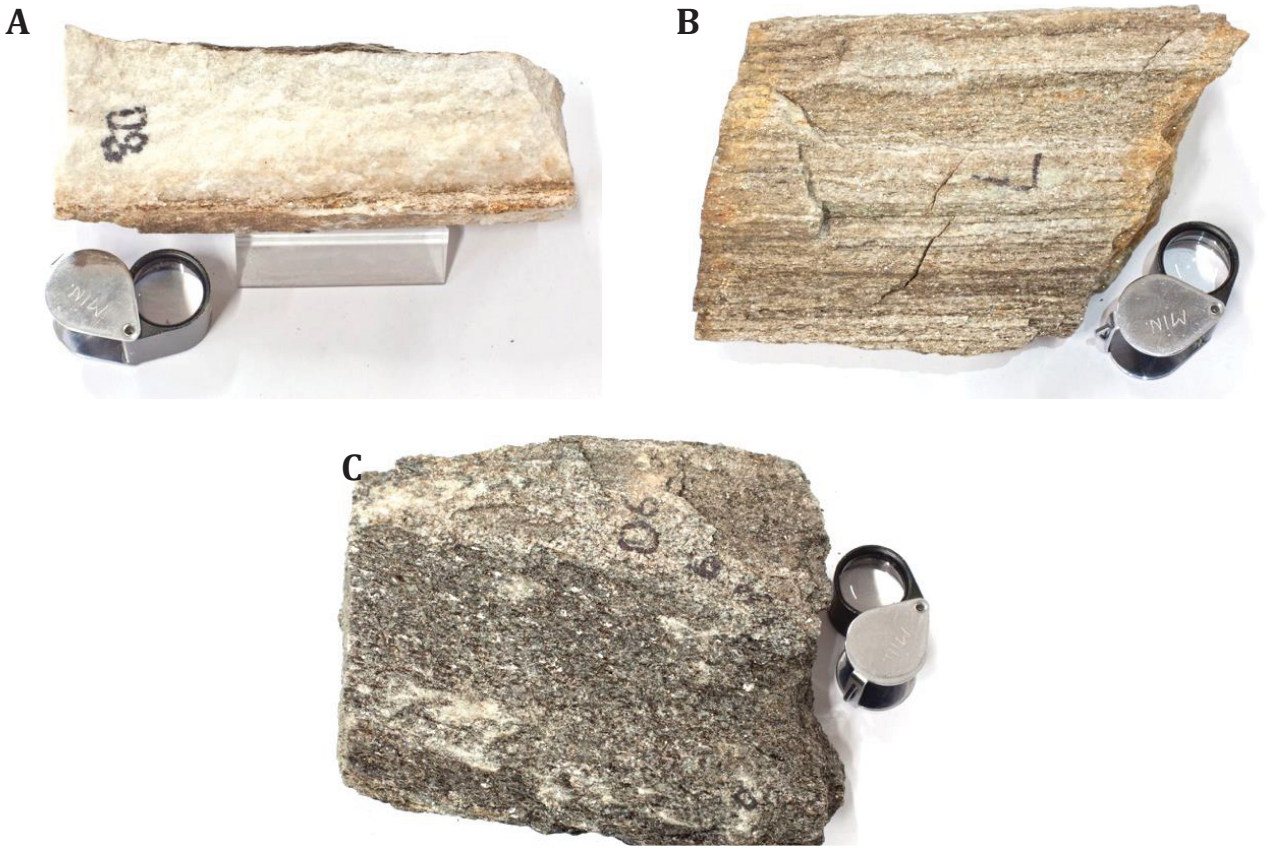

Figure 51: Pictures of hand specimens of meta-sediments from eastern flank of Messelingkogel. **A** Coarse-grained white marble (sample 07-08). **B** Quartzite containing about 10-20% biotite showing linear fabric (sample 07-07). **C** Biotite schist that normally separates marble from quartzite (07-06). The magnifier has a diameter of 2.5 cm.

6.6. Calc-silicate rocks and associated lithologies from Messelingscharte

Calc-silicate rocks occur in the working area as veins, layers and massive- to semi-massive lenses or pods (Chapter 5.3.1). The most prominent scheelite-bearing lens is only few metres east of Messelingscharte. Additionally, calc-silicate rocks form thin, deformed, discordant veins or concordant boudinaged layers (Figure 59) in amphibolite (e.g. Messelingkogel east flank, Hochgasser west flank).

6.6.1. Scheelite-bearing clinozoisite-plagioclase-calc-silicate fels and associated lithologies

Samples: 03-13 (thin section), 03-14 (thin section), 03-16, 03-17, 03-18, 03-19, 04-12, 04-13, 04-14, 04-15, 04-16, 04-17, 04-22, 05-03 (thin section), 05-04 (thin section), 06-01, 06-02 (thin section), 06-03 (thin section), 06-19, 06-20 (thin section), 06-26

The calc-silicate fels from the outcrop east of Messelingscharte is a bright, pale green, non-foliated rock that can be either dense or vuggy (Figure 52; Figure 53). It consist of very coarse-grained clinozoisite, quartz, plagioclase, calcite, chlorite and scheelite (

Table 16). Clinozoisite dominates large portions of the rock. Plagioclase occurs either fine-grained together with clinozoisite or coarse-grained in vuggy druses. Quartz builds irregularly distributed, massive, nearly monomineralic accumulations. Fine-grained quartz builds irregular bodies <8 cm in length.

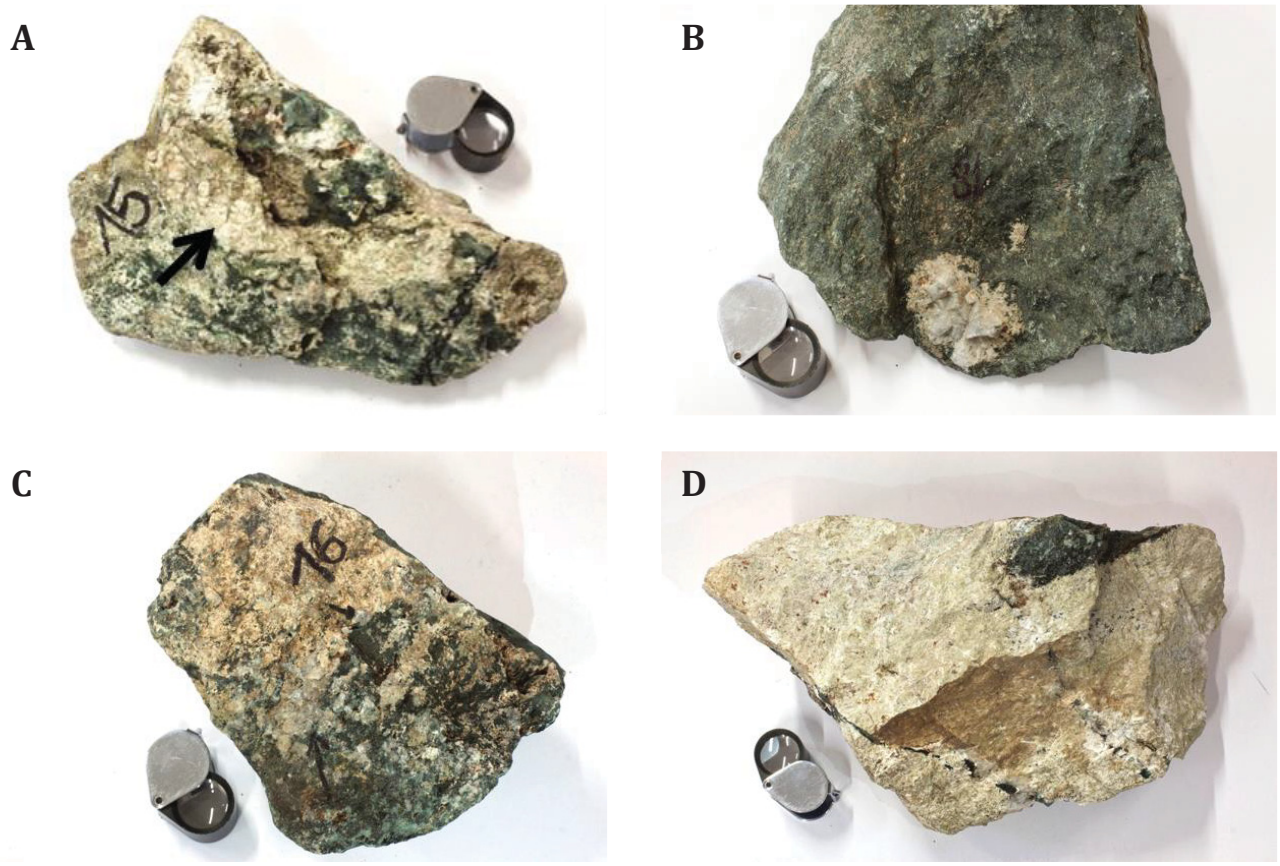

Figure 52: Photos of samples of scheelite-rich calc-silicate rocks from the outcrop east of Messelingscharte. **A** Black arrow marks large accumulation of scheelite (sample 03-15). **B** Amphibole schist with nest of calc-silicate rock (sample 03-18). **C** Sample contains about 50% calc-silicate rock and 50% amphibole schist and lots of scheelite (sample 03-16). **D** Large sample

(15 kg) of bright calc-silicate fels (sample 04-22). Nest of amphibole schist in upper right. Two discordant amphibole-bearing veinlets crosscut the calc-silicate fels. The diameter of the magnifier is 2.5 cm.

Scheelite occurs as fine- to very coarse-grained, anhedral crystals that are either white (like feldspar) or colourless translucent (like quartz) (Figure 52A,B; Figure 54B). Grain size varies in scheelite-rich hand specimen from 1-50 mm. Scheelite shows predominantly blue luminescence colours but about 10-20% of all scheelite grains are pale to strong yellow under UV light. Very often the core of scheelite crystals is yellow and has a blue rim (Figure 53C,D; Figure 54A) indicating a polyphase formation of scheelite. The yellow core is commonly larger than the blue rim (Figure 53D).

There are very common druses reaching a size from mm to several centimetres. The druses are normally filled with chlorite coated, euhedral quartz crystals and pyrite. The shape can be roundish or irregularly elongated. Scheelite was never spotted inside a druse.

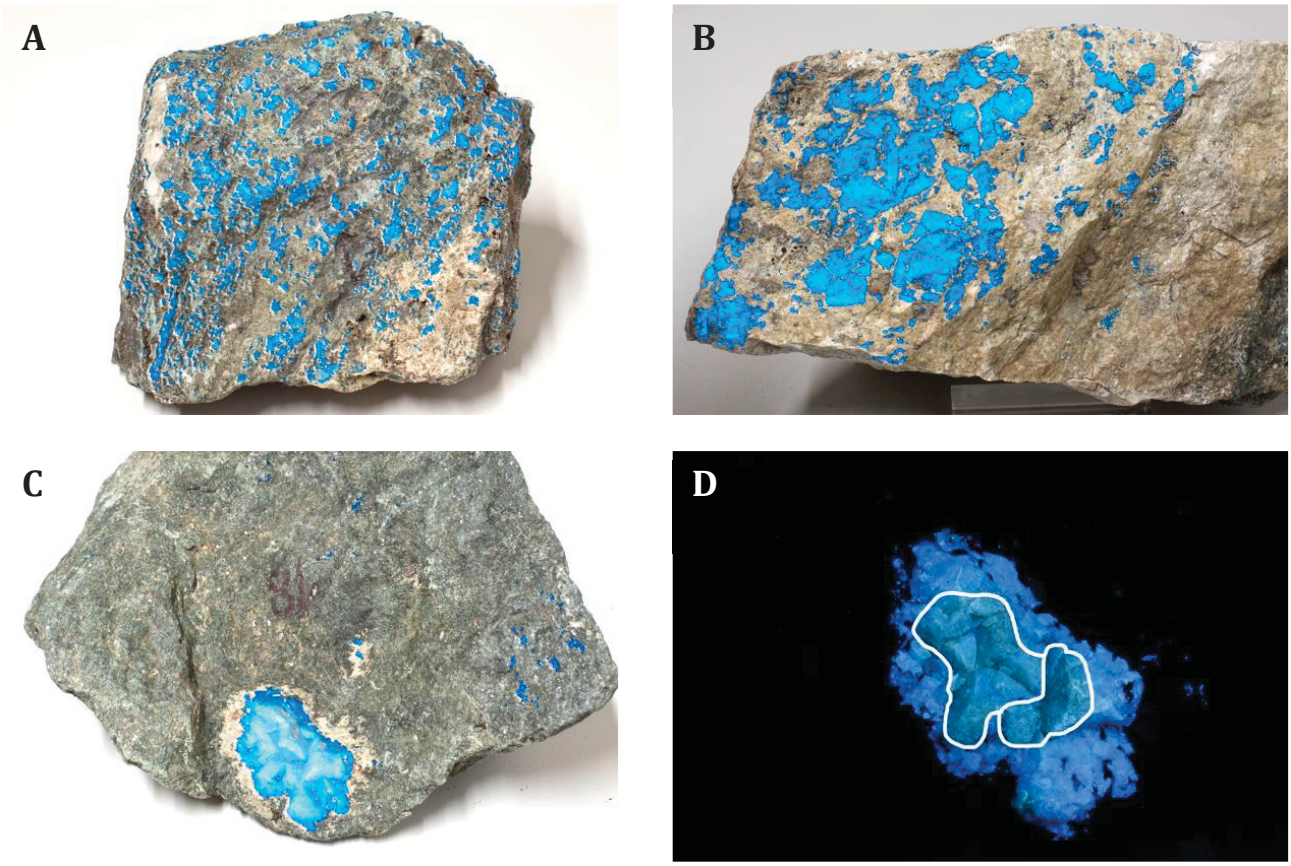

Figure 53: A-C: Processed photos of two separate images. The background image was taken during daylight. The second one was made in darkness under short-wave UV light. Both pictures were combined using selective layer masks in image processing. **A** Large amount of blue and yellow luminescent scheelite. Grain size of scheelite between 1-5 mm (sample 03-16, 10x13 cm). **B** Very coarse-grained blue scheelite (sample 04-22, 25x15 cm) **C** Amphibole schist (sample 03-18) containing a large scheelite crystal (size 4.4x2.5 cm). It has a very coarse-grained yellow luminescent core surrounded by a rim of finer-grained blue luminescent scheelite. The scheelite cluster is enlarged in **D**. The white line outlines irregular contact of the yellow to the blue luminescent scheelite. The yellow scheelite shows perfect cleavage.

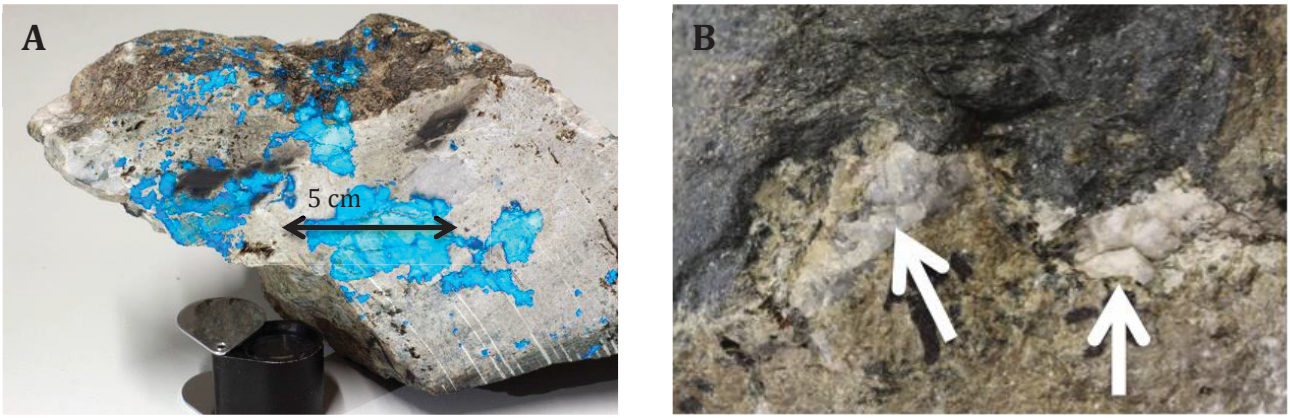

Figure 54: A Very large scheelite crystals with a yellow core and a blue rim. Largest scheelite grain has a length of 5 cm (sample 03-17). The magnifier has a diameter of 2.5 cm. **B** Two scheelite crystals showing different colours in hand specimen (1-2 cm in length). Left one is grey and translucent, right one is white and non-transparent. Picture length 5 cm.

Table 16: Rock forming minerals of plagioclase-epidote-calc-silicate fels.

Mineral	Remarks	Abundance
Clinozoisite	Two types of clinozoisite: (1) very coarse to medium-grained, euhedral, stalky crystals, irregular altered grain boundaries, intimately intergrown with feldspar, (2) fine-to medium-grained, subhedral, alteration product of plagioclase	50%
Plagioclase	poikiloblastic grains with non-oriented iclusions of clinozoisite + chlorite, "saussuritisation", fine- to very large-grained, fills empty spaces between larger epidote/clinozoisite crystals, shows typical polysynthetic twins	20%
Quartz	(1) medium- to very coarse-grained, anhedral, undulose extinction, in contact with clinozoisite (2) fills interstitial spaces between large euhedral crystals, lots of fluid inclusions (L+V) in trails (→ at least two different directions that cross-cut each other in an angle of 110°)	15%
Chlorite	fine-grained; large to very large accumulations, euhedral, platy, radial growth, fills interstitial spaces between straight edges of larger crystals	10%
Calcite	medium- to very coarse grained, deformation twins, anhedral, interstitial	5%
Biotite	subhedral, medium-grained, platy, partly altered to chlorite	accessory
Scheelite	an- to euhedral (rare), medium- to very large-grained, lots of fluid inclusions (L+V), undulose extinction, noticeable pleochroism from colourless to yellow	accessory

Other accessory minerals are titanite, apatite, rutile and pyrite. Apatite occurs as rare, anhedral medium-size grains. Pyrite is normally idiomorphic and shows a thick weathering rim. Titanite occurs rarely as coarse-grained idiomorphic crystals together with quartz and chlorite.

Microscopically the calc-silcate rock show a grano- to nematoblastic fabric. The minerals are randomly oriented. Vugs that can be present likely are the result of weathering.

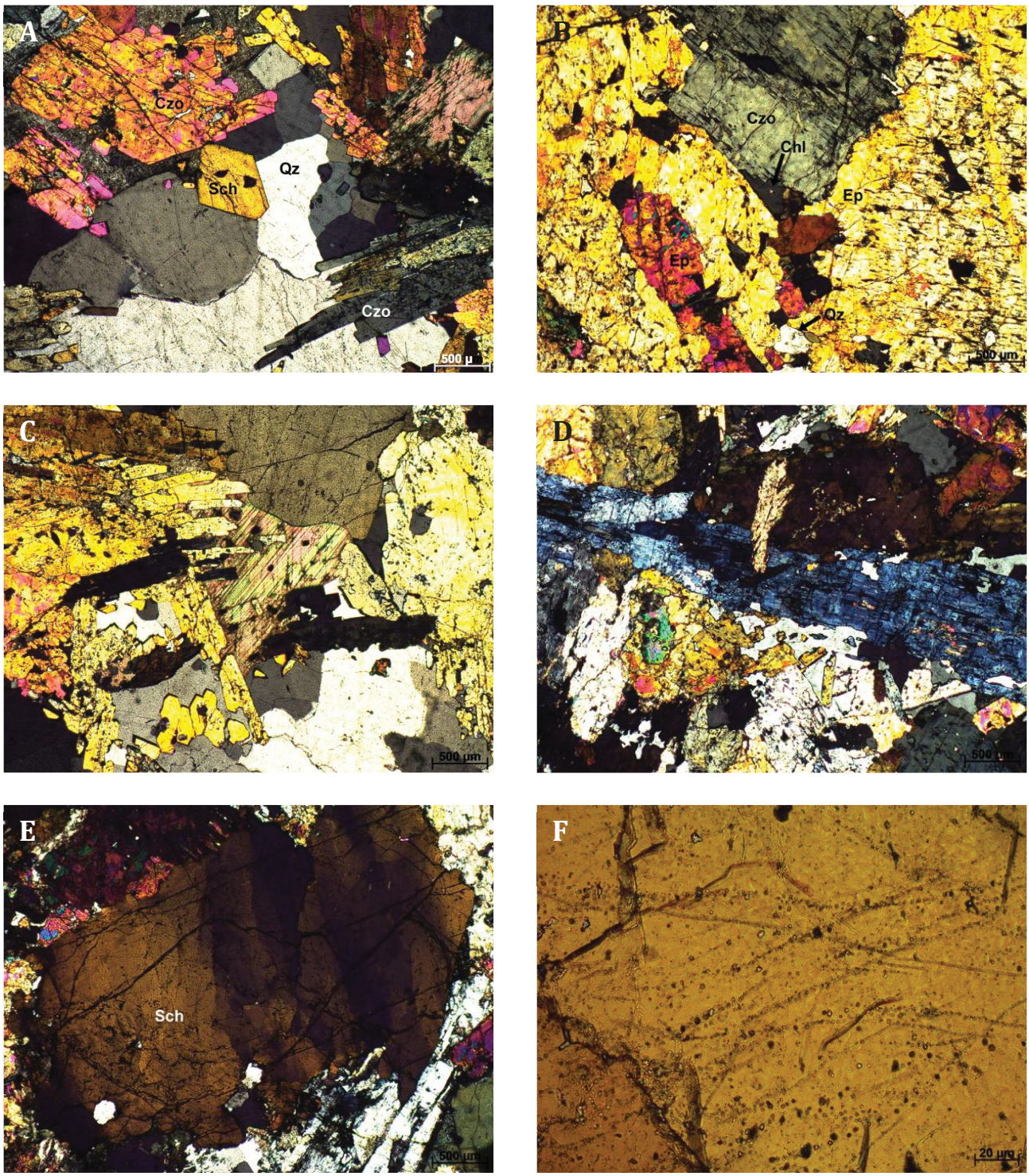

Figure 55: Photomicrographs of a thin section of scheelite-rich calc-silicate rock from main scheelite outcrop east of Messelingscharte. Sample 06-03. **A** Euhedral about 1 mm large scheelite crystal with clinozoisite and quartz. **B** Intergrowth of very coarse-grained clinozoisite and minor interstitial chlorite (arrow). **C.** Calcite (in the centre) with scheelite, clinozoisite and quartz. **D** Several mm-large clinozoisite crystal aggregate associated with quartz and epidote. **E** Very coarse-grained scheelite crystal showing undulose extinction. **F** Trails of secondary two-phase (L+V) fluid inclusions in scheelite. All photos in transmitted light with crossed nicols (+N).

6.6.2. Amphibole schist, scheelite-bearing

Samples: 03-13, 03-18 (thin section), 03-14, 05-03, 05-04, 06-02, 06-03, 06-20 (thin section)

The scheelite-bearing clinozoisite-plagioclase-calc-silicate fels is hosted in amphibole schist and deformed amphibolites. Amphibole schist is a dark-green strongly foliated and deformed rock (Figure 52A,B; Figure 53A,C). The amphibole schist contains dark-green stalky hornblende, quartz and platy

biotite (Table 17). Scheelite can be present in amphibole schist e.g. the second largest identified scheelite crystal was found in amphibole-schist (Figure 53C,D).

Table 17: Rock forming minerals of scheelite-bearing amphibole schist.

Mineral	Remarks	Abundance
Hornblende	green with strong pleochroism, medium-grained, stalky, subhedral, perfectly aligned into foliation	50%
Quartz	medium-grained, irregular anhedral grains	30%
Biotite	medium-grained, euhedral, platy, two generations: (1) medium-grained, together with stalky hornblende aligned in the foliation (2) coarse-grained, late euhedral platy porphyroblasts	20%

Accessory minerals (in total 10%) are pyrite, rutile, garnet, chlorite, scheelite, altered feldspar, clinozoisite and titanite. Scheelite occurs only rarely as fine-grained anhedral grains; most scheelite in amphibole schist is found in small patches of coarse-grained clinozoisite and quartz.

The fabric is intensely foliated to more massive. Intensely foliated parts are characterised by perfectly aligned amphiboles and biotites (Figure 56). More massive ones show biotite and amphibole crystals growing in different directions.

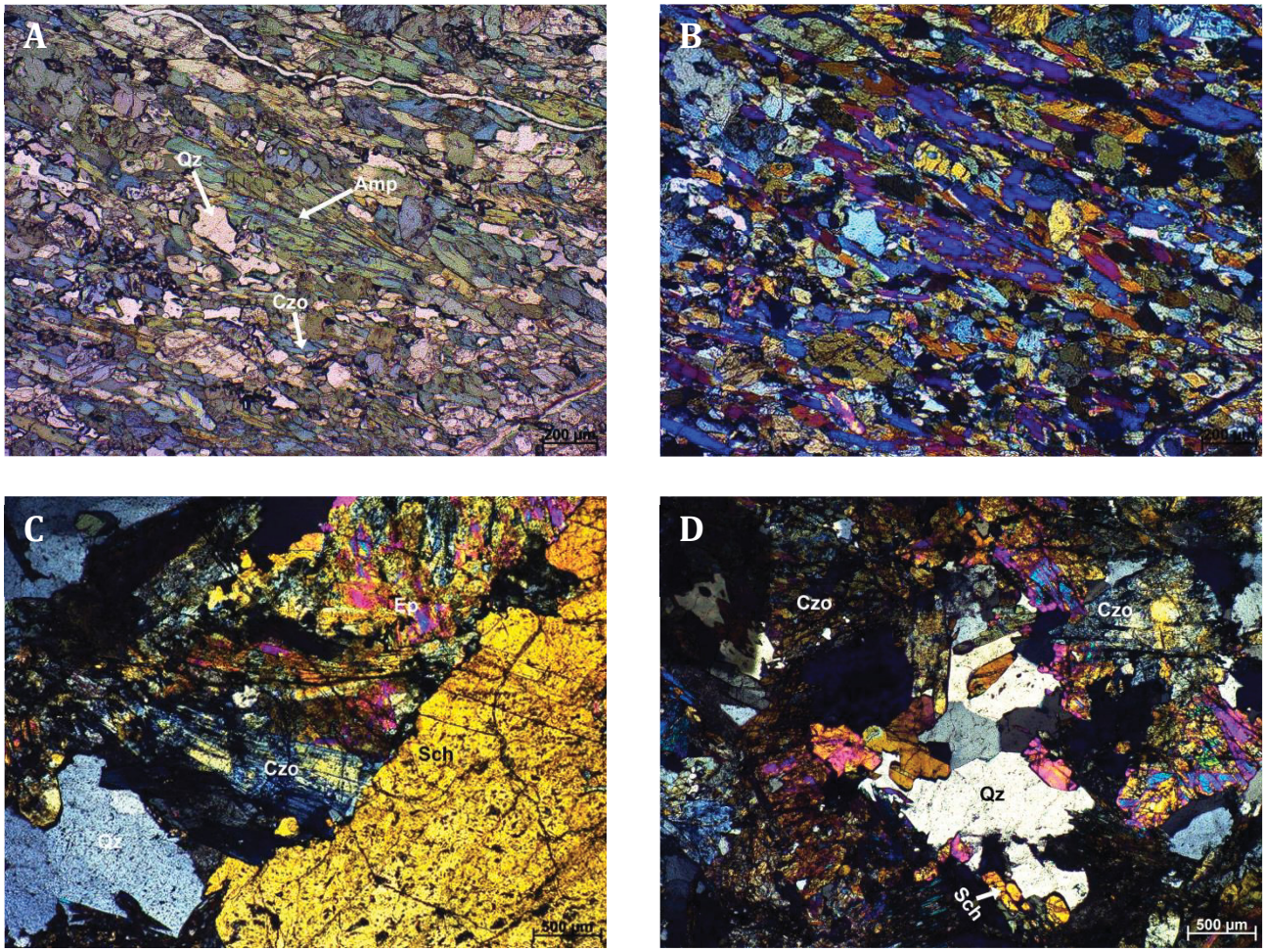

Figure 56: Photomicrographs of a thin section of sample 03-18. **A,B** Overview showing the fabric of amphibole schist. The rock contains mostly amphibole and is foliated. Minor phases are quartz and clinozoisite. **B** as A under crossed nicols. **C** Scheelite with clinozoisite and quartz in amphibole schist. Scheelite is much coarser-grained than surrounding minerals. **D** Fine-grained, recrystallised scheelite in contact with quartz and clinozoisite. All photos in transmitted light.

6.6.3. Calc-silicate veins in the Basal Amphibolite

Samples: 06-06 (thin section), 06-08 (thin section)

Calc-silicates occur in discordant deformed veins and in deformed concordant layers in amphibolites of the Basal Amphibolite. They are present at several locations like on the east flank of Messelingkogel or the west flank of Hochgasser. Two texturally different types can be distinguished:

(1) The first type is a coarse-grained clinozoisite-quartz vein rock with minor calcite, hornblende, chlorite, biotite, (altered) plagioclase showing a nematoblastic fabric (Figure 57). Medium-grained hornblende and chlorite build deformed layers. Cinozoisite makes up about 60% of the vein followed by quartz with 20% and all other minerals with together 20%. This vein type is similar to the scheelite-bearing clinozoisite-plagioclase-calc-silicate fels lenses east of Messelingscharte.

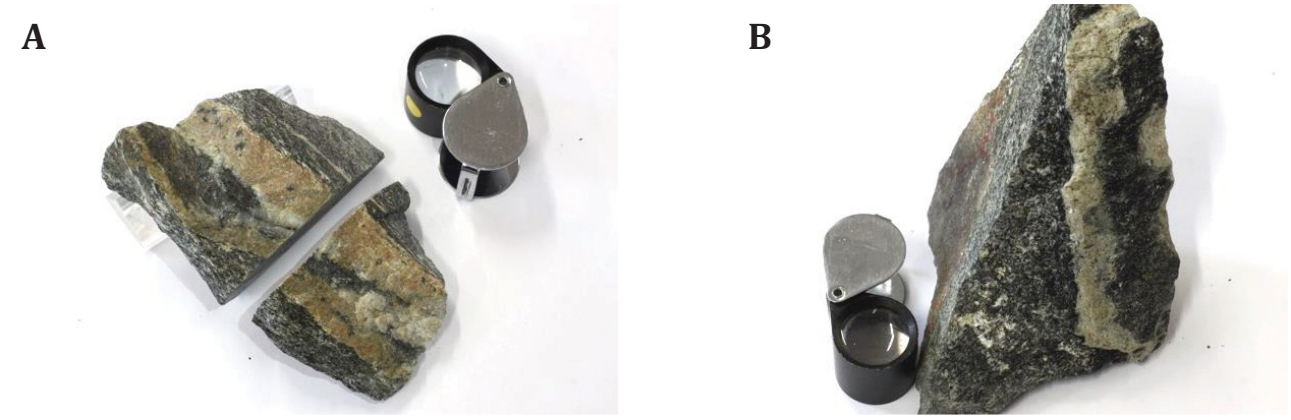

Figure 57: Photos of two different slightly discordant calc-silicate veins in amphibolite. **A** Sample 06-06. **B** Sample 07-14. The magnifier has a diameter of 2.5 cm.

(2) The second type is a medium-grained quartz-clinozoisite rock with minor plagioclase and chlorite (Figure 58C,D; sample 06-08). Clinozoisite is equigranular like quartz and plagioclase forming a granoblastic fabric indicative of metamorphic recrystallisation. Chlorite occurs as platy medium-grained accumulations. The vein consists of 60% clinozoisite, 30% quartz and plagioclase and 10% chlorite. The host rock of the vein is an altered, slightly foliated amphibolite.

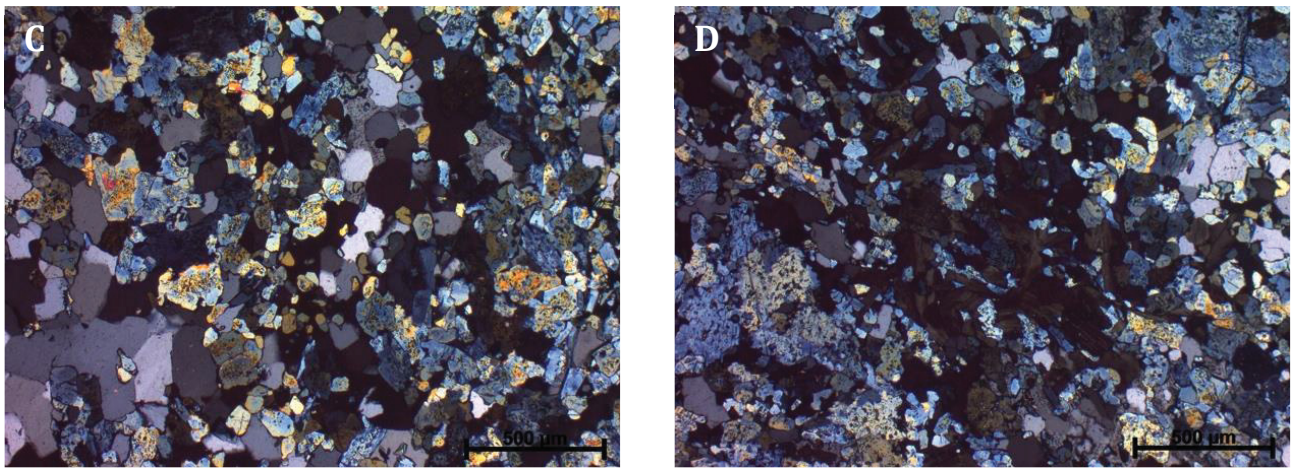

Figure 58: Photomicrographs of thin section of sample 06-06. **A** Clinozoisite and quartz forming granoblastic fabric. Crossed nicols. **B** Dark brown chlorite together with clinozoisite and quartz. Crossed nicols.

Concordant calc-silicate layers were also observed in deformed amphibolite. These layers are much more competent than the surrounding amphibolite and therefore become boudinaged (Figure 59).

They are composed epidote/clinozoisite, plagioclase, quartz and hornblende and have a thickness between 1-10 cm.

Figure 59: Small boudins of calc-silicate rock in strongly deformed amphibolite.

6.7. Calc-silicate rocks from Felbertal tungsten mine

Samples: 08-01 (thin section), 08-02 (thin section)

Calc-silicate rocks occur as patches and lenses in deformed amphibolite (hornblendite) together with quartz-veins in the Felbertal underground mine (sampling locations in Chapter 4.1).

The investigated rock from Felbertal tungsten mine is a scheelite-bearing clinozoisite-calc-silicate rock that is irregularly interfingered with the amphibolite host rock. The mineralogical composition is documented in Table 16 and Figure 60.

Table 18: Rock forming minerals of calc-silicate rock from Felbertal tungsten mine.

Mineral	Remarks	Abundance
Clinozoisite	fine- to medium grained, tightly intergrown with czo and hbl, many areas exclusively built by czo, an- to subhedral	50%
Hornblende	green, euhedral, stalky	10%
Plagioclase	fine-grained, twins, often blurry	10%
Calcite	very coarse-grained, anhedral, in veinlets and nests, interstitial between other minerals	10%
Quartz	Two generations: (1) fine-grained, anhedral, occurs with fine-grained Ep/Cz (2) coarse-grained, anhedral, in veinlets together with biotite, chlorite and hornblende	10%
Biotite	medium-grained, subhedral, platy, two generations: (1) fine-grained, closely intergrown with other minerals (2) isolated, medium-grained, porphyroblasts	5%
Chlorite	coarse-grained, aggregates with radial growth, in nests and veinlets with calcite	5%
Sulphides	Pyrite: subhedral, many small inclusions Chalcopyrite: subhedral, solitary grains and intergrown with pyrite	5%

	with straight grain boundaries Pyrrothite: anhedral, closely intergrown with chalcopyrite Arsenopyrite: coarse-grained, rare, euhedral, occurs with pyrrothite	
Muscovite	Rarely coarse-grained euhedral muscovite is present	accessory
Scheelite	subhedral to euhedral (rare), fine- to medium-grained, roundish grains	accessory

There are 3 types of different veinlets with slightly different petrographic composition crosscutting the calc-silicate rocks:

(1) Chlorite, calcite veinlet: >1 mm thick and about 1 cm long, two different directions that cross-cut each other at an 90° angle
(2) Quartz, hornblende, calcite, chlorite veinlet: >1 mm thick and >1 cm long
(3) Hornblende, quartz veinlet: <1 mm thick and much shorter compared to the other veinlets

There are two different micro-domains inside the calc-silicate rock. First, clinozoisite-dominated ones with just minor amounts of plagioclase, quartz, biotite and coarse-grained calcite. Second, there are coarse-grained micro-domains where quartz, calcite and biotite dominate. Plagioclase is altered. The latter show a granoblastic fabric and host fine-grained scheelite.

Additionally, there is the amphibolite host rock that is tightly foliated and mainly composed of hornblende. Hornblende is green, stalky, medium-grained and perfectly aligned in the foliation (60%). Minor amounts of plagioclase (20%), quartz (10%) and epidote/clinozoisite (10%) are present. Coarse-grained biotite occurs in accessory amounts.

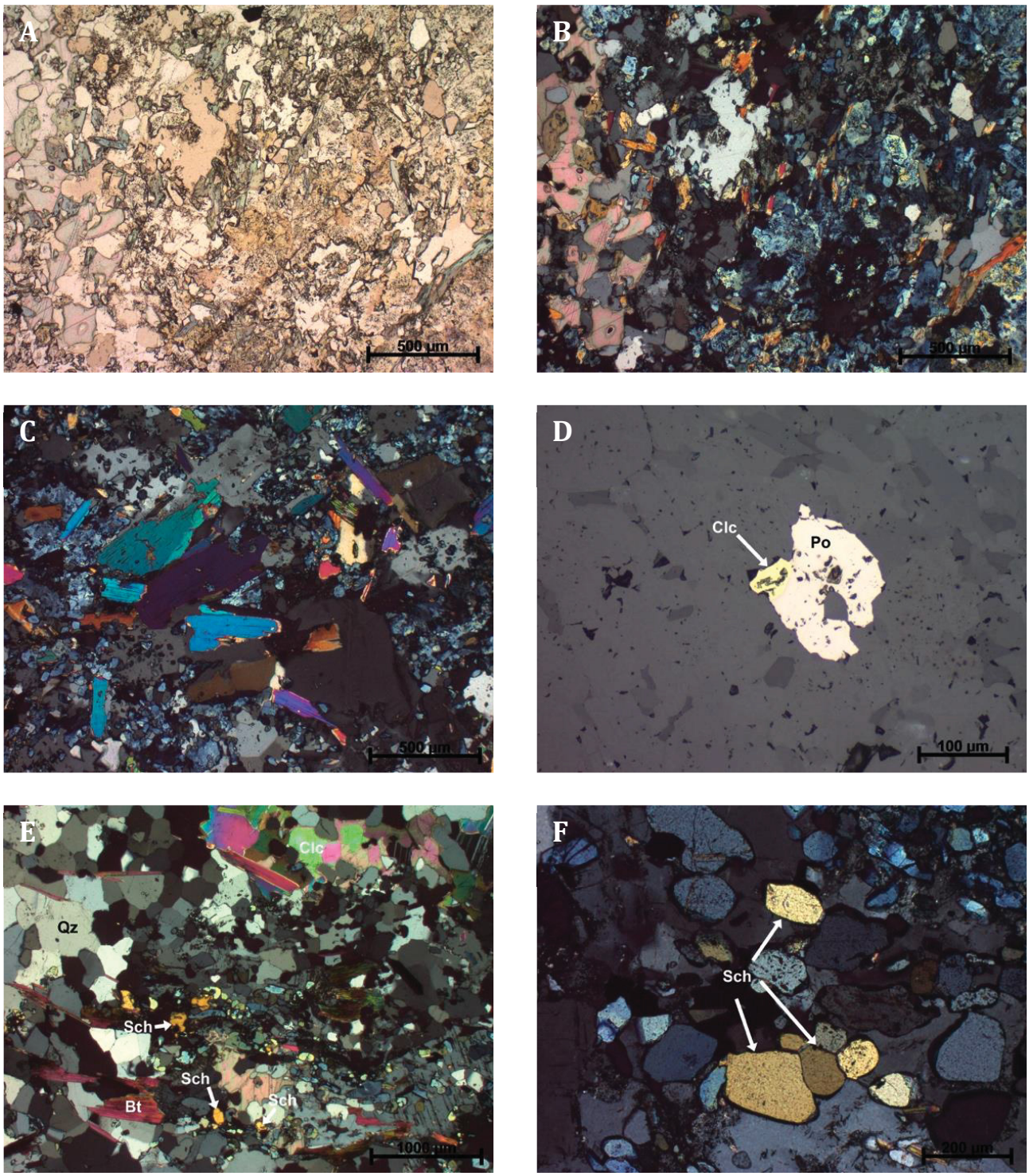

Figure 60: Photomicrographs of thin sections of samples 08-01 (A-D) and 08-02 (E-F). **A,B** Typical random fabric of the calc-silicate rocks from Felbertal tungsten deposit with calcite, clinozoisite, green amphibole, plagioclase and quartz. **B** as A under crossed nicols. **C** Accumulation of coarse-grained biotite. **E** multi-phase sulphide grain with pyrrhotite and chalcopyrite. **E**,F fine-grained recrystallised scheelite with quartz, biotite and calcite. Photos A-E and G-F transmitted light, crossed nicols; photo F reflected light IIN.

Minerals	Central Gneiss and associated lithologies				Mesozoic cover units				Basal Amphibolite		
	Orthogneiss	Weissschiefer	Orthogneiss	Amphibolite	Quartzite	Quartzite (deformed)	Mica schist	Marble	Massive amphibolite	Banded amphibolite	Hbl-bt schist
Qz	xxx	xx	xxx	xxx	xxxx	xxx	xx	o	xx	xx	xxx
Plg	xx	x	xx	o	xx	o	xx	o	xxx	xxx	xxx
K-Fsp	xxx	o	xxx	xxx	o	o	o	o	o	o	o
Hbl	o	o	o	xxx	o	o	o	o	xxx	xxx	xxx
Grt	o	o	o	xx	o	o	o	o	o	o	o
Bt	xx	o	xx	x	o	o	xxx	o	xxx	xxx	xxx
Ms	xxx	xxx	xx	o	o	xx	o	o	o	o	o
Chl	x	o	o	xx	o	o	o	o	x	x	xx
Sch	o	o	o	o	o	o	o	o	o	o	o
Ap	o	o	o	o	o	o	o	o	o	o	o
Ep	o	o	o	x	o	o	o	o	x	x	xx
Zo	x	o	o	x	o	o	o	o	x	x	xx
Clc	x	o	o	o	o	o	o	xxxx	o	o	xx
Sulph	o	o	x	x	xx	o	o	o	o	o	x
other accessories					Zrn						Ap, Rt, Ttn

xxxx = “monomineralic”(>95%)

xxx = major phase (>5%)

xx = minor phase (1-5%)

x = accessory phase (<1%)

	Basal Amphibolite					Basal Schist	Habach Complex	
Minerals	Hornblede fels	Hbl-bt gneiss	Actinolite-rich schist	Calc-silicate fels	Amphibole schist	Amphibole mica schist	Weinbühl amphibolite	Metased-iments
Qz	o	xxx	xxx	xxx	xxx	xxx	xxx	xxx
Plg	xxx	xxx	xx	xxx	o	xxx	xxx	xxx
K-Fsp	o	o	o	o	o	o	o	o
Hbl	xxx	xxx	o	x	xxx	xxx	xxx	o
Grt	o	xx	o	o	x	o	o	o
Bt	o	xxx	xxx	x	xxx	xxx	o	xxx
Ms	o	o	xxx	o	o	o	o	o
Chl	o	x	xxx	xx	x	xx	xx	xxx
Sch	o	o	o	x	x	o	o	o
Ap	o	o	o	x	o	o	o	o
Ep	o	xx	o	xxx	x	o	xx	o
Zo	o	xx	o	xxx	x	o	xx	o
Clc	o	o	o	xx	o	o	o	o
Sulph	xx	x	o	x	o	o	o	xx
other accessories					Ttn, Rt	Rt	Rt	

7. Structural geology

The structural geology is very complex in the study area and was not the main focus of this field campaign. Hence, only basic structural features were mapped and analysed.

The rocks in the whole working area are strongly deformed and were affected by poly-phase deformation. Nearly all contacts between major units are tectonic contacts showing intense deformation (Figure 10; Figure 11). The deformation is indicated by strongly sheared rocks and fault rocks (e.g. Weissschiefer, cataclasite). Granatspitz gneiss is tectonically inserted into Basal Schist at east flank of Messelingkogel producing several metres thick layers of Weissschiefer. The contact between Basal Amphibolite and Granatspitz gneiss is also strongly tectonised. The Habach Complex shows a tectonic contact on Messelingkogel to the Basal Schist in the footwall. The contact is marked by a several metres thick layer of cataclasite.

The most prominent structural feature of most rocks is a prominent metamorphic foliation. Figure 61A shows a contour plot of all measured foliation planes in the working area. Most foliations are subhorizontal to SW dipping. SW dipping foliations predominate at Meselingscharte and Messelingkogel. At Hochgasser they dip gently in different directions because of intense folding. There are two steep dipping joint sets (Figure 61B) striking about 90° and parallel to the main foliation.

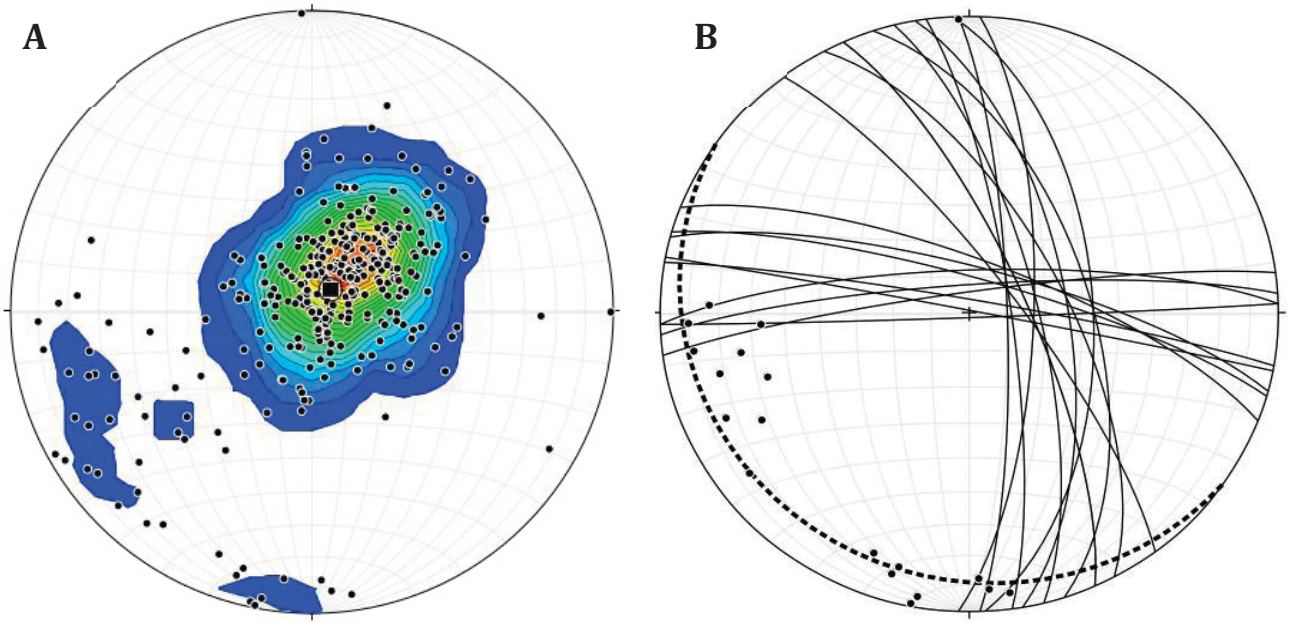

Figure 61: A Contour plot of foliation planes. The Clar-value for the statistical mean vector (95% confidence interval) is 184/08. The Clar-value for the highest concentration of measured values is 225/13. **B** Joint directions (solid) with statistical values of k1 (077/67) and k2 (006/81). Dashed line statistical value for foliation.

Several generation of folds are present in the Basal Amphibolite ranging from large scale to very small scale folds. Deformation is very complex and has built several different stages of folds. The most prominent fold is a very large E-W directed isoclinal fold at mountain Hochgasser (Figure 62). It is most likely of late-Alpine age. Corresponding smaller-scale (dm-m) folds in amphibolite can be found all over the working area refolding the older Alpine penetrative foliation. At Hochgasser these asymmetric parasitic folds allow reconstructing a large-scale fold with its fold hinge in the N (Figure 63). This type of large-scale folding may also explain the dramatic increase of the thickness of the Basal Amphibolite at Hochgasser, which normally is between 100 and 150 m.

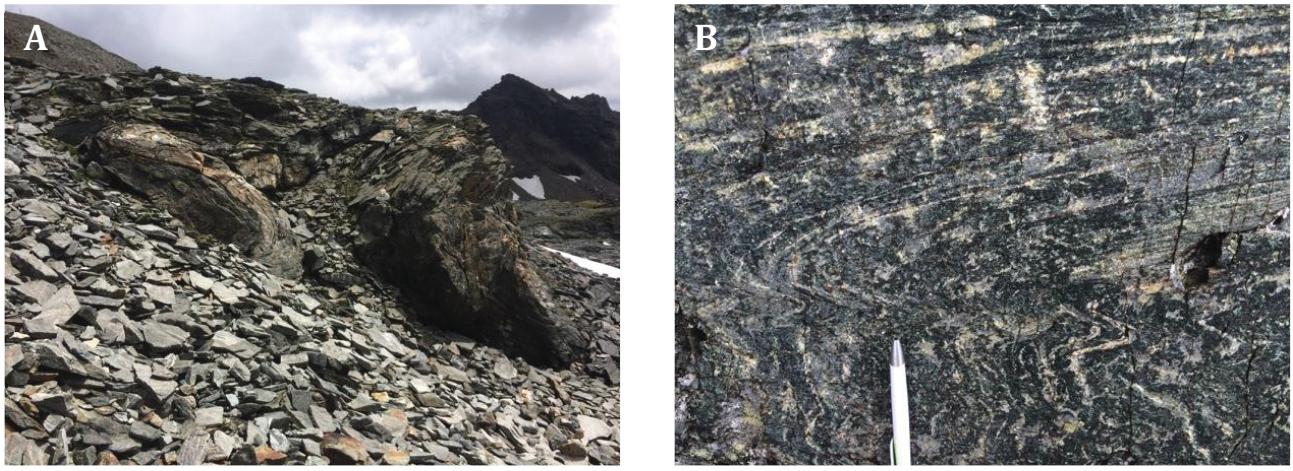

Figure 62: A Two tight folds with opening in the opposite directions (GPS #338) on the west flank of mountain Hochgasser. **B** Small-scale parasitic folds in amphibolite; outcrop (GPS #337) is very close outcrop in A. The asymmetric s-folds indicate that they are developed in the hanging limb of a larger fold closing to the left (i.e. N).

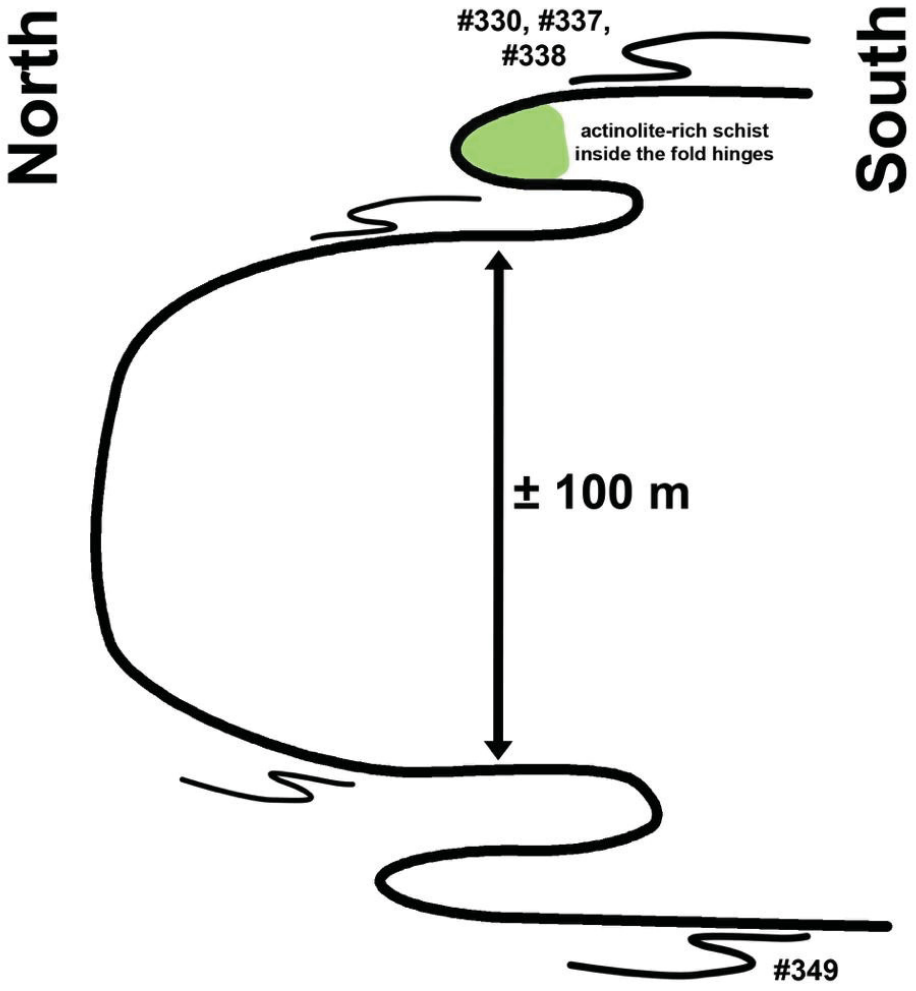

Figure 63: Sketch of a large-scale fold structure at mountain Hochgasser. Asymmetric parasitic s- and z-folds in the limbs indicate the hinge open to the north. The numbers refer to the number of the GPS number of outcrops. Assuming that outcrop #349 is on the lower limb, the large fold has a thickness between the limbs of about 100 m.

8. Geochemistry

8.1. Whole rock geochemical analyses

Whole rock geochemical analyses were performed on 32 samples. The complete bulk chemical analyses and the sample list is to be found in Appendix A.3. Reference data for MORB composition was taken from Pearce et al. (1981) in Bevins et al. (1984). The normalization of REE to chondrite values was performed with data provided from Boynton (1984). Data for comparison and to enlarge the dataset were taken from literature (Kozlik 2016; Frisch and Raab 1987; Fringer et al. 1993; Brunnsmann et al. 2000).

8.1.1. Combined geochemical plots and data

The following legend was used in all plots and diagrams for the various lithologies (Figure 64).

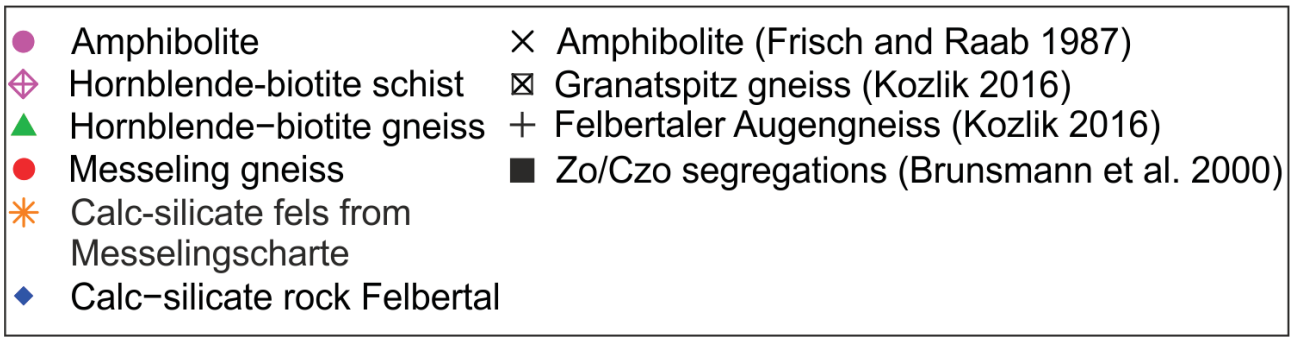

Figure 64: Legend for all following geochemical plots and figures.

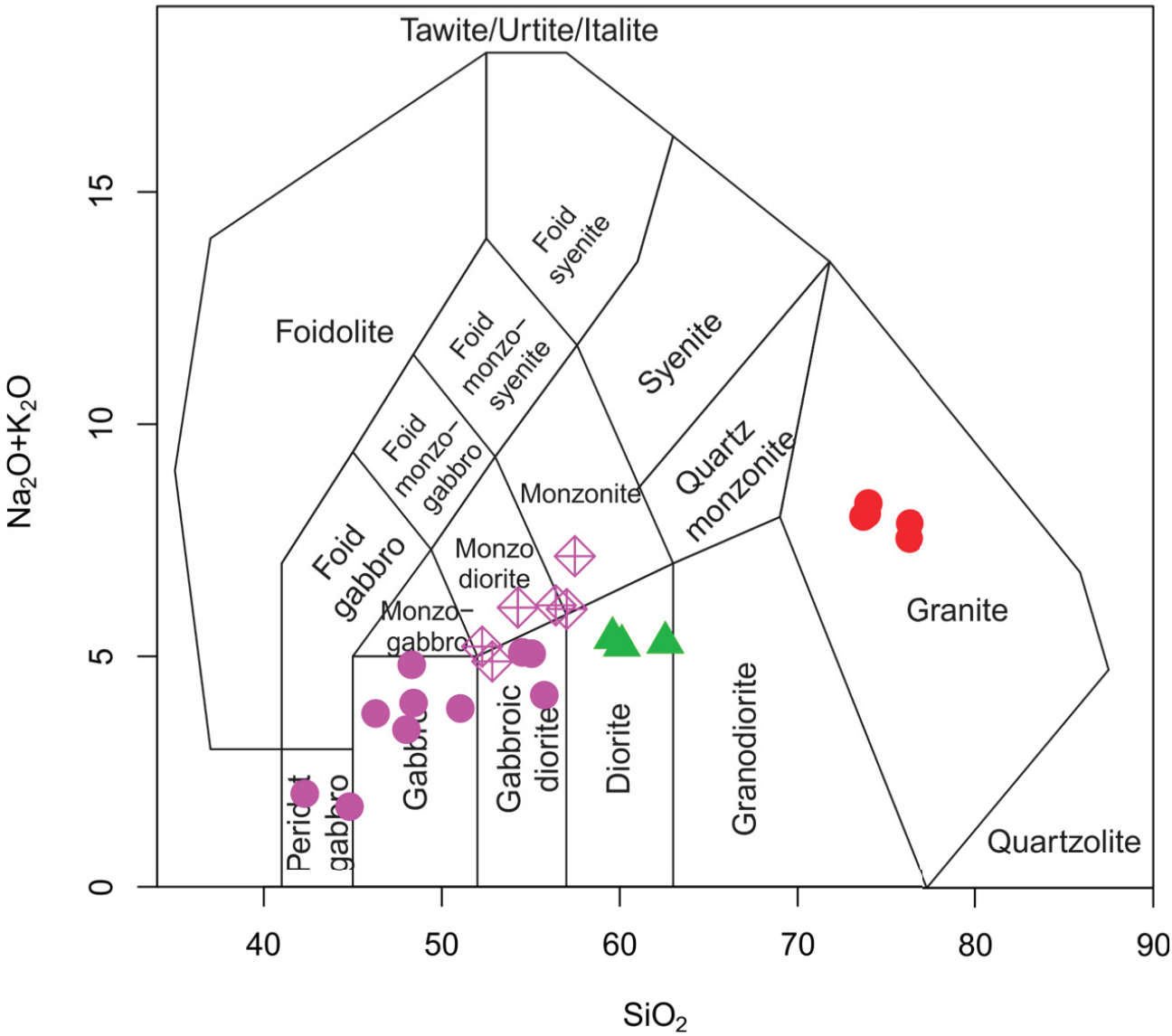

Figure 65: TAS diagram of all rocks from the Basal Amphibolite as well as rocks from the hornblende-biotite gneiss and the Messeling gneiss. For legend see **Figure 64**. Diagram from Middlemost (1994).

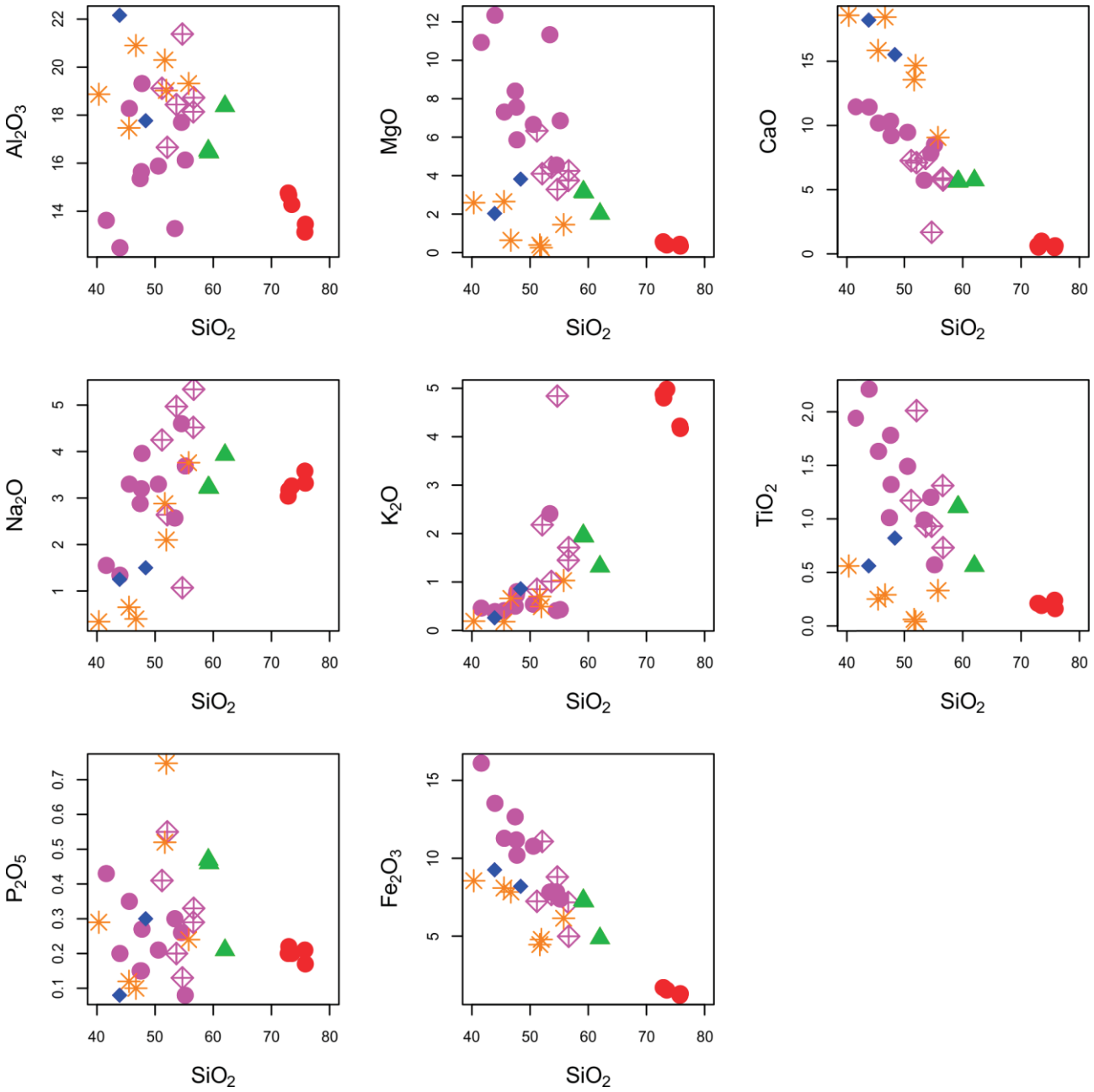

Figure 66: Harker diagrams of major elementsof all analysed samples. Concentrations in mass%. For legend see **Figure 64**.

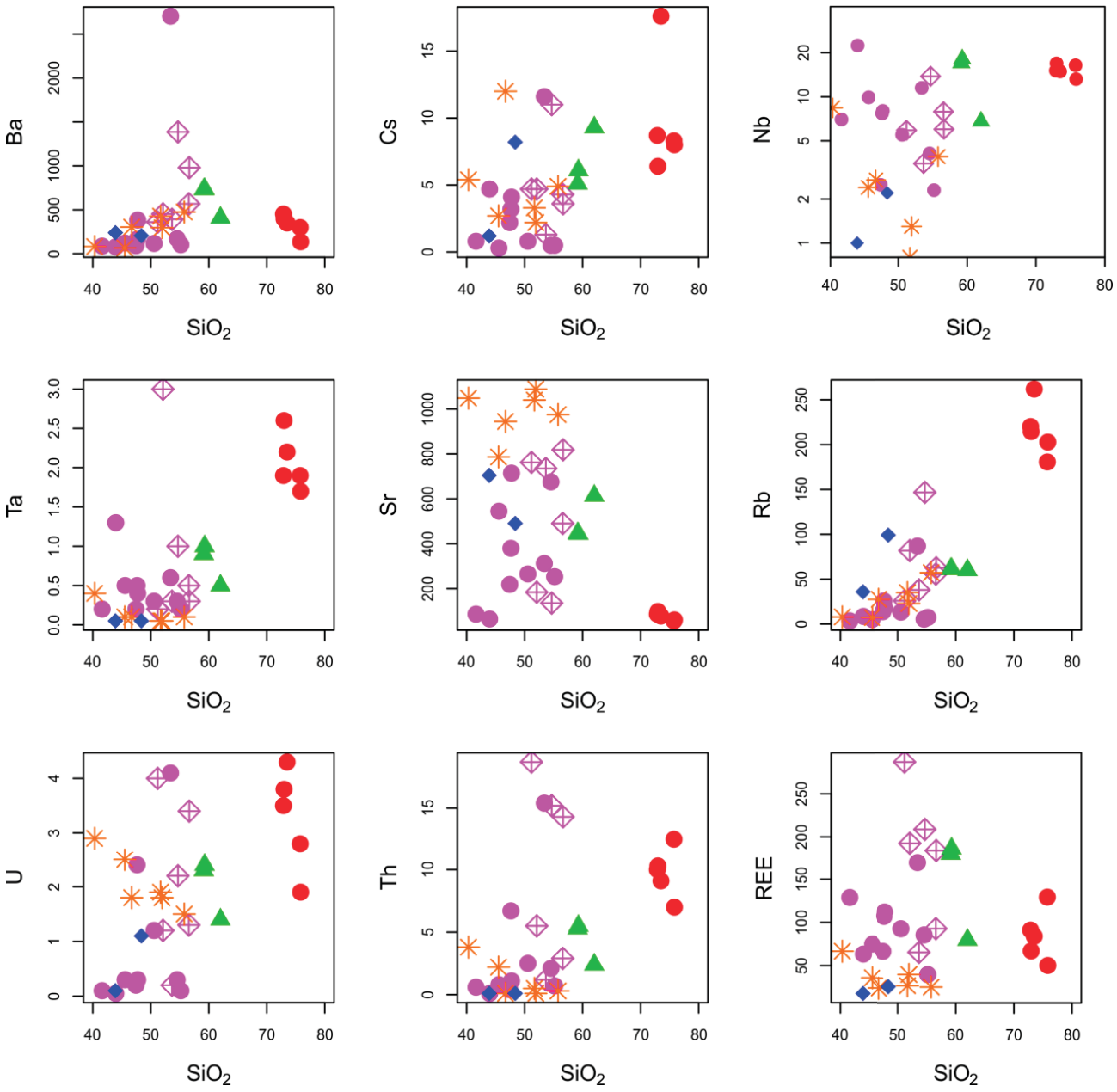

Figure 67: Harker diagrams of important trace elements. Trace elements in ppm, SiO_2 in mass%. For legend see **Figure 64**.

8.1.2. Basal Amphibolite

Ten samples of metabasites from the Basal Amphibolite unit (seven amphibolites, three hornblende felses) and six samples of deformed metabasites (four hornblende-biotite schists, two mylonitic gneisses) were analysed for whole rock geochemical composition. Analyses of basal amphibolites from Frisch and Raab (1983) were added to extend the data set.

Major elements

The analytical results are listed in the Harker diagrams show that the chemical composition of Basal Amphibolite samples varies with SiO_2 which is used as a common differentiation index. Fe, Ca, Mn and Ti decrease systematically with higher SiO_2, whereas the alkalis increase (Figure 66). Most trace elements show a large scatter in Harker diagrams (Figure 67). The largest variations are to be seen for U, Th, Sr and REE.

The SiO_2 content of the analysed metabasites varies between 42-55 mass% with an average of about 48 mass%. The average Al_2O_3 and Fe_2O_3 content is 16 mass% and 11 mass% respectively. The average SiO_2 contents of hornblende-biotite schists are higher compared to the amphibolite. Also Al_2O_3 and K_2O contents are higher, but Fe_2O_3 and MgO contents are lower in hornblende-biotite schists compared to the amphibolite.

Table 19: Major element analyses (mass%) of amphibolite (with hornblende fels) and hornblende-biotite schist (including mylonitic gneisses) from the Basal Amphibolite.

	Amphibolite (n=10)			Hornblende-biotite schist (n=6)		
Component	**Median**	**Min**	**Max**	**Median**	**Min**	**Max**
SiO_2	47.69	41.61	55.18	54.17	51.18	54.17
Al_2O_3	15.77	12.48	19.32	18.59	16.66	18.59
Fe_2O_3 (tot)	10.98	7.39	16.16	7.46	4.99	7.46
MgO	7.44	4.55	12.34	4.18	3.28	4.18
CaO	9.83	5.73	11.45	6.50	1.68	7.43
Na_2O	3.25	1.34	4.6	4.39	1.07	4.39
K_2O	0.48	0.39	2.41	1.58	0.85	1.58
TiO_2	1.41	0.57	2.21	1.05	0.73	1.05
P_2O_5	0.24	0.08	0.43	0.31	0.13	0.31
MnO	0.16	0.11	0.22	0.12	0.07	0.12
Cr_2O_3	0.034	0.019	0.087	0.017	0.005	0.017
LOI	1.05	0.70	1.50	1.1	0.6	2.7
Sum	99.75			99.8		

Classification diagrams of major and trace elements

Several geochemical classification diagrams were used to classify rocks from the Basal Amphibolite unit and assign them to magmatic series and constrain the geotectonic setting.

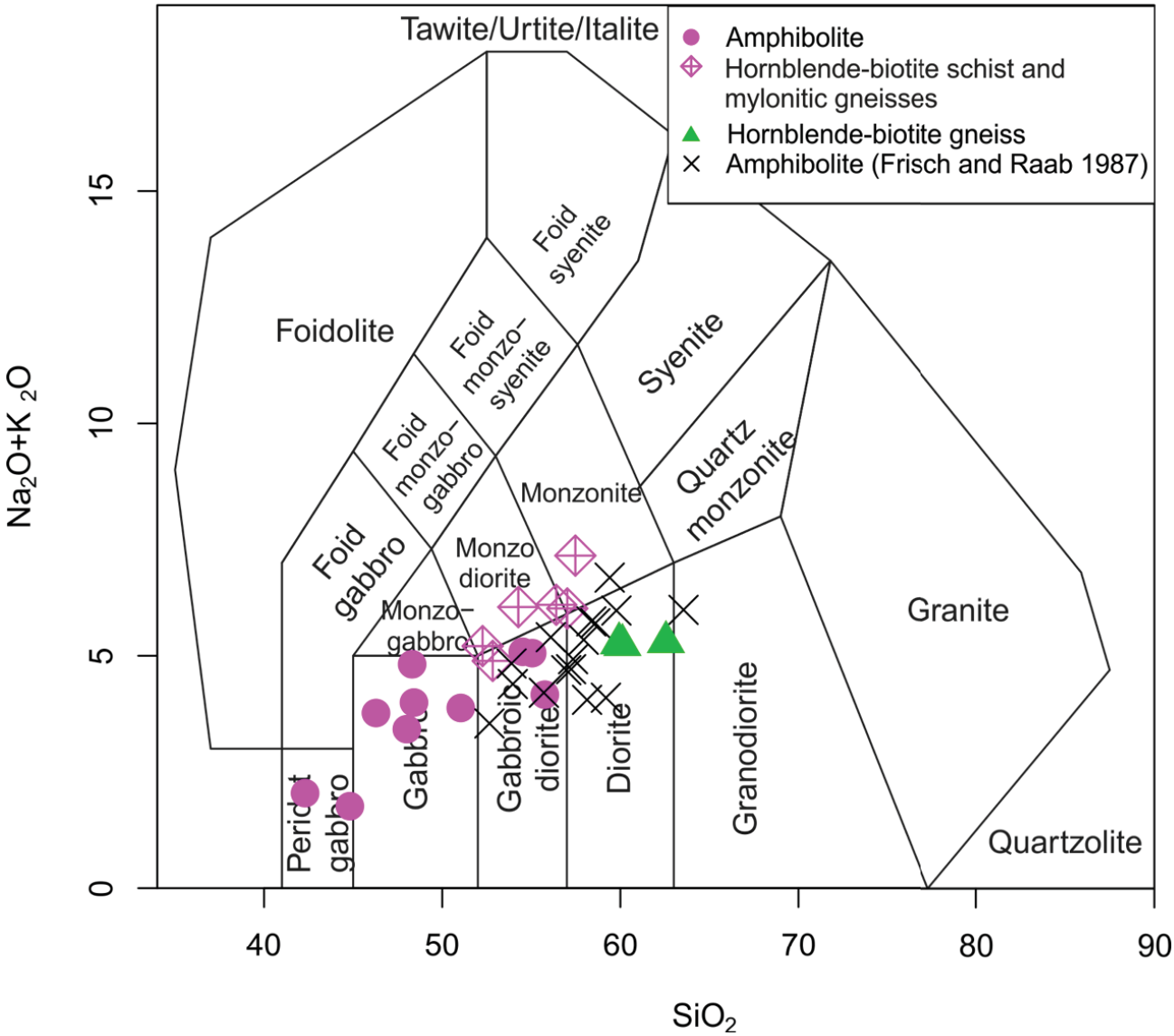

Figure 68: TAS diagram from Middlemost (1994) of all analyses of the Basal Amphibolite including data from Frisch and Raab (1987).

The Total Alkali Silica (TAS) diagram from Middlemost (1994) shows that most samples plot in the field of a gabbro. Data from Frisch and Raab (1983) tends to by richer in SiO_2 therefore plotting preferably in the diorite field. Two outliers plotting in the peridote gabbro field at <45mass% SiO_2 are hornblende fels samples (see Chapter 6.2.4). The TAS diagram also shows the more evolved chemical composition of the hornblende-biotite schists and hornblende-biotite gneiss.

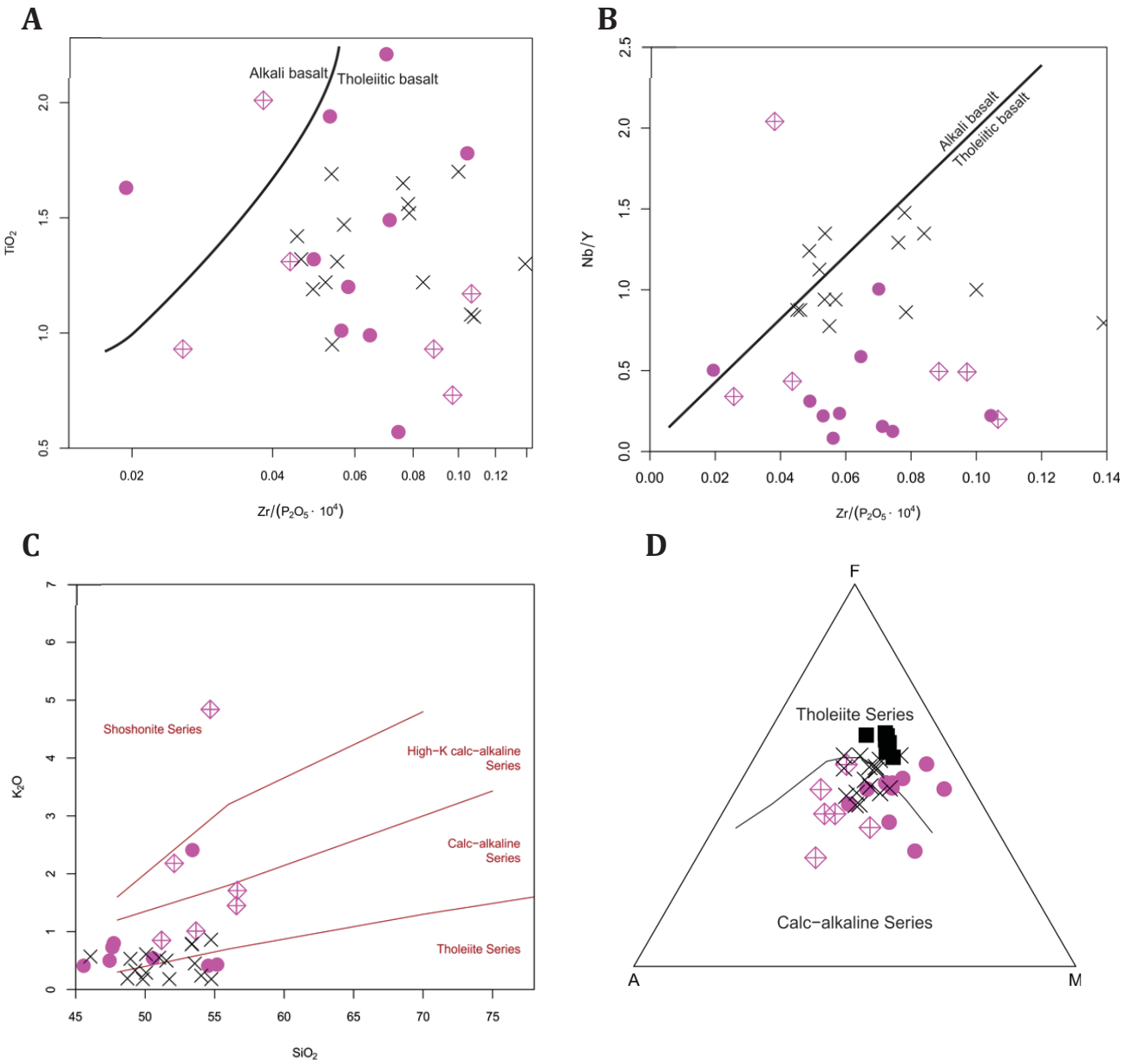

Figure 69: A, **B** Discrimination diagrams for tholeiitic and alkaline mafic igneous rocks using immobile elements. **A,B** Diagrams from Floyd and Winchester (1975) to discriminate between tholeiitic and alkaline mafic igneous rocks. **C** SiO_2-K_2O plot from Peccerillo and Taylor (1976). **D** AFM diagram after Irvine and Baragar (1971). Data from Brunsmann et al. (2000) is additionally included in this plot. For legend see **Figure 64**.

Because alkalis are easily mobilised during metamorphism and alteration diagrams using less mobile elements were used to constrain the magmatic series. The $Zr/P_2O_5{*}10^4$ vs. TiO_2 and $Zr/P_2O_5{*}10^4$ vs. Nb/Y plots (Figure 69A,B) from Winchester and Floyd (1976) shows that nearly all samples are of tholeiitic composition. Data from Frisch and Raab (1987) have all higher Nb/Y and therefore tend to plot closer at the transition between alkali and tholeiitic mafic igneous rocks whereas the new data suggests a clear tholeiitic composition. One explanation could be analytical problems because of low concentrations measured by XRF.

The SiO_2-K_2O plot (Figure 69C) from Peccerillo and Taylor (1976) shows that most amphibolites plot in the transition zone between tholeiitic and calc-alkaline series; most hornblende-biotite schist samples plot in the calc-alkaline field (Figure 69C). Generally, the new data tend to plot at higher K_2O values than the older Frisch and Raab (1987) data. Data from Frisch and Raab (1987) has statistically

significantly different values for mean and variance (confidence interval 95%). Commonly hornblende-biotite schist is significantly enriched in potassium. In the AFM diagram amphibolite plot around the transition from calc-alkaline to tholeiitic, whereas the hornblende-biotite schist clearly plot in the calc-alkaline field (Figure 69D).

Overall, the chemical composition is tholeiitic with a trend to calc-alkaline composition. The main components tend to indicate calc-alkaline composition whereas immobile trace elements clearly argue for a tholeiitic character.

Multi-element spider plots

Incompatible trace elements normalized to MORB (Figure 70A,B) as well as REE normalized to chondrite are depicted in spider plots (Figure 70C,D).

Most elements are slightly enriched (about 1 to 10 times) compared to MORB (Figure 70A). LILE show more variation and no uniform behaviour. The amphibolites are enriched in Rb, K and depleted in Ba. The variation in Th is very large reaching from <1 to 100 times MORB, that of Sr is <1 to about 10 times MORB. Nickel is strongly depleted whereas compatible Cr is slightly enriched relative to MORB.

The trace element pattern of hornblende-biotite schist (Figure 70B) is different to the amphibolite (Figure 70A). LILE (Rb, Ba, K) are more enriched. Thorium shows a positive spike as in the amphibolites, Ta and Sr have negative troughs. The behaviour of Ni and Cr is comparable to the amphibolite.

The REE patterns of the amphibolites (Figure 70C) are rather flat and show a slight enrichment of LREE (between 20-100) over HREE (between 10-30 times) when compared to chondrite. The $(La/Yb)_{cn}$ ratio of the amphibolites, which is used as an indicator of LREE / HREE fractionation, varies between 0.9-13.2 with a median of 3.4.

The REE patterns of the hornblende-biotite schists (Figure 70D) differ from those of the amphibolites. The LREE are generally more enriched and the curve is much steeper towards the HREE. Three samples also show a weak negative Europium anomaly (Eu/Eu* = 0.78-0.90) ($Eu/Eu^* = Eu_N/\sqrt{Sm_{N*}Gd_N}$). The $(La/Yb)_{cn}$ ratio ranges between 6.2-27.9 with a median of 10.7.

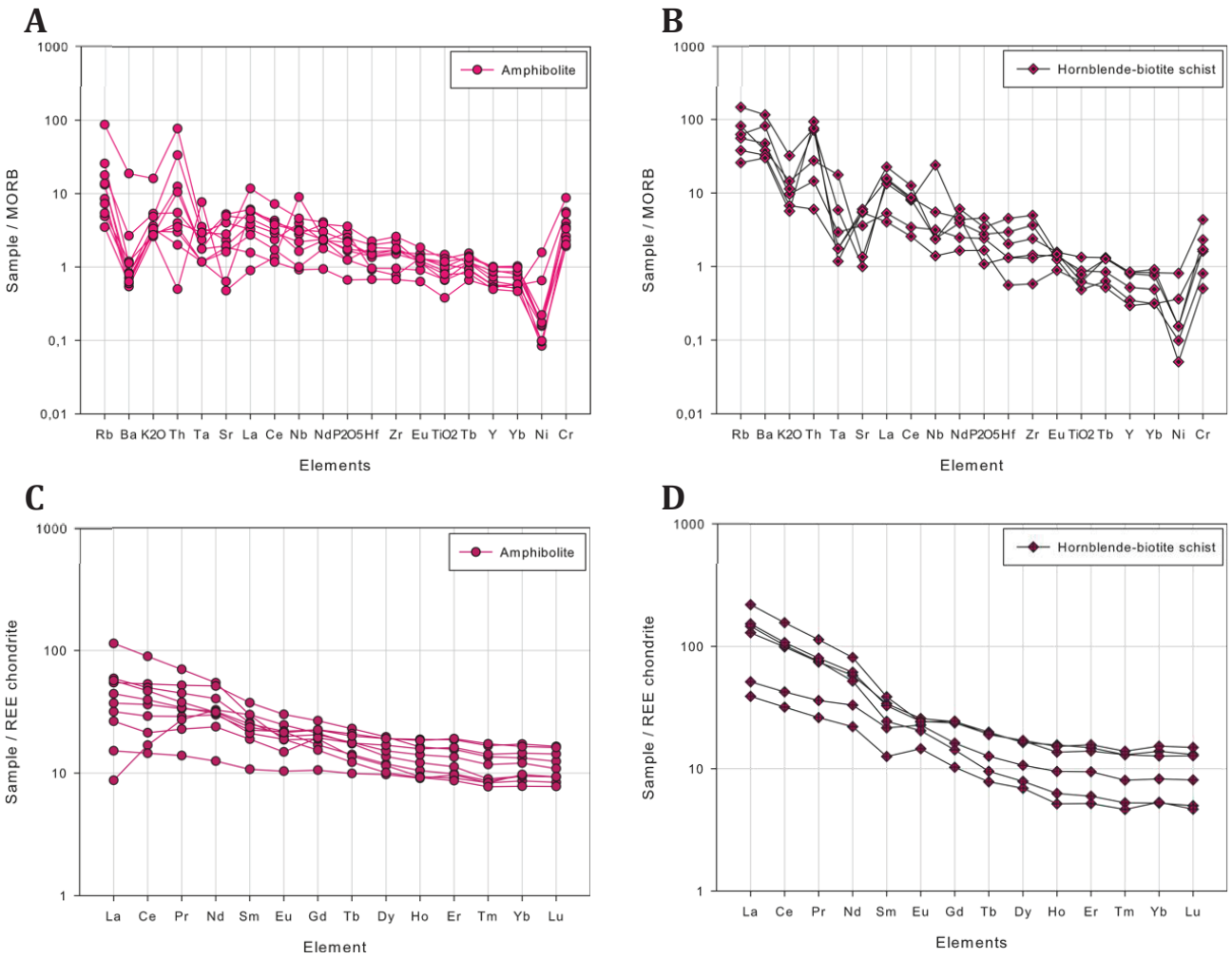

Figure 70: A Spider diagram of trace elements compared to MORB of amphibolites. **B** Spider diagram of trace elements compared to MORB of hornblende-biotite schist. **C** Spider plot of REE normalized to chondrite of amphibolites. **D** Spider diagram of REE normalized to chondrite of hornblende-biotite schist.

Trace elements are relatively independent from the main components. Strontium correlates positively with Al_2O_3 and Na_2O, whereas it shows a negative correlation with MgO. Scandium and vanadium show unexpected positive correlation to all REE elements. Europium also increases with higher Ca content.

Geochemistry of the hornblende-biotite gneiss

The hornblende-biotite gneiss intrusion is a metamorphosed intermediate igneous rock of diorite composition (Figure 65; see Chapter 8.1.2). The average SiO_2 content is about 60% and the average Na_2O+K_2O content is 5.2 mass%. Main and trace elements in the Harker diagram (Figure 66, Figure 67) show little scatter especially because two samples have nearly the same geochemistry although they were taken from different locations. Larger differences are evident for the REE content as well as the U and P_2O_5 content.

Table 20: Main components (mass%) of hornblende-biotite gneiss intrusions in the Basal Amphibolite.

	Hornblende-biotite gneiss (n=3)		
Component	**Median**	**Min**	**Max**
SiO_2	59.28	59.15	62.01
Al_2O_3	16.53	16.45	18.38
Fe_2O_3(tot)	7.24	4.87	7.32
MgO	3.13	2.02	3.17
CaO	5.65	5.63	5.73
Na_2O	3.23	3.22	3.93
K_2O	1.94	1.32	1.97
TiO_2	1.11	0.56	1.11
P_2O_5	0.46	0.21	0.47
MnO	0.12	0.09	0.13
Cr_2O_3	0.010	0.006	0.014
LOI	1	0.7	1.1
Sum	99.81		

Figure 71A-C show spider plots of trace elements and REE normalized to MORB and chondrite, respectively. The trace element plot (Figure 71A) (after Bevins et al. 1984) shows an enrichment of some LILE (Rb, Ba and K) with a decreasing trend to the right side of the plot. Tantal and Sr show a distinct negative trough in two samples. Titanium is slightly depleted, Ni shows the strongest depletion. The Zr/Hf ratio shows very low values of 22.4-6.3.

The REE pattern of the hornblende-biotite gneiss (Figure 71B) is flat dipping and shows a 80-100x enrichment of LREE and 8-20x enrichment regarding HREE compared to chondrite. Two samples show a weak Europium anomaly (Eu/Eu* = 0.84). The $(La/Yb)_{cn}$ ratio ranges between 6.7-8.0 with a median of 7.9.

Figure 71C shows a spider plot (after Pearce 1996) in which the hornblende-biotite gneiss is compared to amphibolite. The gneiss shows a steep dipping trend within the limits of the amphibolite with slightly higher median Th, lower TiO_2 and Y. Such a trend is typical for continental or oceanic arc rocks (Pearce 1996). Similarities to the amphibole and hornblende-biotit schist indicate the same geotectonic setting and geological development.

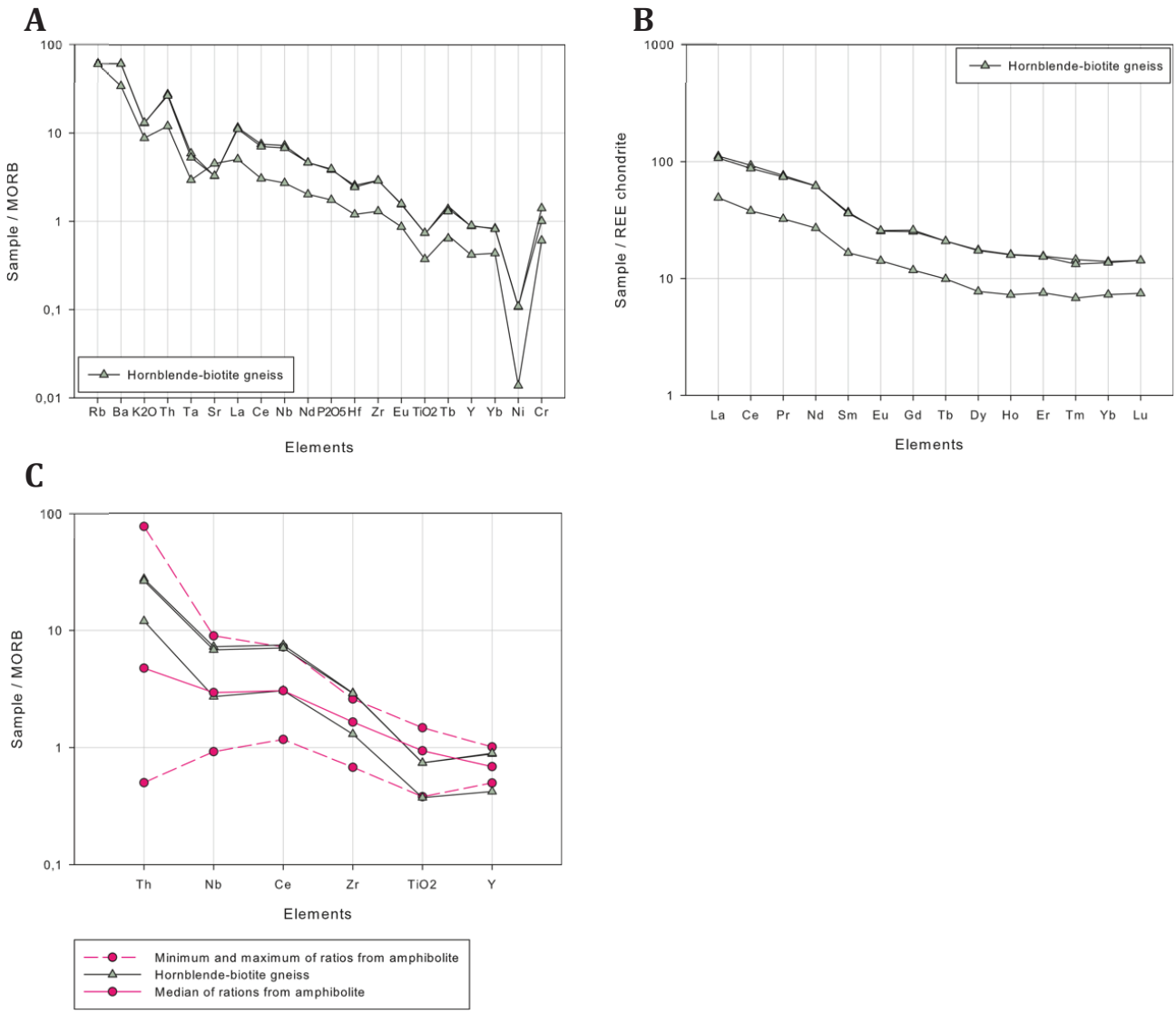

Figure 71: A Spider diagram of trace elements of the hornblende-biotite gneiss normalized to MORB. **B** Chondrite normalized REE plot of hornblende-biotite gneiss. **C** Spider diagram of selected trace elements of hornblende-biotite gneiss compared to the range and median of amphibolite samples (Basal Amphibolite, this study) (after Pearce 1996).

8.1.3. Geotectonic setting of the Basal Amphibolite

Several geochemical discrimination diagrams and element ratios have been used to determine the geotectonic environment of the Basal Amphibolite. Geochemical data from Frisch and Raab (1987) were included for comparison.

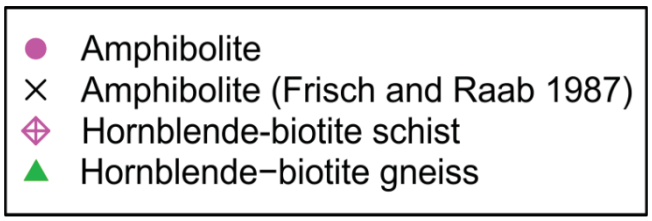

Figure 72: Legend for following figures.

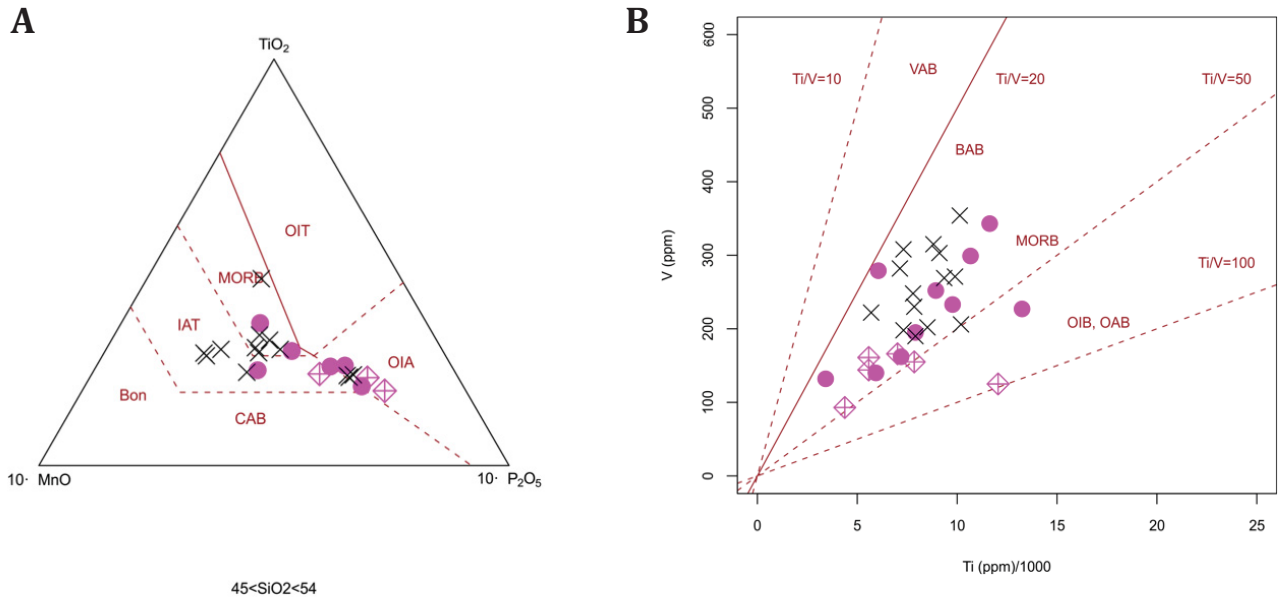

Figure 73: Classification diagrams for mafic volcanic rocks. **A** Plot from Mullen (1983). **B** Plot form Shervais (1982). Amphibolites from the Basal Amphibolite of this study and data from Frisch and Raab (1987). Legend in **Figure 72**.

The classification diagram of Mullen (1983) (Figure 73A) shows a considerable scattering of the data. The samples plot in the IAT (island-arc tholeiite) and MORB fields as well as at the border to OIA (oceanic-island alkali basalt). Therefore, a distinct statement regarding the geotectonic setting is not possible with this diagram. The discrimination diagram from Shervais (1982) (Figure 73B) shows that all data plot between Ti/V = 20 and Ti/V = 50 isolines in the BAB (back-arc basin basalt) MORB segment. Thus, this plot indicates a mixed chemical signature between MORB and back-arc basalts.

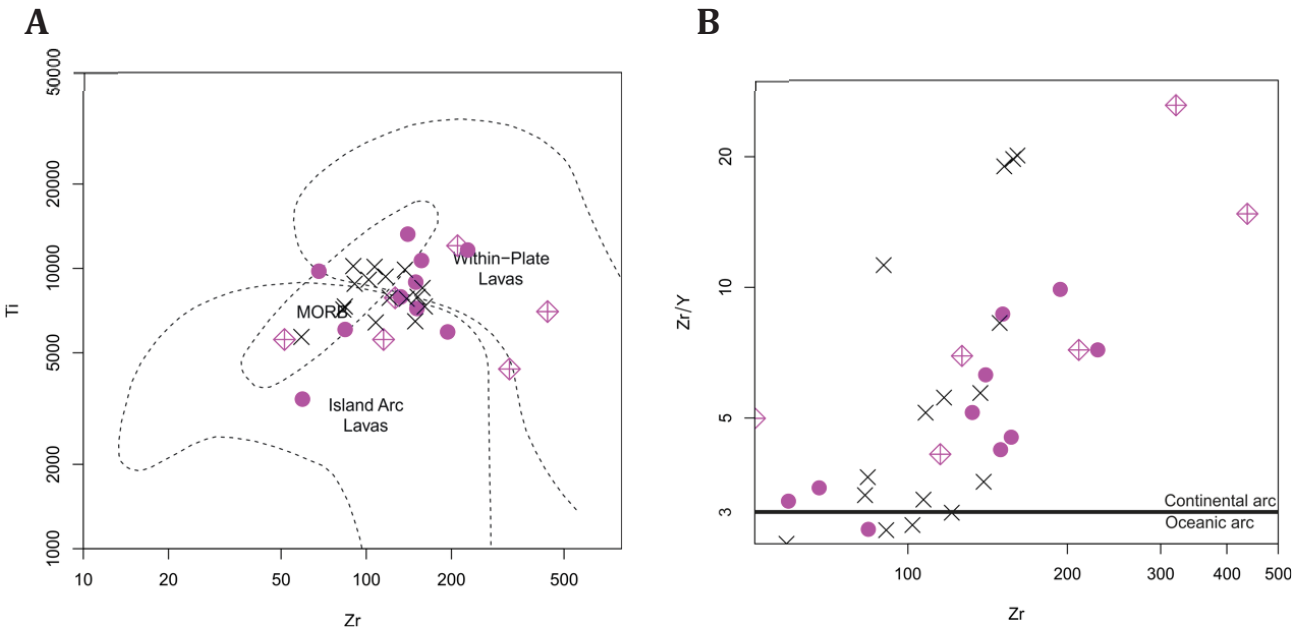

Figure 74: Classification diagrams from Pearce (1982) (**A**) and Pearce (1983) (**B**). The discrimination line between continental and oceanic arcs is defined by a Zr/Y value of 3. Values between 2.5 and 3.5 are the overlap between both arc types. Legend in **Figure 72**.

The Zr vs. Ti diagram (Figure 74A,B; Pearce 1982) shows a wide scatter of the data and may hint to a mixed MORB and arc signature. The Zr-Zr/Y diagram (Figure 74B; Pearce 1983) further discriminates continental and oceanic arc settings. The high Zr/Y indicates the involvement of an active continental margin in the formation of these rocks. Nevertheless, many points plot at low Zr/Y ratios next to the discrimination line resulting in an inconclusive result.

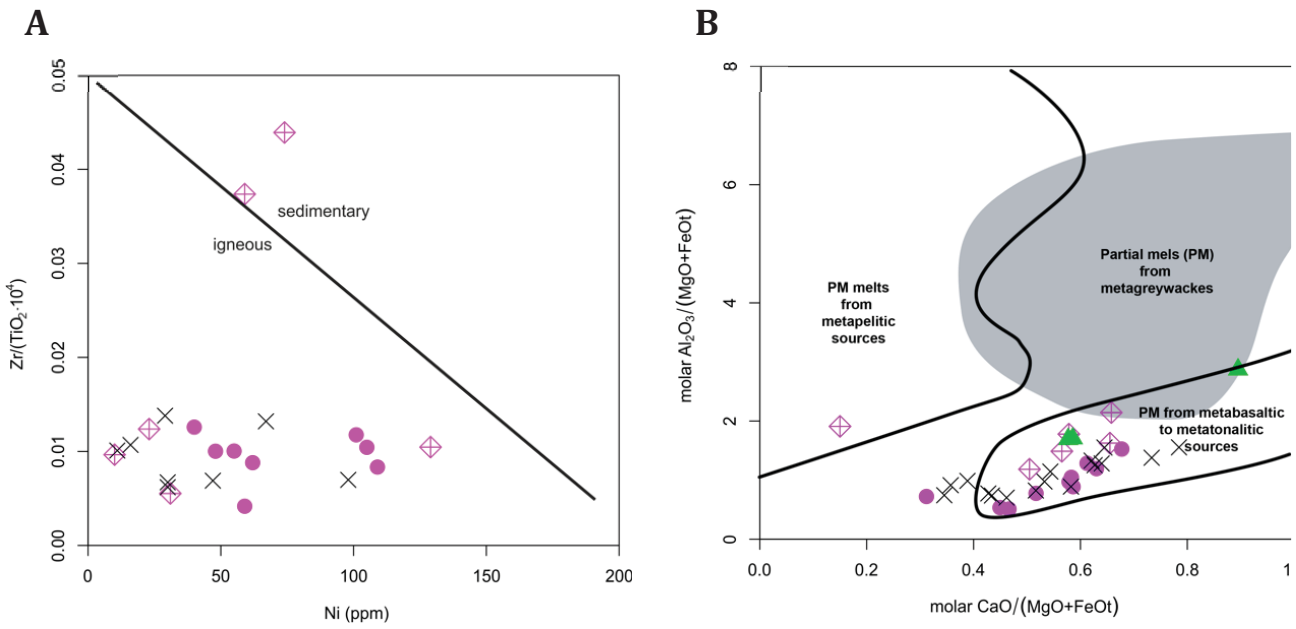

Figure 75: A Discrimination diagram for ortho- and paraamphibolites from Winchester et al. (1980) and Winchester and Max (1982) **B** Plot from Altherr et al. (2000, and references therein) for the origin of partial melts. Legend in **Figure 72**.

The Ni-Zr(TiO_2*10^4) plot (Figure 75A) from Winchester et al. (1980) and Winchester and Max (1982) descriminates between para- and orthoamphibolites. This plot clearly proofs the igneous origin of the amphibolites. However, two samples of hornblende-biotite schist plot in the field for sedimentary origin. This could indicate contribution of sediments to the Basal Amphibolite.

Figure 75B shows a plot of molar $CaO/(MgO+FeO_t)$ vs. $Al_2O_3/(MgO+FeO_t)$ (Altherr et al. 2000). It characterises different types of partial melts derived from various crustal source rocks. Available data for the Basal Amphibolite plots clearly in the field of metabasaltic to metatonaltic source rocks indicated by low $Al_2O_3/(MgO+FeO_t)$ but high $CaO/(MgO+FeO_t)$ ratio. Also, the hornblende-biotite gneiss samples plot clearly in the field of metabasaltic protoliths indicating that all these rocks derived from the same source and partial melting processes.

All presented geotectonic discrimination diagrams result in a mixed arc- and MORB signature of metabasites of the Basal Amphibolite. Only the Ti-V plot from Shervais (1982) results in a clear assignment to BAB (back-arc basalts). BAB typically show a chemical composition transitional between ocean ridge tholeiites and arc basalts, even calc-alkaline island arc basalts are possible (Saunders and Tarney 1984). The major and trace element data argue for a derivation of the metabasites from tholeiitic basalts to basaltic andesites with a trend to calc-alkaline composition which is consistent with a back-arc setting.

Commonly BAB are enriched in LILE compared to MORB and relative to HFSE (Pearce 1982, 1983; Saunders and Tarney 1984; Pearce and Stern 2006). Hydrous fluids squeezed out from the subducting oceanic lithosphere enriching the mantle in LILE that increases LILE content in partial melts derived from the mantle (Pearce 1982; Saunders and Tarney 1984; Donnelly et al. 2004). Depleted HFSE relative to LILE are generally explained by high melting rates above subduction zones (Vavra and Frisch 1989).

The amphibolite (Figure 70) shows a very similar distribution of trace elements like BAB. LILE, except Ba, are more enriched compared to only slightly enriched HFSE (=slight relative enrichment of LILE to HFSE). Hornblende-biotite schist (Figure 71) fits better to the typical chemistry of BAB because of the generally elevated Th and overall enriched alkalis compared to the common amphibolites. Large scattering of Th up to 100 times MORB can also be explained by crustal contamination.

Commonly Nb and Ta are depleted compared to MORB in an arc and back-arc setting. Data from Saunders and Tarney (1984) and Pearce and Stern (2006) show that not all BAB necessarily show reduced Nb concentration (e.g. Mariana Trough, Parece Vela Basin, East Scotia Sea; Figure 76A). Hence, Pearce and Stern (2006) discriminate between depleted BAB and enriched BAB based on multi-element spider plots and the Nb/Yb ratio (Figure 76A). Nb and Yb have the same partition coefficient during mantle melting and therefore can be used as proxy to quantify the subduction influence (Pearce and Stern 2006). Enriched BAB have a N-MORB normalized Nb/Yb ratio of >1 (Figure 77A) (Pearce and Stern 2006). Normalized Nb/Yb ratios of amphibolites from the Basal Amphibolite result in a large spread with values from 1.55-28.97 with a median of 4.44 (Figure 76B) and can be therefore assigned to the enriched BAB category.

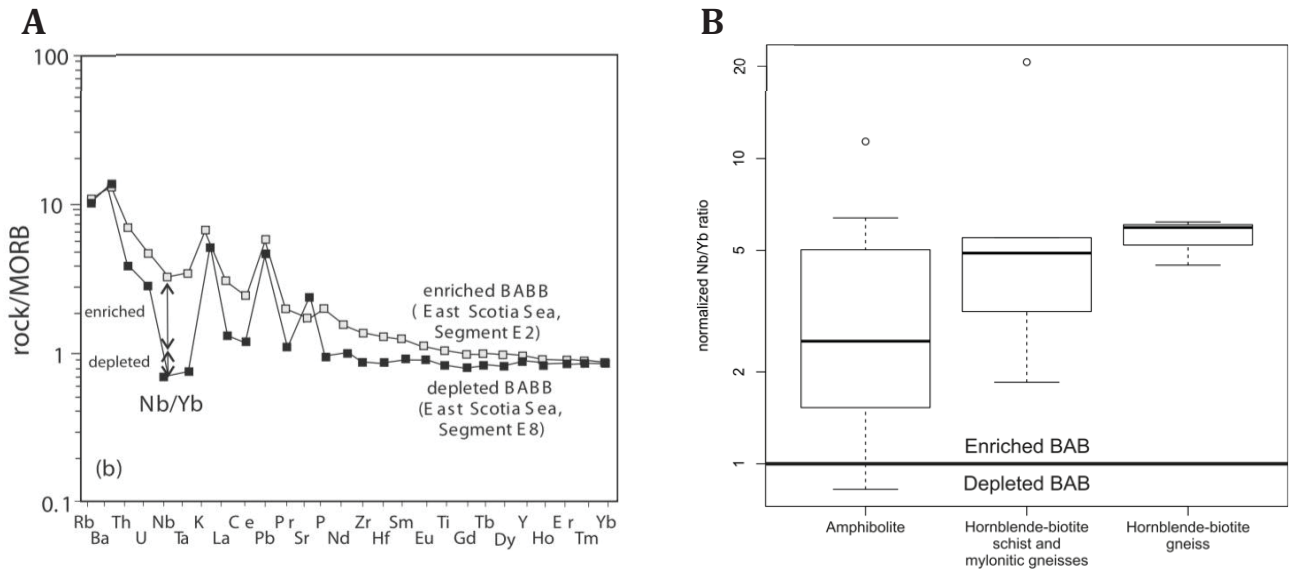

Figure 76: A Multi element spider plot from Pearce and Stern (2006) to discriminate between enriched BAB and depleted BAB. Differences in Nb/Yb ratios are characteristic. **B** Boxplot of all MORB-normalized Nb/Yb ratios of rock-types from the Basal Amphibolite. Values are >1 (median 2.5).

The enriched BAB chemistry could be explained by the long-lasting enrichment of the mantle during subduction at the Gondwana margins (see Chapter 10.1.3). The presence of an enriched mantle is indicated in plots proposed by Pearce and Stern (2006) and Pearce (1983) (Figure 77A,B). In the model of Pearce and Stern (2006), Ba is mobile in aqueous fluids released from the subducting slab whereas Nb and Yb create a fractionation-independent ratio. Samples with very high Ba/Yb ratios are interpreted to represent higher fractionated melts. A similar model with different element ratios is shown in Figure 77B. This plot indicates a (partly?) enriched mantle source and influence of an active continental margin setting. The data points tend to scatter more in this plot because of the large variability of Th (contamination by crustal material?).

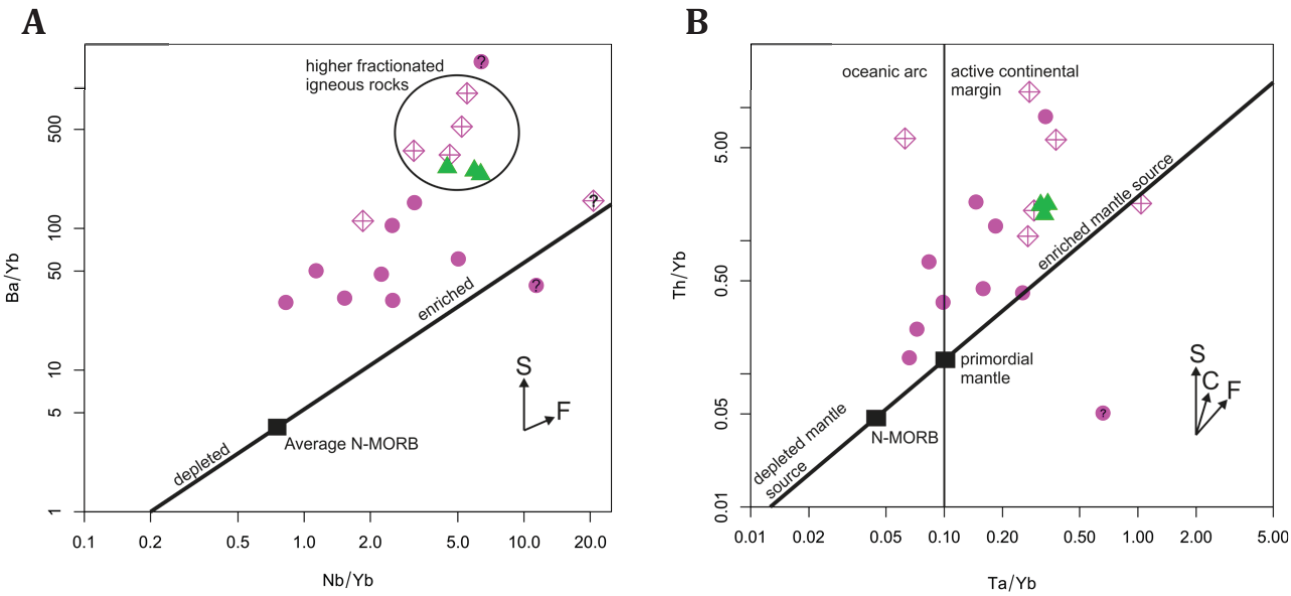

Figure 77: A Nb/Yb vs. Ba/Yb plot from Pearson and Stern (2006) to quantify the subduction input to the mantle. Samples marked with a question mark "questionable". S (subduction trend), F (fractionation trend). Circle highlights higher fractionated rocks in the Basal Amphibolite. **B** Plot from Pearce (1983) for basalt composition from ocean arc or active continental margin. S, F, C as in A. Legend in **Figure 72**.

The proposed back-arc setting developed behind an active continental arc is further supported by the Ti/Zr values (Woodhead et al. 1993). This study presents data from several arc-basalts and BAB revealing differences in Ti/Zr, V/Ti and Sc/Y. IAB are much more depleted in HFSE because of the higher degree of partial melting and therefore they tend to have higher Ti/Zr (100-350) compared to BAB (50-150) (Woodhead et al. 1993). The Ti/Zr ratio of rocks from the Basal Amphibolite range from 50-100 (median 60) which is typical for a back-arc setting. Fine-grained amphibolites and hornblendites from the Lower Magmatic Series (LMS) of the Habach Complex yield much higher values of 68-1438 (median 310) consistent with the interpretation of their formation in an arc setting (Figure 78).

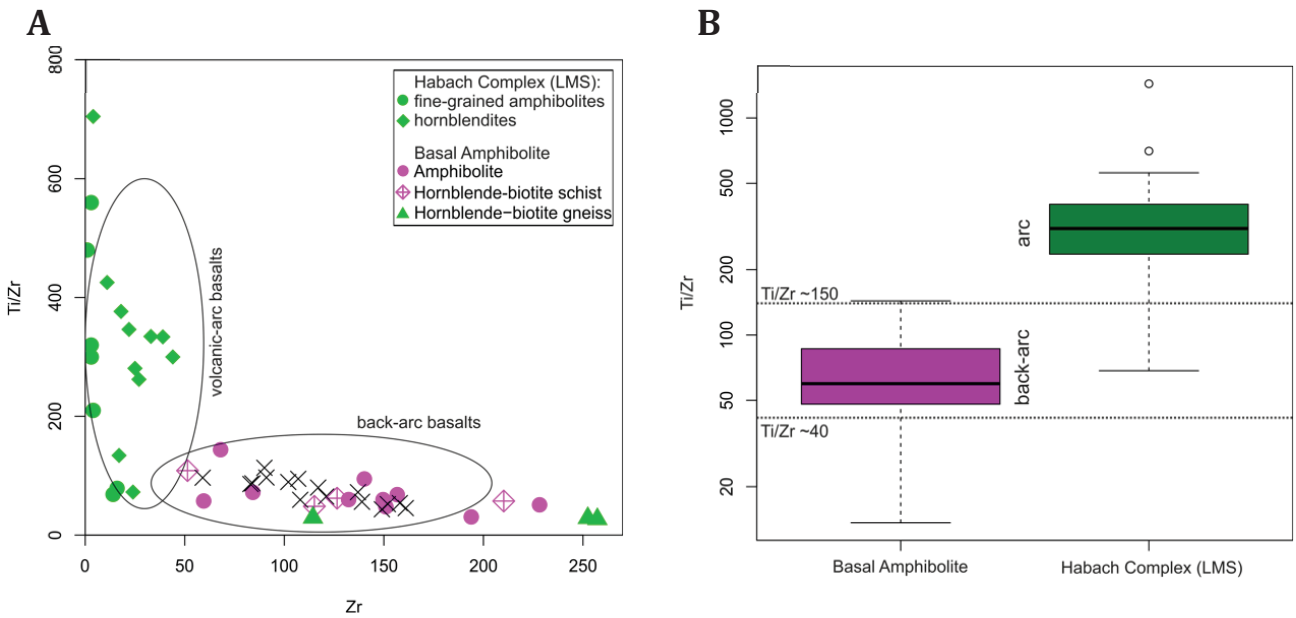

Figure 78: A Zr vs Ti/Zr plot according to Woodhead et al. (1993). Data from the Basal Amphibolite (Frisch and Raab 1987 and this study) and the LMS of the Habach Complex (Höll and Eichhorn 2000). **B** Boxplot of Ti/Zr values of the Basal Amphibolite (n=35) and the Habach Complex (LMS) (n=20). Back-arcs yield Ti/Zr values of 40-150 (Woodhead et al. 1993). Values above 150 are characteristic for an arc system.

The geochemistry indicates partial melting of enriched mantle material likely at an oceanic or active continental margin for the formation of the Basal Amphibolite. Enriched tholeiitic melts (amphibolites) formed in the back-arc setting and evolved towards slightly calc-alkaline magmas (hornblende-biotite schist and gneiss). We can only speculate about the volcanic vs. plutonic origin of the igneous protoliths. From field observations it is assumed that in addition to volcanic basaltic protoliths there were gabbroic protoliths involved. Coarse-grained mafic/ultramafic amphibolites, which occur as deformed layers/lenses/boudins could represent such metagabbros intruded as mafic dykes. Alternatively, they could represent mafic cumulates. The hornblende-biotite gneiss, which clearly preserves intrusive relationships with the host rocks derived from higher fractionated magmas of dioritic composition (meta-diorite), which intruded as stocks.

8.1.4. Messeling gneiss

Major and trace elements

The results of the major element analysis of the orthogneiss exposed at Messelingkogel ("Messeling gneiss") are summarised in Table 21. The data is also shown in the Harker diagrams (Figure 66, Figure 67).

The average SiO_2 content of the Messeling gneiss is around 74 mass% with a high Al_2O_3 content of about 14 mass%. Generally, the major elements show little variation. The CaO content is low with around 0.63 mass% with a Na_2O+K_2O content of around 8 mass%. The P_2O_5 content scatters minor around 0.2 mass%. The trace elements show a non-uniform behaviour (Figure 67). Barium, niobium and strontium show very little variation whereas uranium, thorium, rubidium and REE show a large one.

Al_2O_3, Fe_2O_3 and MgO show a negative correlation with SiO_2. Only Na_2O shows an excellent positive correlation with SiO_2.

Table 21: Major elements of the orthogneiss occurring at Messelingkogel.

	Messeling gneiss (n=5)		
Component	**Median**	**Min**	**Max**
SiO_2	73.5	72.88	75.83
Al_2O_3	14.28	13.13	14.76
Fe_2O_3(tot)	1.54	1.21	1.7
MgO	0.43	0.33	0.56
CaO	0.63	0.48	0.99
Na_2O	3.26	3.04	3.58
K_2O	4.8	4.17	4.98
TiO_2	0.21	0.16	0.24
P_2O_5	0.2	0.17	0.22
MnO	0.03	0.005	0.03
Cr_2O_3	0.011	0.007	0.012
LOI	0.6	0.6	1.1
Sum	99.96		

Figure 79A, B shows spider diagrams normalized to upper continental crust (Taylor and McLennan 1995) and REE plots normalized to chondrite, respectively. The Messeling gneiss is strongly depleted in strontium as well as some HFS elements (Zr, Hf, Ti, La, Ce; except U and Th) (Figure 79A). On the contrary LIL elements like Cs, Rb, K are enriched, whereas Ba is depleted. All samples show a quite uniform behaviour (especially for Sr, Nd, P, Rb and K) with minor outliers for Ba.

The REE patterns show a general declining trend (Figure 79B). The negative Europium anomaly is pronounced (Eu/Eu* = 0.33-0.48, median 0.45). HREE elements are enriched about 10 times compared to chondrite whereas LREE elements are enriched up to 90 times. The $(La/Yb)_{cn}$ ratio is between 5.7-9.7 with a median of 9.1.

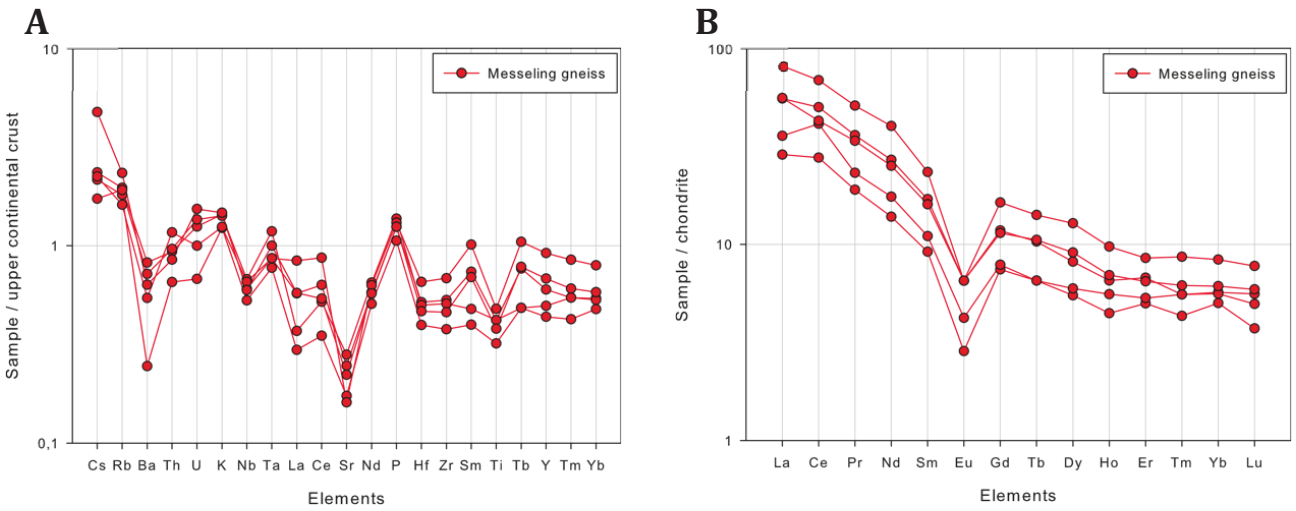

Figure 79: A Spider diagram of trace elements compared to average upper continental crust of Messeling gneiss. **B** Spider diagram REE pattern of Messeling gneiss compared to chondrite.

Many trace elements correlate positively with major elements like Al_2O_3, Fe_2O_3 and MgO and negatively with SiO_2. Barium as well as Sr show perfect negative correlation with increasing SiO_2 content. Copper on the other hand correlates positively with SiO_2 indicating that Cu got enriched during the deformation event.

Classification of Messeling gneiss

Samples from Messeling gneiss have been classified using a non-genetic, non-tectonic approach (Frost et al. 2001). Data from Kozlik (2016) and Kozlik and Raith (2017) are included for direct comparison of the Messeling gneiss with the adjacent Granatspitz gneiss and Felbertauern augengneiss.

Frost et al. (2001) discriminate granitic rocks based on three parameters. First, the ratio of $FeO_t/(FeO_t+MgO)$ discriminates between "ferroan" and "magnesian" granitic rocks. This ratio reflects different differentiation histories. The second parameter is based on the MALI (modified alkali-lime index) and indicates the plutonic composition inherited from the source rock. The third parameter is the alumina saturation index (ASI). The ASI subdivides granitic rocks in metaluminous, peraluminous and peralkaline using the molar ratio of $Al_2O_3/(CaO-1.67\cdot P_2O_5+Na_2O+K_2O)$.

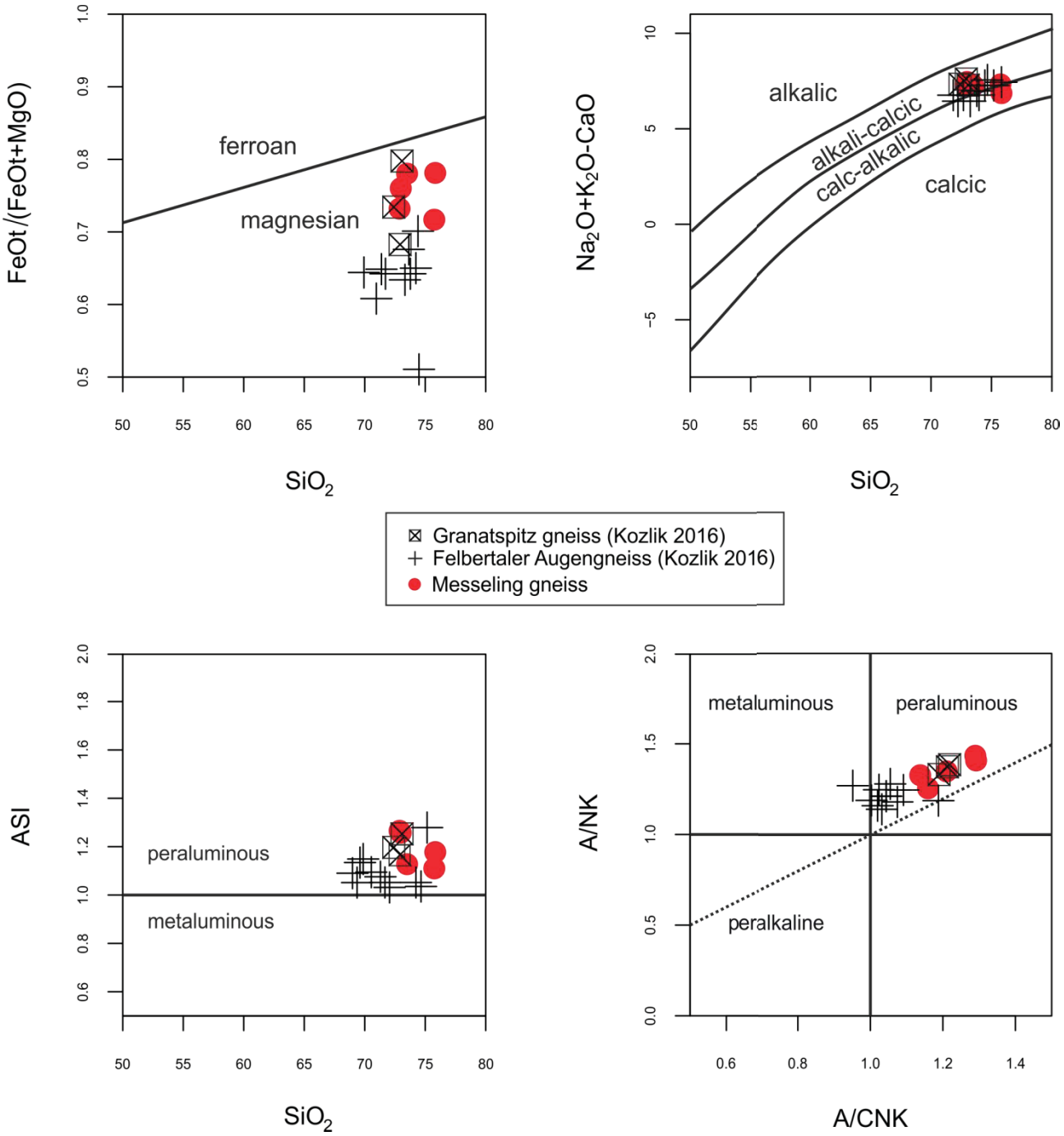

Figure 80: Geochemical classification scheme for granitic rocks from Frost et al. (2001) and Shand (1943). Data from Kozlik and Raith (2017) is included. The legend corresponds to **Figure 64**.

The approach of Frost et al. (2001) classifies the Granatspitz gneiss and Messeling gneiss into the same categories (Figure 80). Both gneisses are magnesian, alkali-calcic (one sample plots in the calcic field) and strongly peraluminous (ASI > 1.1). In constrast the Felbertauern augengneiss is weakly peraluminous to slightly metaluminous, shows lower Fe* ratios (magnesian) and is alkali-calcic/calc-alkalic. Kozlik (2016) and Kozlik and Raith (2017) give a more detailed chemical characterisation of Central Gneisses including the Felbertauern augengneiss and the Granatspitz gneiss.

8.1.5. Calc-silicate rocks from Messelingscharte and Felbertal tungsten mine

Overall 6 calc-silicate rocks from Messelingscharte and two from Felbertal tungsten mine were chemically analysed.

Major elements

The major elements of the calc-silicate rocks from Messelingscharte and Felbertal tungsten mine are listed in Table 22. The corresponding Harker diagrams are shown in Figure 66 and Figure 67.

The average SiO_2 content of the rocks from Messelingscharte is about 49 mass% with an average Al_2O_3 content of 19 mass%. The high CaO content of 15 mass% mirrors the Ca-rich nature of calc-silicate rocks. Na_2O shows a large scatter between 0.3-3.8 mass% whereas K_2O scatters slightly around 0.5 mass%. The Fe_2O_3 content ranges from 4.5-8.6 mass%.

Alkalis show good positive correlation to SiO_2 whereas FeO, MgO and CaO tend to decrease with higher SiO_2 content. Detailed correlations are plotted in Figure 82.

The average SiO_2 content of the two calc-silicate rocks from Felbertal is with 46% slightly lower compared to rocks from Messelingscharte. The Al_2O_3 content of the two samples varies considerably (17.8-22.2 mass%). The CaO, Na_2O, K_2O and Fe_2O_3 contents are very similar to calc-silicate rocks from Messelingscharte whereas TiO_2 is enriched (0.27 compared to 0.69 mass%).

Table 22: Main components of the clinozoisite-plagioclase-calc-silicate fels from Messelingscharte and calc-silicate rocks from Felbertal tungsten mine. WO_3 is considered as major element.

	Clinozoisite-plagiolase-calc-silicate fels (n=6)			Calc-silicate rock from Felbertal mine (n=2)
Component	**Median**	**Min**	**Max**	**Median**
SiO_2	49.19	40.32	55.77	46.14
Al_2O_3	19.18	17.47	20.90	19.97
Fe_2O_3(tot)	7.00	4.46	8.56	8.73
MgO	1.05	0.25	2.65	2.93
CaO	15.26	9.06	18.58	16.87
Na_2O	1.38	0.34	3.76	1.38
K_2O	0.58	0.18	1.03	0.56
TiO_2	0.27	0.04	0.56	0.69
P_2O_5	0.27	0.10	0.75	0.19
MnO	0.10	0.07	0.17	0.16
Cr_2O_3	0.017	0.012	0.022	0.032
WO_3	3.24	585 ppm	6.14	0.2
LOI	2.10	1.30	2.50	1.95
Sum	99.53			99.78

Trace elements

Figure 81 shows spider plots of trace elements normalized to MORB and REEs normalized to chondrite. The Harker diagrams of the trace elements (Figure 67) show intense scattering. Barium shows a positive linear correlation with SiO_2. Strontium is strongly enriched with mostly more than 1000 ppm.

Figure 81A shows that LIL elements (Cs, Rb, K, Sr), P_2O_5 and Eu of calc-silicate rocks from Messelingscharte are (strongly) enriched compared to MORB. HFS elements (Ti, Ta, Nb, Hf, Zr) and Ni are generally depleted. Thorium shows a positive peak for two samples. Many less mobile elements (La, Ce, B, Tb, Y, Yb, Cr) show a similar concentration to MORB. The higher Sr content can be explained with substitution of Sr for Ca in plagioclase, calcite and epidote (Frei et al. 2004). In comparison, calc-

silicate rocks from Felbertal tungsten mine are enriched in LILE (Cs, Rb, Sr). All other elements are slightly depleted (between 0.7-0.9) compared to MORB. Only Ni is in one sample more depleted than the average.

The REE patterns of calc-silicate rocks from Messelingscharte (Figure 81B) show a large spread of the absolute REE concentrations but consistent and similar trends. The LREE from La to Sm decrease, Eu shows a strong positive anomaly (Eu/Eu* = 1.7-4.7; median = 2.0) and the HREE from Gd to Lu show an increase. The $(La/Yb)_{cn}$ ratio scatters strongly between 0.2-2.5 with a median of 0.8. Strontium correlates well with Eu (R^2=0.77) indicating that Eu^{2+} is the dominating Eu species and that it its substituting together with Sr^{2+}in Ca^{2+} in plagioclase, clinozoisite and calcite. Samples from Felbertal tungsten mine are depleted in LRRE show a flat pattern, parallel to MORB, between Gd and Lu. Lanthanum and Ce show the lowest rations compared to all other REE. The Europium anomaly is positive in one sample with Eu/Eu* values around 1.7. The $(La/Yb)_{cn}$ mirrors the enrichment of HREE compared to LREE with values around 0.5.

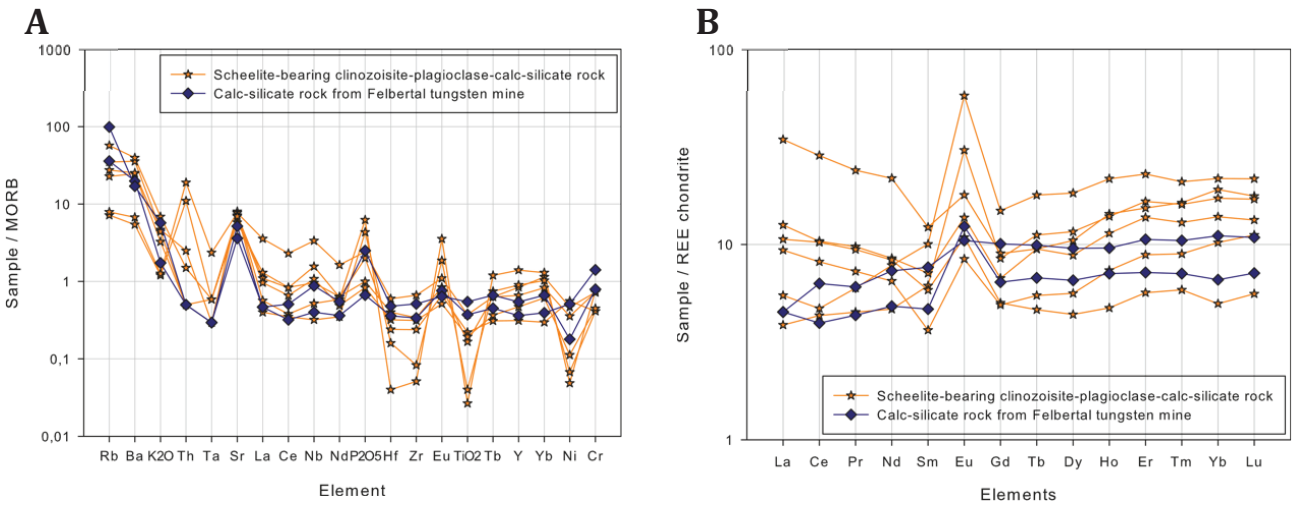

Figure 81: Spider plots of calc-silicate rocks from Messelingscharte and Felbertal tungsten mine. **A** Trace element pattern normalized to MORB. **B** REE pattern normalized to chondrite.

Figure 82 shows plots of several major and trace elements against tungsten including regression lines and correlation coefficients. Rocks from Felbertal tungsten mine are additionally plotted for comparison. The SiO_2, Al_2O_3 and K_2O contents correlate negatively with the W content of the rock. All three elements correlate negatively with R^2>0.7 indicating that scheelite was introduced at cost of major rock forming minerals. Potassium shows perfect negative linear correlation with W-content with R^2=0.94. The CaO content displays a positive correlation trend with W (including one outlier: R^2=0.33, without outlier: R^2=0.87).

Furthermore, the trace elements Rb, Ba and Sc also correlate well with tungsten. Rubidium and Ba show a negative linear correlation with R^2=0.86 and R^2=0.81 respectively. Scandium shows a clear positive correlation with W (R^2=0.96). The REE including Y correlate positively with W (R^2=0.62); so does Mo (R^2=0.76).

Samples from Felbertal mine are not directly comparable with calc-silicate rocks from Messelingscharte. Normally, the concentration of both sample show a large difference. Only K_2O, Al_2O_3, CaO, Ba and Sc concentrations are in the range of those from Messelingscharte. Rubidium is generally

higher in Felbertal mine samples (Messelingscharte ~25 ppm, Felbertal tungsten mine ~68 ppm). Additionally, K-Rb, U-Th, Nb-Ta and Cu-Co show strong correlation with R^2>0.9.

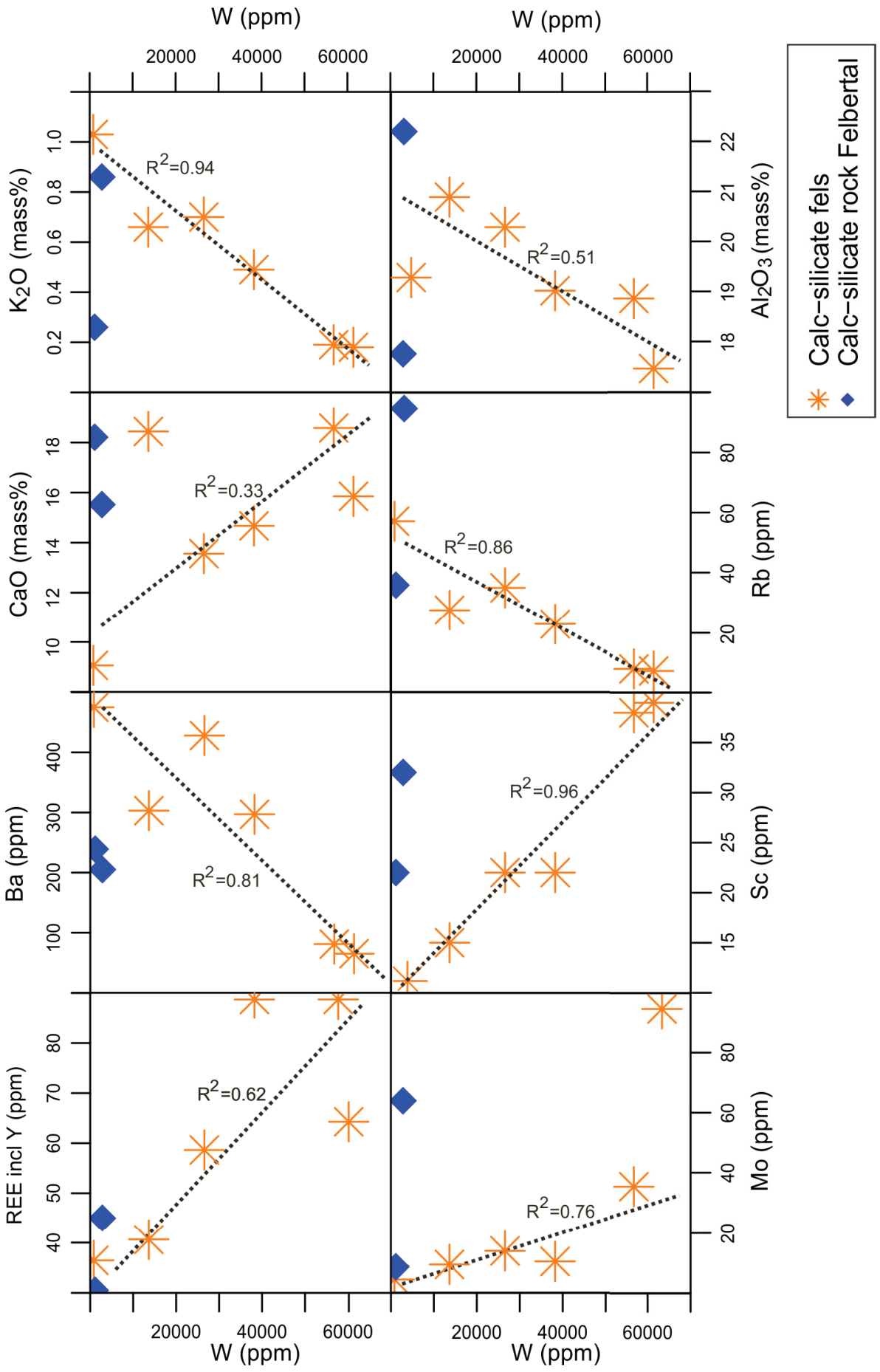

Figure 82: Selected main component and trace element concentration plotted against tungsten. Regression lines calculated for rocks from Messelingscharte only. The samples from Felbertal tungsten mine for comparison.

Figure 83 shows a plot of 56 elements of the calc-silicate rocks from Messelingscharte normalized to the average values of the amphibolite host rocks. Interestingly, several elements (W, Sn, Be, Mo, Cu, Pb, U) are enriched compared to the host rock. Tungsten, tin and beryllium show the highest enrichments.

Tin occurs in concentrations between 259-1580 ppm (median 477 ppm). Beryllium shows concentrations between 7-41 ppm (median 24 ppm) compared to background concentrations around 1 ppm in the amphibolite. The crustal average after Tayler and McLennan (1995) is 3 ppm. Noble and base metals (Au, Ag, Cu, Pb) are also enriched in the calc-silicate rocks together with sulphur indicating that they are hosted by sulphides. Rusty brown staining on some outcrops and observation of incompletely weathered pyrite confirm the presence of sulphides (see Chapter 6.6.1).

The LIL elements Ba, Rb, Sr, Cs show a very uniform enrichment between 3-5 times (with larger uncertainties). Carbon is enriched because of calcite in the calc-silicate rocks.

Zirconium, Hf, Ti, Mg and LREE are the most prominent depleted elements. The sum of all REEY is only slightly depleted. Especially Zr and Hf are believed to be very immobile but a depletion factor of 10 is evident. Magnesium is the most depleted element; Ti the third most depleted element (average amphibolite 1.41 mass% TiO_2 as rutile, calc-silicate fels 0.27 mass% TiO_2 as titanite).

Several main components like SiO_2, K_2O, Al_2O_3 and P_2O_5 occur in very similar concentrations in calc-silicate rocks and amphibolites. CaO is enriched twice but still only to minor extend compared to before-mentioned trace elements (W, Sn, Be).

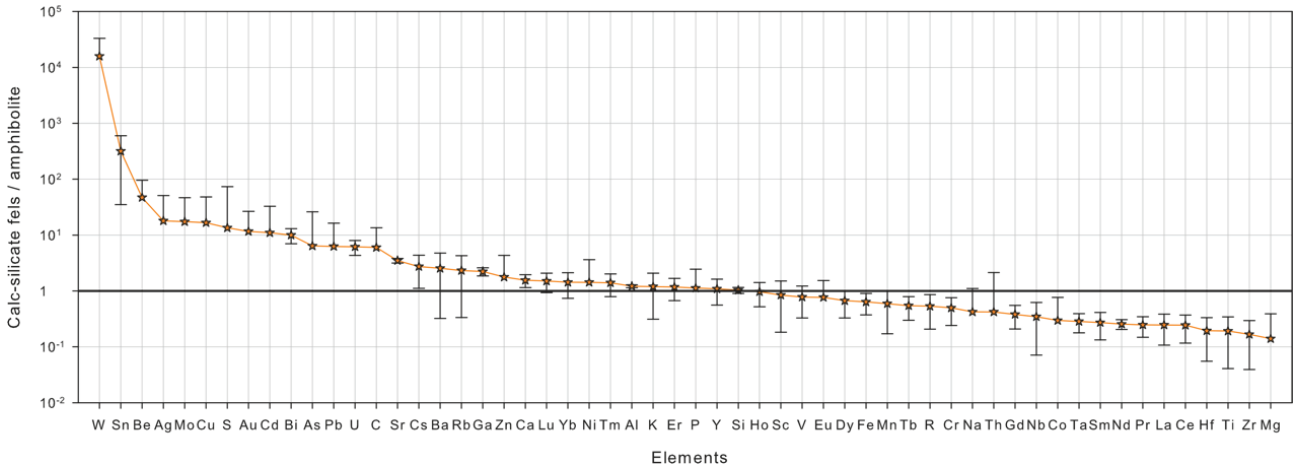

Figure 83: Median values of W-mineralised calc-silicate rocks from Messelingscharte normalized to median value (n=10) amphibolite host rocks. Data is sorted from high to low values. R abbreviation for REE+Y. Error bars calculated using statistically robust IQR (interquartile range; IQR = $x_{0.75}$-$x_{0.25}$; x_y: quartile y of the sample x). Error is often very large because of intense scattering and a low sample number (n=6).

8.2. XRD analyses of scheelite-bearing calc-silicate rocks

Qualitative and quantitative XRD measurements of scheelite-bearing calc-silicate rocks from Messelingscharte as well as Felbertal tungsten mine were used to determine the overall modal mineralogical composition. For better comparison, the XRD measurements were made on rock powders also used for whole rock geochemistry. Table 23 lists the modal compositions of calc-silicate rocks from Messelingscharte as well as Felbertal tungsten mine. The mineralogical composition of each sample is listed in Table 24.

Table 23: Average modal composition (in mass%) calc-silicate rocks from Messelingscharte and Felbertal tungsten mine determined by XRD. The category of "other phyllosilicates" refers to the sum of clay minerals, phlogopite, muscovite and biotite.

Sample	Qz	Czo	Plg	Sch	Clc	Chl	other phyllosilicates	Act
Messelingscharte	21	50	15	6	2	5	1	0
Felbertal deposit	12	47	14	1	5	3	4	14

Table 24: Modal composition (in mass%) of individual calc-silicate rock samples from Messelingscharte. The accuracy is about 2-4% absolute. Sample 06-02 was dismissed because of weathering.

Sample	Qz	Czo	Plg	Sch	Clc	Chl	other phyllosilicates
03-17	22	37	11	8	2	10	1
04-12	16	31	46	5	0	1	1
04-17	8	51	8	8	1	12	2
04-22	13	25	55	3	1	2	1
06-03	27	54	9	2	2	3	1

Calc-silicate rocks from Messelingscharte are dominated by 50% clinozoisite (Figure 84A). Other main phases are quartz (21%), plagioclase (15%), scheelite (6%) and chlorite (5%). The plagioclase content can vary strongly between 8-55%.

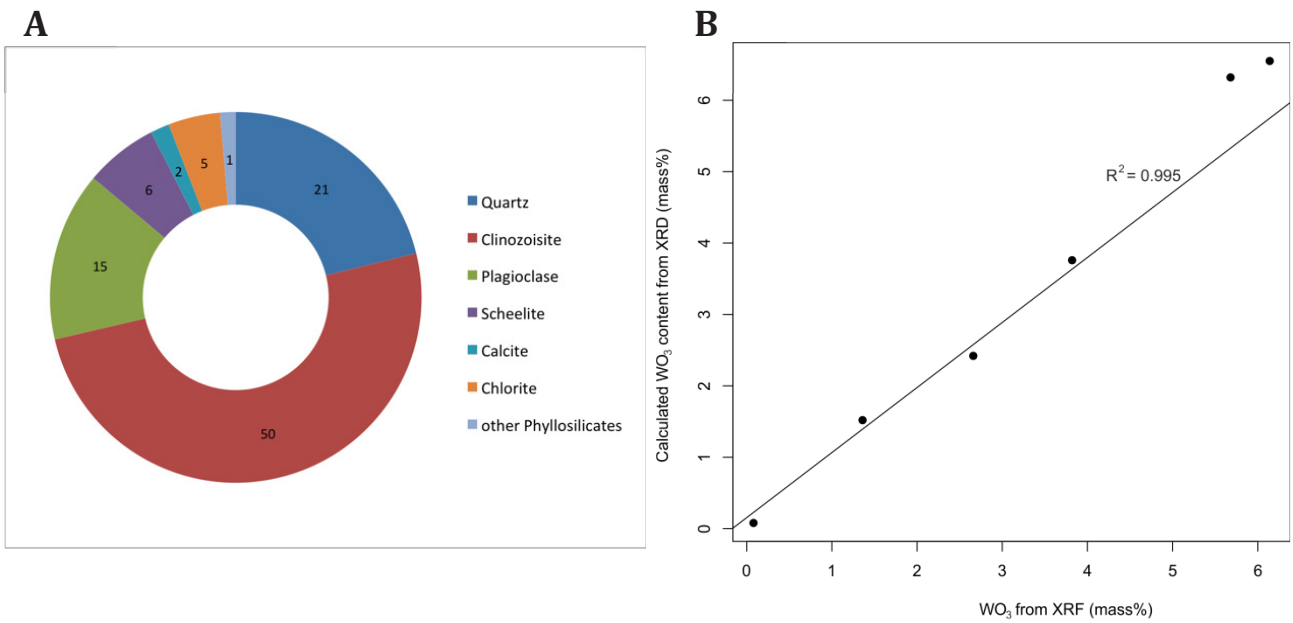

Figure 84: A Modal composition of scheelite-bearing calc-silicate rocks from Messelingscharte (n=5). Numbers in mass%. **B** Linear regression between WO_3 concentrations determined by XRF and WO_3 calculated from scheelite content of XRD measurements.

The WO_3 content measured by XRF and that calculated from XRD data show a very good correlation (Figure 84B). The median of the XRF analyses is 3.24 mass% WO_3 compared to a calculated value from XRD of 3.09%. The correlation coefficient is 0.995 (Figure 84B). Calculated WO_3 content for high scheelite concentrations tend to be overrated compared to XRF data.

The modal mineralogical composition of calc-silicate rocks from Felbertal tungsten mine (Figure 85) is similar to samples from Messelingscharte. The clinozoisite content is only slightly lower (47%). The quartz content is much lower (14%). Calcite builds about 5% of the rock. Scheelite (1%) and chlorite (3%) are accessory/minor components. Samples from Felbertal tungsten mine additionally contain 14% actinolite.

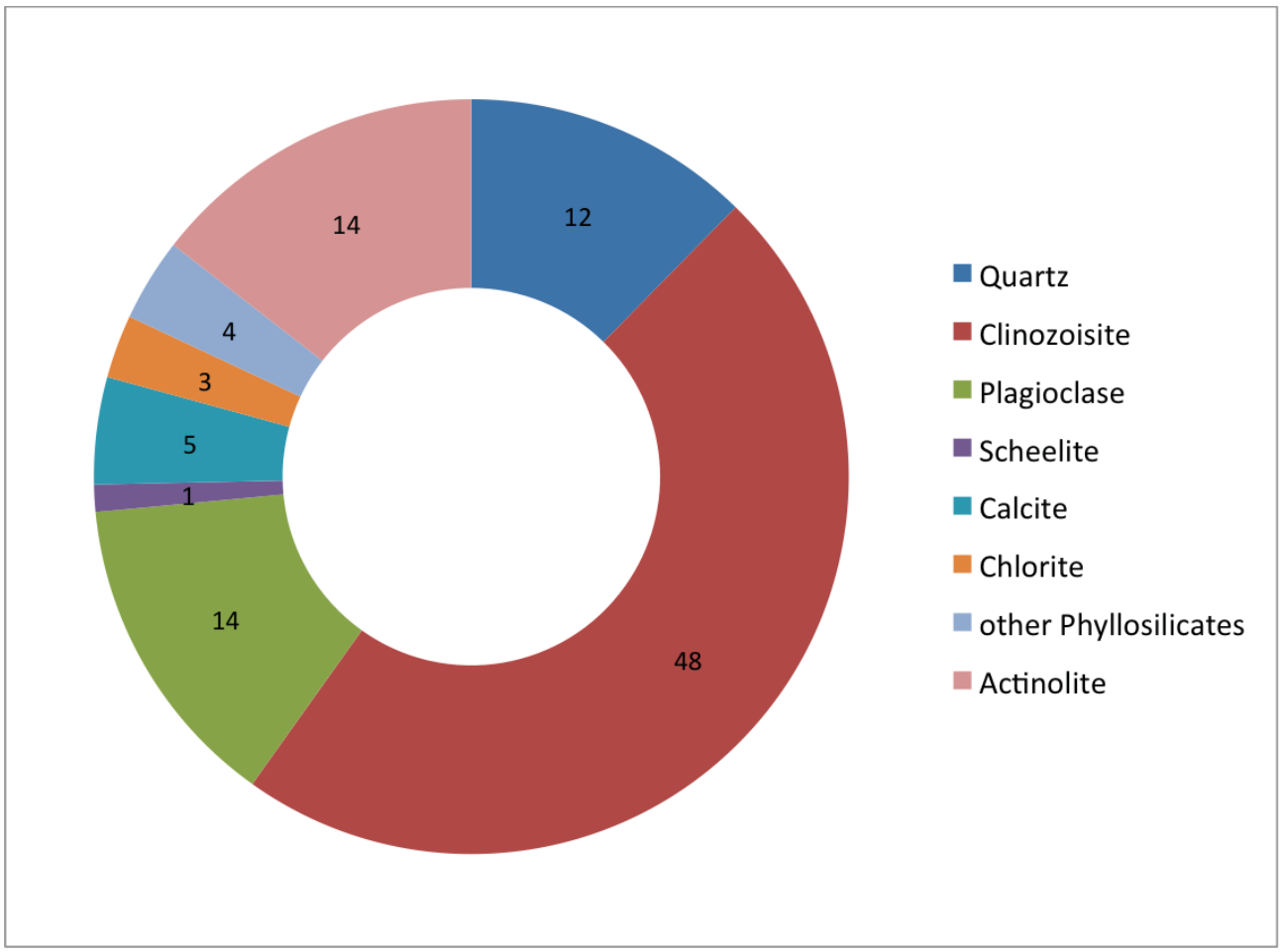

Figure 85: Representative mineralogical composition of calc-silicate rock samples from Felbertal tungsten mine. Numbers in mass%.

9. Mineral chemical analyses

9.1. Scheelite

Major and trace element concentrations of scheelite ($CaWO_4$) in the calc-silicate rocks from Messelingscharte were analysed by electro probe microanalyser (EPMA). Measured elements are Ca, W, Mo, Sr and Sn. Two samples (03-17', 05-03) were investigated. The analytical conditions are presented in Chapter 4.8.

Under UV light yellow and blue luminescent scheelite can be distinguished (see Chapter 6.6.1). Yellow scheelite normally forms the cores of scheelite crystals which are surrounded by blue rims of varying thickness (Figure 88). There are fine-grained as well as very coarse-grained zoned scheelite crystals. The core is commonly several times larger than the surrounding rim.

Molybdenum is the only element showing a systematic and characteristic variation. Strontium and tin are generally below detection limit. Figure 86A shows a Q-Q-plot of MoO_3 of all measurements and the corresponding box plots (Figure 86B) for each population. Statistically there are three different populations discriminated (Figure 86A). There is a lack of data between 0.6-0.8 mass% MoO_3 (Figure 86A; Figure 87) possibly indicating a compositional gap between generation 1 and 2. Therefore 0.75% mass MoO_3 will be used as threshold for discrimination between generation 1 and 2.

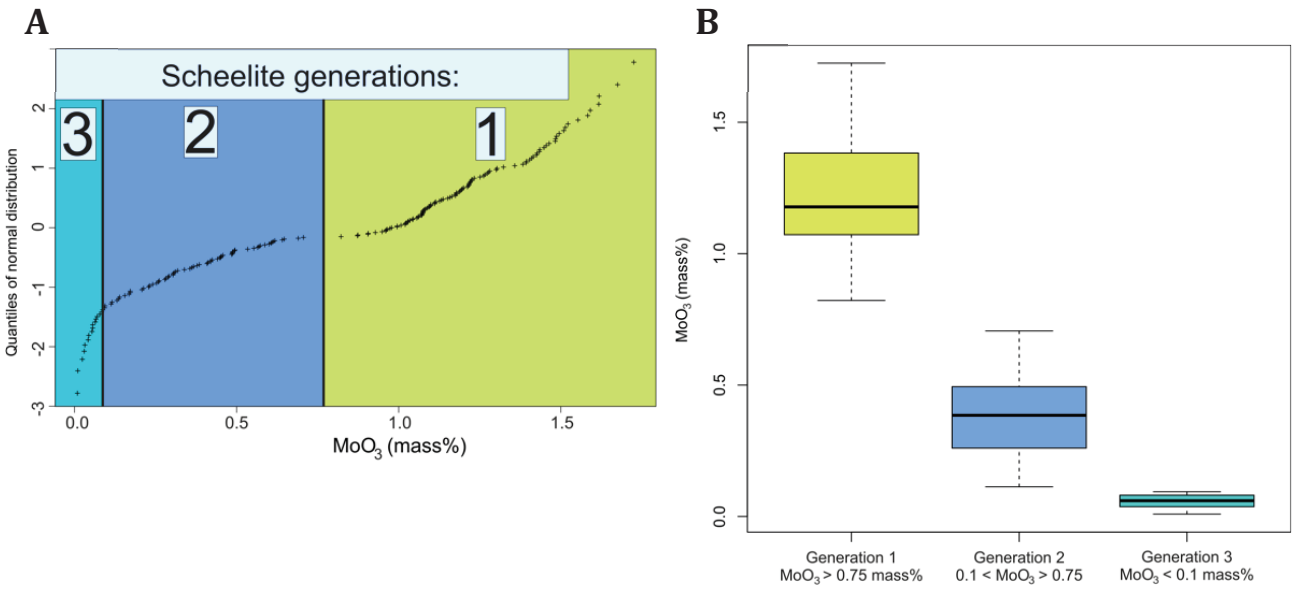

Figure 86: A Q-Q-plot of all scheelite measurements. A Q-Q-plot compares two probability distributions by plotting their quantiles against each other. Kinks in the distribution are typical for different populations. **B** Boxplot of the corresponding three populations.

Table 25: Summary MoO_3 concentrations of scheelite generations.

MoO_3 (mass%)	Generation 1	Generation 2	Generation 3
CL brightness	dark	bright	white
Spatial position in scheelite grains	core	rim	outer rim, cracks
Min	0.822	0.100	bdl
Max	1.73	0.706	0.100
Median	1.18	0.304	0.060
n	104	65	16

Scatter plots of CaO, WO_3 and MoO_3 support the presence of at least two different populations (Figure 87). The MoO_3 concentrations vary considerably defining two sharply defined clusters in the diagrams. Furthermore, Figure 87A proofs that Mo is substituting W in the crystal lattice (scheelite-powellite series) because there is a negative correlation between the two elements. The populations are also distinguishable in the CaO-MoO_3 binary plot (Figure 87B).

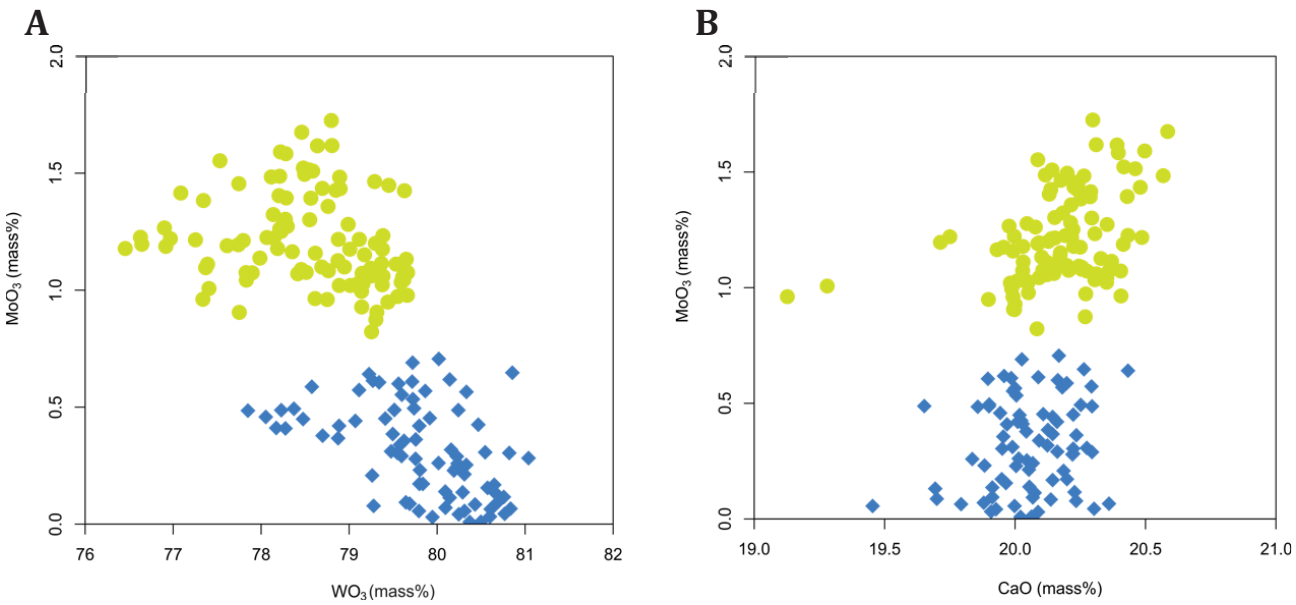

Figure 87: Scatter plots of WO_3 vs MoO_3 (**A**) and CaO vs MoO_3 (**B**) of all scheelite measurements. Yellow = generation 1 scheelite, blue = generation 2,3 scheelite as in **Figure 86**B.

The location of point measurements and line scans is shown on CL photomicrographs (Figure 88). The zonation of scheelite is clearly visible in CL images (contrast in brightness). Line scans across zones with transitions in brightness reveal that the Mo-content is directly related to the CL brightness. Darker colours are typical for Mo-rich scheelite (generation 1) that forms the core of zoned crystals. The Mo-poor scheelite rims (generation 2) are characterised by bright CL signal.

Table 26 lists the average values of MoO_3 concentrations shown in Figure 88.

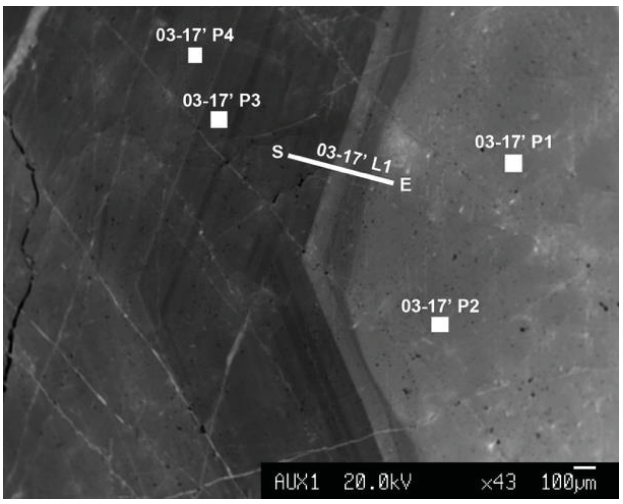

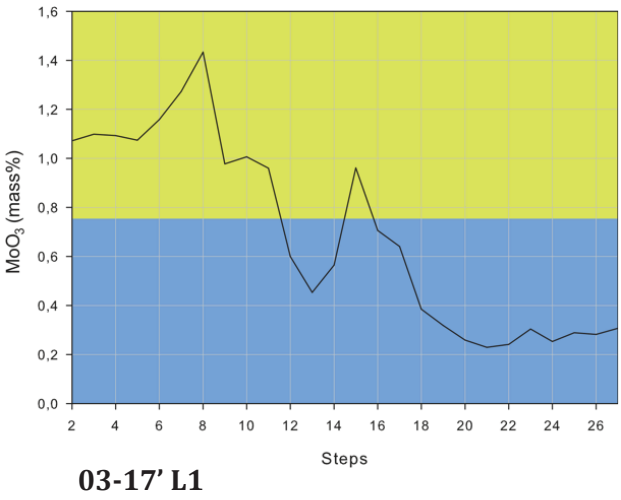

03-17' L1

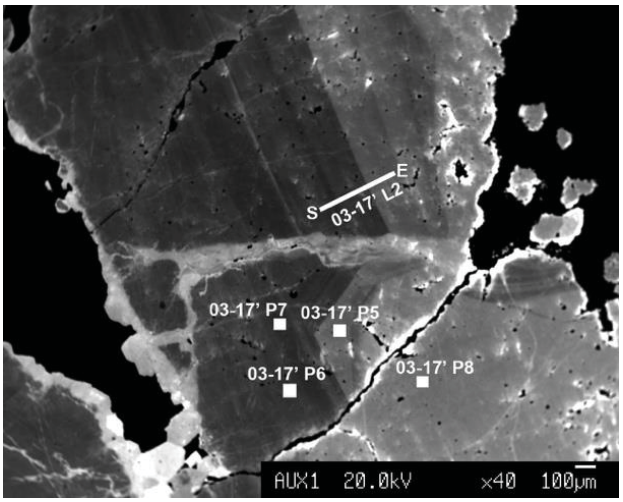

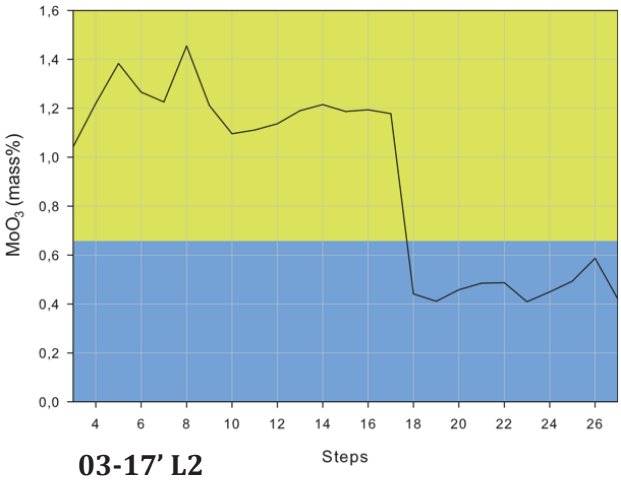

03-17' L2

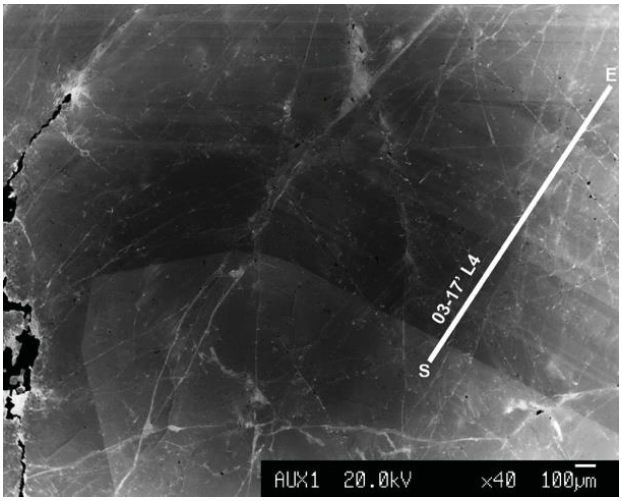

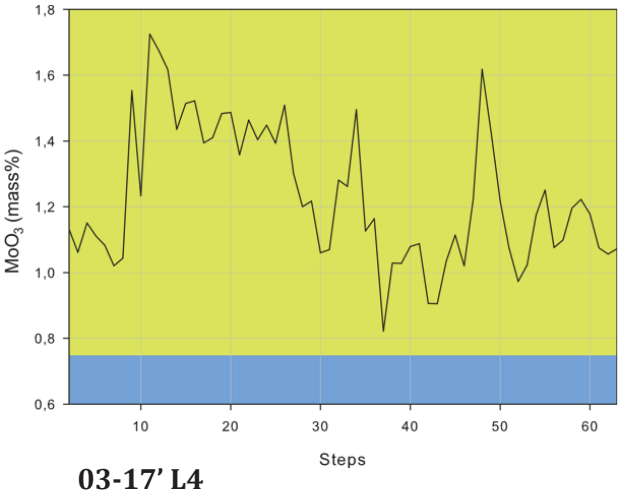

03-17' L4

Figure 88: CL photomicrographs of scheelite (sample 03-17'). Black areas are silicate minerals. Point measurements and position of line scans (S=start, E=end) on left side, results of the line scans on the right side. Start of the scan in on the left side of the line plot. Label of the line scan below the line plot. The background colour (yellow, blue) corresponds to the luminescence colour of two generations (**Figure 86**B).

Table 26: MoO_3 content of point measurements and line scans presented in **Figure 88**.

Sample	Average MoO_3 (mass%)	
	Dark CL (generation 1)	**Bright CL (generation 2)**
03-17' P1-4, L1	1.05	0.357
03-17' P2-8, L2	1.23	0.449
03-17' L4	1.11	-

Mo-rich scheelite crystals can also show a weak oscillatory zonation as demonstrated in line scan 03-17' L4 (Figure 88). The core of the scheelite grain (start of the line scan) has an average MoO_3 content of 1.10 mass% whereas the next rim shows the highest measured MoO_3 contents up to 1.73 mass%. The individual zones have variable thickness and are strongly variable in MoO_3 content but never are below the threshold of 0.75 mass% MoO_3.

Mo-poor scheelite (generation 2) shows an irregular internal structure and strongly varying MoO_3 contents (Table 27, Figure 89, Figure 90). It incorporates fine-grained (10-100 µm), euhedral molybdenite inclusions. Molybdenite has a patchy internal structure and was microscopically (reflected light) identified by its morphology and very strong reflection pleochroism and anisotropy. Locally, vague "relict" oscillatory zoning is persevered (Figure 88, Figure 89). Scheelite generation 2 has normally more cracks and inclusions than generation 1 scheelite.

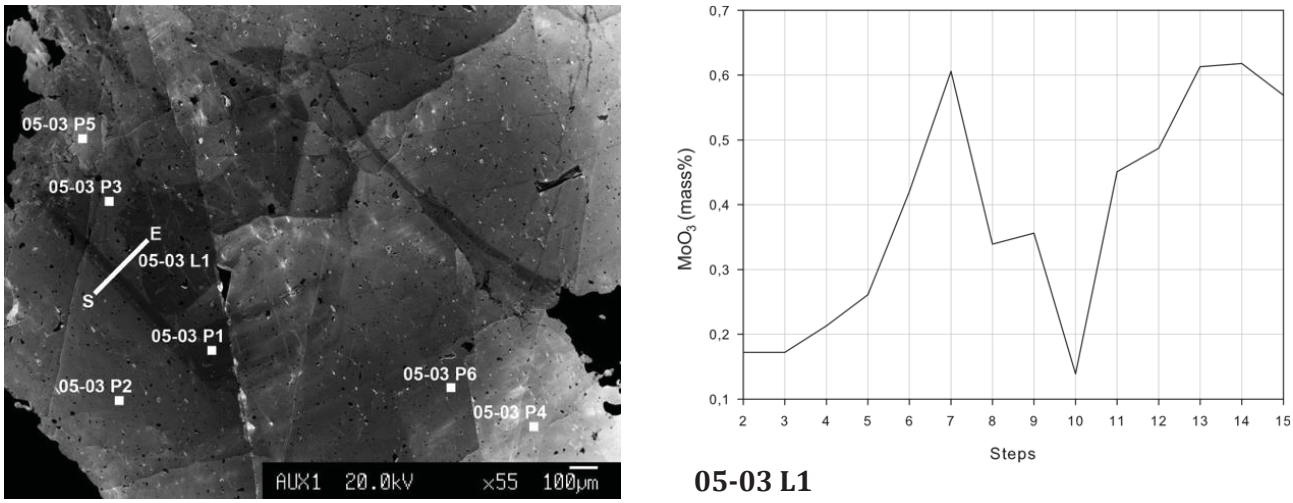

Figure 89: Complex internal structure of Mo-poor generation 2 scheelite. Point measurements and position of line scans (S=start, E=end) on left side, results of the line scans to the right. Label of the line scan below the line plot.

Generation 3 is characterised by very low Mo content, often below the detection limit. Mo-free scheelite forms overgrowths on earlier formed scheelite (Figure 90) and is also present in micro-cracks. The average MoO_3 content is 0.06 mass%.

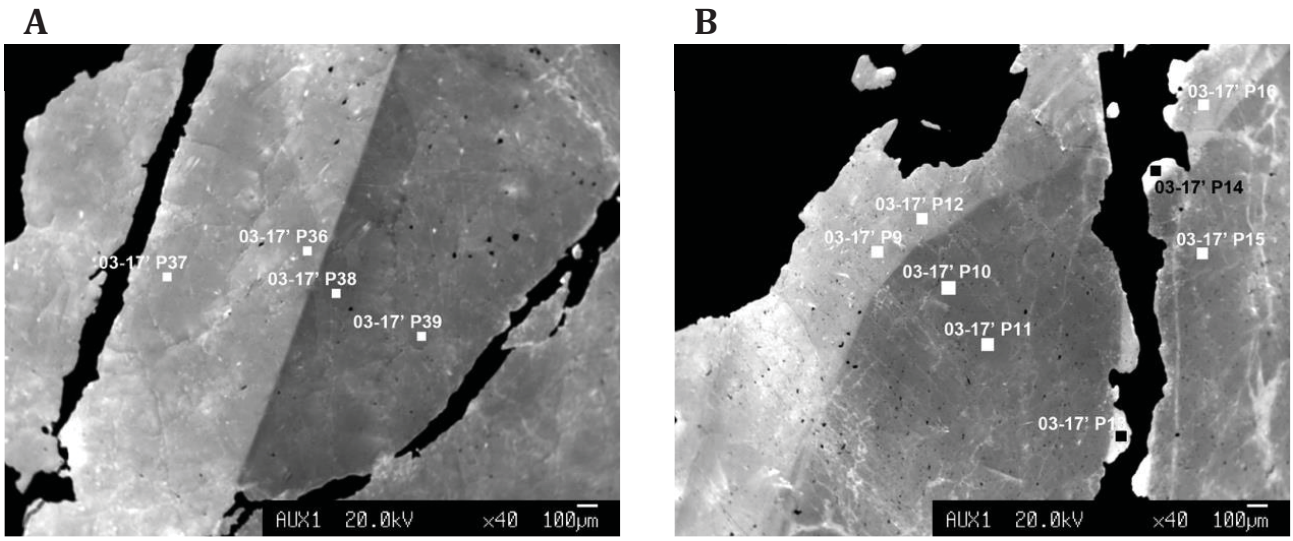

Figure 90: CL photomicrographs and point measurements of Mo-poor generation 2 (medium dark) and Mo-free (bright) generation 3 (sample 03-17').

Table 27: MoO_3 content of point measurements and line scans presented in **Figure 89** and **Figure 90**.

Sample	Average MoO_3 mass%		
	Generation 2		**Generation 3**
	Dark CL	Medium CL	Bright CL
05-03	0.539	0.354	0.146
03-17'	-	0.487	0.037

9.2. Clinozoisite

Major and trace elements of clinozoisite ($Ca_2(Al_2Fe^{3+})(Si_2O_7)(SiO_4)O(OH)$) were measured in two samples of calc-silicate rocks from Messelingscharte (03-18, 05-03) and one sample from Felbertal tungsten mine (08-01). Measured elements were Na, K, Mg, Ca, Mn, Fe, Al, Si, Ti, Sn and F. Mineral formulae were calculated on the basis of 12.5 O atoms. Special consideration was given to Sn because of elevated Sn concentration detected in the whole rocks (Chapter 8.1.5). For analytical conditions see Chapter 4.8.

The nomenclature for epidote-group minerals of Armbruster et al. (2006) is used. Clinozoisite incorporates 3 Al^{3+} cations in the octaedral M1-3 position. Epidote has at least one Fe^{3+} in the M1-3 position. Fe^{3+} is preferably incorporated in the tetragonal distorted M3 site (Frei et al. 2004). Therefore, analyses with an Al/Fe^{3+} (apfu-) ratio of >2 are named clinozoisite, those with <2 epidote. Frei et al. (2004) also noticed that Fe^{3+} rarely exceeds 0.6 apfu.

Clinozoisite can incorporate significant amounts of trace elements like LILE, Sr, Pb, REE and transition metals (Frei et al. 2004) and has diverse possibilities for substitution at different sites in the crystal structure. The most substitutions most relevant for the investigated samples are:

$2(Al,Fe)^{3+} \Leftrightarrow (Sn,Ti)^{4+} + (Fe,Mg,Mn)^{2+}$	M1-3 sight	*(1)*
$Ca^{2+} \Leftrightarrow (Mn,Fe)^{2+}$	A1 sight	*(2)*
$Ca^{2+} + (Al,Fe)^{3+} \Leftrightarrow REE^{3+} + (Fe,Mg,Mn)^{2+}$	A2 sight	*(3)*

9.2.1. Clinozoisite from Messelingscharte

Clinozoisite in calc-silicate rocks from Messelingscharte is characterised by an average Al/Fe^{3+} (apfu-) ratio of 4.55 (Figure 92A) and an exceptional high amount of substituting Sn reaching up to 3.00 mass% (=0.094 apfu) SnO_2 (Table 28). Na, K and Mg are generally very low in concentration. Mn concentration can reach concentrations up to 0.67 mass% (=0.044 apfu). Titanium is generally below the detection limit but when detectable it is above 1 mass% (≤0.06 apfu).

Petrographically two generations of clinozoisite can be distinguished (Chapter 6.6.1). The first generation (generation 1) comprises very coarse-grained, partly heavily altered grains that show often a zonation based on Sn/Ti (Figure 91A). The zonation comprises linear, as well as irregular patchy and roundish structures (Figure 91C; Figure 93A). The individual zones have sharp margins. Sn/Ti-rich zones occur normally in the centre grains. No well-defined growth zonation was found because of strong alteration of generation 1 grains. Generation 2 (generation 2) forms euhedral, small crystals that represent recrystallized grains (Figure 91B).

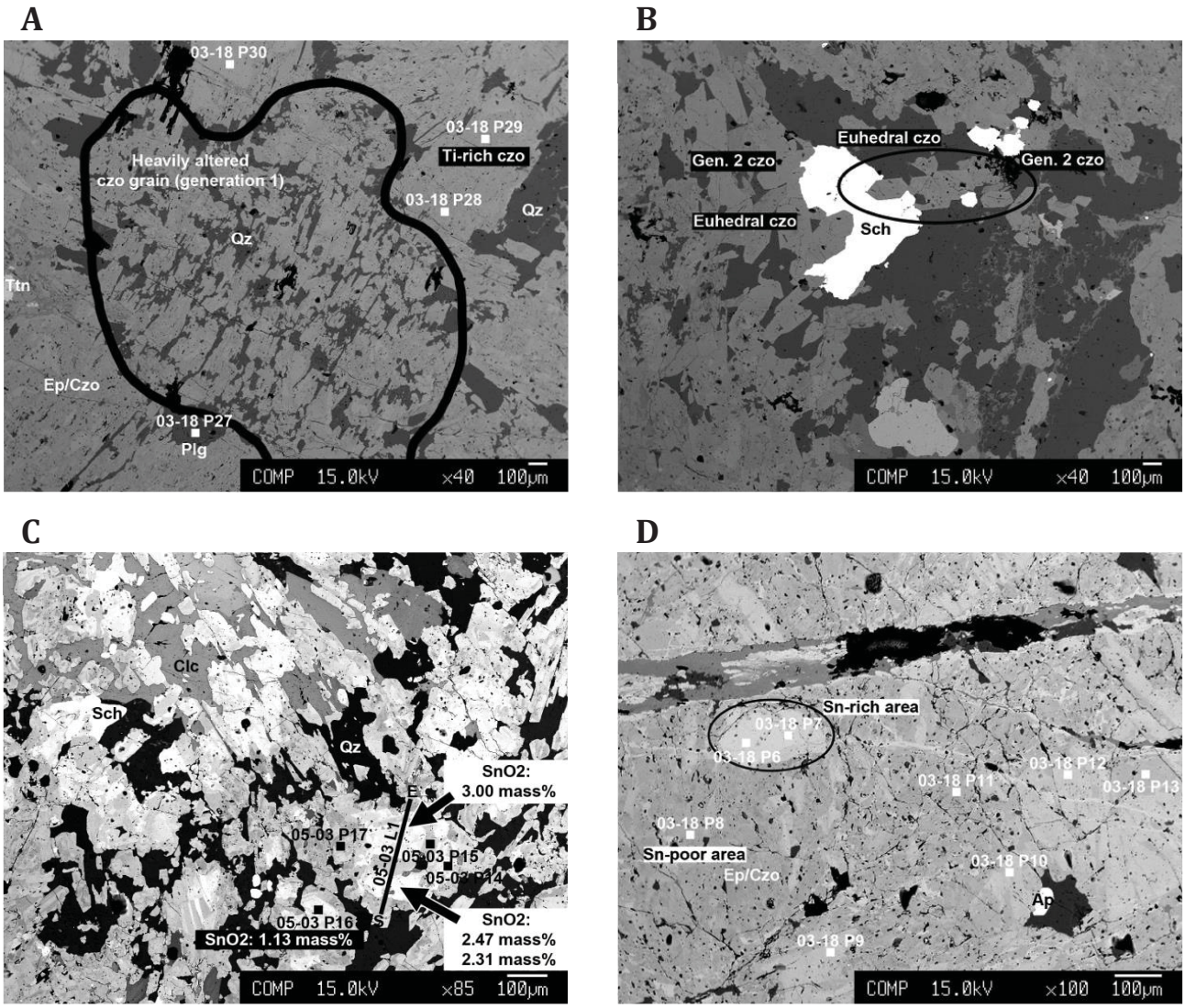

Figure 91: BSE images showing micro-textures of clinozoisite and spots of analyses in sample 03-18 (**A**,**B**,**D**) and 05-03 (**C**). **A** Heavily altered coarse-grained clinozoisite grain (outlined with black line). **B** Euhedral generation 2 clinozoisite intergrown with scheelite (Sch). **C** Line scan documenting exceptional high Sn concentrations in clinozoisite in domains of higher brightness (details in **Figure 93**). Sn-rich areas tend to be brighter than Sn-free areas in the BSE images (**C**, **D**).

Table 28: Selected EMPA analyses of clinozoisite. H_2O calculated with 18.015/((12.5/∑oxides)*2).

	Generation 1						Generation 2			
	03-18 P7		05-03 P3		05-03L1L 5		05-03 P9		05-03 P10	
	mass%	apfu	mass%	apfu	mass%	apfu	mass%	apfu	mass%	apfu
Na_2O	0.02	<0.00	0.01	<0.00	0.01	<0.00	bdl	<0.00	bdl	<0.00
SiO_2	39.25	3.08	38.68	3.00	38.61	3.03	39.86	3.08	39.17	3.05
MnO	0.10	0.01	0.18	0.01	0.07	<0.00	0.19	0.01	0.02	<0.00
CaO	22.47	1.89	22.66	1.88	22.66	1.91	22.68	1.88	22.92	1.91
MgO	bdl	<0.00	0.07	0.01	bdl	<0.00	0.03	<0.00	0.04	<0.00
FeO_{tot}	11.23	0.74	10.06	0.65	9.22	0.61	10.10	0.65	8.39	0.55
Fe^{2+} (calc)	np	np	1.84	0.10	1.21	0.07	np	np	np	np
K_2O	bdl	<0.00	bdl	<0.00	bdl	<0.00	bdl	<0.00	bdl	<0.00
Al_2O_3	23.91	2.21	25.60	2.34	24.97	2.31	25.42	2.31	26.63	2.44
SnO_2	0.46	0.01	0.07	<0.00	2.47	0.08	bdl	bdl	0.049	<0.00
TiO_2	bdl	<0.00	0.89	0.05	bdl	<0.00	bdl	<0.00	0.05	<0.00
Total	97.73	7.94	98.23	7.95	98.62	7.93	98.29	7.94	97.22	7.96
H_2O	1.91		1.93		1.91		1.94		1.93	

Clinozoisite displays two populations with respect to Sn concentrations as seen in the Q-Q Plot (Figure 92B). The low-Sn population is characterised by ≤0.3 mass% SnO_2 (=0.01 apfu Sn; median 0.079 mass%). The high-Sn population reaches values up to 3.00 mass% SnO_2 (median 1.11 mass% Sn). The high-Sn population corresponds roughly to the generation 1 clinozoisite that has higher Sn-contents (median 0.30 mass% = 0.015 apfu; ≤3.00 mass% SnO_2; Figure 92C). The low-Sn population incorporates all generation 2 clinozoisite and several measurements of generation 1 clinozoisite. Generation 2 clinozoisite incorporates on average 0.09 mass% Sn (=0.01 apfu).

For charge balance reasons significant amounts of Fe^{2+} must be incorporated in clinozoisite together with minor amounts of other divalent cations like Mg^{2+}. The re-calculated FeO content ($Fe^{2+}/Fe^{3+}*FeO_{tot}$, Fe^{x+} in apfu, FeO_{tot} in mass%) reaches up to 4.01 mass% (median 0.62 mass%; Figure 92D). Mn can be incorporated as Mn^{3+} into the M site or as Mn^{2+} for Ca in the A site (Frei et al. 2004).

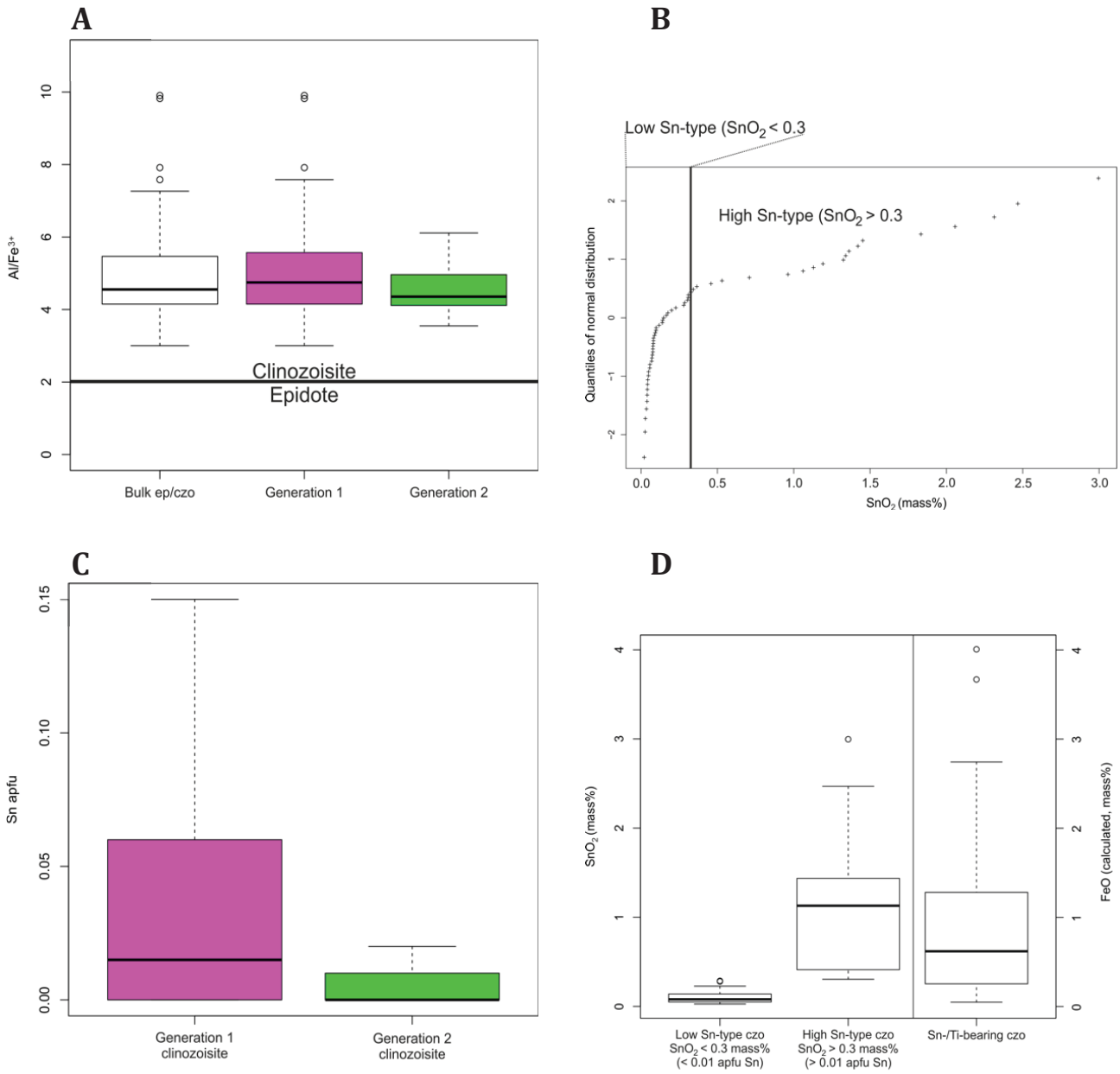

Figure 92: A Boxplot of Al/Fe^{3+} ratio from clinozoisite from Messelingscharte. **B** Q-Q-Plot for SnO_2 values in clinozoisite allowing the discrimination of two populations. **C** Boxplot of Sn (apfu) for clinozoisite generation 1 and 2. **D** Boxplot of SnO_2 and FeO (recalculated) concentrations (mass%).

Figure 93 shows a BSE image and results of a line scan through a heavily "altered", internally zoned clinozoisite grain (generation 1). Sn-rich and Sn-poor clinozoisite are irregularly intergrown. Locally, Sn-poor clinozoisite forms roundish rims around Sn-rich clinozoisite. Thin Sn-rich lamella are locally preserved. Normally, Sn-rich clinozoisite doesn't form the margin of clinozoisite grains but is surrounded by Sn-free clinozoisite.

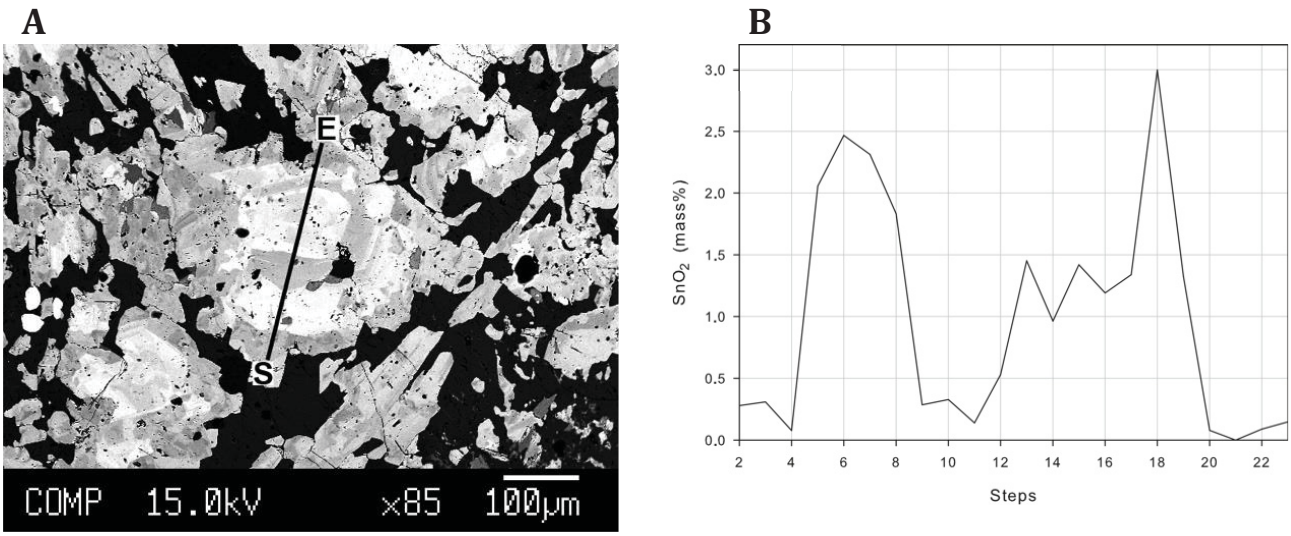

Figure 93: A Position of line scan across gen.1 clinozoisite. **B** SnO_2 content along the line scan. Highest value is 3.00 mass% SnO_2.

In clinozoisite from Messelingscharte Sn^{4+} and Ti^{4+} are the most important substitution for Al^{3+} and Fe^{3+} in the M1-3 sites in the high-Sn population. To sustain charge balance mostly Fe^{2+} is incorporated (see substitution *(1)* above). Mn and Mg contribute only to a minor extent. It is assumed that all divalent ions substitute the M1-3 position rather than the A1-2 position (occupied by Ca). The investigated clinozoisite shows striking fit to the ideal substitution *(1)* (Figure 94). The calculated regression line has a slope of -0.54 (ideally -0.5000) and the fit of the data is 0.95.

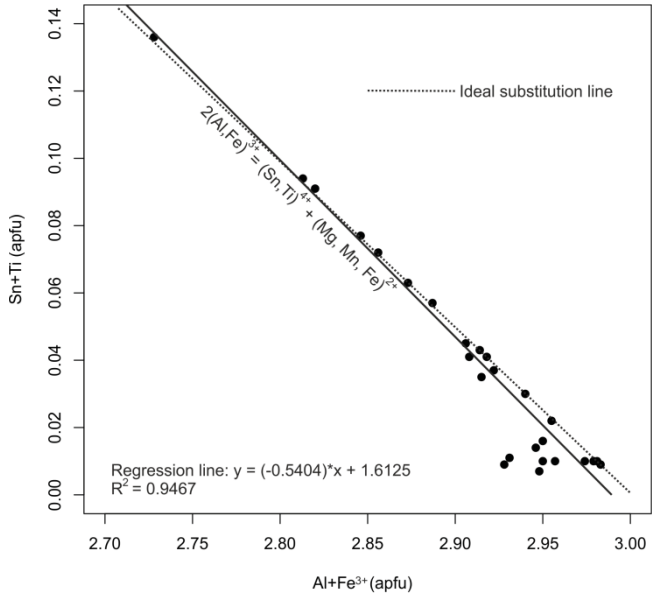

Figure 94: Scatter plot of $(Al,Fe)^{3+}$ substituted by 4+ charged (Sn,Ti) cations.

9.2.2. Clinozoisite from Felbertal mine

Clinozoisite from deformed irregular calc-silicate patches (Figure 95A; see Chapter 6.7) from Felbertal tungsten mine is Al-rich clinozoisite with an average Al/Fe^{3+} (apfu-) ratio of 6.65 (

Table 29; Figure 95B). It hosts minor amounts of substituting elements like Mn and Mg (average concentrations of 755 ppm and 435 ppm, respectively). A single point analysis yielded a Sn concentration of 1490 ppm (=0.009 apfu). Another rare substituting cation is Ti that in one measurement reached 8540 ppm (=0.049 apfu). Charge balance for 4+ cation is achieved through incorporation of Fe^{2+} in the M1-3 sights.

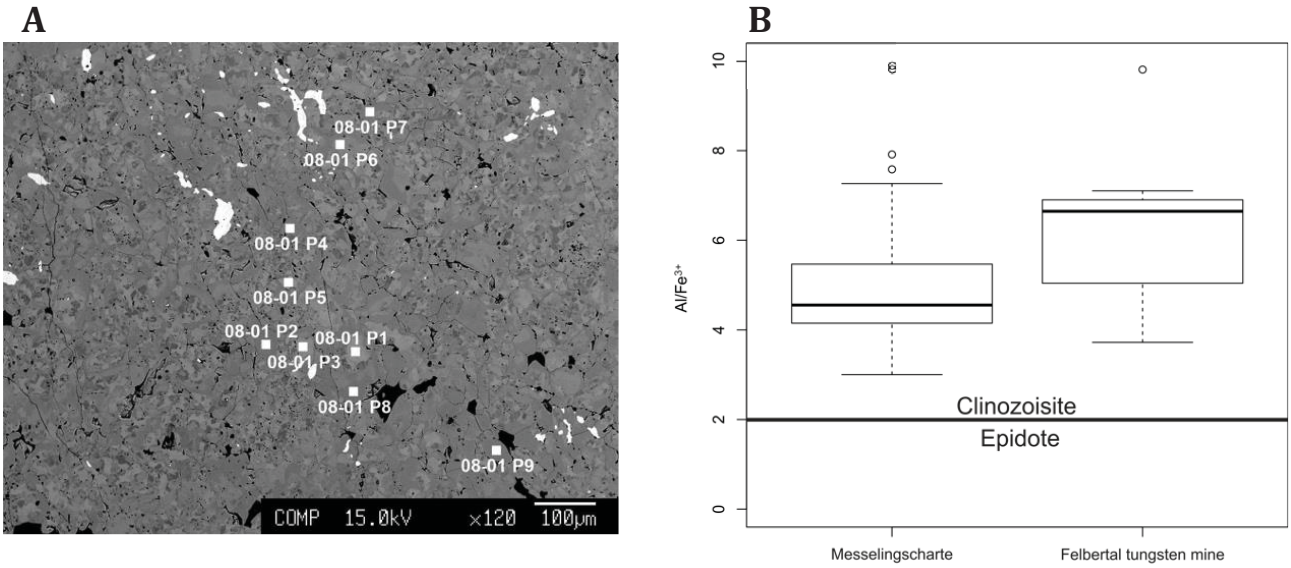

Figure 95: A BSE image of fine-grained clinozoisite showing measurement points. Bright grains are sulphides. **B** Boxplot of Al/Fe^{3+} (apfu-) ratio of clinozoisite comparing Messelingscharte and Felbertal tungsten mine.

Table 29: Selected EMPA analyses of clinozoisite from Felbertal tungsten mine. H_2O calculated 18.015/((12.5/∑Oxides)*2).

	08-01 P2		08-01 P12		08-01 P13	
	mass%	apfu	mass%	apfu	mass%	apfu
Na_2O	bdl	<0.00	0.02	<0.00	bdl	<0.00
SiO_2	40.65	3.09	39.36	3.03	40.19	3.08
MnO	0.06	<0.00	0.09	0.01	0.05	<0.00
CaO	22.94	1.87	22.98	1.90	23.24	1.91
MgO	0.04	0.03	bdl	<0.00	bdl	<0.00
FeO_{tot}	6.56	0.38	6.59	0.42	0.03	0.48
Fe^{2+} (calc)	np	np	1.03	0.06	np	np
K_2O	bdl	<0.00	bdl	<0.00	bdl	<0.00
Al_2O_3	28.74	2.58	27.92	2.53	27.44	2.48
SnO_2	0.02	<0.00	bdl	<0.00	bdl	<0.00
TiO_2	bdl	bdl	0.85	0.05	bdl	<0.00
Total	99.16	7.96	97.82	7.94	98.37	7.97
H_2O	1.97		1.95		1.96	

9.3. Titanite

Titanite ($CaTiSiO_4(O,OH,F)$) was analysed in two samples (03-18, 05-03) from calc-silicate rocks from Messelingscharte. Measured elements were Ca, Ti, Si, Al, Fe, F, Sn, Zr, Nb and Ta. Mineral formulae were calculated on the basis of 1 Si atom. OH was calculated after OH = Al + Fe^{3+} - F (Ulmer 1993) assuming that all Fe is present as Fe^{3+}. Measuring conditions are presented in Chapter 4.8.

Euhedral and anhedral titanite crystals were analysed by EMPA to characterise the complex internal zonation visible in the BSE image. Special consideration was given to Sn because titanite can be an important Sn carrier in calc-silicate rocks (Aleksandrov and Troneva 2007). Other analysed trace elements were W, Nb, Ta and Zr. All these trace elements except Sn were below the detection limit.

Titanite forms euhedral sphenoidal (Figure 96; Figure 97B,C) to anhedral granular textured (Figure 97A,D) crystals that show patchy irregular internal zoning in BSE images. Occasionally, there are 1-3 µm small, roundish inclusions of cassiterite and zircon. Accumulations of euhedral titanite grains (Figure 96A) occur typically at the margin between amphibolite schist and the clinozoisite-rich calc-silicate rock. Euhedral titanite with patchy zoning occurs located most common at the margin to amphibole schist and overgrows clinozoisite generation 1. Anhedral titanite could be older than euhedral titanite (metamorphic recrystallization?). There is evidence of titanite being overgrown by young clinozoisite (generation 2) indicating a pre-metamorphic formation of titanite. However, no distinct populations can be distinguished based on mineral chemical composition. Hence, all titanites are collectively dealt with in the following.

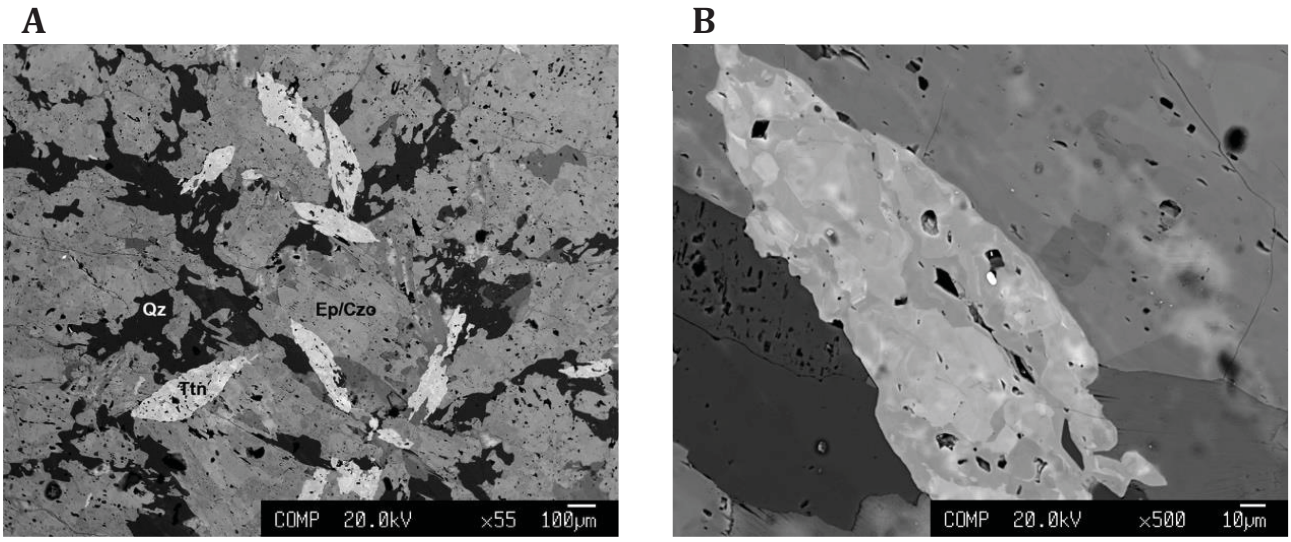

Figure 96: BSE image of titanite (bright), clinozoisite (medium grey) and quartz (dark). **A** Euhedral titanite crystals intergrown with clinozoisite and quartz (sample 05-03) **B** Detailed BSE image of euhedral titanite showing irregular to patchy internal zoning. Small bright spot is probably cassiterite.

Table 30: Selected EMPA analyses of titanite.

	05-03ttnP5		05-03ttnP16		05-03ttnP15		03-18ttnP40	
	mass%	apfu	mass%	apfu	mass%	apfu	mass%	
SiO_2	28.99	1.00	28.91	1.00	29.80	1.00	29.89	1.00
TiO_2	33.85	0.85	31.57	0.82	39.00	0.98	38.30	0.96
Al_2O_3	2.58	0.10	3.39	0.14	2.09	0.08	2.43	0.10
SnO_2	5.51	0.07	6.48	0.09	1.18	0.02	0.32	0.00
FeO_{tot}	1.65	0.05	1.26	0.04	0.50	0.01	0.39	0.01
CaO	26.20	0.94	26.19	0.97	26.94	0.97	27.16	0.97
F	0.83	0.09	1.20	0.13	0.67	0.07	0.65	0.07
Sum	99.78		99.16		100.23		99.17	
OH	0.27	0.06	0.19	0.04	0.11	0.03	0.17	0.04
O	0.35	0.85	0.50	0.83	0.28	0.90	0.27	0.89
Sum excl. H_2O	100.13	4.01	99.66	4.06	100.51	4.07	99.45	4.05

Several substitution schemes have been reported for titanite in the literature. Some common substitution mechanisms are:

$(Al,Fe)^{3+} + (OH,F)^{-} \Leftrightarrow Ti^{4+} + O^{2-}$ (Saham 1946; Ribbe 1982) *(1)*

$Ca^{2+} + Ti^{4+} \Leftrightarrow REE^{3+} + (Al,Fe)^{3+}$ (Green and Pearson 1986) *(2)*

$2\ Ti^{4+} \Leftrightarrow (Nb,Ta)^{5+} + (Al,Fe)^{3+}$ (Clark 1974) *(3)*

$Sn^{4+} \Leftrightarrow Ti^{4+}$ (Takenouchi 1971) *(4)*

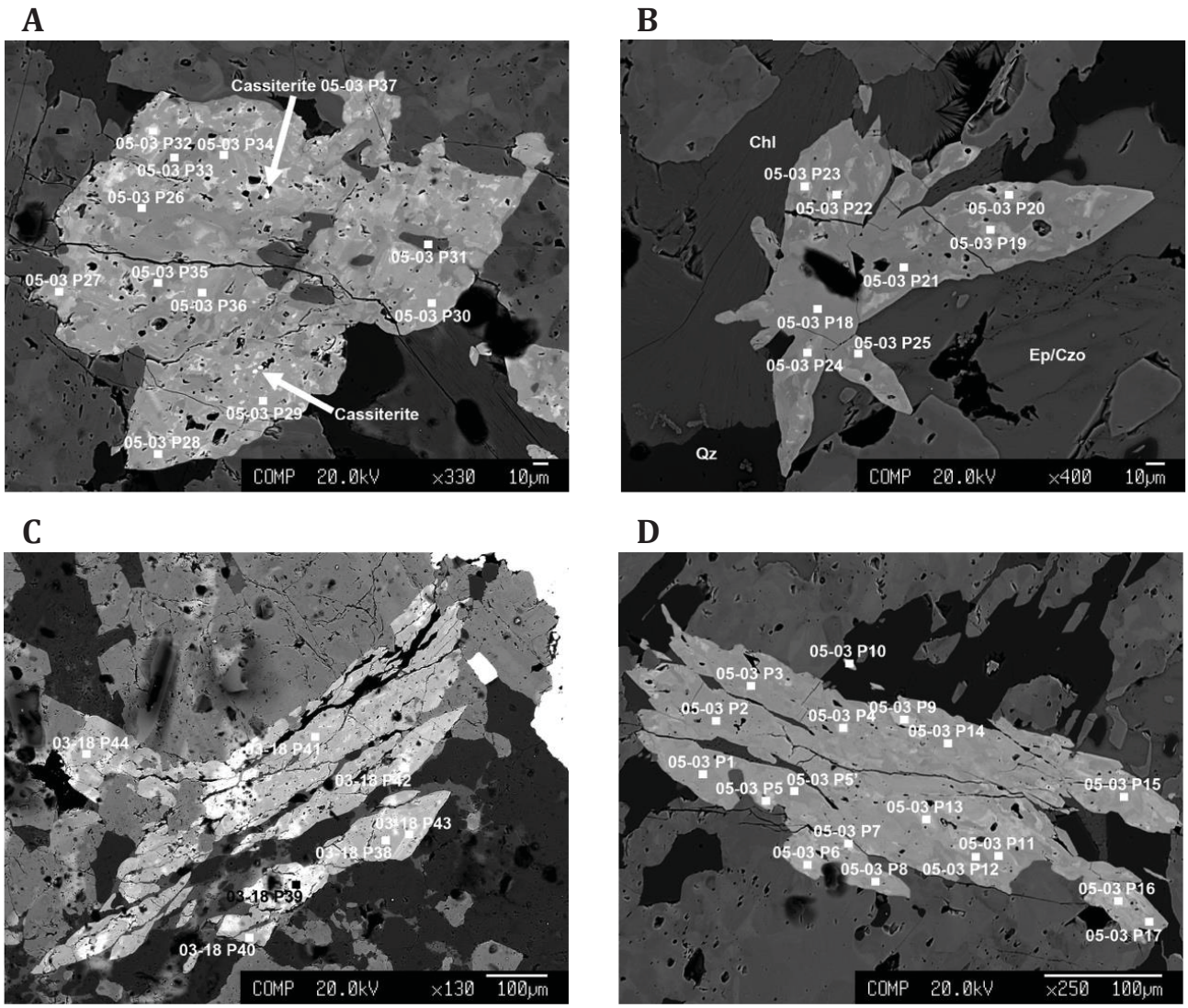

Figure 97: BSE images documenting spots of titanite analyses. Anhedral patchy titanite (**A**,**D**) (sample 05-03) with inclusions of fine-grained cassiterite (**A**). Euhedreal to subhedral titanite crystals intergrown with clinozoisite (medium grey) and quartz (dark) (**B**,**C**) (samples 03-18, 05-03). Grey to black minerals are clinozoisite, chlorite and quartz.

Titanite has a very variable content of SnO_2 from 0.07-6.48 mass% (median 2.29 mass%). There is only one population of titanite compositions in the dataset (Figure 98A). Titanite shows a complete solid solution with malayaite ($CaSnSiO_4(O,OH,F)$) after substitution mechanism *(4)* (Takenouchi 1971). Measured Sn concentrations correspond to 0.01-0.09 apfu Sn (median 0.031 apfu) and an average x(Sn) value of 0.029 (Figure 98B).

The F concentration scatters between 0.498-1.57 mass% with a median of 1.06 mass% (=0.119 apfu). CaO values scatter only slightly with an average of 26.54 mass% (=0.968 apfu). Ca has to be 1 apfu in the ideal formula of titanite. Our results are <1 apfu Ca falling short by ~0.03 apfu. One possibility for a deficiency in Ca could be incorporation of REE in the Ca position (substitution *(2)* above). However, qualitative WDS measurements of Sn-poor and Sn-rich portions of titanite resulted in no detectable REE (WDS spectra in Appendix A.5.4). *(2)*. An alternative could be the substitution $Ca^{2+} \Leftrightarrow 2H^{+}$ (Hollabaugh and Rosenberg, 1983).

Oberti et al. (1991) classifies titanite in high-aluminous x(Al)>0.25) and low-aluminous x(Al)<0.25 ones. The x(Al) is calculated by Oberti et al. (1991) as follows: x(Al) = Al / (Al+Fe+Ti) (all values in

apfu). Here, a modified calculation of x(Al) = Al / (Al+Fe+Sn+Ti) will be used to include Sn. Values of x(Al) for Messelingscharte titanites range from 0.075-0.236 with a median of 0.125. All values are below the threshold (x(Al)>0.25); therefore all measured titanites are assigned to the low-Al group. The x(Sn) value is calculated by Sn / (Al+Fe+Sn+Ti). It gives the ratio of Sn occupying the M2 position in titanite. For titanite in this study, values are generally low with a median of 0.029.

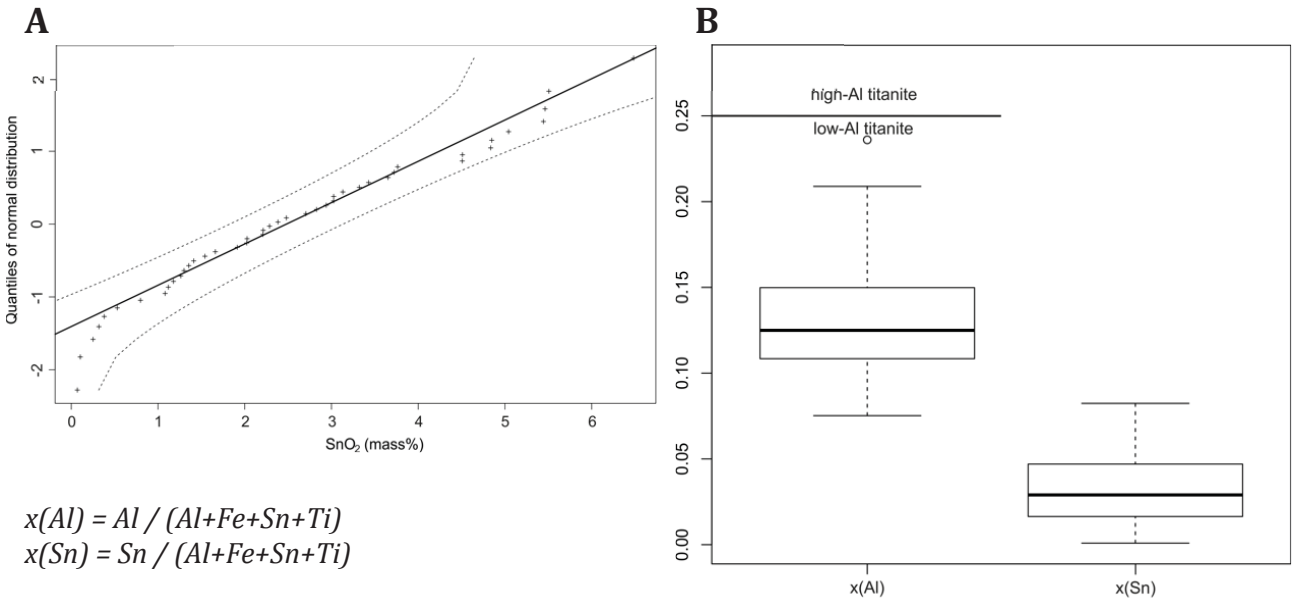

Figure 98: A Q-Q-plot of SnO_2 concentration in titanite. **B** Boxplot of x(Al) and x(Sn).

All investigated low-Al titanites are characterised by an excess of F+OH over Al (Figure 99A) indicating that Fe^{3+} must be involved in the substation *(1)*. Aluminus and iron are the main substituents for Ti compared to Sn. 82% of the total substituting Al+Fe is taken by Al (see also Oberti et al. 1991). Titanium and all the other substituting cations (Fe, Al, Sn) follow a well defined 1:1 substitution trend supporting substitution schemes *(1)* and *(4)* (Figure 99B). The substitution of Ti by Sn *(4)* is connected to a preferred incorporation of Fe (Figure 99C) over Al.

There is an uncommon excess of cations in the M2 position in all titanite measurements (Figure 99D). The calculation of apfu as used here is based on the assumption of 1 Si at the M3 position per formula. The sum of all elements (Ti, Sn, Fe, Al; in apfu) located at the M2 position is generally >1 (median 1.065 apfu). Analytical problems with Si cannot be excluded. The average Si content is also 1.15 mass% lower (29.50 mass%) than in the ideal titanite formula (ideal 30.65 mass%). Therefore Ti could be substituting Si to minor degree to average out the excess in the M2 position (Hollabaugh and Rosenberg 1983).

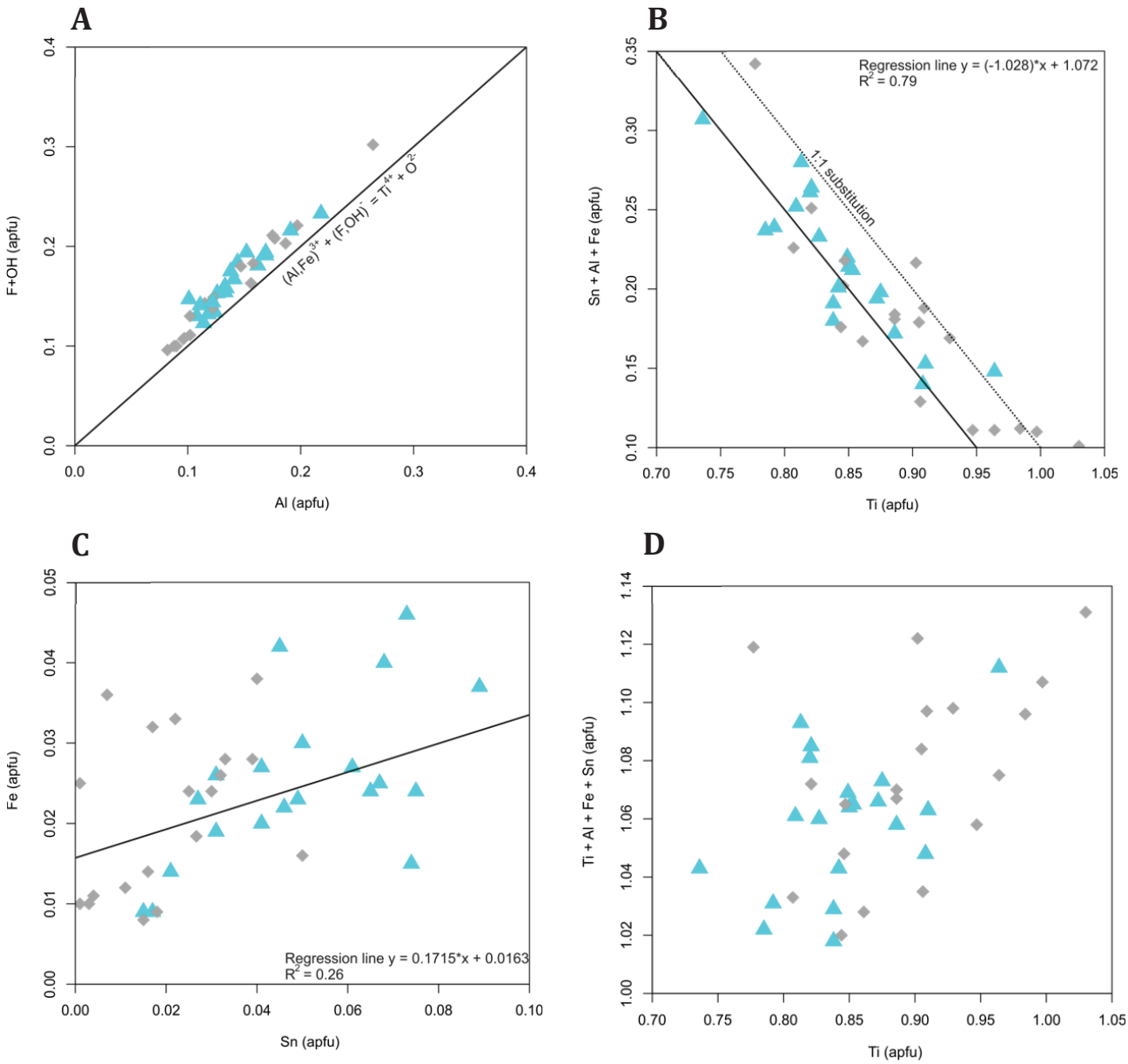

Figure 99: Binary plots of different cations of investigated titanite; grey diamonds = dark area in BSE, cyan triangle = bright area in BSE. **A** Cation plot showing the nearly perfect substitution of $(Al,Fe)^{3+}$ + $(OH,F)^{-}$ ⇔ Ti^{4+} + O^{2-}. **B** Substitution of Ti by Sn+Fe+Al. All values scatter around a regression line parallel to the ideal substitution line (1:1). **C** Cation plot of Sn versus Fe showing a weak positive correlation. **D** Cation plot of Ti vs. Ti + Al + Fe + Sn showing an excess of cations at the M2 site.

The patchy irregular zonation seen in the BSE images results from variations in Sn, Fe and Al (Figure 100). Sn-rich areas are enriched in Fe^{3+} and depleted in Al^{3+} compared to Sn-poor ones (Figure 99C; Figure 100). Incorporation of even small amounts of Sn^{4+} makes titanite structurally incompatible to further incorporation of Al^{3+} + $(F,OH)^{-}$ (Higgins and Ribbe 1976; Oberti et al. 1991; Groat et al. 1996; Kunz et al. 1997). The structure of malayaite and titanite is basically topologically identical but titanite shows an out-of-centre distortion on the octahedral site (= Ti-O bonds have two different lengths) and malayaite doesn't (Oberti et al. 1991; Kunz et al. 1997). The structure of less distorted Sn-titanite seems therefore be more suitable for Fe^{3+} than Al^{3+}.

Bright spots in the Sn element distribution map (Figure 100B,D) are probably 1-3 µm large roundish inclusions of cassiterite. The adjacent clinozoisite grain incorporates notable Sn concentrations (Figure 100D).

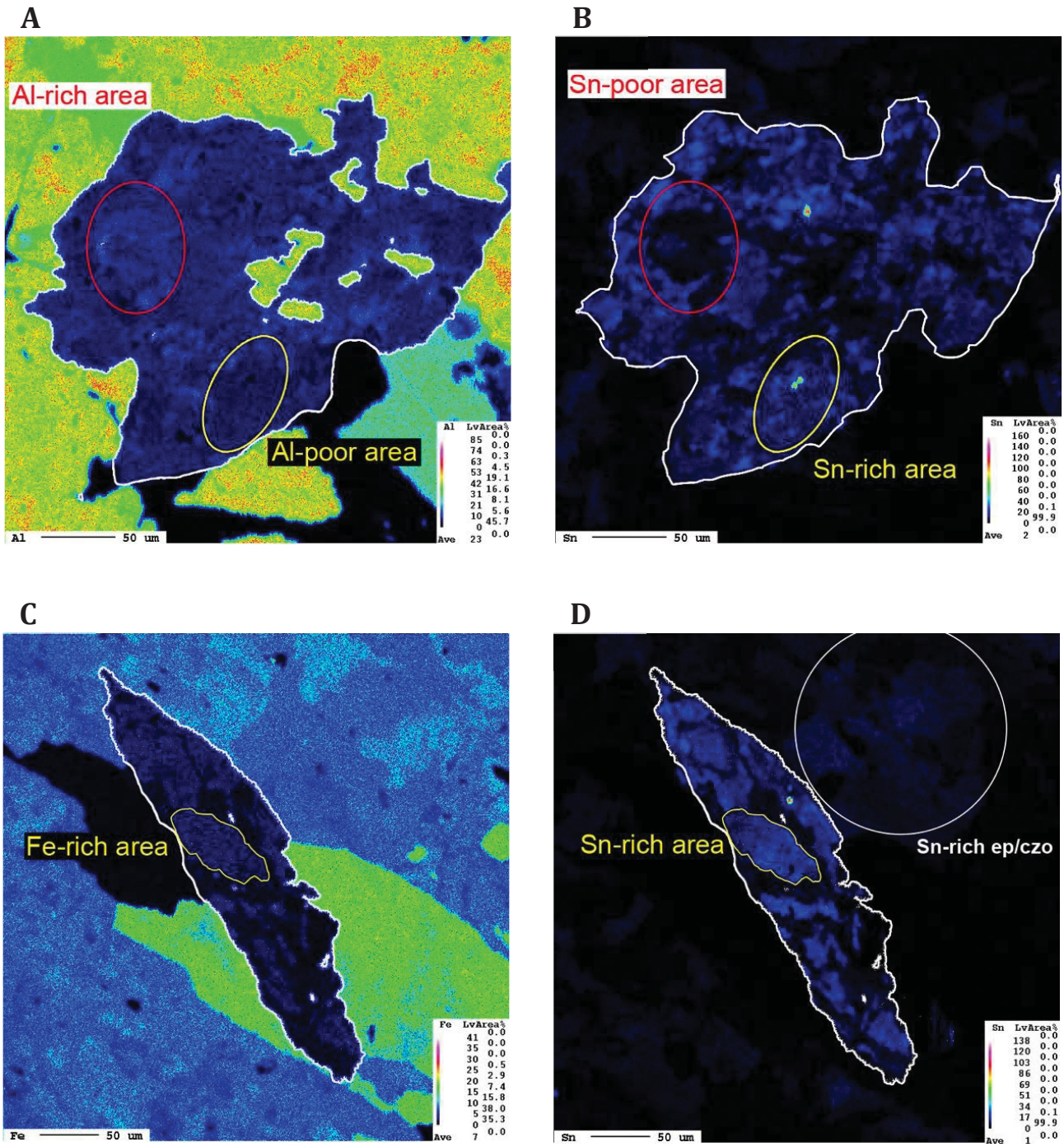

Figure 100: Element maps of Fe, Al and Sn of titanite **A,B** Titanite shown in **Figure 97**A (sample 05-03). **C,D** Mapping of Fe and Sn of titanite shown in **Figure 96**B (sample 05-03).

10. Discussion

10.1. Whole rock geochemistry

10.1.1. Comparison of Messeling gneiss with Granatspitz gneiss and Felbertal Augengneiss

The bulk trace element geochemistry of Messeling gneiss is characterised by low concentration of HFS elements (except U, Th) as well as low Sr. LIL elements are generally enriched (Cs, Rb, K), only Ba is low. Samples of Messeling gneiss fit very well to data from Granatspitz gneiss (Figure 101A). The main indicator are similar concentrations of LILE (Rb, Ba, K) and HFSE (Zr, Hf) and low U (2-4 ppm) and Th (7-12 ppm). Furthermore, the low strontium, niobium and tantalum values are very similar too. Data of the Granatspitz gneiss from Kozlik (2016) tends to slightly higher Cs, U and P values. The Felbertal Augengneiss shows striking elevated concentrations of U (12-30 ppm), Th (26-42 ppm), Nb (20-36 ppm), and Ta (2.7-5.3 ppm) compared to the moderate contents of Nb (16-18 ppm), U (4-6 ppm) and Th (7-12 ppm) in the Granatspitz gneiss (Figure 101A,B). Beside some similar characteristics between Felbertal Augengneiss and Granatspitz gneiss like the low TiO_2 and Sr content, significant disparities are the higher Al_2O_3 (14.6 compared to 13.4 mass%) and P_2O_5 (0.20 compared to 0.10 mass%). Therefore, it is unlikely that Messeling gneiss is a slice of Felbertal Augengneiss.

Messeling gneiss displays $(La/Yb)_{cn}$ values similar to Granatspitz gneiss with 5.74-9.74 with an median of 9.11. The Granatspitz gneiss has commonly higher $(La/Yb)_{cn}$ values between 9.17-9.55 with a median of 9.25 (Figure 101C). The europium anomaly Eu/Eu* is also similar between Granatspitz gneiss (0.41-0.48, median 0.43) and Messeling gneiss (0.33-0.48, median 0.45) compared to slightly lower values for the Felbertauern augengneiss (0.27-0.45, median 0.37). The Felbertal Augengneiss is strongly enriched in LREE and HREE with $(La/Yb)_{cn}$ between 3.69-10.51 (median 5.74) (Figure 101D) compared to Granatspitz gneiss. The content of HREE of the Felbertauern augengneiss is generally higher than in Messeling gneiss.

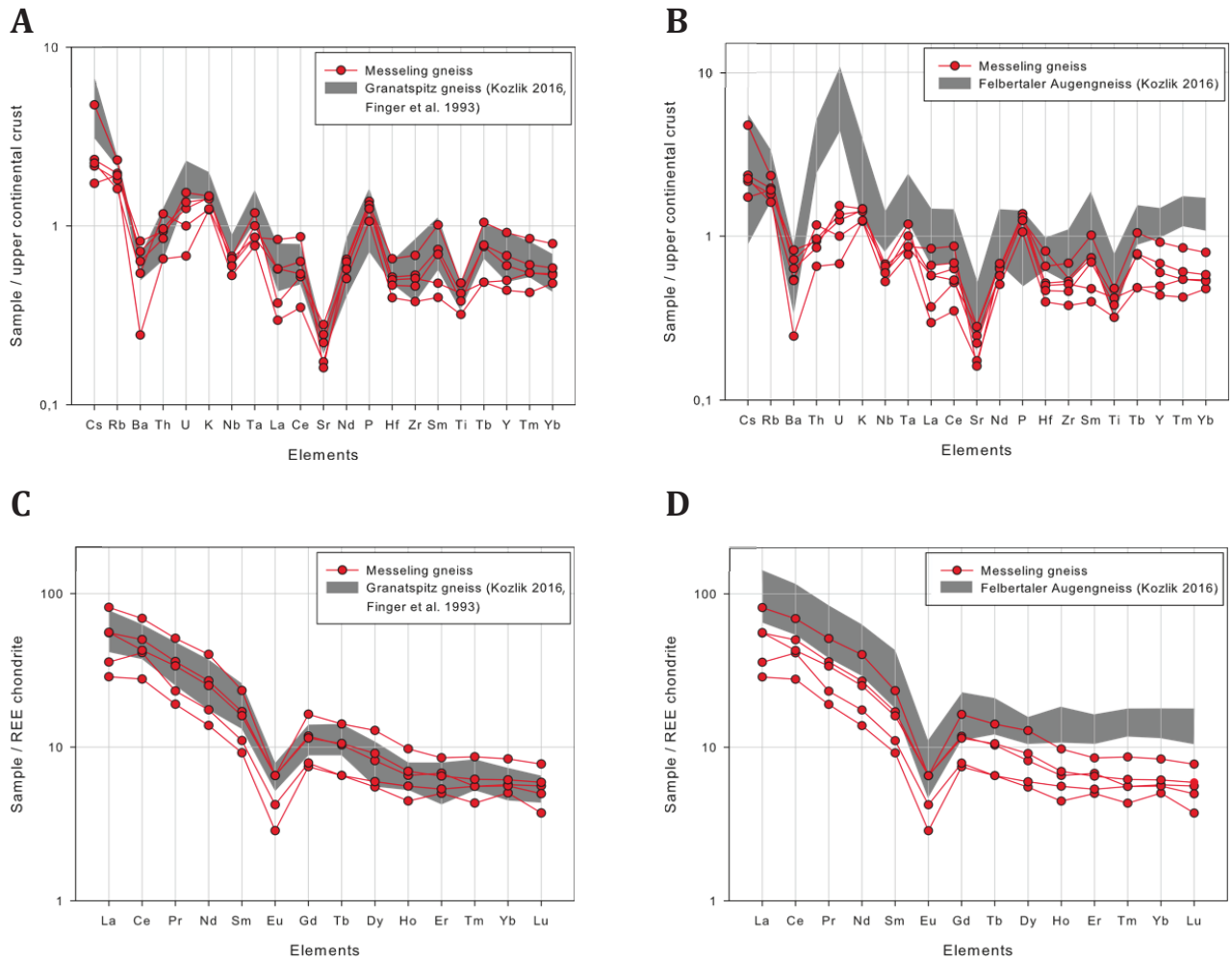

Figure 101: Spider plots of trace elements and REE of Messeling gneiss and data from Kozlik (2016) and Finger et al. (1993). **A** Trace elements of Messeling gneiss and Granatspitz gneiss (normalized after Taylor and McLennan 1995). **B** Trace elements of Messeling gneiss and Felbertauern augengneiss (after Taylor and McLennan 1995). **C** REE pattern of Granatspitz gneiss compared to Messeling gneiss. **D** REE pattern of Felbertauern augengneiss compared to Messeling gneiss.

In summary, considering the chemical similarities seen in the granite classification plots (see Chapter 8.1.4; Figure 80) and in the multi-element spider and REE diagrams (Figure 101) it is clear that the Messeling gneiss belongs to the Granatspitz gneiss; it clearly differs from the Felbertal Augengneiss. In accordance with the field relations (e.g. occurrences of Weissschiefer) the Messeling gneiss is interpreted as a tectonic slice of Granatspitz gneiss within the Basal Schist.

10.1.2. Relationship between amphibolite, hornblende-biotite schist and hornblende-biotite gneiss of the Basal Amphibolite

Hornblende-biotite schists occur together with amphibolites and garniferous gneisses in stronger deformed areas of the Basal Amphibolite. The comparison of trace elements and REE ($(La/Yb)_{cn}$ amphibolite = 3.4, $(La/Yb)_{cn}$ hornblende-biotite schist = 10.7) patterns (Figure 102) indicates significant chemical differences between these rocks. These differences are also revealed when comparing the LIL elements Rb, Ba and Th. In contrast to Frisch and Raab (1987) who concluded that the alkali content depends on degree of deformation (i.e. it is a secondary feature), large scattering of LILE, especially of Th, could be a primary nature. Different REE patterns for these two lithologies support this view. Possible processes causing the chemical differences are: melting of different protoliths, crustal contamination or magmatic differentiation. Whereas the strong variation in Th

could indicate contamination with (continental?) crustal material the systematic differences in REE patterns are best explained with either different protoliths or magmatic differentiation. In the latter case, the hornblende-biotite schist/gneiss would have derived from more evolved melts as reflected in the enrichment of the LREE.

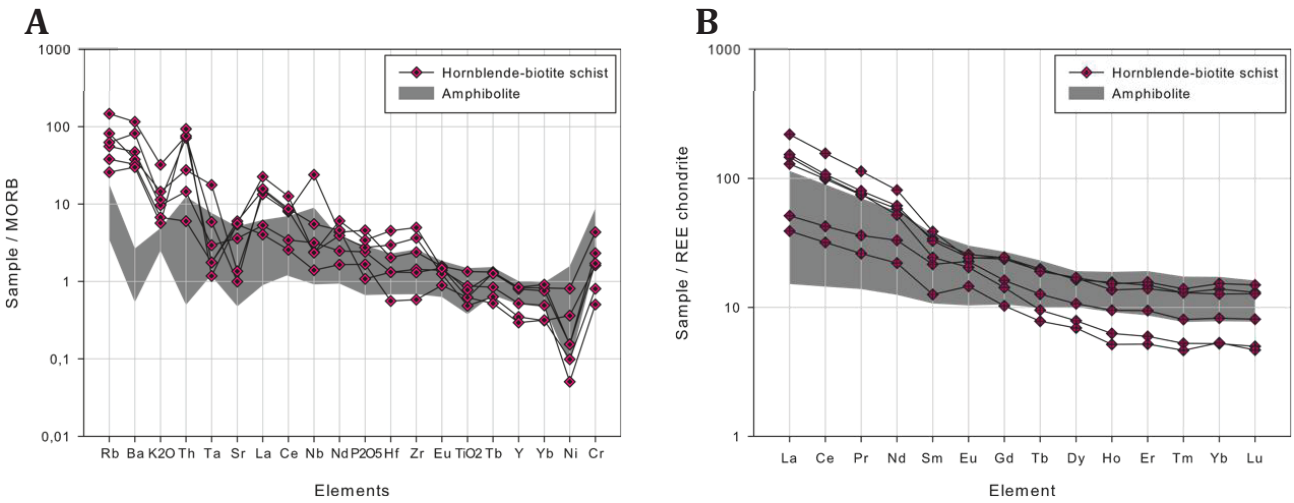

Figure 102: Comparison of trace elements (**A**) and REE (**B**) for amphibolite and hornblende-biotite schist.

The hornblende-biotite gneiss is best interpreted as a late-stage diorite intrusion in the Basal Amphibolite unit (see Figure 38). The most important difference compared to the amphibolite is the elevated concentration of LIL (Rb, Ba and K_2O) (Figure 103A). Cr and Ni are depleted in the hornblende-biotite gneiss compared to amphibolite. The REE patterns are quite similar (Figure 103B).

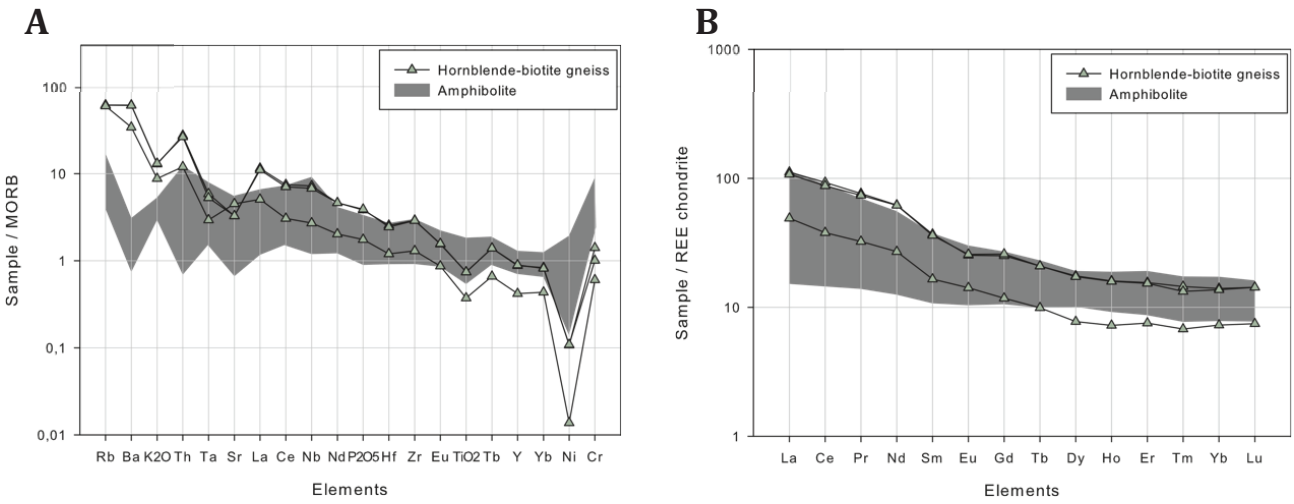

Figure 103: Spider plots of incompatible elements (**A**) and REE (**B**) of amphibolite and hornblende-biotite gneiss.

The trace elements and REE patterns (Figure 104) of the hornblende-biotite schist are indistinguishable from the hornblende-biotite gneiss. Both rock types show sometimes a slightly negative Europium anomaly (minimum Eu/Eu* = 0.83 (gneiss), minimum Eu/Eu* = 0.78 (schist)) indicating fractionation of plagioclase. The Ni content tends to be lower in the hornblende-biotite gneiss. Several main components differ distinguishably (Table 31).

Table 31: Selected main components of hornblende-biotite schist and hornblende-biotite gneiss. Greenish shaded elements display characteristic differences.

Selected main component	Hornblende-biotite schist (median, mass%)	Hornblende-biotite gneiss (median, mass%)
SiO_2	54.17	59.28
Al_2O_3	18.59	16.53
MgO	4.18	3.13
CaO	6.50	5.65
Na_2O	4.39	3.23
K_2O	1.58	1.94
P_2O_5	0.31	0.46

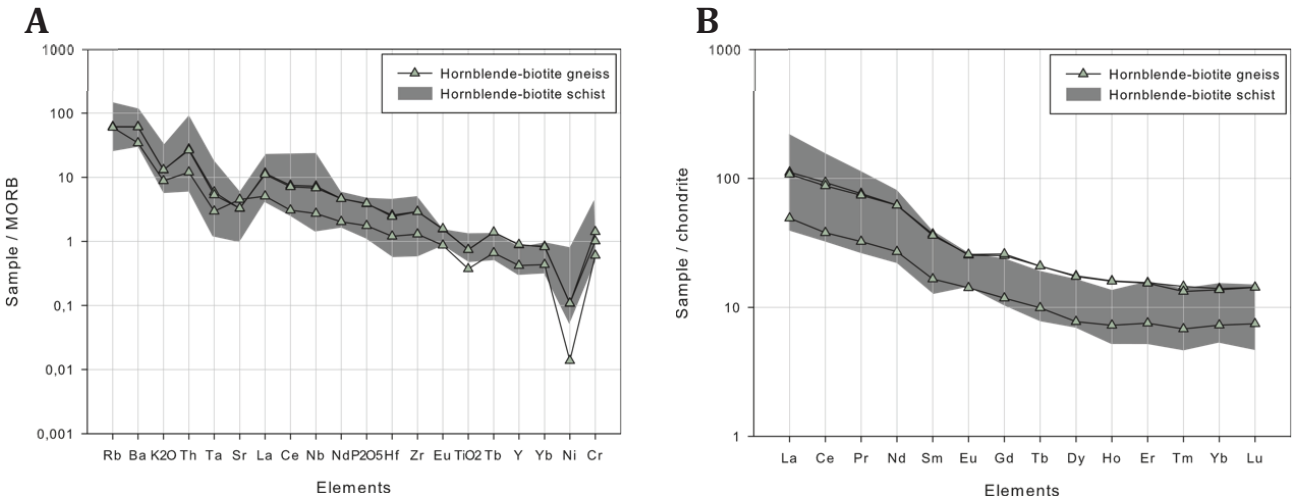

Figure 104: Spider plots of incompatible elements (**A**) and REE (**B**) of hornblende-biotite schist and hornblende-biotite gneiss.

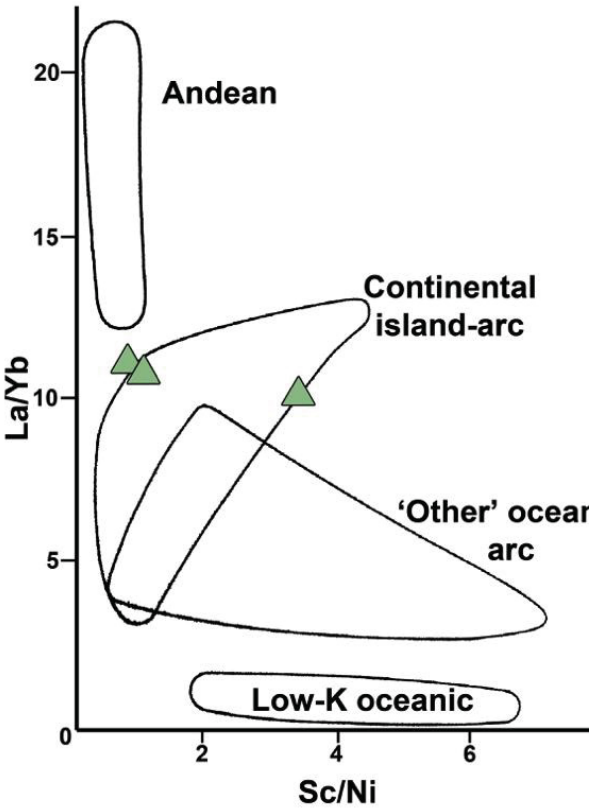

Figure 105: Geotectonic discrimination diagram for intermediate volcanic rocks (Bailey et al. 1981).

The geotectonic classification of intermediate igneous rocks from Bailey et al. (1981) (Figure 105) shows that all three samples of hornblende-biotite gneiss plot closely to boarder of the continental island-arc field indicating an island-arc environment.

Differences of trace element composition between amphibolite and hornblende-biotite schist/gneiss (referred as “evolved rocks”) can be explained by fractional crystallization. The higher content of incompatible alkalis and the lower content of compatible Ni and Cr in hornblende-biotite schist/gneiss indicate a higher degree of differentiation compared to the amphibolite (Figure 102A). Furthermore, the SiO_2 content is higher (evolved rocks: 51.18-62.01 mass%, amphibolite: 41.61-55.18 mass%) and the MgO is notable lower (evolved rocks: 3.17-6.33 mass%, amphibolite: 4.55-12.34 mass%). It formed slightly after emplacement of protoliths of the amphibolite and hornblende-biotite schist. Saunders and Tarney (1984) and Weaver et al. (1979) refer to a suite of primitive to more evolved rocks (up to rhyodacitic igneous rocks) that can be associated with a back-arc setting. Therefore, it is plausible that mafic-intermediate volcanic rocks form are existing within the Basal Amphibolite unit.

10.1.3. Palaeogeographic setting of the Basal Amphibolite

The following, literature and new geochemical results will be used for an updated palaeogeographic model for the Basal Amphibolite, Habach Complex and parts of the Austroalpine basement units (Figure 107). The most recent model was published by Eichhorn et al. (2001) which is not compatible with advance in paleogeographic reconstruction. Most age determinations yield Late Neoproterozoic to Early Cambrian ages (551-539 Ma) for the Basal Amphibolite (Eichhorn et al. 2001; Loth and Höll 1994; von Quadt 1992) but recent data from Kebede et al. (2005) have indicated a Variscan formation age of 350-341 Ma. The more accepted view (e.g. Eichhorn et al. 2001) of an early Palaeozoic formation age is used for further discussion.

Mafic volcanism predating the opening of the Rheic ocean during early Cambrian is widespread throughout the European Variscides (e.g. Massif Central, Bohemian Massive, Iberian Massif) (Crowley et al. 1995, 2000; Stampfli et al. 2002a,b). The Basal Amphibolite is believed to be a part of this rock suite. Crowley et al. (1995, 2000) compiled a comprehensive dataset for pre-Variscan meta-basaltic rocks from the Variscan basement and reports a mixed signature between MORB and VAB similar to the Basal Amphibolite (Chapter 8.1.3).

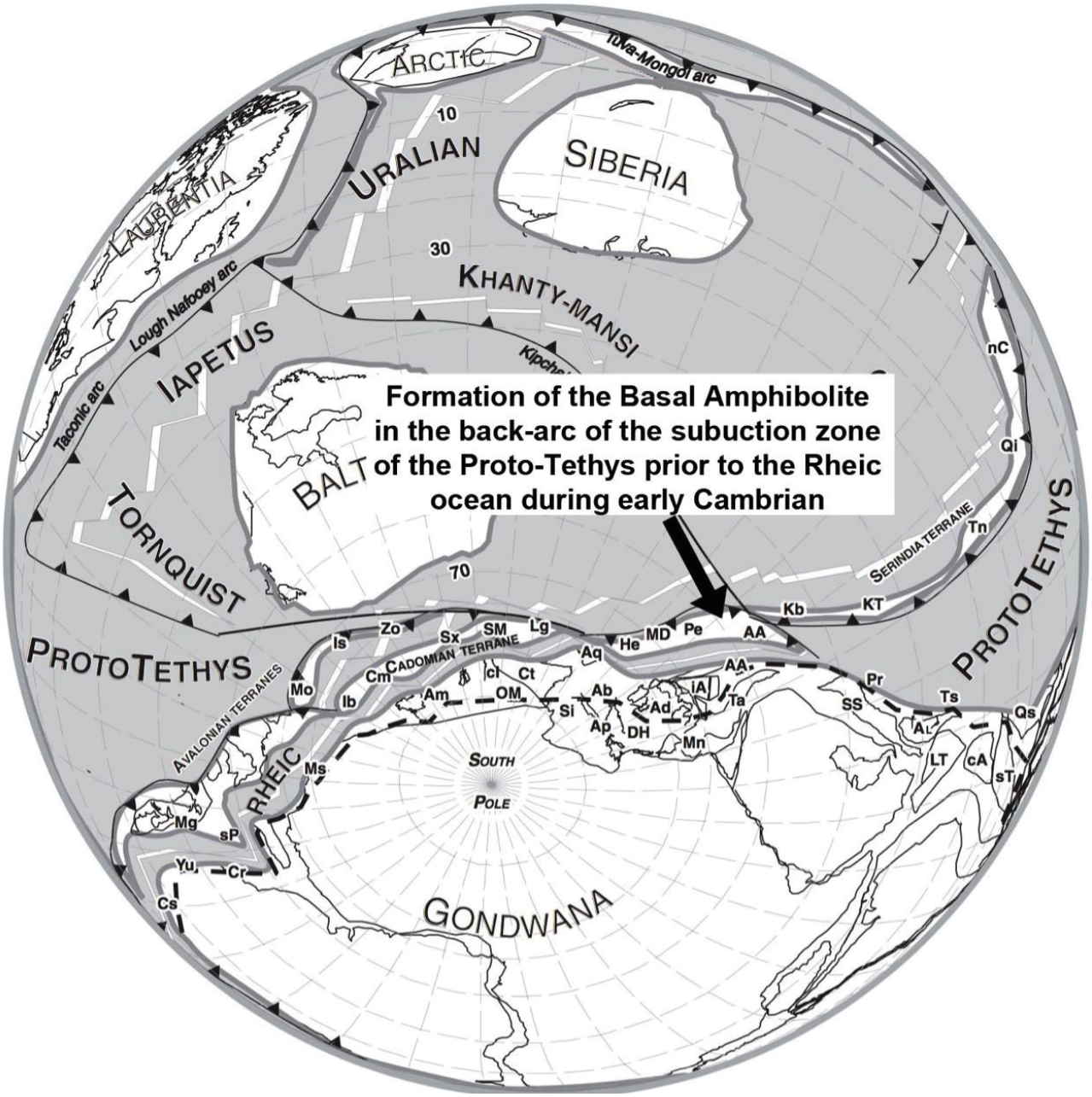

Figure 106: Reconstruction of pre-Variscian basement units around the Gondwana margin during early Ordivician (490 Ma). Postulated aborted Rheic ocean is not shown but was located very close to the indicated Rheic ocean. AA = Austro Alpine terrane. Modified after Stampfli et al. (2002b).

Stampfli et al. (2002a,b) present a palaeogeographic reconstruction of the pre-Variscan basement units (Figure 106) from Early Palaeozoic to Variscan times. Gondwana was surrounded by an active continental margin (Figure 106) (von Raumer et al. 2002). The Proto-Tethys and the Iapetus ocean separated Gondwana from Baltica (Stampfli et al. 2002b; von Raumer et al. 2002). The formation of an active continental margin starting at about 550 Ma (Stampfli et al. 2011) was related with back-arc spreading that detached several terranes from Gondwana. Several back-arcs started to form between the Neoproterozoic and Silurian until the Rheic ocean finally opened (Stampfli et al. 2002b; von Raumer et al. 2002). One of those aborted back-arcs is the proto-Rheic ocean (Stampfli et al. 2002b) that developed during Cambrian times in northwestern Iberia, in the Alpine basement units and the Bohemian Massif (see also Crowley et al. 2002; von Raumer et al. 2015). Rocks from the Basal Amphibolite and the LMS of the Habach Group could be part of this proposed arc and aborted back-arc system. The evolution of the proto-Rheic ocean ended around 500 Ma with a period of crustal

extension along the Gondwana margin with the emplacement of mafic to granitic rocks (Raumer et al. 2015). Von Raumer et al. (2013) suggested formation of the mafic rocks in the Alpine basement rather in an oceanic island arc than at an active Cordillera type continental margin.

The Rheic ocean started to open in the Early Ordovician and the Austroalpine terranes were finally detached from Gondwana when the Rheic ocean continued to open (460 Ma; Stampfli et al. 2011). The earlier formed arc rocks were then transported to the north (Stampfli et al. 2002a,b; von Raumer et al. 2002). Von Raumer et al. (2002) did not exclude the possibility that several separate terranes with back-arcs separated from Gondwana and moved to the north.

The Iapetus ocean and parts of the Proto-Tethys were closed due to the opening of the Rheic ocean during the Caledonian orogeny (collision between Gondwana-derived terranes and Laurentia-Baltica). Rocks from the volcanic arc and the back-arc were obstructed on the Austro-Alpine units during the Caledonian orogeny (probably during Llandovery; Stampfli et al. 2002a) and were metamorphosed (see Eichhorn et al. 2001; Neubauer 2002). Caledonian metamorphism is recorded in the Habach Complex (415-422 Ma; von Quadt et al. (1997) and the Basal Amphibolite (422-415 Ma; von Quadt et al. 1987, 1989, 1997).

The palaeogeographic model for the formation of the Basal Amphibolite (Figure 107) contains three major steps as described already. First, an active continental margin developed during Late Neoproterozoic at the northern Gondwana margin. Second, during Early Cambrian back-arc extension led to the formation of the mafic to intermediate rocks from Basal Amphibolite (Proto-Rheic ocean). Typical volcanic arc basalts (VAB) and “old” I-type granites (K2 orthogneisses) from the Habach Complex formed at the same time in the nearby arc. Third, the Rheic ocean finally opened during Early Ordovician and separated Avalonia containing Austro Alpine Basement rocks, the Basal Amphibolite and the Habach Complex from Gondwana. Avalonia got subsequently pushed northwards to Baltica subducting the Iapetus ocean southwards. Around 420 Ma the Caledonian orogeny accreted rocks from Avalonia to Baltica finally.

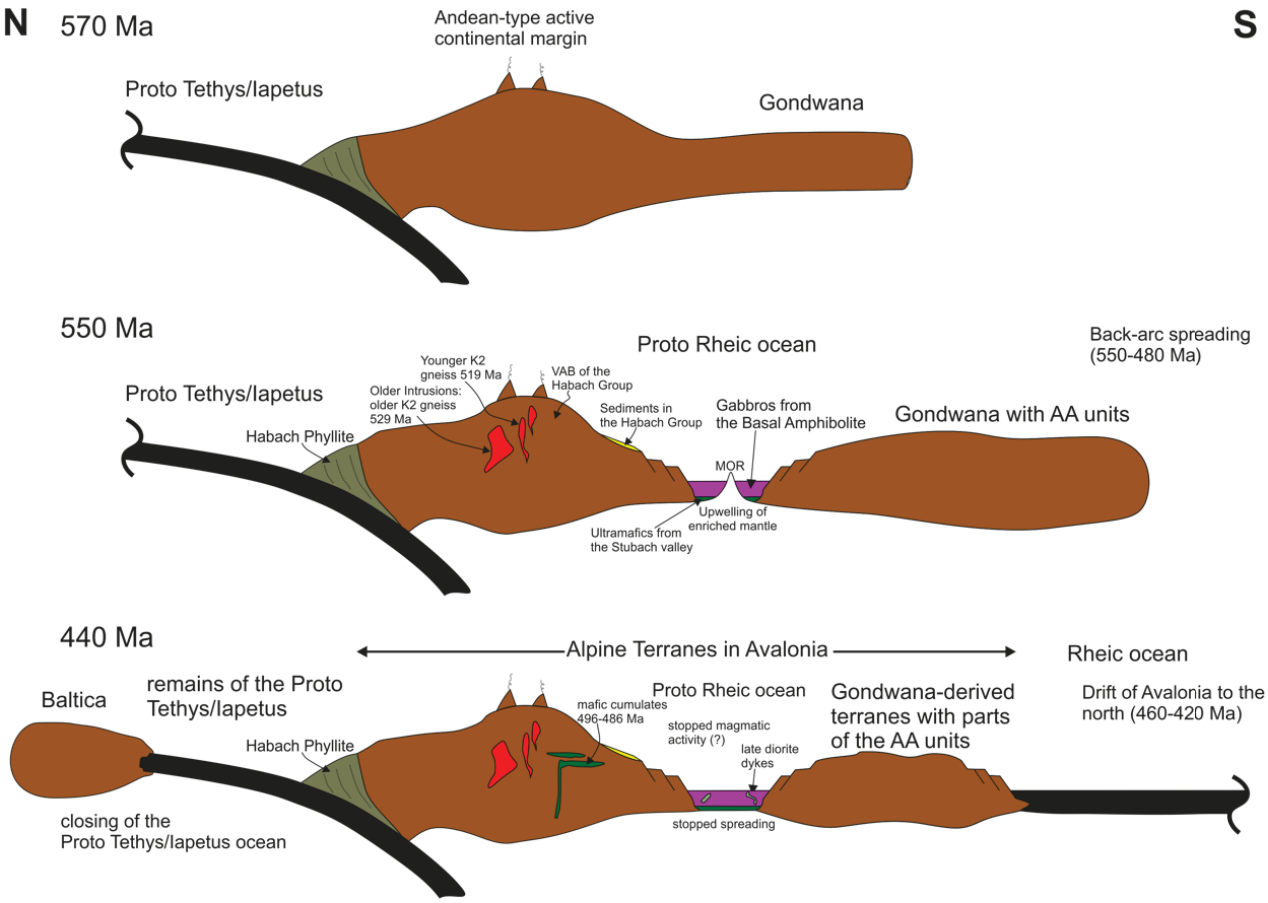

Figure 107: Model for geotectonic setting for the Basal Amphibolite and Habach Complex. Selected events are shown. AA = Austroalpine. Not to scale. Based on Frisch and Raab (1987), Vavra and Frisch (1989), Eichhorn et al. (1999, 2000, 2001), Neubauer (2002), Stampfli et al. (2002a,b), Raumer et al. (2002), Stampfli et al. (2011) and Raumer et al. (2013).

10.2. Mineral chemistry

10.2.1. Scheelite generations in calc-silicate rocks from Messelingscharte

Three scheelite generations are distinguished at Messelingscharte (Table 32) based on luminescence colours, micro-texture and MoO_3 contents (Figure 108; see Chapter 9.1). In comparison, four scheelite generations, commonly referred to as "stages" have been recorded from the Felbertal scheelite deposit (Höll and Eichhorn 2000).

Table 32: Comparison and tentative correlation of scheelite generations at Felbertal tungsten mine with those at Messelingscharte. Data and summary on scheelites from Felbertal are from Höll and Eichhorn (2000).

Felbertal mine				
	Stage 1	**Stage 2**	**Stage 3**	**Stage 4**
Lum. colour	slightly yellow	yellow	blue	pale blue
Grain size, shape, zoning	<0.4mm; fine oscillatory growth zoning	euhedral, mm-cm; rare broad oscillatory growth zoning	replacement, crack filling, overgrowths; recrystallisation textures	euhedral porphyroblasts; in Alpine quartz veins and joints
MoO_3	~1 mass%	0.1-1.7 mass%	100 ppm	2-500 ppm
Age	Variscan magmatic-hydrothermal, 335.5 ± 4.6 Ma[1]	Variscan magmatic-hydrothermal, ~335 Ma[2]	Variscan metamorphic 319 ± 34 Ma[3]	Alpine metamorphic 31 ± 4 Ma[4]
Messelingscharte				
	Generation 1		**Generation 2**	**Generation 3**
Luminescence colour	intensely yellow		blue	blue
Grain size, shape, zoning, Spatial relationship	fine- to very coarse grained, core often euhedral, core, coarse oscillatory zoning		fine- to coarse grained, re-placement rim, relict oscillatory zoning	fine- to medium grained, re-placement outer rim, crack filling, porphyro-blasts
MoO_3	1.18 mass%		0.30 mass%	<100-600 ppm
Age	Pre-Alpine, Variscan (?)		metamorphic Variscan (?), Permian (?), Alpine (?)	metamorphic Alpine

[1] Raith et al. (2011); [2]Kozlik et al. (2015); [3] Eichhorn et al. (1997); [4] Eichhorn et al. (1995)

The earlier scheelite generations are Mo-rich scheelite both at Messelingscharte and Felbertal (generation 1 Messelingscharte; stage 1&2 Felbertal mine). Scheelite 1 from Felbertal shows characteristic tightly spaced oscillatory zoning; scheelite 2 shows much coarser spaced zoning (details in Höll and Eichhorn 2000). Scheelite generation 1 from Messelingscharte contains between 0.8-1.7 mass% MoO_3 whereas scheelite 1&2 in the Felbertal deposit shows a lower bottom threshold (>0.1 mass%). The average Mo-content is, however, similar in both locations (~1 mass%). Generation 1 scheelite from Messelingscharte shows similarly spaced oscillatory zoning (Figure 108A-D) as well as Mo-content as stage 2 scheelite from Felbertal. The formation of stage 1&2 scheelite in Felbertal is interpreted to be coeval with emplacement of the K1-K3 orthogneiss at Felbertal (Raith and Stein 2006; Raith et al. 2011; Kozlik and Raith 2017).

At both localities Mo-rich scheelite is replaced/overgrown by blue luminescent Mo-poor scheelite. The inner scheelite rims (generation 2; Figure 108A,B) at Messelingscharte contain more MoO_3 (generation 2: 0.30 mass%) compared to Felbertal (Stage 3, ~100 ppm; Höll and Eichhorn 2000).

There are relicts of primary oscillatory growth zoning preserved in scheelite generation 2 from Messelingscharte, which could represent an intermediate stage between generation 1 and 2. Generation 2 formed by incomplete metamorphic (?) replacement or recrystallization. No evidence for primary growth zoning is known from stage 3 scheelite at Felbertal. Mo-poor scheelite 3 there has been interpreted as product a of Variscan regional metamorphism (e.g. Höll and Eichhorn 2000). The age of the (non-dated) Mo-bearing scheelite generation 2 at Messelingscharte is unknown. As at Felbertal it could also have formed during Variscan regional metamorphism but similarly during the Alpine metamorphic overprint.

Generation 3 scheelite from Messelingscharte has the lowest MoO_3-contents (<100-600 ppm). It forms the outermost rims of scheelite grains, occurs along micro-fractures in earlier scheelite 1 and 2 (Figure 108A,B,E) as well as in cracks together with clinozoisite-quartz and as medium-grained recrystallized scheelite in the metamorphic calc-silicate matrix (Figure 108F). Stage 4 scheelite in Felbertal mine occurs as individual porphyroblasts in young Alpine veins and joints containing 2-500 ppm MoO_3 (Höll and Eichhorn 2000). Generation 3 from Messelingscharte has similar re-crystallization textures and Mo-content than scheelite 3 from Felbertal but doesn't occur as individual porphyroblasts in Alpine joints and quartz veins like scheelite 4.

Generation 2 scheelite from Messelingscharte could represent the (peak) Alpine metamorphism whereas generation 3 scheelite could be formed during retrograde recrystallization (brittle deformation indicated by cracks Figure 108A).

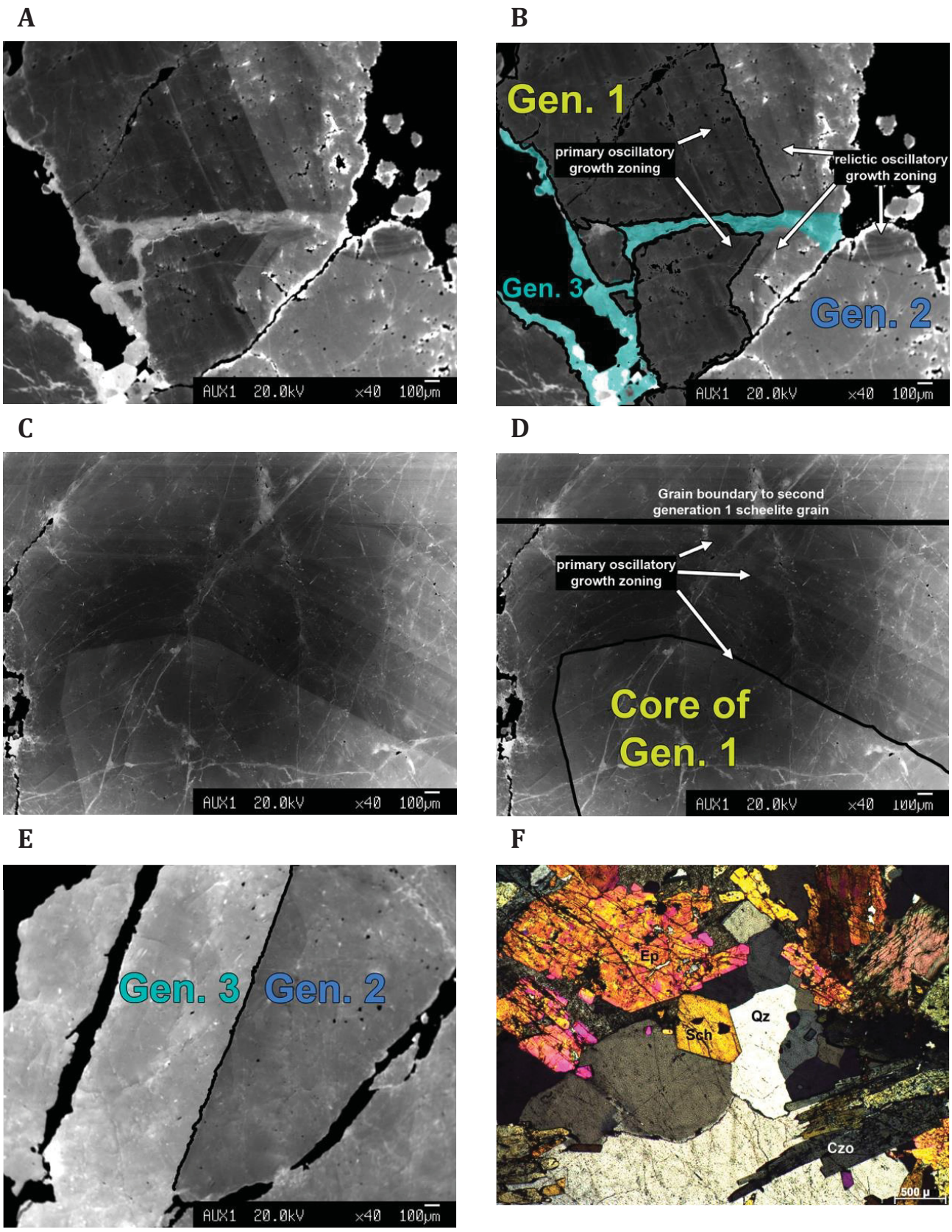

Figure 108: A,B Scheelite generations 1 (dark CL), 2 (bright CL) and 3 (artificially coloured in cyan, A unmodified picture) (sample 03-17'). **C,D** Large core of generation 1 with distinct oscillatory growth zoning. Two generation 1 scheelite grains in contact (unmodified picture C). **E** Gen. 2 and 3 in contact. Gen. 3 builds the outermost rim. **F** Euhedral recrystallized scheelite assigned to gen. 3. A-C Cathodoluminescence (CL) images, D Microphotograph, crossed polars.

10.2.2. Sn-bearing clinozoisite from Messelingscharte

Clinozoisite from Messelingscharte incorporates high amounts of Sn^{4+}, Ti^{4+} and Fe^{2+} in its crystal lattice. Epidote/clinozoisite is a common sorosilicate composed of cations (M1-3) arranged in endless chains of octahedra parallel b that are crosslinked by isolated SiO_4 tetrahedra and Si_2O_7 groups (Frei et al. 2004). The M1-2 position is taken by Al^{3+} whereas the tetragonal distorted M3 positions hosts normally Fe^{3+}. Spaces between cross-linked octahedral chains host non-equivalent A1 and A2 polyhedral sites normally occupied by Ca and suitable for substitution (e.g. REE^{3+}, Mg^{2+}, Mn^{2+}) (Frei et al. 2004).

Assuming that the total amount of Sn+Ti does not exceed 1 apfu (=31.94 mass% SnO_2) at M3 position and that Mg^{2+} and Mn^{2+} are not substituting Ca^{2+}, the formula of clinozoisite can be expressed as (modified from van Marcke de Lummen 1986):

$$Ca_2Al_2(Sn^{4+},Ti^{4+})_x(Fe^{2+},Mg^{2+},Mn^{2+})_x(Fe^{3+},Al^{3+})_{1-2x}Si_3O_{12}(OH,F)$$

As pointed out, two generations of clinozoisite can be distinguished at Messelingscharte (see Chapter 6.6.1 and 9.2.1). The first generation (Sn-rich) represents the "primary" assemblage of the calc-silicate rocks. The second generation formed during a metamorphic overprint of unknown age (Variscan and/or Alpine?). Metamorphism of pre-existing clinozoisite explains the recrystallization textures and neo-formation of metamorphic generation 2 clinozoisite (see also Figure 113). It is notable that, metamorphism dispersed Sn resulting in lower Sn content of the metamorphic clinozoisite.

In the literature only four occurrences of Sn-bearing epidote/clinozoisite are described so far (Table 33). Sn-bearing epidote/ clinozoisite can be present in skarn deposits (Eadington and Kinealy 1983) and in calc-silicate veins associated with magmatic-hydrothermal activity (Alderton and Jackson 1978). Other Sn-bearing minerals in skarns are garnet, amphibole, malayaite, cassiterite, and rarely sulphides (Eadington and Kinealy 1983).

Table 33: Reported occurrences and maximum SnO_2 contents of Sn-bearing epidote/clinozoisite. This work presents the highest SnO_2 value in these minerals so far reported in the literature. Concentrations of SnO_2 (mass%) of other associated minerals are given in brackets.

Locality	Occurrence	Assemblage	Max SnO_2 (mass%) of ep/czo	Reference
Messelingscharte, Tauern Window, Austria	skarn (?), calc-silicate fels	Czo (3.00), Ttn (6.48), Chl, Qz, Amp, Clc, Sch	3.00	this work
Baja California, Mexico	hydrothermal vein	?	0.38	Myer (1965)
Cassiar district northern Britisch Columbia	massive skarn	Ep (0.8), Cpx, Amp, And (0.9), Qz, Clc	0.8	Mulligan and Jambor (1986)
Chycornish Carn Botallack, Cornwall, England	vein	Axianite, Amp (0.1), Tur	0.16	Alderton & Jackson (1978)
The Crowns, Botallack, Cornwall, England	massive skarn	Ep (2.84), Amp (0.7), Cas, Ttn (7.0), Chl, Mal	2.84	van Marcke de Lummen (1986)

Mulligan and Jambor (1986) describe Fe-rich calc-silicate minerals (andradite, epidote, ferroactinolite, hedenbergite) in an unusual skarn in the Cassiar district (northern British Columbia). The skarn is Sn-

rich but more common Sn minerals like cassiterite, malayaite or stannite are lacking. Tin is incorporated in epidote and Ca-garnet (Table 34).

Alderton and Jackson (1978) studied discordant calc-silicate veins in metabasalts in the St. Just aureole, Cornwall. Calc-silicate veins are composed of the prograde assemblage of garnet, diopside, magnetite, amphibole overprinted by a retrograde assemblage of epidote, sphene, chlorite and calcite. Garnet, epidote and amphibole host minor amounts of Sn (Table 34). The veins are associated with coarse-grained, green amphibole that formed as alteration product of the host rock. These calc-silicate veins formed by metasomatic reaction of hydrothermal fluids derived from the underlying granite body with the mafic host rock. They display strongly elevated concentrations of Ca, Sn, Be, Zn and B compared to the host rock.

Van Marcke de Lummen (1986) studied Sn-bearing epidote ($Al/Fe^{3+} \sim 2.6$) from a skarn at The Crowns, Botallack, Cornwall occurring in the aureole of the Land's End granite (Table 34). Epidote is associated with cassiterite, malayaite, titanite and ferroan pargasitic amphibole. Sn-bearing epidote occurs in a dark brown calc-silicate rock with cassiterite, malayaite, Sn-bearing titanite and Sn-free chlorite. Epidote, chlorite and amphibole are considered to have formed during the retrograde stage of skarn formation.

Table 34: SnO_2 concentrations (mass%) and proposed substitution mechanisms for Sn in silicates from Cassiar district, northern British Columbia; St. Just aureole, Cornwall (Alderton and Jackson 1978); Land's End aureole, Cornwall (von Marcke de Lummen 1986). Substitution mechanism for amphiboles from Cameron and Papike (1979).

	Cassiar district, BC, Can.[1]	**Chycornish Carn Botallack, Cornwall, England[2]**	**Land's End granite, Cornwall, England[3]**	
Mineral	**SnO_2 (mass%)**	**SnO_2 (mass%)**	**SnO_2 (mass%)**	**Substitution mechanism**
Andradite	0.9	0.2	-	$2Fe^{3+} \Leftrightarrow Sn^{4+} + Fe^{2+}$
Epidote/ clinozoisite	0.8	0.12	2.84	$2(Al,Fe)^{3+} \Leftrightarrow Sn^{4+} + Fe^{2+}$
Amphibole	0.27	0.09	0.7	$2Al^{3+} + Sn^{4+} \Leftrightarrow 2Si^{4+} + Mg^{2+}$

[1]Mulligan and Jambor (1986); [2]Alterton and Jackson (1978); [3]van Marcke de Lummen (1986)

Clinozoisite from Messelingscharte incorporates a maximum Sn-content of 3.00 mass% SnO_2 (=0.094 apfu) which is the highest value ever recorded in literature to the knowledge of the author. At the other localities where Sn-rich epidote/clinozoisite occurs (Table 33) scheelite has not been reported, in contrast to Messelingscharte. Moreover, Sn-rich epidote/clinozoisite is commonly associated with Sn-rich titanite, amphibole or Ca-garnet (e.g. St. Just aureole Cornwall, Alderton and Jackson 1978) but less common with cassiterite (e.g. Cassiar district BC, Mulligan and Jambor 1986). At Messelingscharte, Sn-rich titanite is associated with Sn-bearing clinozoisite. Minute inclusions of cassiterite were observed in Sn-rich titanite (see Chapter 9.3). At Messelingscharte typical high-temperature skarn minerals like Ca-garnet and calcic pyroxene are absent.

Summing up, clinozoisite from Messelingscharte is comparable regarding mineral composition and Sn contents to other occurrences from where Sn-rich epidote/clinozoisite has been reported. There are, however, differences in the mineral assemblage. Aspects of possible differences in the genesis will be addressed in Chapter 10.4.

10.2.3. Sn-bearing titanite from Messelingscharte

Bulk geochemistry revealed that Ti is depleted in calc-silicate rocks compared to the amphibolite host rock (see Chapter 8.1.5). This is explained with chemical changes caused by fluid infiltration during formation of the calc-silicates. Patchy irregular zoning of titanite reflecting heterogeneous distribution of Ti, Sn, Al and Fe could be caused by changing activity of these elements in the fluid during primary growth or subsequent metamorphism. The source of Ti, which behaved mobile during calc-silicate formation (see Chapter 10.4.1) are Ti minerals (rutile) in the amphibolites.

Titanite from Messelingscharte is low-Al titanite and host significant amounts of Sn. Low-aluminium titanite (typical 2-3 mass% Al_2O_3; 2.5-4.3 mass% Al_2O_3 at Messelingscharte) is common for low-to medium P metamorphic conditions (e.g. regional metamorphism) (Oberti et al. 1991).

Franz and Spear (1985) describe chemically different titanite in the different tectonic units of the Tauern Window. Titanite from "Untere Schieferhülle" (Basal Amphibole, Basal Schist, "Glimmerschieferlamelle") is low-Al titanite (x(Al)=0.072-0.118). Most titanite from the eclogite zone is high-Al titanite with high F-contents (0.76-5.46 mass%). Comparison of the Lower Schist Cover data set with titanite from Messelingscharte shows that the x(Al) and x(F) values of titanite are much higher at Messelingscharte. Moreover, there was no Sn analysed in titanite by Franz and Spear (1985). The different chemical composition results in a different formation process. It is not likely that titanite from Messelingscharte is altered primary titanite from the host rock. They were newly formed in-situ during calc-silicate formation.

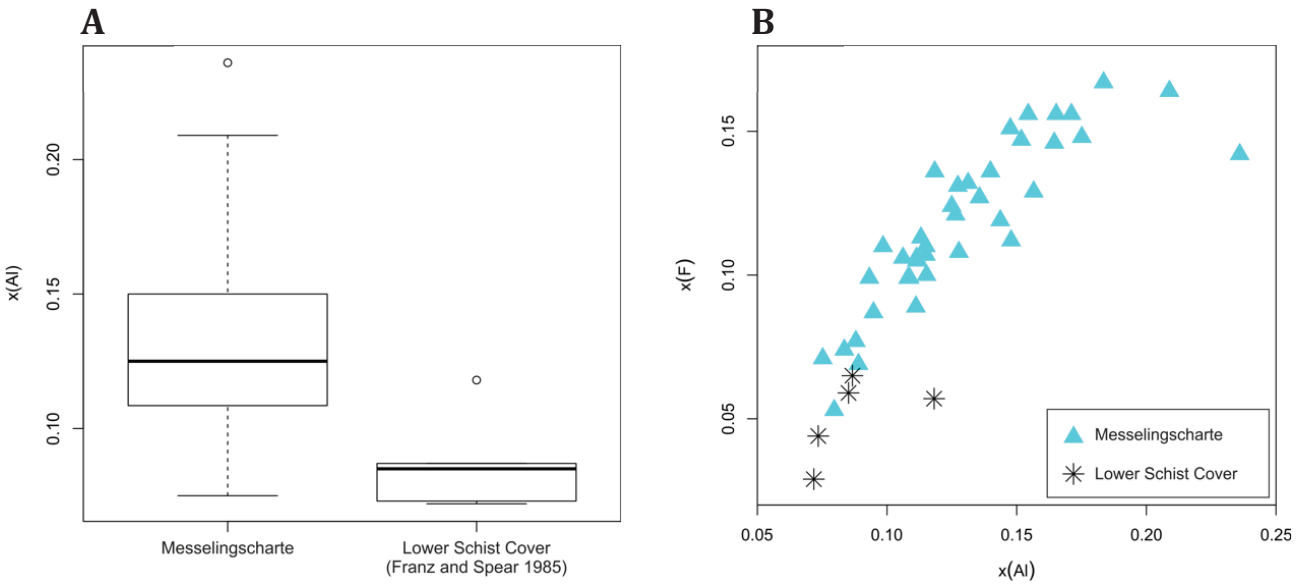

Figure 109: A x(Al) of titanite from Messelingscharte and Lower Schist Cover from Franz and Spear (1985). **B** x(Al) vs. x(F) (x(F) = F/(O+OH+F) in apfu) of titanite from Messelingscharte and Lower Schist Cover from Franz and Spear (1985).

Sn-bearing, F-rich titanite has been reported from different types of ore deposits but are most common in Sn-bearing skarns (Table 35).

Table 35: Selected occurrences of Sn-bearing titanite.

Locality	Occurrence	Paragenesis (max SnO_2 content, mass%)	Max SnO_2 of titanite (mass%)	Reference
Messelingscharte, Tauern Window, Austria	skarn (?)	Czo (3.0), Amp, Sch, Clc, Ttn (6.48)	6.48	this work
The Crowns, Botallack, Cornwall, England	skarn	Czo (2.84), Amp (0.7), Cas, Ttn (7.0), Chl, Mal	7.0	van Marcke de Lummen (1986)
Several skarn deposits in Yukon and Britisch Columbia, Canada	skarn	Cpx, Grt, Sch, Qz, Clc, Ttn (1.0),	1.0	Che et al. (2013)
El Hammam, Marocco	skarn	Cpx, Wollastonite, Gro (0.2), And (5.6), Dio, Hed, Mal, Sch	>50% (malayaite)	Sonnet and Verkaeren (1989)
Bol'shoi Kan'on, Russia	skarn	Cpx (0.1), Vesuvianite, Gar (1.4), Axinite (0.31), Ttn (8.85), Mal (>44.81)	8.85; malayaite (>44.81%)	Aleksandrov and Troneva (2007)
Pisek, Czech Republic	skarn	Cpx, Grt, Phl, Clc, Ep/Czo, Sch	0.41	Cempírek et al. (2009)
Doradilla, New South Wales, Australia	skarn	Gro (3.5), Cpx (0.11), Mal, Ttn, Clc	>50% (malayaite)	Plimer (1984)
Qitianling granite, greisen-type Sn-deposit, Hunan Province, southern China	magmatic	Ttn, Bt	1.12	Xie et al. (2008)
Cu-Ni-PGE deposit, North Range Footwall Environment, Sudbury, Canada	magmatic, hydrothermal	PGM, Cas, Mal, Mag	?	Kjarsgaard and Ames (2010)

The Sn content of titanite from Messelingscharte (<6.48 mass% SnO_2; <0.89 apfu) is comparable with other skarn known deposits (Table 35). Che et al. (2013) investigated magmatic, hydrothermal and skarn titanite in Yukon and British Columbia, Canada. They concluded that the major and trace element budget of ttn from skarns varies greatly. Generally, Che et al. (2013) report combined higher Sn concentrations in bulk chemical data and in titanite for scheelite-hosting skarns. Their magmatic as well as hydrothermal titanite has a very different chemical composition as well as internal zonation compared to titanite from Messelingscharte. Titanite from skarns investigated by Che et al. (2013) are not so high in Sn (≤1.00 mass%) but in Al (≤9.82 mass%) and F (≤3.72 mass%). They have bright cores and a thin dark rims in BSE images or show intense oscillatory growth zoning (Figure 110B), i.e. very different to titanite from Messelingscharte.

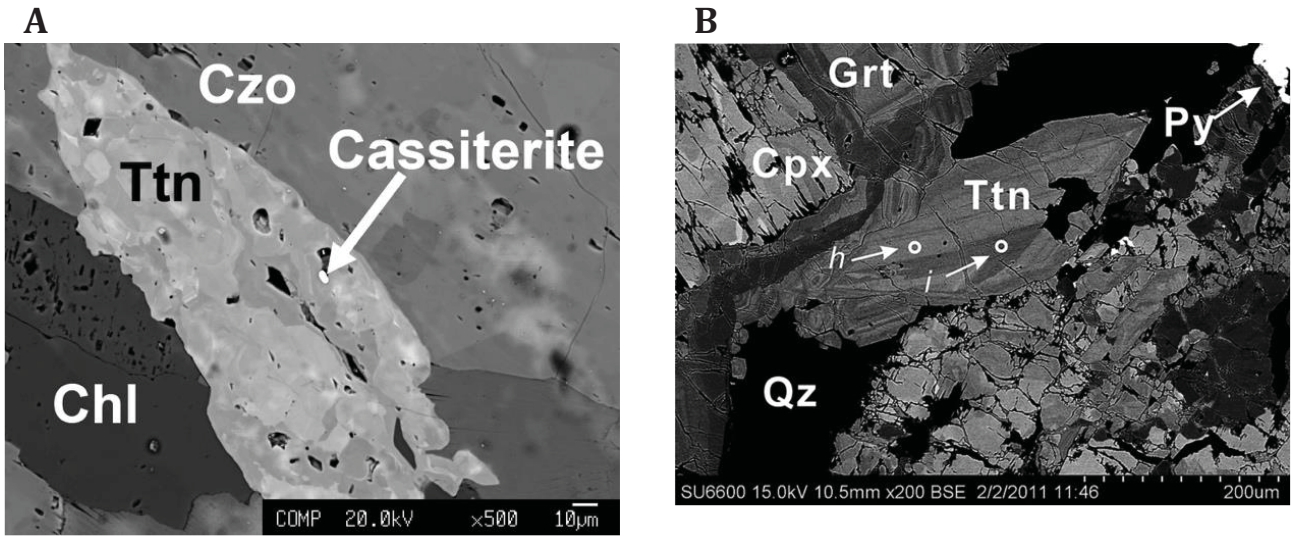

Figure 110: Titanite from calc-silicate rocks. **A** Patchy zoned subhedral titanite with miniscule cassiterite inclusions from Messelingscharte. **B** Oscillatory zoned titanite in scheelite skarn from the Max deposit British Columbia (Canada) (in Che et al. 2013).

Another Sn-rich titanite-bearing skarn was investigated by Cempírek et al. (2008) (hedenbergite skarn in Pisek, Czech Republic). Titanite displays a patchy zoning (Figure 111) similar to titanite from Messelingscharte. A major difference is the lack of Nb and Ta. This example shows that patchy zoned titanite does occur in skarn deposits. Cempírek et al. (2008) also noticed that $Sn^{4+} \Leftrightarrow Ti^{4+}$ substitution corresponds negatively with Al+F and Al+Nb because of incompatible structure (see Chapter 9.3; Figure 100).

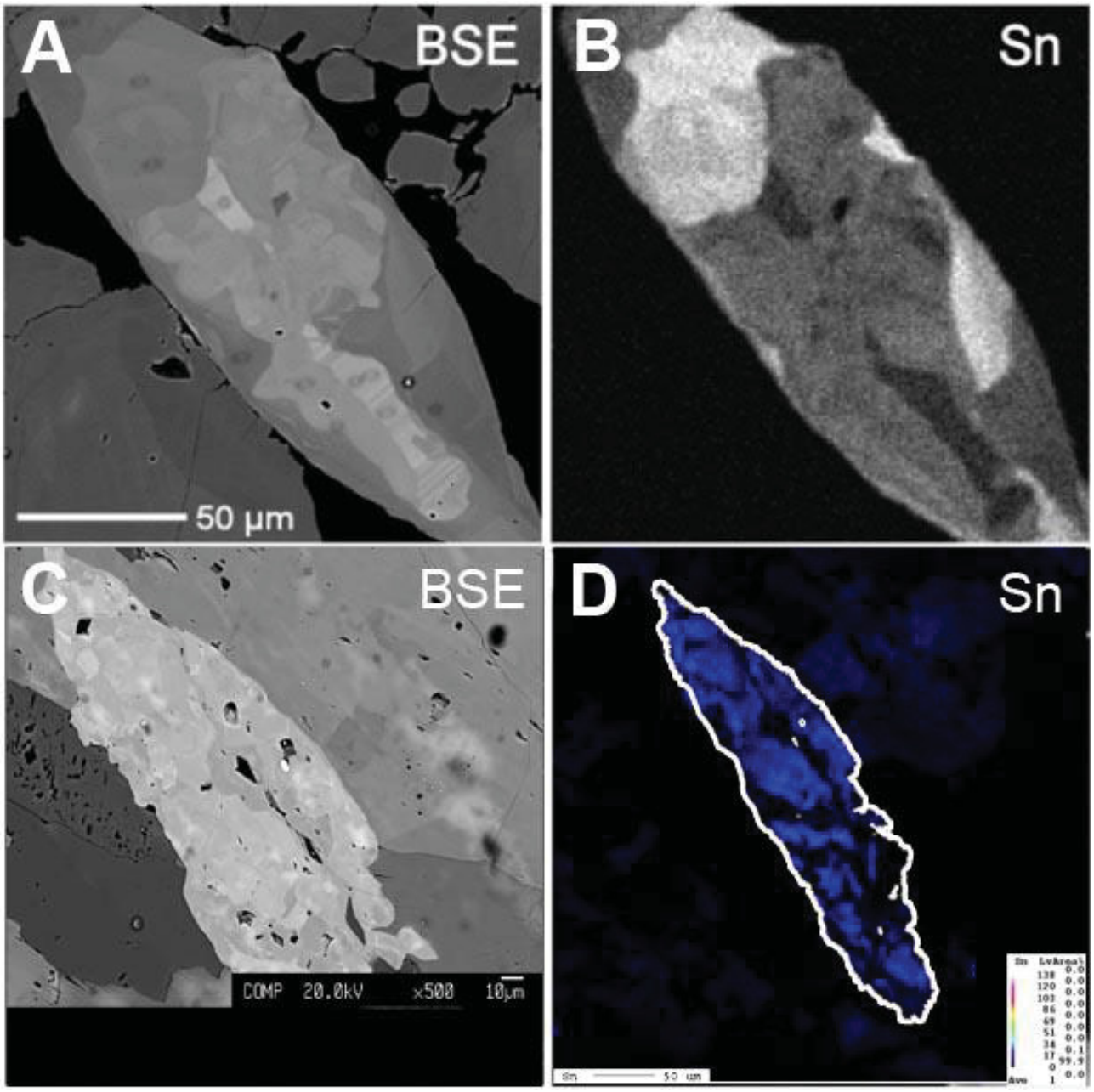

Figure 111: BSE image of titanite and distribution of Sn in zoned titanite crystal from Pisek hedenbergite skarn, Czech Republic (**A,B**) and Messelingscharte (**C,D**). Zoning has a very similar shape and is governed partly by Sn content.

Kozlik (2016) presented data of titanite from Felbertal tungsten deposit. Titanite from Felbertal forms euhedral sphenoidal crystals showing oscillatory zoning or anhedral grains with irregular patchy zoning. Oscillatory zoned titanite occurs in mineralised orthogneisses from the Felbertal deposit and in barren Central Gneisses. Titanite from Felbertal is characterised by higher concentrations of Nb, Fe and REEY. Primary magmatic titanite is high in REE but low in F and Al (low-Al titanite). The secondary patchy titanite, interpreted to be of hydrothermal origin, is high in F, Nb and Fe but low in REE (high-Al titanite).

Table 36: Comparison of titanite from Messelingscharte (this study), the Felbertal Augengneiss and the K1-K3 orthogneiss at Felbertal tungsten deposit (data from Kozlik 2016).

	Messelingscharte	**Felbertal tungsten deposit**		
Characteristics	Scheelte-bearing calc-silicate rocks	Felbertauern augengneiss	Dark K1-K3 gneiss	Bright K1-K3 gneiss
Crystal shape	anhedral, euhedral	anhedral, subhedral, anhedral		
Grain size	<1mm	<1mm		
Zoning	irregular patchy	oscillatory, chaotic to irregular patchy		
Selected elements (mass%)				
Nb_2O_5	bdl	0.68-1.62	bdl-2.02	0.26-2.01
Fe_2O_3	0.29-1.83	0.35-2.91	bdl-3.6	bdl-2.93
Al_2O_3	2.09-6.77	2.04-7.01	1.54-9.55	1.78-9.43
$REEY_2O_3$	bdl	1.26-5.13	0.34-4.26	0-5.25
F	0.49-1.57	0.07-0.64	0.12-1.19	0.13-3.65
SnO_2	0.07-6.48	na[1]	na[1]	na[1]

[1]na = not analysed;

Titanite from the K1–K3 orthogneiss at Felbertal tungsten deposit and from Messelingscharte differs in some aspects (Table 36). The grain shape and grain size are similar but the oscillatory zoning typical for magmatic titanite is not seen in titanite from Messelingscharte. However, irregular to chaotic patchy zoned titanite occurs at both localities. Changing REEY, Nb and Fe/Al contents are responsible for the chaotic patchy zoning at Felbertal (Kozlik 2016) whereas Sn predominantly controls zoning of titanite from Messelingscharte. Nb, Ta and REEY are generally bdl in titanite from Messelingscharte but can reach higher concentrations in the Felbertal deposit (Table 36). Hydrothermal alteration during Sn-W skarn formation could be responsible for removal of REE from titanite (Deng et al. 2015).

The lack of Nb in titanite at Messelingscharte indicates that in contrast to Felbertal this element was not enriched with W during the mineralisation process. This is supported by the low Nb and Ta concentrations in the bulk analyses of calc-silicate rocks and depletion of these elements relative to the host amphibolites (see Chapter 8.1.5). Tin was most likely brought in together with W by the mineralising fluids during calc-silicate formation because of the very low concentrations of Sn in the amphibolite host rock.

10.3. Origin of calc-silicate rocks at Messelingscharte

Calc-silicate rocks may form in different geologic environments showing various host rocks and formation processes. Generally speaking, calc-silicate formation can be subdivided in two major categories: isochemical, allochemical formation.

10.3.1. Isochemical calc-silicate formation

Isochemical metamorphism can derive calc-silicate minerals through reaction of silicates and carbonates. First, mineral reactions in an **impure carbonate rock** – mixtures of carbonate and detrital quartz ± clay minerals - occur regularly from lower greenschist to granulite facies (Winter 2001). Decarbonatisation (± combined with dehydration) reactions are important in SiO_2-bearing limestone/dolostones and results in the liberation of CO_2 ($\pm H_2O$) during prograde metamorphism. The simplest reaction takes place between quartz and calcite in siliceous limestone resulting in the formation of wollastonite and the release of CO_2 ($CaCO_3 + SiO_2 \Leftrightarrow CaSiO_3 + CO_2$). Reactions of dolomite with quartz in siliceous dolostones result in formation of assemblages with talc, tremolite, diopside and olivine. If Al_2O_3 is also available in the protoliths Al-rich Ca-silicates such as grossular-rich garnet or clinozoisite may form. Commonly regionally metamorphosed SiO_2-bearing limestones show a characteristic zoning of isograds on the regional scale (e.g., Lepontine Alps, Italy, Switzerland; Trommsdorff 1966).

Second, calc-silicate rocks can also form at the **contacts between shales and limestones** during metamorphism due to local fluid-rock interaction or differences in the chemical potential of elements in the different lithologies. Common minerals are Ca-rich garnet, diopside, clinozoisite and amphibole. Calc-silicate rocks are mostly sharply zoned defined by different mineral assemblages (e.g. Thompson 1975).

Third, Formation of calc-silicate minerals can be triggered by **high heat flux** from a proximal intrusion. Contact metamorphism creates different calc-silicate zones for different temperatures (Eskola 1922; Bowen 1940; Tilley 1951). Zonation is characterised by a stepwise decarbonatisation governed by temperature gradient (e.g. Joesten 1974).

10.3.2. Allochemical calc-silicate formation

Calc-silicate rocks can form by fluids removing and/or introducing elements. There are several different types of calc-silicate rocks known.

Stratiform scheelite-bearing calc-silicate rocks are known from regionally-metamorphosed complexes (Austroalpine Crystalline Complex, Raith 1991; pre-Cambrian units in Australia USA, Variscan rocks in Europe, Plimer 1987; Bindal Area, Norway, Skaarup 1974) and are commonly associated with tourmalinites. Fluids were probably involved in forming stratiform scheelite-bearing calc-silicate rocks. Generally, they are unrelated to the coincidental intrusion of granite plutons and dykes (e.g. pegmatite) (Plimer 1987). Host rocks are mainly metavolcanics (e.g. Paraiba, Brazil), metaclastic rocks (e.g. Australpine Crystalline Complex). Plimer (1987) points out a spatial connection of exhalative rocks (iron formations, Pb-Zn sulphide beds) to scheelite-bearing rocks. Therefore, also stratiform scheelite-bearing calc-silicate rocks are interpreted to be metamorphosed exhalative W-rich beds (Plimer 1987; Raith 1991).

Rodingites are metamorphic calc-silicate rocks associated with ultramafic rocks. They form during metamorphism of ophiolites incorporated in orogenies (e.g. East Liguria, Barriga and Fyfe 1983; Dorfertal, Penninic Unit (Tauern Window), Dietrich et al. 1986; Habachtal, Habach Complex (Tauern Window), Koller and Richter 1984) or in the contact aureoles of intrusions (Frost 1975). They consist of garnet, clinopyroxene, tremolite, titanite, epidote, chlorite, calcite and varying amounts of vesuvian, talc and prehnite/pumpellyite. Rodingites are characterised by strong Ca-input and intense removal of alkalis and moderate changing Si, Fe and Mg (Dietrich et al. 1986; see also Thompson 1975). Immobile race elements resemble more or less the composition of the original host rock (Koller and Richter 1983; Dietrich et al. 1986). Rodingites commonly show a zonation and occur next to metasomatic blackwall zoning. Rodingites build concordant irregular layers, vein-like structures or pods.

Metamorphic calc-silicate segregations can form in mafic rocks during (high-pressure) metamorphism. Brunsmann et al. (2000) investigated zoisite-clinozoisite segregations in the amphibolites of the Lower Schist Cover close to the Eclogite Zone in the southern Tauern Window. They interpreted these rocks as remnants of a Hercynian high-pressure event.

Magmatic skarns (US: tactites) are calc-silicate rocks formed by metamsomatic interactions between carbonates and SiO_2-rich rocks or fluids. Commonly they are spatially connected to granites but can also form along faults and major shear zones (Meinert 1992, 1993; Meinert et al. 2005). To avoid confusion, the term “skarn” is used in this work exclusively for calc-silicate rocks associated spatially and temporally with igneous activity. Commonly the first step of skarn formation is high temperature metamorphism producing a prograde assemblage (Cpx, Grt, Amp). Retrograde assemblage forms during cooling of the pluton and infiltration of cooler oxygenated meteoric waters and commonly consists of epidote/clinozoisite, chlorite, amphibolite and calcite (Meinert 1992). Ore precipitation occurs in a complex polyphase process involving mixing meteoric and magmatic fluids. Several different types of skarns can be distinguished:

Endoskarn: Endoskarns are located in the igneous mass itself forming usually a narrow rim immediate around the intrusive contact. Diagnostic is the assemblage pyroxene + plagioclase in reduced in W-Mo-Cu-skarns or epidote + quartz + garnet in oxidised W-Sn-F skarns (Kwak and White 1982; Einaudi und Burt 1982).

Exoskarn: Exoskarns form outside of the intrusions altering and replacing the wall rock. Exoskarns are generally zoned and incorporate majority of worldwide skarn deposits.

Distal skarn: Distal skarns form relatively large distances away from the granitic pluton (300-1000 m) in the outer aureole of the granite body (Kwak 1987). They are known for hosting large Sn ore bodies (e.g. Gejiu, Dachang, P.R. China; Kwak 1987). Typical high-T skarn minerals like clinopyroxene and garnet are missing (Kwak 1987).

Calcic/magnesian-skarn: Calcic-skarn refers to the dominant composition of the protolith (calcite-dominated carbonate rock). Magnesian-skarns are formed out of a Mg-rich dolostone. They host minerals like humite, periclase, talc, serpentine and brucite that are normally not present in calcic-skarns (Meinert 1992).

Skarns can host several different commodities depending on the composition, emplacement depth and redox potential of the skarn-producing pluton. Meinert et al. (2005) distinguishes seven skarn types based on commodity (Fe, Au, Cu, Zn, W, Mo and Sn). Tungsten skarns are generally associated with

calc-alkalic plutons located in major orogenic belts (Meinert 1992; Meinert et al. 2005). Main minerals of the prograde assemblage are hedenbergitic pyroxene, grandite garnet with scheelite; later garnets are subcalcic (spassartine- and almandine-rich) (Meinert et al. 2005).

10.3.3. Comparison of calc-silicate rocks from Messelingscharte to common types of calc-silicate rocks

Calc-silicate rocks from Messelingscharte show no indication of replacement of marble or reaction between metapelites and marble. Moreover, they are neither continuously stratiform nor associated with tourmaline which excludes an exhalative (?) origin of tungsten. There are small deformed patches of ultramafic rocks present in the Basal Amphibolite at Messelingscharte. Ultramafic hornblende fels builds unaltered strongly deformed small irregular vein-like structures; though, blackwall zoning and the typical mineral assemblage of garnet + clinopyroxene are absent excluding rodingites. Moreover, there is no contact aureole present like described in Frost (1975) making a heat flux induced calc-silicate formation doubtful.

Brunsmann et al. (2000) describes calc-silicate segregations from the Basal Amphibolite that share several similarities to calc-silicate rocks from Messelingscharte like mineral assemblage and host rock. Figure 112 shows spider plots of zoisite/clinozoisite (zo/czo) segregations (Brunsmann et al. 2000) compared to calc-silicate rocks from Messelingscharte and Felbertal tungsten mine. The trace element patterns of zo/czo segregations differ strongly from Felbertal mine but share similarities with those from Messelingscharte. They are similar regarding Sr, La, Ce, Nb, Nd and Eu. Major differences are, however, the much lower alkalis, P_2O_5 and Yb contents. The REE spider plot shows striking differences (Figure 112B). The zo/czo-segregations are enriched in LREE and strongly depleted in HREE defining an almost linear trend with a negative slope. Rocks from Messelingscharte as well as Felbertal tungsten mine rather show a flat to even increasing trend towards HREE. Moreover, zo/czo segregations show only a weak Eu-anomaly whereas rocks from Messelingscharte have a pronounced positive Eu-anomaly.

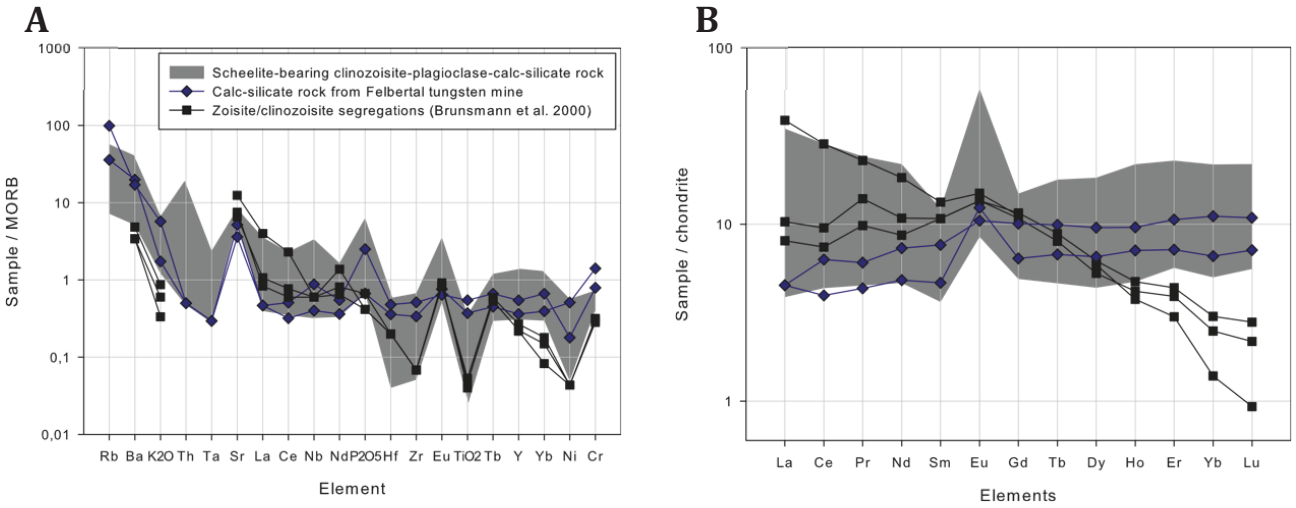

Figure 112: Trace elements (**A**) and REE (**B**) patterns of clinozoisite rich calc-silicate rocks from Messelingscharte, Felbertal tungsten mine and the southern Tauern Window (data for the latter from Brunsmann et al. 2000).

The geological occurrence, mineral assemblages and chemical data (e.g. REE patterns), clearly indicate a different origin of zo/czo segregations from the southern Tauern Window and the calc-silicate rocks

from Messelingscharte. The geometry of the segregations is vein-like with a vague, linear internal fabric compared to the more irregular, pod-like shape of the calc-silicate body at Messelingscharte. Another important difference is that zo/czo segregations are not associated with W-Sn mineralization; they lack scheelite, Sn-rich titanite and Sn-rich clinozoisite.

The only remaining calc-silicate forming process is a skarn produced by magmatic hydrothermal fluids. All other possibilities have to be excluded. The following, skarn formation will be discussed in more detail.

10.4. Messelingscharte: a skarn occurrence?

The most plausible mechanism for formation of scheelite-bearing calc-silicate rocks at Messelingscharte is the involvement of magmatic hydrothermal fluids similar to what is found in (distal?) skarn deposits.

The regional setting of Messelingscharte could be suitable for skarn occurrences. The world-class W-deposit Felbertal is located in the vicinity from Messelingscharte in the nearby Felbertal valley. The Felbertauern augengneiss is involved in the ore forming process and crops out closely to Messelingscharte to the west. Messelingscharte is hosted in amphibolites like the Felbertal deposit indicating suitable conditions for emplacement of W-rich rocks in amphibolite.

There is no obvious spatial relationship to any highly fractionated orthogneiss. The Basal Amphibolite is located in the periphery of the large Granatspitz gneiss intrusion which is also present as tectonic slice in the Basal Schist in the hanging wall of the Basal Amphibolite. However, studies by Kozlik (2016) and Kozlik and Raith (2017) proofed that the Granatspitz gneiss doesn't have suitable geochemical characteristics accounting for a W-mineralization like Felbertal (or Messelingscharte). Several studies in Felbertal deposit revealed a genetic link between the ore forming process and highly fractionated K1-K3 orthogneisses (e.g. Briegleb 1987; Pestal 1983; Raith and Stein 2006; Kozlik 2016; Kozlik and Raith 2017). K1-K3 display geochemical affinities to the Felbertauern augengneiss (Kozlik 2016; Kozlik and Raith 2017). The contact between Basal Amphibolite and Felbertauern augengneiss is strongly tectonised. Timing of thrusting is debated for decades (Variscan versus Alpine thrusting) (Frisch 1980a; Fringer et al. 1993). Assuming late-Variscan or Alpine thrusting, it is possible that there was an intrusive contact between Felbertal Augengneiss and the Basal Amphibolite. It is supported by missing rock of the Habach Complex west of Messelingkogel at the contact between Basal Amphibolite and Felbertal Augengneiss. Messelingscharte is about 1500 m (linear distance) away from the closest contact between Basal Amphibolite and Felbertauern augengneiss west of Messelingkogel. The true distance can't be determined reasonably but is probably smaller than the linear distance (sum of thicknesses of Basal Amphibolite and Habach Complex underlying the Felbertauern augengneiss at Weinbichl is ~500 m). Several distal skarns are known to be further away than 500 m from the correlating pluton (Kwak 1987). There is only one location in the Basal Amphibolite that hosts leucocratic orthogneisses (see Chapter 6.2.7). It is highly dubious if such a small orthogneiss occurrences can produce a W-rich calc-silicate rock. However, this outcrop could be the only exposure of a larger hidden orthogneiss body.

Whole rock geochemistry reveals usual concentration of granitophile element suite with W, Sn, Be and non-ferrous metals suggesting a genetic relationship to highly-fractionated granites. Magmatogenic skarns are well known for hosting high (sometimes economic) grades of W (e.g. Cantung, Canada; King Island, Australia; Bergen-Zobes, Germany) and Sn (e.g. Lost River, Alaska; JC, Yukon Territory, Canada). Skarns can show elevated concentrations of Be and F (e.g. Moina, Australia, Kwak and Askins 1981; Mt. Lindsey Australia, Kwak 1983). Other elements associated with highly fractionated granites like Bi, U, Rb are generally low but still enriched compared to the amphibolite host rock (Figure 83).

The mineral assemblage of calc-silicate rocks from Messelingscharte is similar to retrograde assemblage (ep/czo, chl, amp, clc) of common skarn deposits (Meinert 1992). Sn-rich generation 1 clinozoisite, low-Al Sn-rich titanite and Mo-rich scheelite seem to build the primary mineral assemblage. All previous described occurrences of Sn-rich epidote/clinozoisite (Table 33) are directly associated with magmatic hydrothermal activity. Patchy zoned Sn-titanite can occur in Sn-bearing skarns (e.g. Pisek, Czech Rep., Cempírek et al. 2008). Furthermore, Mo-rich scheelite is common in reduced skarns (Meinert 1992). Because of unknown reason (temperature not high enough?), a classical prograde mineral assemblage of clinopyroxene, garnet and amphibole is absent. Probably a possible magmatic source was too far away to allow formation of such a high-temperature minerals. This has been observed at distal Sn-W skarns (e.g., Sangdong, Korea, Gejiu, Dachang, P.R. China) lacking typical high-T skarn minerals (Kwak 1987). Distal skarns occur rarely in non-carbonate rocks (granite, gabbro, hornfels, volcanic rocks) and are commonly associated with cassiterite, amphibole, chlorite and sulphides (Kwak 1987).

10.4.1. Characteristics of the fluids involved in calc-silicate formation

Interaction of the amphibolite host rock with hydrothermal fluids is a key process in forming the calc-silicate rocks at Messelingscharte. Fluid rock interaction led to depletion of Mg, Zr, Hf and Ti and to enrichment of W, Sn, Be, Ca and transition metals in the calc-silicate rocks compared to the host rocks (see Chapter 8.1.5). In the following, it is tried to constrain the composition of the mineralising fluids qualitatively.

The redox state of fluids could be estimated by three geochemical parameters. First, calc-silicate rocks show a pronounced positive Eu-anomaly (Figure 81, Figure 112). Therefore, fluids were enriched in reduced Eu^{2+}. Second, clinozoisite incorporates significant amounts of Fe^{2+} via charge balance due to $(Ti,Sn)^{4+}$ incorporation (Figure 94). This indicates favourable conditions for ferrous iron. Third, low oxygen fugacity inhibits formation of cassiterite that makes Sn available for incorporation into clinozoisite and titanite (see Heinrich and Eadington 1986).

Calc-silicate rocks are enriched in divalent cations like Ca^{2+} (average 15.02 mass% CaO in calc-silicate rock; 9.44 mass% CaO in amphibolites), Eu^{2+} (positive Eu-anomaly) and Sr^{2+} (enrichment ~3.5 compared to amphibolite). Therefore calc-silicate forming fluids have to be enriched Ca^{2+}, Eu^{2+} and Sr^{2+} that were probably derived by breaking down plagioclase from the amphibolite host rock or from the granitic source of magmatic hydrothermal fluids.

At Messelingscharte, W is hosted exclusively in scheelite. In older publications it was stated that Cl^- and F^- complexes play a role for transport of W in hydrothermal fluids (Krauskopf 1978). This was not confirmed by experimental and thermodynamic data; in their compilation Wood and Samson (2000)

could show that W-Cl^- and W-F^- complexes are not necessary for the transport of W in hydrothermal fluids of granitic affinity. On the contrary the importance of Cl^- complexes for transporting Sn in granitic hydrothermal systems was pointed out by Heinrich (1990).

From incorporation of F in titanite (~1 mass%) it is concluded that F^- was present in the mineralizing fluid. As pointed out, Al-F substitution cannot only be explained with high metamorphic pressures but seems to be a primary signature of the calc-silicate rocks. In SiO_2-saturated igneous rocks Zr and Hf are incorporated in zircon. Zircon is believed to be very stable in most geological environments. The average Zr content in the amphibolite at Messelingscharte is about 150 ppm whereas the calc-silicate fels contains only about 20 ppm. To explain this depletion solubility of Zr during the hydrothermal alteration must be assumed. Zr shows high solubility in F-rich acidic fluids and Zr is commonly transported as a F-complex (Rubin et al. 1993). $CaCl_2$ bearing fluids (Geisler et al. 2003) and strongly alkaline ones ($Na(OH)_2$, $Ca(OH)_2$) (Lewerentz 2011) also increase the solubility of Zr strongly.

Titanium oxides are practically insoluble in pure water but show increasing solubility in acidic saline aqueous solutions (Correns 1971, 1972). Rapp et al. (2010) determined experimentally that rutile is 2-4 times more soluble in chloride and 20-100 times more soluble in F-brines than in pure H_2O at high temperatures and 5 kbar.

Hence, higher F^- content of the fluid phase can facilitate breakdown of zircon and rutile and may have played a role in transport of W. Whatever the exact role of F is in the formation of W(-Sn) deposits it is an element that is often enriched in highly fractionated Li-F granites and pegmatites associated with Sn, W, U, Ta mineralization (e.g. Badanina et al. 2006; Förster et al. 1999), or with Sn, W, Be, F skarn and greisen deposits (e.g. Aleksandrov 2010; Tornos et al. 2008; Hösel 2002; Audédat et al 2000; Kwak and Askins 1981).

10.4.2. Model for calc-silicate formation and evolution of rocks at Messelingscharte

Figure 113 presents a sketch of a thin section and corresponding characteristics of poly-stage minerals. Detailed data are given in Chapter 6.6.1 and 9.

Scheelite as well as clinozoisite and titanite record polyphase formation. Especially scheelite displays three clearly defined generations starting with primary Mo-rich likely magmatic hydrothermal scheelite rimmed/replaced by two different metamorphic Mo-poor/free scheelite generations; the latter partly show molybdenite exolutions. The earliest formed clinozoisite is Sn-rich ("lamellae" or irregularly shaped intra-grain domains). Sn-rich clinozoisite grains are often transformed to euhedral Sn-poor clinozoisite; the latter also forms new crystals in the matrix coexisting with quartz, plagioclase, chlorite and calcite and is part of the metamorphic (Alpine, late Variscan/Permian?) assemblage. Titanite also shows complex intra-grain replacement/recrystallization features. The Sn-rich titanite also being rich in F and containing minute inclusions of cassiterite becomes isochemically recrystallized producing sharper grain boundaries and re-equilibrating with the surrounding phases. The high Sn contents of the early clinozoisite and presence of Sn and F in titanite are key arguments for the magmatic hydrothermal nature of the fluids.

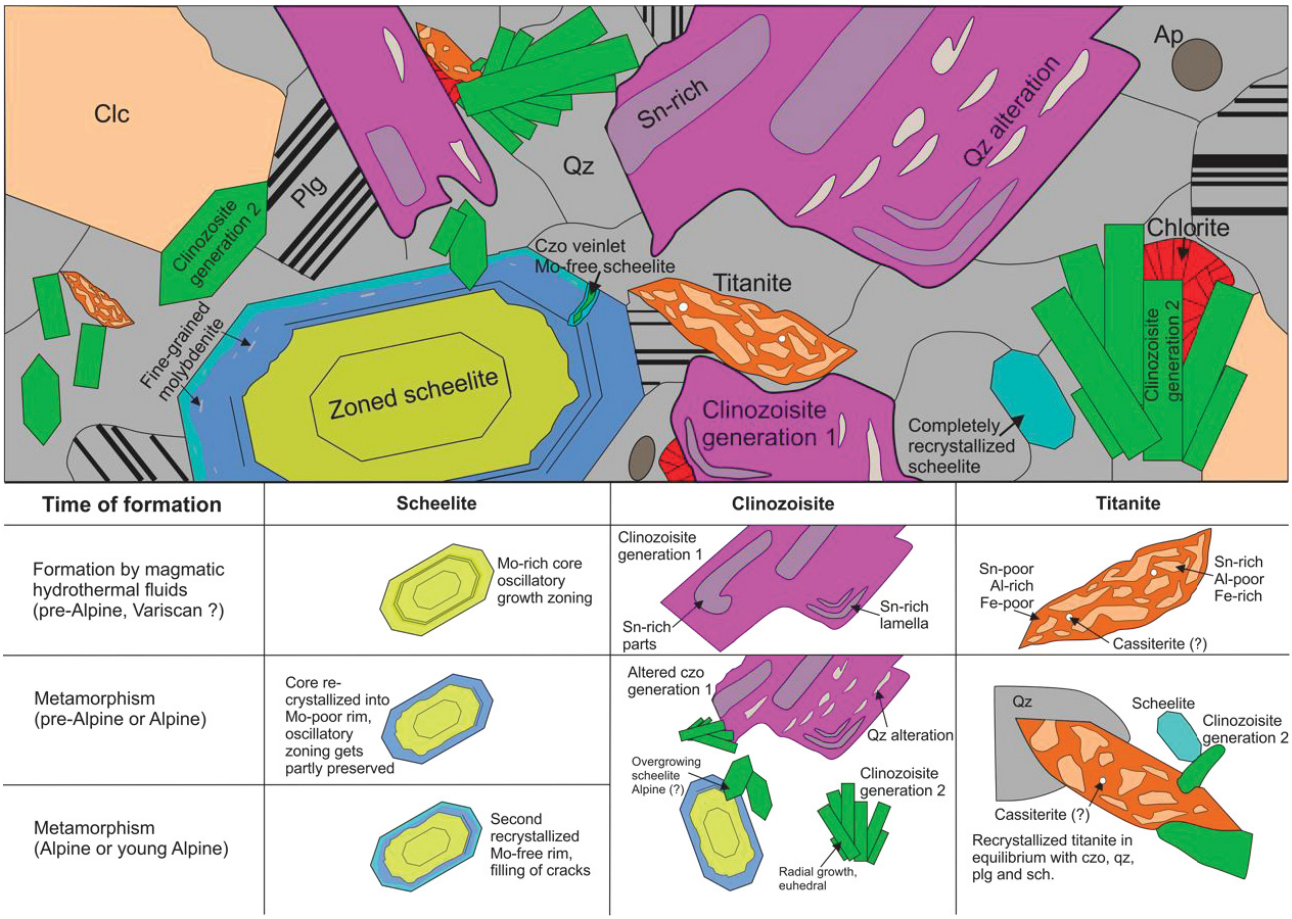

Figure 113: Idealized sketch of mineral assemblage of scheelite-bearing calc-silicate rocks from Messelingscharte. Description of generations of scheelite, clinozoisite and titanite. Quartz content is exaggerated slightly.

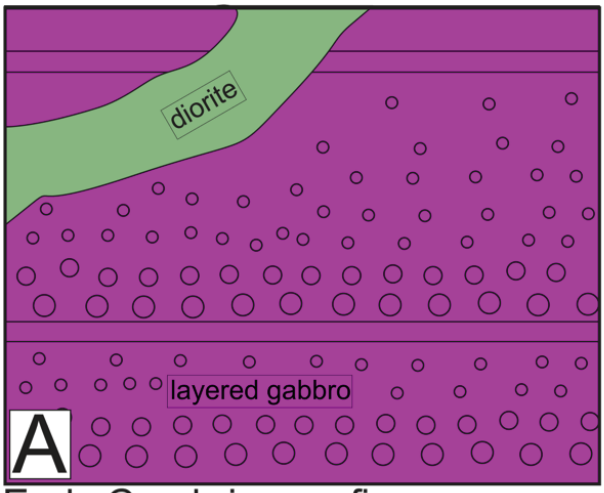

Early Cambrian mafic magmatism

Formation of gabbros, basalts and late diorite intrusion

Enriched-BAB geochemistry

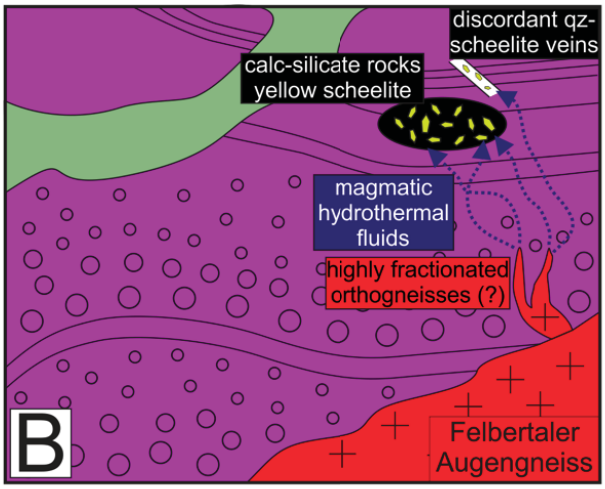

Early Carboniferous magmatism

Emplacement of Felbertal Augengneiss in pre-Variscan basement. Formation of K1-K3 equivalents in the Basal Amphibolite (source for W, Sn and Be).

Formation of W-bearing calc-silicate rocks Clinozoisite generation 1, scheelite generation 1, Sn-titanite

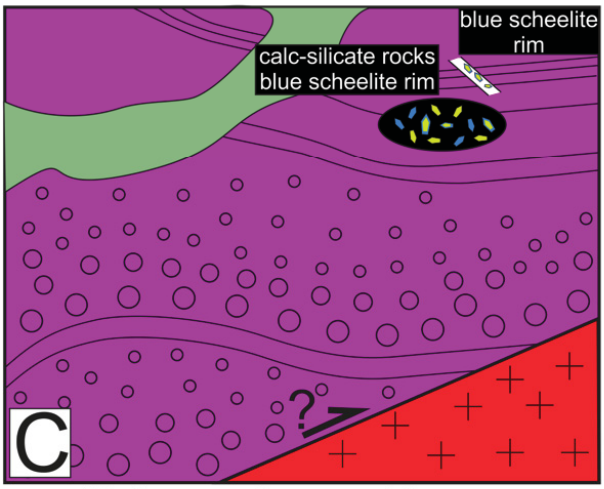

pre-Alpine metamorphism

Variscan or Permian metamorphism

Mo-poor scheelite generation 2 (?), clinozoisite generation 2 (?), recrystallization of titanite

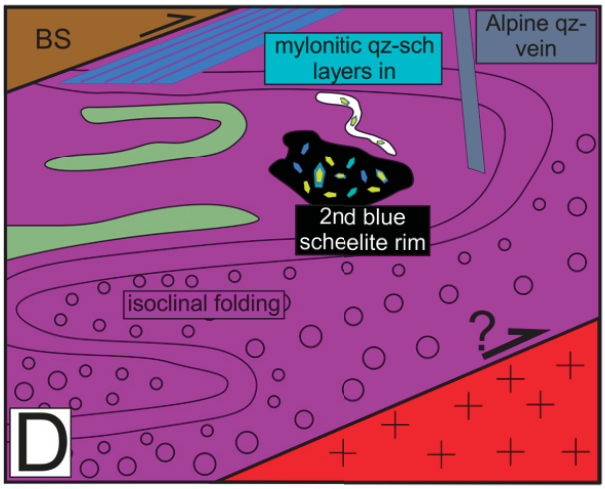

Alpine metamorphism

Major deformation event (e.g. thrusting, isoclinal folding)

Clinozoisite generation 2, Mo-free scheelite generation 3

Mylonitic quartz-scheelite veins in sheared amphibolite

Figure 114: Schematic model for the geological evolution and formation of scheelite-bearing rocks at Messelingscharte; for detailed explanation see text.

A schematic model of the geological evolution and formation of the W-bearing rocks at Messelingscharte is shown in Figure 114. Protoliths of the Basal Amphibolite were formed as layered gabbros, basalts with BAB composition and were intruded by more evolved diorite (Figure 114A). It can be speculated that this back-arc system formed as part the proto-Rheic ocean in the Cambrian.

Felbertauern augengneiss intruded into the succession during Variscan orogeny accompanied by highly fractionated subsidiaries like K1-K3 orthogneisses (Figure 114B). It is highly speculative if there are highly fractionated orthogneisses similar to K1-K3 orthogneisses in the Basal Amphibolite too (Figure 114B-D). Magmatic hydrothermal fluids produced scheelite-bearing calc-silicate rocks and discordant quartz-scheelite veins. Fluid alteration seems to be focussed and not pervasive like in Felbertal deposit. Variscan metamorphism overprinted the Basal Amphibolite heavily and could have led to recrystallization of Mo-rich scheelite and Sn-rich clinozoisite.

The Basal Amphibolite got isoclinally folded during the Alpine orogeny (Figure 114D). Scheelite shows Mo-free recrystallization of (young?) Alpine age. Mylonitic quartz-scheelite layers are an expression of W-remobilisation during thrusting of the Basal Schist. E-W or N-S striking Alpine quartz-veins are emplaced hosting scheelite to a minor extent.

10.4.3. Comparison to magmatogenic skarn deposits

Sn-bearing calc-silicate veins from St. Just aureole in Cornwall (Alderton and Jackson 1978) display striking similarities to Messelingscharte (Table 37). First, the host rocks are metamorphosed mafic igneous rocks. Second, there are veins in the St. Just aureole composed of 40% epidote/clinozoisite, 40% hornblende and titanite; i.e. with similar mineral assemblage as Messelingscharte. These veins are associated with coarse-grained, green amphibolite that formed during the reaction between hydrothermal fluids and the mafic host rock (Alderton and Jackson 1978). Third, Ca, Sn and Be are strongly enriched in both locations but W is not present in calc-silicate veins from St. Just aureole. A vein-like geometry of calc-silicate rocks around Messelingscharte similar calc-silicate veins from St. Just aureole is uncommon but locally present (e.g. boulder east of the large calc-silicate outcrop, Figure 21).

Table 37: Comparison between calc-silicate rocks from Messelingscharte and calc-silicate veins from St. Just areole (Alderton and Jackson 1978).

	Messelingscharte	**St. Just aureole**
Host rock	poly-metamorphosed basalt and gabbros	low-grade metamorphosed or intensely contact-metamorphosed basalts (hornfels)
Mineral assemblage	**clinozoisite-plagioclase-calc-silicate fels:** Czo, Ttn, Qz, Plg, Chl, Sch **amphibole schist:** Amp,Ttn, Chl, Plg	**prograde:** Gar, Dio, Hed, Hbl, Mag **retrograde:** Chl, Clc, Ep/Czo, Ttn sometimes associated with green coarse-grained amphibole
Grain size	fine- to coarse-grained	commonly coarse-grained
Geochemical characteristics	**enrichment of:** W, Sn, Ca, Be, Mo, Cu **depletion of:** Zr, Hf, Ti, Mg, (Si, K, Na)	**enrichment of:** Sn, Ca, Be, P, Mn, B **depletion of:** Si, Mg, Na, K
Mineral geochemistry	Sn-bearing clinozoisite, Sn-Ttn	Sn-bearing /epidoteclinozoisite, Sn-Ttn, Sn-bearing amphibole, Sn-bearing garnet
Fluid inclusions	aqueous (?) L+V inclusions common; not analysed	saline, aqueous L+V inclusions, $NaCl_{equ}$ = 26%
Geometry	massive, pod (<3m), minor thin discordant veins	discordant vein (<1m), sheet
Genesis	magmatic-hydrothermal fluids from undefined source (?)	magmatic-hydrothermal fluids from underlying Hercynian St. Just pluton

The large scale geological setting of the two localities although is different. A clear spatial association with the contact metamorphic roof zone of a granitic pluton is lacking at Messelingscharte. But it must be considered that the Cornish Sn-(W) granites are post-orogenic whereas in the Tauern Window all

rocks were affected by the Alpine orogeny. Hence, Alpine tectonics and metamorphism could have blurred a lot of the primary features of mineralisation at Messelingscharte.

The K/Rb ratio has been suggested long time ago as an indicator for alteration by magmatic hydrothermal fluids derived from (evolved) granites (e.g. Exley 1957). Fluids derived from highly fractionated granitic melts become strongly enriched in Rb resulting in low K/Rb values of the altered rocks. In Felbertal tungsten deposit, the whole ore deposit is characterised by K/Rb <100 and low K/Rb has been suggested as a possible exploration criterion for W mineralisation (Kozlik 2016). This is also seen in the two analysed calc-silicate samples from Felbertal yielding K/Rb of 60-72 (Figure 115). However, all rocks from Messelingscharte including the scheelite-bearing calc-silicate rocks show considerably higher K/Rb ratios (Figure 115) with values close to the crustal average (~200). Therefore, large scale pervasive alteration of the host rocks by magmatic hydrothermal fluids similar to Felbertal tungsten deposit is unlikely.

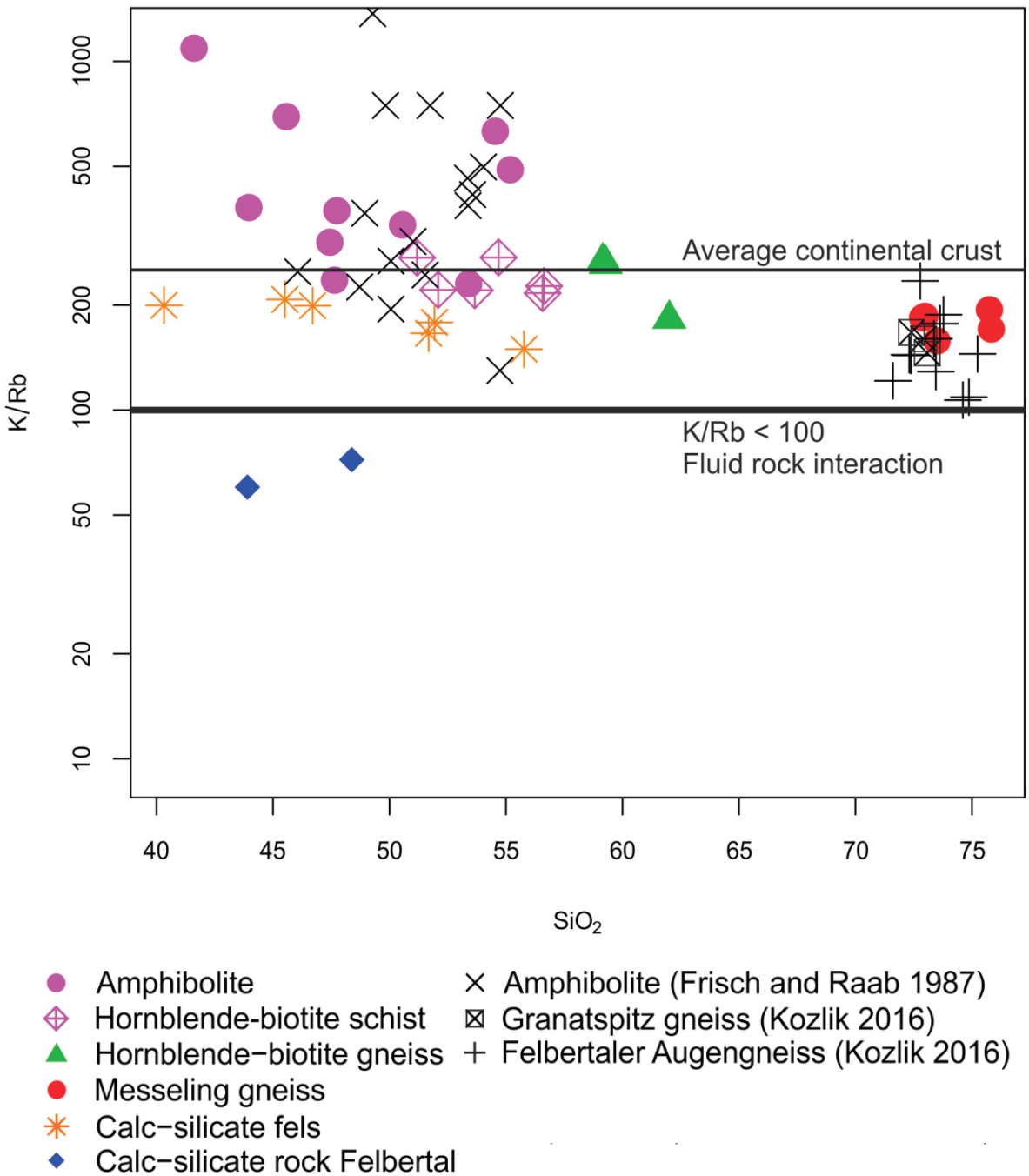

Figure 115: Whole rock SiO_2 vs. K/Rb plot. Low K/Rb values indicate fluids or melts derived from evolved granitic sources.

Summing up, mineralised calc-silicate fels at Messelingscharte resembles unusual distal (?) Sn-bearing (but W-free) skarn veins from St. Just aureole, Cornwall for which a granitic magmatic hydrothermal genesis is undoubted. The W-(Sn) bearing calc-silicate rocks at Messelingscharte formed via alteration/replacement of the amphibolitic host rocks. To a lesser degree W mineralisation formed in (now deformed) quartz veins. Infiltration of fluids rich in Ca, W, Sn, F etc. interacted with the host rocks producing calc-silicate assemblages characterised by Sn-rich clinozoisite, Sn-titanite, Mo-rich scheelite and minor sulphides. The granitophile element suite with W, Sn, Be, F and Cu suggests a genetic relationship to highly-fractionated granites. Thus, a magmatic hydrothermal origin similar to

magmatogenic skarns seems plausible although a clear spatial relationship with evolved (meta)granites has not been observed.

10.5. Comparison of calc-silicate rocks from Messelingscharte and Felbertal tungsten mine

Bulk geochemistry and composition of clinozoisite will be used to assess fluid-rock interaction and to compare differences of the calc-silicate producing fluid. Major element concentrations of clinozoisite-rich calc-silicate rocks from both locations are similar but concentrations of specific trace elements differ strongly (Figure 116; Table 38). Moreover, clinozoisite from Felbertal tungsten mine and Messelingscharte have very different mineral chemical composition (Table 39).

Table 38: Concentrations of selected trace elements (median) for calc-silicate rocks. Listed elements show characteristic differences between Messelingscharte and Felbertal tungsten mine.

Element	Messelingscharte (ppm)	Felbertal tungsten mine (ppm)
W	32397	1983
Sn	477	71
Sr	1008	597
Cu	355 (up to 2438)	270
Rb	25	68
Be	24	5
Mo	12	36
As	2	60
Bi	bdl	3

The tungsten content of rocks from Messelingscharte ranges from 832-61383 ppm (median 32397 ppm); the WO_3 content of rocks from Felbertal mine is between 392-2646 ppm. Interestingly, the Sn content of rocks from Messelingscharte is notably higher (259-1580, median 477 ppm) compared 56-86 ppm of rocks from the mine. Arsenic has much higher concentrations in the Felbertal samples because of regular occurrence of accessory arsenopyrite.

Surprisingly, the average Be content is much higher in rocks from Messelingscharte (24 ppm) compared to Felbertal tungsten mine (5 ppm) although beryl has been reported as a common mineral in quartz-scheelite veins in the Felbertal mine. A possible explanation is that Be can be incorporated in several calc-silicate minerals (e.g. vesuvianite, grossular, allanite; Grew 2002). Already Machatschki (1948) pointed out that Be can probably be incorporated in epidote-group minerals. Because Be is a very light element that cannot be analysed with EPMA it is hard to prove which phases incorporate Be. Generally, beryl has been reported from W-bearing skarns (e.g. Lost River USA, Mt. Bischoff Australia), ultramafic blackwall zones (e.g. Reft River Russia) or magmatic hydrothermal deposits like Felbertal.

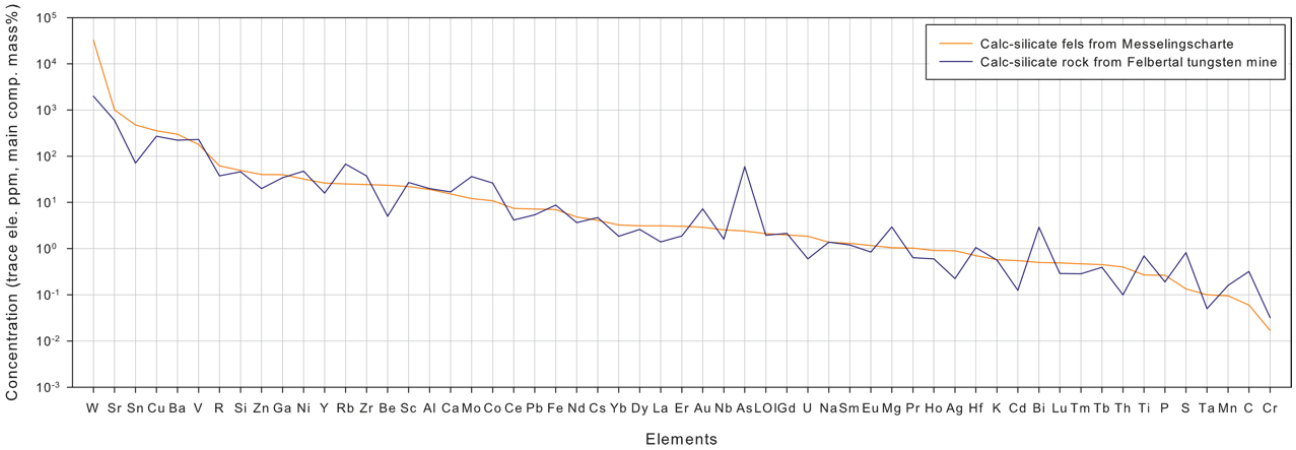

Figure 116: Multi-element spider plot of average calc-silicate rocks from Messelingscharte compared to calc-silicate rocks from Felbertal tungsten mine. Median of all analysed samples plotted. R=REEY.

Moreover, clinozoisite from sample locations shows very different trace element signature (Table 39). Most important, Sn is commonly below the detection limit in clinozoisite from Felbertal but occurs in high concentrations in clinozoisite from Messelingscharte. Moreover, clinozoisite from Felbertal tends to higher Al/Fe^{3+} ratios. The MnO content of clinozoisite from Felbertal is about half compared to Messelingscharte.

Table 39: Comparison of clinozoisite from Messelingscharte and Felbertal tungsten mine.

Sample location	**Messelingscharte**	**Felbertal tungsten mine**
Grain size	very coarse-grained, fine-grained	fine-grained
Generations	2	1
Al/Fe^{3+} ratio (median)	4.55	6.65
SnO_2 (mass%)	bdl-3.0	normally bdl
MnO (median; mass%)	0.138	0.076

The chemical composition of calc-silicate rocks reflect the protolith and with regard to allochemical processes i.e. the interaction between fluids transporting and/or removing certain elements and the host rock. The different REE and trace element patterns (Figure 81) indicate different conditions during the formation of calc-silicate rocks at the two locations. The amphibolite protoliths from Messelingscharte and Felbertal tungsten mine have different chemical composition (BAB vs. VAB; see Chapter 8.1.3) resulting in different starting compositions for calc-silicate formation. Calc-silicate rocks from Messelingscharte inherited some unique geochemical characteristics of the amphibolite host rock like high and strongly scattering Th values. Interaction with fluid led to a relative depletion of Zr, Hf, Ti and Mg in the calc-silicate rocks from Messelingscharte whereas at Felbertal these elements are similar to the host rock. Calc-silicate rocks from Felbertal mine show low K/Rb ratios (Figure 115) and low Sn similar to the host rocks of the deposit. Therefore, it is concluded that calc-silicate forming fluids had very different characteristics at Messelingscharte and Felbertal tungsten mine. Calc-silicate rocks could have formed before or during the ore forming process because they exhibit similar alteration of ore-forming fluids like the host rock (e.g. low K/Rb).

11. Conclusions

11.1. Regional geological aspects

Messelingscharte is located at the western margin of the Granatspitz gneiss dome within the Basal Amphibolite unit in the Tauern Window. The Basal Amphibolite represents Neoproterozoic to Cambrian basic to intermediate igneous rocks formed in a back-arc basin ("Proto Rheic ocean"?) at the northern margin of Gondwana. The Basal Amphibolite consists of amphibolites (metagabbro/metabasalt), hornblende-biotite schist (meta-basalt?, meta-tuffite?) and late-stage discordant hornblende-biotite gneiss (meta-diorite) dykes. Hornblende-biotite schist and amphibolite show different trace element as well as REE patterns. This could be due to higher degrees of differentiation, different protoliths or crustal contamination. Trace element and REE patterns of hornblende-biotite gneiss are indistinguishable from the hornblende-biotite schist. However, main components like SiO_2, MgO and Na_2O differ significantly indicating a higher degree of differentiation of hornblende-biotite gneiss compared to hornblende-biotite schist. Strongly scattering, and high concentrations of Th is a general feature of rocks from the Basal Amphibolite possibly indicating varying degree of crustal contamination (?).

Schists of the Basal Schist cover the Basal Amphibolite more or less concordantly at Messelingkogel. A slice of Granatspitz gneiss got tectonically inserted into the Basal Amphibolite during Alpine deformation.

Rocks of the Habach Complex got thrust upon the Basal Schist at Messelingkogel. There the Habach Complex starts with a several metres thick cataclasite horizon followed by a succession of strongly deformed metasediments (graphitic schists, quartzites, gneisses) and the Weinbühl amphibolite. A similar profile is exposed on the east flank of mountain Weinbichl north of Messelingkogel.

The Habach Complex itself is overlain by a plate-like sheet of quartzite followed by orthogneiss and garnet-amphibolite of unclear assignment. Probably they represent an inverse succession of the Old Gneiss Series as already proposed by Frank et al. (1987).

11.2. Tungsten mineralisation at Messelingscharte

There are four different types of scheelite mineralisation at Messelingscharte.

(1) Scheelite-bearing calc-silicate rocks could represent an unusual (distal?) skarn type. Bulk geochemistry reveals an enrichment of granitophile elements like W (≤6.14 mass% WO_3), Sn (≤1580 ppm), Be (≤41 ppm) and non-ferrous metals compared to the amphibolite host rock. Immobile trace element and REE patterns indicate that the calc-silicate rocks were formed by alteration of amphibolite. The calc-silicate rocks consist of Sn-rich clinozoisite (≤3.00 mass% SnO_2), Sn-titanite (≤6.48 mass% SnO_2), plagioclase, quartz, chlorite and polystage scheelite. Primary scheelite has a Mo-rich (≤1.7 mass% MoO_3) core (yellow fluorescence) showing oscillatory growth zoning. It is interpreted to represent pre-Alpine (Variscan?) scheelite that shows affinity to stage 2 (primary magmatic hydrothermal) scheelite from Felbertal tungsten deposit. The core is rimmed by two different Mo-poor/free scheelite rims (blue fluorescence) that incorporate fine-grained molybdenite

grains. Both rims are interpreted as metamorphic mobilisations and recrystallizations (Variscan (?) and/or Alpine). All other known occurrences of Sn-rich clinozoisite and Sn-titanite are directly associated with magmatic hydrothermal activity (e.g. calc-silicate veins in Cornwall). Sn-rich titanite even hosts miniscule (~3 µm) roundish cassiterite grains and has an average F-content of ~1 mass%. Mo-rich scheelite is also common in W-skarn deposits. Therefore, a granite-related magmatic hydrothermal origin of calc-silicate rocks from Messelingscharte is proposed although the granitic source is unclear yet. Therefore, calc-silicate rocks could be classified as distal skarn deposit (Kwak 1987).

The Felbertauern augengneiss could have played a role in the calc-silicate forming process because it is exposed in vicinity to Messelingscharte and is known for having a genetic relationship to the K1-K3 orthogneiss in the Felbertal tungsten deposit (Kozlik 2016; Kozlik and Raith 2017). Small granitic "offshoots" of the Felbertauern Augengneiss in the Basal Amphibolite could be the source for the W-Sn-Be-F-bearing fluids that produced the calc-silicate rocks.

Nevertheless, the exact control of the ore forming process is still unknown. A lithological control seems unlikely because of lack of differences between the host rock of the calc-silicate rock and amphibolite far away from the mineralization. A structural control could be possible; the Alpine orogeny probably obscured the pre-Alpine structural features. However, the local restriction of W-mineralisation and chemical criteria such as high Rb/K ratios of the host rock and the calc-silicate rocks are an important difference to Felbertal tungsten deposit where a pervasive alteration by magmatic hydrothermal fluids took place (Kozlik 2016).

(2) Deformed discordant quartz-scheelite veins crosscutting sheared amphibolite occur west of Messelingscharte. They are interpreted as pre-Alpine veins incorporating also poly-stage scheelite. Scheelite there also has a yellow core surrounded by a blue rim in UV light. They could have formed contemporary to the scheelite-bearing calc-silicate rocks.

(3) Scheelite is hosted at the contact between strongly deformed mylonitic quartz veins and amphibolite. Scheelite there has blue luminescence colours and is generally fine-grained and dispersed in the hornblende-rich sheared amphibolite. This mineralization is interpreted to be an Alpine mobilization of W, eventually associated with thrusting of the Basal Schist over the Basal Amphibolite.

(4) Scheelite occurs rarely on joint surfaces in amphibolite. Surprisingly, there is also yellow fluorescent scheelite present but the majority of scheelite has blue luminescence colours.

11.3. Calc-silicate rocks from Felbertal tungsten deposit

Clinozoisite-rich calc-silicate rocks occur as irregular patches in deformed amphibolites in Felbertal tungsten deposit. Geochemical analyses revealed significant differences to the calc-silicate rocks from Messelingscharte (e.g. REE patterns; bulk content of W, Sn, Be, Rb, Sr). Grain size and lacking of Sn^{4+} in clinozoisite are the major differences to clinozoisite from Messelingscharte. Hence, they reflect different composition of the host rock and processes of calc-silicate formation. Calc-silicate rocks were probably formed before or during the ore forming process.

12. Recommendations for further exploration

The high grade scheelite mineralisation at Messelingscharte is bound to clinozoisite-dominated calc-silicate rocks and it is this mineralisation type which is regarded as the economically most interesting one. Hence, further exploration should focus on locating this type of calc-silicate rocks in addition to UV prospecting for scheelite. Searching for these specific calc-silicate rocks can be done during daytime in the well exposed study area. Furthermore, the meter-sized mineralised calc-silicate outcrop at Messelingscharte produces an about 100 m long and 50 m wide talus fan where scheelite-bearing bolders can be traced back to the exposed mineralisation. Outcrops elsewhere could also show a fan of similar size simplifying the localisation scheelite-bearing outcrops.

So far there is no well defined proxy available to identify hidden calc-silicate hosted scheelite mineralisation and discriminate it from late metamorphic scheelite (e.g. from Alpine clefts). The observed chemical association of W with Sn in calc-silicate rocks could be used as a proxy. Tin is very low (~1 ppm) in the amphibolite and other mafic-intermediate volcanic rocks. Therefore, higher concentrations of Sn in stream sediments in the catchment area dominated by mafic rocks (not orthogneisses!) could indicate presence of W-bearing calc-silicate rocks. Heavy mineral concentrates are not recommended as sampling media because, as as been shown in this study, Sn is incorporated in clinozoisite and titanite and not in cassiterite. Both Sn-bearing silicates have a similar specific density (3.2-3.6 g/cm^3) than other common rock forming minerals (e.g. hornblende 3-3.4 g/cm^3) making gravitative enrichment by panning difficult. Thus, preferably the fine fraction of stream sediments has to be sampled and higher concenetrations of Sn and positive correlations of Sn and W could be used as mineralisation indicators. Panning for scheelite could be feasible for localising scheelite-bearing outcrops but only the presence of yellow fluorescent Mo-rich scheelite would strongly suggest calc-silicate rocks.

The map below (Figure 117) points out areas for further prospecting and suggests locations for additional stream sediment sampling. First, the steep and rough area west of Messelingscharte between the hiking path to St. Pöltener Hütte and the Felbertauern Augengneiss was not investigated so far. Large portions of the Basal Amphibolite are exposed in this area. There are also several temporary and few permanent creeks in this area that could be used for stream sediment sampling (Figure 117). Second, the WSW directed ridge of Messelingkogel between the peak at 2694 m and the road to St. Pöltener Hütte should be mapped. This area could clarify the extent of the Basal Schist and the Granatspitz gneiss at Messelingkogel. Third, the western flank of Hochgasser should be prospected again for W-bearing calc-silicate rocks in detail. So far no scheelite-bearing outcrop was identified although previous studies by Gold Consultants indicated outcrops with high-grade scheelite mineralisation there (see Chapter 5.1).

From the scientific point of view, identification of the source of the mineralising hydrothermal fluids is of major interest. From the mineral chemical characteristics and bulk geochemistry it is hypothesized in this study that W-(Sn) mineralisation is similar to distal magmatogenic skarns. If this is correct, a genetic and spatial link with a potential granitic source has to be looked for. The previous study by Kozlik (2016) established that the best candidate among the Zentralgneis varieties in the central Tauern Window is the Felbertal Augengneis and not the Granatspitz gneiss. Hence, the nearby slice of Granatspitz gneiss at Messelingkogel has to be excluded as potential granite source. Follow-up studies

should therefore focus on the contact zone of the Felbertal Augengneiss to the Basal Amphibolite unit; in the available geological maps this contact is interpreted as tectonic but it has to be checked if small (?) granite “offshoots” of this granite are eventually present in the Basal Amphibolite between Messelingkogel and the main Felbertal Augengneiss body in the west (Figure 117).

A major drawback for exploration is that neither a stratigraphic nor tectonic/structural control of W-Sn mineralisation could so far be established. The main calc-silicate hosted high-grade scheelite outcrop is of limited extent and a continuation of this irregular pod can hardly be predicted. In part this is caused by the poly-deformational (and metamorphic) overprint of the scheelite-bearing calc-silicate rocks, which has been well documented in this study. Similar to Felbertal scheelite deposit, unravelling the complex structural evolution of this area remains major future challenge.

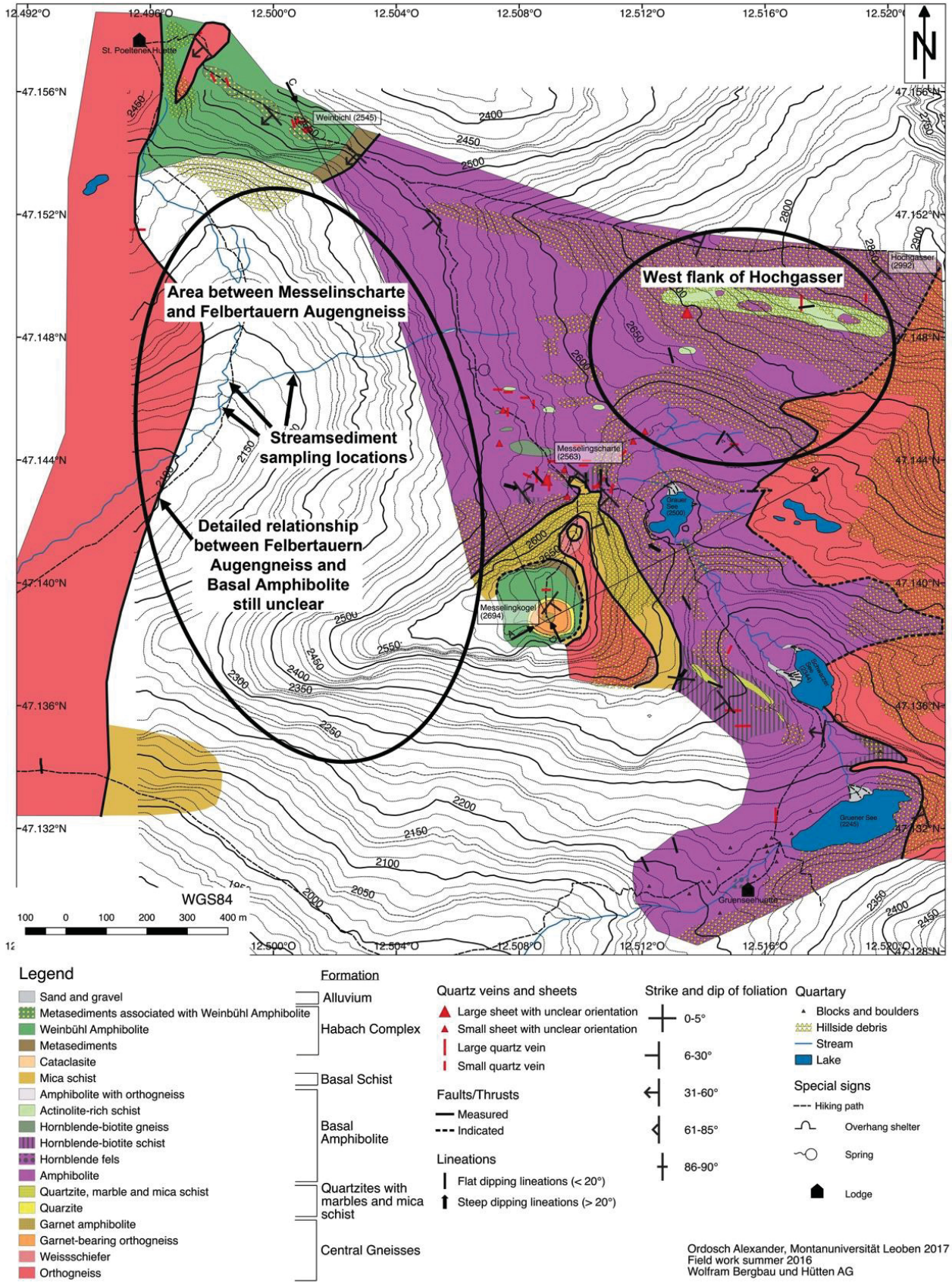

Figure 117: Geological map with recommendations for further exploration and sampling.

References

Alderton DHM and Jackson NJ (1978) Discordant calc-silicate bodies from the St. Just aureole, Cornwall. Mineralogical Magazine 42:427-434

Aleksandrov SM and Troneva MA (2007) Composition, Mineral Assemblages, and Genesis of Titanite and Malayaite in Skarns. Geochemistry International 45:1012-1024

Aleksandrov SM (2010) Skarn-greisen deposits of the Lost River and Mount Ear ore field, Seward Peninsula, Alaska, United States. Geochemistry International 48:1220-1236

Altherr R, Holl A, Hegner E, Langer C, Kreuzer H (2000) High-potassium, calc-alkaline I-type plutonism in the European Variscides: northern Vosges (France) and northern Schwarzwald (Germany). Lithos 50:51-73

Armbruster T, Bonazzi P, Akasaka M, Bermanec V, Chopin C, Gieré R, Heuss-Assbichler S, Liebscher A, Manchetti S, Pan Y and Pasero M (2006) Recommended nomenclature of epidote-group minerals. European Journal of Mineralogy 18:551-567

Audédat A, Günther D and Heinrich CA (2000) Magmatic-hydrothermal evolution in a fractionating granite: A microchemical study of the Sn-W-F-mineralized Mole Granite (Australia). Geochimica et Cosmochimica Acta 64:3373–3393

Badanina EV, Trumbull RB, Dulski P, Wiedenbeck M, Veksler IV, Syritso LF (2006) The behaviour of rare-earth and lithophile trace elements in rare-metal granites: a study of fluorite, melt inclusions and host rocks from the Khangilay Complex, Transbaikalia, Russia. The Canadian Mineralogist 44:667-692

Bailey JC (1981) Geochemical criteria for a refined tectonic discrimination of orogenic andesites. Chemical Geology 32:139-154

Barriga F and Fyfe WS (1983) Development of rodingite in basaltic rocks in serpentinites, East Liguria, Italy. Contributions to Mineralogy and Petrology 84:146-151

Beran A, Göd R, Götzinger M and Zemann J (1985) A scheelite mineralization in calc-silicate rocks of the Moldanbicum (Bohemian Massif) in Austria. Mineralium Deposita 20:16-22

Bevins RE, Kokelaar BP and Dunkley PN (1984) Petrology and geochemistry of lower to middle Ordovician igneous rocks in Wales: a volcanic arc to marginal basin transition. Proceedings of the Geologists' Association 95:337-347

Bowen NL (1940) Progressive metamorphism of siliceous limestones and dolomite. Journal of Geology 48:225-274

Boynton WV (1984) Geochemistry of the rare earth elements: meteorite studies. In: Henderson P (ed) Rare earth element geochemistry, Elsevier, Amsterdam, 63-114

Breiter K, Förster HJ, Seltmann R (1999) Variscan silicic magmatism and related tin- tungsten mineralization in the Erzgebirge-Slavkovský les metallogenic province. Mineralium Deposita 34:505-521

Briegleb D (1987) Geologische Verhältnisse im Bereich der Scheelitlagerstätte im Felbertal, Pinzgau (Land Salzburg). Uni Aktuell Salzburg 10:10-11

Briegleb D (1991) Die Scheelitlagerstätte im Felbertal bei Mittersill (Land Salzburg). Berichte der Deutschen Mineralogischen Gesellschaft 2:48-50

British Geological Survey (2011) Tungsten.

Brunsmann A, Franz G, Erzinger J and Landwehr D (2000) Zoisite- and clinozoisite-segregations in metabasites (Tauern Window, Austria) as evidence for high-pressure fluid-rock interaction. Journal of Metamorphic Geology 18:1-21

Cameron M and Papike JJ (1979) Amphibole crystal chemistry: a review. Fortschritte der Mineralogie 57:28-67

Cempírek J Houzar S and Novák M (2008) Complexly zoned niobian titanite from hedenbergite skarn at Písek, Czech Republic, constrained by substitutions Al (Nb, Ta) Ti–2, Al (F, OH)(TiO)–1 and SnTi–1. Mineralogical Magazine 72:1293-1305

Clark AM (1974) A tantalum-rich variety of sphene. Mineralogical Magazine 39:605-607

Che XD, Linnen RL, Wang RH, Groat LA and Brand AA (2013) Distribution of trace and rare earth elements in titanite from tungsten and molybdenum deposits in Yukon and British Columbia, Canada. The Canadian Mineralogist 51:415-438

Cornelius (1944) Beoabchtungen am Nordostende der Habachzunge (Venedigermassiv, Hohe Tauern). Bericht Reichsamt Bodenforschung Wien: 25-31

Correns CW (1971, 1972) Zur Geochemie des Titans. Bulletin de l'Ins. de Recherches Gèologiques 29/30 Beograd

Crowley QG, Floyd PA, Stedra V, Windechester JA, Kachlík V, Holland JG (1995) The Mariánské-Lázne Complex, NW Bohemian Massif: development and estruction of an early Palaeozoic seaway. Geological Society, London, Special Publication 201:177-195

Crowley QG, Floyd PA, Windester JA, Franke W and Holland JG (2000) Early Palaezoic rift-related magmatism in Variscan Europe: fragmentation of the Armorican Terrane Assemblage. Terra Nova 12:171-180

Dietrich H, Koller F, Richter W and Kiesl W (1986) Petrology und Geochemie des Rodingitvorkommens vom Islitzfall (Dorfertal, Hohe Tauern). Schweizerische Mineralogische und Petrologische Mitteilungen 66:163-192

Donnelly KA, Goldstein SL, Langmuir CH, Spiegelman M (2004) Origin of enriched ocean ridge basalts and implications for mantle dynamics. Earth and Planetary Science Letters 226:347-366

Deng XD, Li JW, Zhou MF, Zhao XF and Yan DR (2015) In-situ LA-ICPMS trace elements and U–Pb analysis of titanite from the Mesozoic Ruanjiawan W–Cu–Mo skarn deposit, Daye district, China. Ore Geology Reviews 65:990-1004

Dr. Otto Gold Consulting Engineers Metallische Erz (1978) Bericht Scheelit-Exploration – Messeling Kogel Matrei/Osttirol – Österreich, Köln

Dr. Otto Gold Consulting Engineers Metallische Erz (1979) Bericht Scheelit-Exploration – Messeling Kogel Matrei/Osttirol – Österreich, Köln

Droop GTR (1983) Pre-Alpine eclogites in the Pennine Basement Complex of the Eastern Alps. Journal metamorphic Geology 1:3-12

Eadington PF and Kinealy K (1983) Some aspects of the hydrothermal reactions of tin during skarn formation. Journal of the Geological Society of Australia 30:461-471

Eichhorn R, Schärer U, Höll R (1995) Age and evolution of scheelite-hosting rocks in the Felbertal deposit (Eastern Alps): U-Pb geochronology of zircon and titanite. Contributions to Mineralogy and Petrology 119:377-386

Eichhorn R, Höll R, Jagoutz E, Schärer U (1997) Dating scheelite stages: A strontium, neodymium, lead approach from the Felbertal tungsten deposit, Central Alps, Austria. Geochimica et Cosmochimica Acta 61:5005-5022

Eichhorn R, Höll R, Loth G, Kennedy A (1999) Implications of U–Pb SHRIMP zircon data on the age and evolution of the Felbertal tungsten deposit (Tauern Window, Austria). International Journal of Earth Sciences 88:496-512

Eichhorn R, Loth G, Höll R, Finger F, Schermaier A, Kennedy A (2000) Multistage Variscan magmatism in the central Tauern Window (Austria) unveiled by U/Pb SHRIMP zircon data. Contributions to Mineralogy and Petrology 139:418-435

Eichhorn R, Loth G, Kennedy A (2001) Unraveling the pre-Variscan evolution of the Habach terrane (Tauern Window, Austria) by U-Pb SHRIMP zircon data. Contributions to Mineralogy and Petrology 142:147-162

Einaudi MT and Burt DM (1982) Introduction; terminology, classification, and composition of skarn deposits. Economic Geology 77:745-754

Eskola P (1922) On the contact phenomena between gneiss and limestone in western Massachusetts. Journal of Geology 30:265-294

Exley CS (1957) Magmatic differentiation and alteration in the St. Austell granite. Quarterly Journal of the Geological Society 114:197-230

Finger F, Kraiger H and Steyrer HP (1985) Zur Geochemie des K1-Gneises der Scheelitlagerstätte Felbertal (Pinzgau, Salzburg)-Ein Vorbericht. Der Karinithin 92:225-235

Finger F, Frasl G, Haunschmid B, Lettner H, von Quadt A, Schermaier A, Schindlmayr AO, Steyrer HP (1993) The Zentralgneise of the Tauern Window (Eastern Alps): Insight into an intra-Alpine Variscan batholith. In: Raumer JF, Neubauer F (eds) Pre-Mesozoic geology of the Alps. Springer Verlag, Berlin Heidelberg New York 375-391

Floyd PA and Winchester JA (1975) Magma-type and tectonic setting discrimination using immobile elements. Earth Plante. Sci. Lett. 27:211-218

Floyd PA, Winchester JA, Seston R, Kryza R and Crowley QG (2000) Review of geochemical variation in Lower Palaeozoic metabasites from the NE Bohemian Massif: intercratonic rifting and plume-ridge interatction. In: Franke W (ed) Orogenic Processes: Quantification and Modelling in the Variscan Belt. Geological Society, London, Special Publication 179:155-174

Förster HJ, Tischendorf G, Trumbull RB and Gottesmann B (1999) Late-collisional granites in the Variscan Erzgebirge, Germany. Journal of Petrology 40:1613-1645

Frank W, Miller C, Pestal G (1987) Geologische Karte der Republik Österreich. 152 Matrei in Osttirol 1:50.000. Geologische Bundesanstalt, Wien

Franz G, Spear FS (1985) Aluminous titanite (sphene) from the Eclogite Zone, south- central Tauern Window, Austria. Chemical Geology 50:33-46

Frasl, G (1958) Zur Seriengliederung der Schieferhülle in den Mittleren Hohen Tauern. Jahrbuch der Geologischen Bundesanstalt 101:323-472

Frei D, Liebscher A, Franz Gerhard and Dulski P (2004) Trace Element Geochemistry of Epidote Minerals. Reviews in Mineralogy & Geochemistry 55:553-605

Frisch W (1977) Der alpidische Internbau der Venedigerdecke im westlichen Tauernfenster. Neues Jahrbuch Geologische und Paläontologische Monatshefte 11:675- 696

Frisch W (1980a) Tectonics of the Western Tauern window. Mitteilungen der Österreichischen Geologischen Gesellschaft 71/72:675-696

Frisch W (1980b) Post-Hercynian formations of the western Tauern window: sedimentological features, depositional environment and age. Mitteilungen der Österreichischen Geologischen Gesellschaft 71/72: 49–63

Frisch W and Raab D (1987) Early Paleozoic Back-Arc and Island-Arc Settings in Greenstone Sequences of the Central Tauern Window (Eastern Alps). Jahrbuch der Geologischen Bundesanstalt 129:545-566

Frisch W and Neubauer F (1989) Pre-Alpine terranes and tectonic zoning in the Eastern Alps. Geological Society of America Special Papers 230:91-100

Frisch W, Vavra G and Winkler M (1993) Evolution of the Penninic Basement of the Eastern Alps. In: Raumer JF, Neubauer F (eds) Pre-Mesozoic geology in the Alps. Springer, Berlin Heidelberg New York 347-360

Frost RB (1975) Contact Metamorphism of Serpentinite, Choritic Blackwall and Rodingite at Paddy-Go-Easy Pass, Central Cascades, Washington. Journal of Petrology 16:272-313

Frost BR, Barnes CG, Collins WJ, Arculus RJ, Ellis DJ, Frost CD (2001) A geochemical classification for granitic rocks. Journal of Petrology 42:2033-2048

Fuchs G (1958) Beitrag zur Kenntnis der Geologie des Gebietes Granatspitze- Großvenediger, Hohe Tauern. Jahrbuch der Geologischen Bundesanstalt 101:201-248

Geisler T, Pidgeon RT, Kurtz R, van Bronswijk W and Schleicher H (2003) Experimental hydrothermal alteration of partially metamict zircon. American Mineralogist 88:1496-1513

Green TH, Pearson NJ (1987) An experimental study of Nb and Ta partitioning between Ti-rich minerals and silicate liquids at high pressure and temperature. Geochimica et Cosmochimica Acta 51:55-62

Grew ES (2002) Mineralogy, Petrology and Geochemistry of Beryllium: An Introduction and List of Beryllium Minerals. Reviews in Mineralogy and Geochemistry 50:1-76

Groat LA, Carter RT and Hawthorn FC (1985) Tantalian niobian titanite from the Irgon claim, southeastern Manitoba. The Canadian Mineralogist 23:569 571

Harris NBW, Pearce JA and Tindle AG (1986) Geochemical characteristics of collision-zone magmatism. In: Coward MP and Reis AC (eds) Collision tectonics. Geological Society, London, Special Publications 19:67-81

Heinrich CA and Eadington PJ (1986) Thermodynamic Predictions of the Hydrothermal Chemistry of Arsenic, and Their Significance for the Paragenetic Sequenceof Some Cassiterite-Arsenopyrite-Base Metal Sulfide Deposits. Economic Geology 81:511-529

Heinrich CA (1990) The Chemistry of Hydrothermal Tin(-Tungsten) Ore Deposition. Economic Geology 85:457-481

Higgins JB and Ribbe PH (1976) The crystal chemsitry and space groups of natural and synthetic titanites. American Mineralogist 61:878-888

Hösel G (2002) Die polymetallische Skarnlagerstätte Pöhla-Globenstein. Sächsisches Landesamt für Umwelt und Geologie

Hoschek G (2001) Thermobarometry of metasediments and metabasites from the Eclogite zone of the Hohe Tauern, Eastern Alps, Austria. Lithos 59:127-150

Höck V (1993) The Habach-Formation and the Zentralgneis - A Key in Understanding the Palaeozoic Evolution of the Tauern Window (Eastern Alps). In: Raumer JF, Neubauer F (eds) Pre-Mesozoic geology in the Alps. Springer, Berlin Heidelberg New York 361- 374

Höll R (1971) Scheelitvorkommen in Österreich. Erzmetall 24:273-282

Höll R (1975) Die Scheelitlagerstätte Felbertal und der Vergleich mit anderen Scheelitvorkommen in den Ostalpen. Verlag der Bayerischen Akademie der Wissenschaften, München

Höll R and Maucher A (1967) Genese und Alter der Scheelit-Magnesit-Lagerstätte Tux. Sitzungsbericht Bayerische Akademie der Wissenschaften, Mathematische-Naturwissenschaftliche Klasse 1967:1-11

Höll R (1975) Die Scheelitlagerstätte Felbertal und der Vergleich mit anderen Scheelitvorkommen in den Ostalpen. Verlag der Bayerischen Akademie der Wissenschaften, München

Höll R and Maucher A (1976) Strata-bound ore deposits in the eastern Alps. In: In Wolf KH (ed) Handbook of strata-bound and stratiform ore deposits. Elvsevier Amsterdam-Oxford-New York 1-35

Höll R (1977) Early Paleozoic ore deposits of the Sb-W-Hg formation in the Eastern Alps and their genetic interpretation. In: Klemm DD and Schneider HJ (eds) Time- and Stratabound Ore Deposits. Springer, Berlin-Heidelberg-New York

Höll R and Eichhorn R (2000) Tungsten mineralization and metamorphic remobilization in the Felbertal scheelite deposit, central Alps, Austria. In: Spry PG, Marshall B, Vokes FM (eds) Metamorphosed and metamorphogenic ore deposits. Reviews in Economic Geology 11:233-264

Hollabaugh CL and Rosenberg PE (1983) Substitution of Ti for Si in titanite and new end-member cell dimensions for titanite. American Mineralogist 68:177-180

Irvine AJ and Barager WRA (1971) A guide to the chemical classification of the common volcanic rocks. Canadian journal of earth sciences 8:523-770

Janousek V, Farrow CM and Erban V (2006).Interpretation of whole-rock geochemical data in igneous geochemistry:introducing Geochemical Data Toolkit (GCDkit).Journal of Petrology 47:1255-1259

Joesten R (1974) Local Equilibrium and metasomatic growth of zoned calc-silicate nodules from a contact aureole, Christmas Mounts, Big Bend Region, Texas. American Journal of Science 274:876-901

Kebede T, Klötzli U, Kosler J, Skiöld T (2005) Understanding the pre-Variscan and Variscan basement components of the central Tauern Window, Eastern Alps (Austria): constraints from single zircon U-Pb geochronology. International Journal of Earth Sciences 94:336-353

Kjarsgaard IM and Ames DE (2010) Ore Mineralogy of Cu-Ni-PGE Deposits in the North Range Footwall Environment, Sudbury, Canada. 11th International Platinum Symposium, Ontario Geological Survey, Miscellaneous Release–Data 269

Koller F and Richter W (1983) Die Metrodingite der Habachformation, Hohe Tauern (Österreich). TMPM Tschermaks Mineralogische und Petrographische Mitteilungen 33:49-66

Koller F and Pestal G (2003) Die ligurischen Ophiolite der Tarntaler Berge und der Matreier Schuppenzone. In Rockenschaub M (ed) Arbeitstagung 2003 der Geologischen Bundesanstalt Trins im Gschnitztal 65-76

Kozlik M, Gerdes A, Raith JG (2015) Strontium isotope systematics of scheelite and apatite from the felbertal tungsten deposit, Austria – result of in-situ LA-MC-ICP-MS analysis. Mineralogy and Petrology 110:11-27

Kozlik M (2016) Mineralogical, petrological and (isotope-) geochemical studies on the Felbertal scheelite deposit, Austria: Development of an epigenetic model for W mineralization in the context of Variscan magmatism in the Tauern Window. Dissertation Montanuniverstität Leoben

Kozlik M, Raith JG, Gerdes A (2016) U–Pb, Lu–Hf and trace element characteristics of zircon from the Felbertal scheelite deposit (Austria): new constraints on timing and source of W mineralization. Chemical Geology 421:112–126

Kozlik M and Raith JG (2017) Variscan metagranitoids in the central Tauern Window (Eastern Alps, Austria) and their role in the formation of the Felbertal scheelite deposit. Lithos 278:303-320

Kraiger H (1987) Geologie, Petrographie und Geochemie der Habachformation: am Beispiel des Unterfahrungsstollens der Scheelitlagerstätte Felbertal. na

Krauskopf KB (1978) Tungsten (Wolfram). In Wedepohl KH (ed) Handbook of Geochemistry II/5.

Kunz M, Xirouchakis D, Wang Y, Parise JB and Lindsley DH (1997) Structural investigations along the join $CaTiOSiO_4$-$CaSnOSiO_4$. Schweizerische mineralogische und petrographische Mitteilungen 77:1-11

Kurz W, Neubauer F, Genser J, Dachs E (1998) Alpine geodynamic evolution of passive and active continental margin sequences in the Tauern Window (eastern Alps, Austria, Italy): a review. Geologische Rundschau 87:225-242

Kurz W (2006) Penninic Paleogeography from the Western toward the Eastern Alps—still open questions? International Geology Review 48:996–1022

Kurz W, Handler R and Bertoldi C (2008) Tracing the exhumation of the Eclogite Zone (Tauern Window, Eastern Alps) by 40Ar/39Ar dating of white mica in eclogites. Swiss Journal of Geosciences 101:191–206

Kwak TAP, Askins PW (1981) Geology and genesis of the F-Sn-W(-Be-Zn) skarn (wrigglite) at Moina, Tasmania. Economic Geology 76:439-467

Kwak TAP and White AJR (1982) Contrasting W-Mo-Cu and W-Sn-F Skarn Types and Related Granitoids. Mining Geology 32:339-3151

Kwak TAP (1983) The Geology and Geochemistry of the Zoned, Sn-W-F-Be Skarns at Mt. Lindsay, Tasmania, Australia. Economic Geology 78:1440-1465

Kwak TAP (1987) W-Sn Skarn Deposits: And Related Metamorphic Skarns and Granitoids. Elsevier

Lafuente B, Downs R, Yang H and Stone N (2015) The Power of Databases: The RRUFF Project. In Armbruster T and Danisi RM (eds) Highlights in Mineralogical Crystallography 1-30

Lammerer B (1986) Das Autochthon im westlichen Tauernfenster. Jahrbuch der Geologischen Bundesanstalt 128: 51–67

Lammerer B, Weger M (1998) Footwall uplift in an orogenic wedge: the Tauern Window in the Eastern Alps of Europe. Tectonophysics 285:213-230

Lewerentz A (2011) Experimental zircon alteration and baddeleyite formation in silicate saturated systems: implications for dating hydrothermal events. Master's thesis 293, Department of Earth- and Ecosystem Sciences, Division of Geology, Lund Unviersity

Loth G, Höll R (1994) Zircon morphology and typology studies of rocks from the polymetamorphic Stubach complex (Altkristallin Formation) in the vicinity of the Felbertal tungsten deposit (Eastern Alps). In Seltmann R, Kämpf H, Möller P (eds) Metallogeny of collisional orogens. Czeck Geological Survey: 357-363

Machatschki F (1948) Welche Schlüsse sind aus der Existenz von Berylliumorthiten auf die Struktur der Epidote zu ziehen? Tschermaks Mineral Petrogr Mitt 1:19-23

Meinert LD (1992) Skarns and skarn deposits. Geoscience Canada 19.4

Meinert LD (1993) Igneous Petrogenesis and Skarn Deposits. Mineral deposit modeling 40:569-583

Middlemost EAK (1994) Naming materials in the magma/igneous rock system. Earth-Science Reviews 37:215-224

Mullen ED (1983) $MnO/TiO_2/P_2O_5$: a minor element discrimination for basaltic rocks of oceanic environments and its implications for petrogenesis. Earth and Planetary Science Letters 62:53-62

Mulligan R and Jambor JL (1968) Tin-bearing silicates from skarn in the Cassiar district, northern British Columbia. The Canadian Mineralogist 9:358-370

Myer GH (1965) X-ray determinative curve for epidote. American Journal of Science 263:78-86

Neinavaie MH (1979) Schichtgebundene Metallanreicherungen in der Schieferhülle und in der Matreier Zone Osttirols. Dissertation Innsbruck.

Neinavaie MH, Ghasemi B, Fuchs HW (1983) Die Erzvorkommen Osttirols. Veröffentlichungen des Tiroler Landesmuseums Ferdinandeum 63:69-113

Neinavaie H, Thalmann F, Ataii B, Beran A (1989) Wolframite- and scheelite-bearing carbonate rocks of the Nock mountains, Austria: A new type of tungsten mineralization in the Eastern Alps. Mineralium Deposita 24:14-18

Neubauer F (2002) Evolution of late Neoproterozoic to early Paleozoic tectonic elements in Central and Southeast European Alpine mountain belts: review and synthesis. Tectonophysics 352:87-103

Oberti R, Smith DC, Rossi G, Caucia F (1991) The crystalchemistry of high-aluminum titanites. European Journal of Mineralogy 3:777-792

Palme H (2014) Cosmochemical Estimates of Mantle Composition. Treatise on Geochemistry 2nd Edition 3:1-39

Parker RL (1967) Data of Geochemistry, Sixth Edition, Chapter D. Composition of the Earth's Crust. United States Government Printing Office, Washington.

Pearce JA, Alabaster T, Shelton AW and Searle MP (1981) The Oman ophiolite as a Creaceous arc-basin complex: evidence and implications. Philosophical Transactions of the Royal Society of London A: Mathematical, Physical and Engineering Sciences 300:399-317

Pearce JA (1982) Trace element characterisitcs of lavas from destructive plate boundaries. In Thorpe RS (ed) Andesites:525-548

Pearce JA (1983) Role of the sub-continental lithosphere in magma genesis at active continental margins. In Hawkesworth CJ and Norry MJ (eds) Continental basalts and mantle xenoliths:230-249

Pearce JA (1996) A User's Guide to Basalt Discrimination Diagrams. In Wyman DA (ed) Trace Element Geochemistry of Volcanic Rocks: Applications for Massive Sulphide Exploration. Geological Association of Canada, Short Course Notes 12:79-113

Pearce JA and Stern RJ (2006) Origin of Back-Arc Basin Magmas: Trace Element and Isotope Perspectives. In Christe DM, Fisher CR, Lee SM and Givens S (eds) Back-Arc Spreading Systems: Geological, Biological, Chemical, and Physical Interactions, American Geophysical Union, Washington, D. C.

Percillo R and Taylor SR (1976) Geochemistry of Eocene calc-alkaline volcanic rocks rocks from the Kastamonu area, northern Turkey. Contributions to Mineralogy and Petrology 58:63-81

Pestal G (1983) Beitrag zur Kenntnis der Geologie im mittleren Hohen Tauern Bereich des Amer- und Felbertals. Dissertation, University of Vienna

Pestal G, Hejl E, Braunstingl R, Schuster R (2009) Erläuterungen Geologische Karte von Salzburg 1:200.000. Land Salzburg & Geologische Bundesanstalt, Salzburg, Wien

Plimer IR (1984) Malayaite and tin-bearing silicates from a skarn at Doradilla via Bourke, New South Wales. Australian Journal of Earth Sciences 31:147-153

Plimer IR (1987) The association of tourmalinite with stratiform scheelite deposits. Mineralium Deposita 22:282-291

Pohl WL (2011) Economic Geology: Principles and Practise. Wiley-Blackwell

Portugaller T (2010) Scheelitvererzungen im Thurntaler Quarzphyllitkomplex, Osttirol: Petrographische und chemische Untersuchungen an Nebengesteinen und Bachsedimenten. Diplomarbeit Montanuniversität Leoben

Raith JG (1991) Stratabound tungsten mineralization in regional metamorphic calc-silicate rocks form the Austroalpine Crystalline Complex, Austria. Mineralium Deposita 26:72-80

Raith JG, Grum W, Prochaska W and Frank W (1995) Polymetamorphism and Polyphase Deformation of the Strat-Bound Magnesite-Scheelite Deposit, Tux-Lanersbach, Eastern Alps, Austria. Economic Geology 90:763-781

Raith JG, Stein HJ (2006) Variscan ore formation and metamorphism at the Felbertal scheelite deposit (Austria): constraining tungsten mineralisation from Re–Os dating of molybdenite. Contributions to Mineralogy and Petrology 152:505-521

Raith JG, Schmidt S (2010) Tungsten deposit Felbertal, Salzburg, Austria. Acta Mineralogica-Petrographica, Field Guide Series 3:1-24

Raith JG, Gerdes A, Cornell DH (2011) In situ U-Pb dating of scheelite: Constraints on the age and genesis of the Felbertal tungsten deposit. Mineralogical Magazine 75:1690

Rapp JF, Klemme S, Butler IB and Harley SL (2010) Extremely high solubility of rutile in chloride and fluoride-bearing metamorphic fluids: An experimental investigation. Geology 38:323-326

Reichl C, Schatz M, Zsak G (2016) World-Mining-Data 31, Vienna

Reitz E and Höll R (1988) Jungproterozoische Mikrofossilien aus der Habachformation in den mittleren Hohen Tauern und dem nordostbayerischen Grundgebirge. Jahrb Geol Bundesanst 131:329–340

Ribbe PH (1982) Titanite. In: Ribbe PH (ed) Orthosilicates. Mineralogical Society of America, Reviews in Mineralogy & Geochemistry 137-154

Rubin JN, Henry CD and Price JG (1993) The mobility of zirconium and other “immobile” elements during hydrothermal alteration. Chemical Geology 110:29-47

Sahama ThG (1946) On the chemistry of the mineral titanite. Bulletin de la Commission géologique de Finlande 138:88-120

Schmid SM, Fügenschuh B, Kissling E, Schuster R (2004) Tectonic map and overall architecture of the Alpine orogeny. Eclogae Geologicae Helvetiae 97:93-117

Schmid SM, Scharf A, Handy M, Rosenberg C (2013) The Tauern Window (Eastern Alps, Austria): a new tectonic map, with cross-sections and a tectonometamorphic synthesis. Swiss Journal of Geosciences 106:1-32

Schuster R, Pestal G and Reitner JM (2006) Erläuterungen zu Blatt 182 Spittal an der Drau. Geologische Karte der Republik Österreich 115. Geologische Bundesanstalt Wien

Shand SJ (1943) Eruptive rocks. Their genesis, composition, classification, and their relation to ore-deposits, 3rd edition. J. Wiley & Sons, New York

Shervais JW (1982) Ti-V plots and the petrogenesis of modern and ophiolitic lavas. Earth Planet. Si. Lett. 59:101-118

Skaarup P (1974) Strata-Bound Scheelite Mineralisation in Skarns and Gneisses from the Bindal Area, Northern Norway. Mineralium Deposita 9:299-308

Sonnet PH and Verkaeren J (1989) Scheelite-, Malayaite-, and Axinite-Bearing Skarns from El Hammam, Central Morocco. Economic Geology 84:575-590

Stampfli GM, von Raumer JF, Borel GD (2002a) Palaeozoic evolution of pre-Variscan terranes: From Bondwana to the Variscan collision. Geological Society of America Special Paper 364:263-280

Stampfli GM, Borel GD (2002b) A plate tectonic model for the Paleozoic and Mesozoic constrained by dynamic plate boundaries and restored synthetic oceanic isochrones. Earth and Planetary Scientific Letters 196:17-33

Stampfli GM, von Raumer J and Wilhelm C (2011) The Distribution of Gondwana-derived Terranes in the Early Palaeozoic. Ordovician of the World 14:567-574

Saunders AD and Tarney J (1984) Geochemical characteristics of basaltic volcanism within back-arc basins. Geological Society, London, Special Publications 16:59-76

Takenouchi S (1971) Hydrothermal synthesis and consideration of the genesis of Malayaite. Mineralium Deposita 6:335-347

Taylor SR, McLennan SM (1995): The geochemical evolution of the continental crust. Review of Geophysics 33:241-265

Thalhammer OAR, Stumpfl EF, Jahoda R (1989) The Mittersill scheelite deposit, Austria. Economic Geology 84:1153-1171

Thompson AB (1975) Calc-Silicate Diffusion Zones between Marble and Pelitic Schist. Journal of Petrology 16:314-346

Tilley CE (1951) A note on the progressive metamorphism of siliceous limestones and dolomites. Geological Magazine 88:175-178

Tornos F, Galindo C, Crespo JL, Spiro BF (2008) Geochemistry and origin of calcic tungsten-bearing skarns, Los Santos, Central Iberian Zone, Spain. The Canadian Mineralogist 46:87-109

Trommsdorf V (1966) Progressive Metamorphose kieseliger Karbonatgesteine in den Zentralalpen zwischen Bernina und Simplon. Schweizerische Mineralogische und Petrographische Mitteilungen 46:431-460

Ulmer P (1993) Norm-program for cation and oxygen mineral norms. Computer Library IMP-ETH, Zürich

Vavra G, Frisch W (1989) Pre-Variscan back-arc and island-arc magmatism in the Tauern Window (Eastern Alps). Tectonophysics 169:271-280

van Marcke De Lummen G (1986) Tin-bearing epidote from skarn in the Land's end aureole Cornwall, England. Canadian Mineralogist 24:411-415

von Quadt A (1985) Geochronologische, geochemische und isotopengeochemische Untersuchungen an Gesteinen der Habach-Formation, der Scheelitlagerstätte und des angrenzenden Altkristallins im Felbertal (Land Salzburg). Dissertation, Eidgenössische Technische Hochschule Zürich

von Quadt A (1987) U-Pb- und Sm-Nd-Datierungen der Habach-Formation und des Basisamphibolites im Bereich der mittleren Hohen Tauern. Uni-aktuell Salzburg 10:28

von Quadt A (1989) Sm-Nd and U-Pb systematics of zircon fractions, garnet and whole rock amphibolititic rocks of the Tauern window (Eastern Alps). Terra Abstracts 1:349

von Quadt A (1992) U-Pb zircon and Sm-Nd geochronology of mafic and ultramafic rocks from the central part of the Tauern Window (eastern Alps). Contributions to Mineralogy and Petrology 110:57-67

von Quadt A, Günther D, Frischknecht R, Zimmermann R and Franz G (1997) The evoluation of pre-Variscan eclogites of the Tauern Window (Eastern Alps): A Sm/Nd-, conventional Laser ICP-MS zircon U-Pb study. Schweizerische mineralogische und petrographische Mitteilungen 77:265-279

von Raumer JF, Stampfli GM, Borel G, Bussy F (2002) Organization of pre-Variscan basement areas at the north-Gondwanan margin. International Journal of Earth Sciences 91:35-52

von Raumer von JF, Bussy F, Schaltegger U, Schulz B and Stampfli G (2013) Pre-Mesozoic Alpine basements— Their place in the European Paleozoic framework. GSA Bulletin 125:89-108

von Raumer von JF, Stampfli GM, Arenas R, Martinez SS (2015) Ediacaran to Cambrian oceanic rocks of the Gondwana margin and their tectonic interpretation. International Journal of Earth Sciences 104:1107-1121

Weaver SD, Saunders AD, Pankhurst RJ and Tarney J (1979) A Geochemical Study of Magmatism Associated With the Initial Stages of Back-Arc Spreading. Petrology 68:151-169

Wenger H (1964) Die Scheelitlagerstätte Tux. Radex Rundschau 1964:109-132

Wieser B (2010) Samarium-Neodym Datierung und Spurenelementanalysen an Scheelit aus der Au-(W) Lagerstätte Schellgaden/Salzburg. Diplomarbeit Montanuniverstität Leoben

Winchester JA and Floyd PA (1976) Geochemical magma type discrimination; application to altered and metamorphosed basic igneous rocks. Earth and Planetary Scientific Letters 28:459-469

Winchester JA, Park RG and Holland JG (1980) The geochemistry of Lewisian semipelitic schists from the Gairloch District, Wester Ross. Scottish Journal of Geology 16:165-179

Winchester JA and Max MD (1982) The geochemistry and origins of the Precambrian rocks of the Rosslare Complex, S. E. Ireland. Journal of the Geological Society 139:309-319

Winter JD (2010) Principles of Igneous and Metamorphic Petrology. Pearson

Wood SA and Samson IM (2000) The Hydrothermal Geochemistry of Tungsten in Granitoid Environments: I. Relative Solubilities of Ferberite and Scheelite as a Function of T, P, pH, and m_{NaCl}. Economic Geology 95:143-182

Woodhead , Eggins S and Gamble J (1993) High field strength and transition element systematics in island arc and back-arc basin basalts: evidence for multi-phase melt extraction and a depleted mantle wedge. Earth and Planetary Scientific Letters 114:491-504

Xie L, Wang R, Chen J, Zhu J, Zhang W, Wang D and Yu A (2008) Primary Sn-rich titianite in the Qitianling granite, Hunan Province, southern China: An important type of tin-bearing mineral and its implications for tin exploration. Chinese Science Bulletin 54:798-805

Zimmermann R and Franz G (1988) Die Eklogite der unteren Schieferhülle; Frosnitztal/Südvenediger (Tauern, Österreich). Mitteilungen Österreichische Geologische Gesellschaft 81:167-188

Zimmermann R, Franz G, Hammerschmidt K, von Quadt A (1990) Polymetamorphic evolution of the Penninic basement (lower Schieferhülle) in the Tauern window: constraints from structural and petrologic data. Terra Abstracts 2:35-36

Zimmermann R (1992) Rekonstruktion der variskischen und alpinen Hochdruckmetamorphose in der penninischen Unteren Schieferhülle des zentralen, südlichen Tauernfensters (Österreich). PhD Thesis, Technischen Universität Berlin

Zimmermann R, Hammerschmidt K and Franz G (1994) Eocene high pressure metamorphism in the Penninic Units of the Tauern Window (Eastern Alps)—evidence from Ar40–Ar39 dating and petrological investigations. Contributions to Mineralogy and Petrology 117:175–186

Web resources

Bundesministerium für Wissenschaft, Forschung und Wirtschaft (2017) IRIS database. https://www.geologie.ac.at/services/webapplikationen/iris-interaktives-rohstoffinformationssystem

Landesregierung Tirol (2016) tirisMaps 2.0. https://www.tirol.gv.at/statistik-budget/tiris/ (accessed 5th July 2016)

Siivola J and Schmid R (2007) List of Mineral Abbreviations. Systematics of Metamorphic Rocks: Web version 01.02.07

U.S. Geological Survey (2016) Mineral commodity summaries 2016. http://dx.doi.org/10.3133/70140094 (accessed 27th November 2016)

Appendix

A.1 Sample list

Table 40: Whole rock geochemistry samples.

Sample	Description
02-10	Amphibolite
03-04	"Meta-agglomerate"
03-10	Hornblende-biotite gneiss
03-11	Hornblende-biotite gneiss
03-17	Czo-plg-calc-silicate fels
04-12	Czo-plg-calc-silicate fels
04-17	Czo-plg-calc-silicate fels
04-18	Orthogneiss
04-19	Orthogneiss
04-20	Orthogneiss
04-22	Czo-plg-calc-silicate fels
06-02	Czo-plg-calc-silicate fels
06-03	Czo-plg-calc-silicate fels
06-04	Hornblende fels
06-09	Amphibolite
06-10	Hornblende fels
06-13	Hornblende-biotite gneiss
06-21	Hornblende schist
06-22	Amphibolite
06-23	Amphibolite
06-24	Amphibolite
06-25	Amphibolite
07-02	Hornblende-biotite schist
07-03	Hornblende-biotite schist
07-04	Hornblende-biotite schist
07-09	Hornblende fels with sulphides
07-10	Orthogneiss
07-13	Hornblende-biotite schist
07-17	Hornblende-biotite schist
07-18	Orthogneiss
08-01	Calc-silicate rock Felbertal tungsten mine
08-02	Calc-silicate rock Felbertal tungsten mine

List of thin sections.

Sample	Mikroscopic description
02-05	Amphibolite
02-09	Hornblende-biotite gneiss
02-10	Amphibolite
03-03	Weinbühl Amphibolite
03-12	Amphibole schist
03-13	Czo-plg-calc-silicate fels
03-14	Czo-plg-calc-silicate fels
03-18	Amphibole schist
04-03	Fine-grained gneiss
04-09	Mylonitic garnet-biotite gneiss
04-11	Quartzite
05-01	Amphibole gneiss
05-02	Amphibole micaschist
05-03	Czo-plg-calc-silicate fels
05-04	Czo-plg-calc-silicate fels
02-07	Amphibole schist
04-06	Garnet amphibolite
04-07	Garnet orthogneiss
06-02	Czo-plg-calc-silicate fels (sulphide-rich)
06-08	Calc-silicate vein
06-06	Calc-silicate vein
06-05	Gneiss
06-12	Gneiss
06-13-13''	Hornblende-biotite gneiss
06-20	Czo-plg-calc-silicate fels
06-03	Czo-plg-calc-silicate fels
04-08	Garnet amphibole schist
06-11	Amphibolite with orthogneiss
02-04	Amphibole biotite schist
04-18	Orthogneiss
08-01	Calc-silicate rock Felbertal tungsten mine
08-02	Calc-silicate rock Felbertal tungsten mine
03-17	Czo-plg-calc-silicate fels
03-17'	Czo-plg-calc-silicate fels

Table 41: Samples analysed by XRF and XRD at WBH lab in Mittersill.

Sample	Description
03-17	Clinozoisite-plagioclase-calc-silicate fels from Messelingscharte
04-12	Clinozoisite-plagioclase-calc-silicate fels from Messelingscharte
04-17	Clinozoisite-plagioclase-calc-silicate fels from Messelingscharte
04-22	Clinozoisite-plagioclase-calc-silicate fels from Messelingscharte
06-02	Clinozoisite-plagioclase-calc-silicate fels from Messelingscharte
06-03	Clinozoisite-plagioclase-calc-silicate fels from Messelingscharte
08-01	Calc-silicate rock from Felbertal tungsten mine (Habach Complex)
08-02	Calc-silicate rock from Felbertal tungsten mine (Habach Complex)

A.2 Scheelite-bearing outcrops and boulders

Table 42: Coordinates and description of scheelite-bearing outcrops and boulders. Coordinate system WGS84. Elev. = elevation in m above sea level. Scheelite findings: major = lots of scheelite, yellow and blue scheelite, important outcrop; minor = little bit of scheelite, yellow and blue scheelite; traces = only few commonly blue scheelite grains.

ID	Latitude	Longitude	Elev.	Type	Lithology	Structures	Scheelite
162	47.143248	12.508974		in-situ	Qz-vein		traces
202	47.143357	12.508797	2.548	boulder			minor
204	47.143927	12.508515	2.540	in-situ	Hornblende schist		minor
205	47.143277	12.508813	2.549				minor
206	47.142842	12.509270	2.552	boulder			minor
292	47.143131	12.511110	2.537	boulder			major
301	47.143067	12.511009	2.551	in-situ			major
302	47.143001	12.511069	2.560	boulder			major
303	47.143499	12.510878	2.556	boulder			major
304	47.142982	12.509102	2.552	in-situ	Amphibolite		traces
305	47.143357	12.508889	2.547	in-situ	Quarz layer		traces
306	47.143488	12.508656	2.549	boulder			traces
315	47.142651	12.508032	2.532	in-situ	Chl-fsp-alteration of amphibolite	joint surface	minor
317	47.143132	12.507724	2.531	in-situ	Chl-fsp-alteration of amphibolite	isoclinal folds, sheared	traces
329	47.148150	12.518512	2.758	in-situ	Actinolite-biotit-talk schist		minor
345	47.147608	12.513460	2.669	in-situ	Actinolite -biotite schist		minor
350	47.144460	12.510342	2.585	in-situ	Amphibolite		minor
351	47.146814	12.511546	2.633	in-situ	Amphibolite		minor
369	47.141926	12.512122	2.513	in-situ			minor
370	47.141462	12.512284	2.512	in-situ	Amphibolite		minor
371	47.141729	12.512187	2.508	in-situ	Amphibolite		traces
372	47.142752	12.508332	2.546	in-situ	Amphibolite	isoclinal folds, sheared	traces
373	47.142821	12.508233	2.545	in-situ	Amphibolite	discordant qz-vein	minor
374	47.142878	12.508177	2.545	in-situ	Amphibolite	discordant qz-vein	minor
375	47.142929	12.508185	2.546	in-situ	Amphibolite	discordant qz-vein	minor
376	47.142922	12.508144	2.544	in-situ	Amphibolite	discordant qz-vein	minor
377	47.142986	12.508138	2.545	in-situ	Amphibolite	discordant qz-vein	minor
378	47.142983	12.508108	2.545	in-situ	Amphibolite	discordant qz-vein	minor
379	47.142984	12.508007	2.544	in-situ	Amphibolite	discordant qz-vein	minor
430	47.142932	12.509266	2.546	boulder	Amphibolite with qz-layers		traces
431	47.143064	12.509047	2.547	in-situ	Amphibolite with qz-layers		minor
432	47.143050	12.509014	2.549	in-situ	Amphibolite with qz-layers		minor
433	47.143155	12.509015	2.549	in-situ	Amphibolite with qz-layers		minor
434	47.143305	12.508776	2.548	in-situ	Amphibolite with qz-layers	pinch-and-swell	minor
435	47.143318	12.508972	2.548	in-situ	Amphibolite with qz-layers		minor
436	47.143350	12.508756	2.551	in-situ	Amphibolite with qz-layers		traces
437	47.143527	12.508465	2.547	boulder	Amphibolite		traces
438	47.149191	12.506041	2.516	boulder	Qz-layer		minor

A.3 Whole rock geochemistry

Basal Amphibolite (amphibolite)												
Analyte	**02-10**	**03-04**	**03-10**	**03-11**	**06-04**	**06-09**	**06-10**	**06-22**	**06-23**	**06-24**	**06-25**	**07-09**
SiO2	45.57	53.4	59.28	59.15	43.96	41.61	47.74	55.18	50.56	47.44	54.54	47.64
Al2O3	18.28	13.28	16.45	16.53	12.48	13.62	19.32	16.13	15.88	15.36	17.7	15.65
Fe2O3	11.28	7.83	7.24	7.32	13.53	16.16	10.2	7.39	10.78	12.66	7.84	11.18
MgO	7.31	11.33	3.13	3.17	12.34	10.93	5.86	6.86	6.66	8.4	4.55	7.56
CaO	10.18	5.73	5.65	5.63	11.43	11.45	9.21	8.51	9.47	10.23	7.86	10.33
Na2O	3.3	2.57	3.22	3.23	1.34	1.55	3.96	3.69	3.3	2.88	4.6	3.2
K2O	0.41	2.41	1.94	1.97	0.39	0.46	0.8	0.43	0.54	0.5	0.41	0.73
TiO2	1.63	0.99	1.11	1.11	2.21	1.94	1.32	0.57	1.49	1.01	1.2	1.78
P2O5	0.35	0.3	0.46	0.47	0.2	0.43	0.27	0.08	0.21	0.15	0.26	0.15
MnO	0.15	0.11	0.13	0.12	0.21	0.22	0.14	0.12	0.17	0.18	0.11	0.18
Cr2O3	0.026	0.087	0.014	0.01	0.056	0.04	0.019	0.035	0.023	0.053	0.02	0.033
TOT/C	0.05	<0.02	<0.02	<0.02	0.06	<0.02	<0.02	<0.02	<0.02	0.03	0.04	<0.02
TOT/S	<0.02	<0.02	<0.02	0.03	<0.02	<0.02	0.05	<0.02	<0.02	<0.02	<0.02	0.45
LOI	1.2	1.3	1.1	1	1.5	1.3	0.9	0.8	0.7	0.9	0.7	1.3
Sum	99.74	99.69	99.81	99.81	99.7	99.68	99.75	99.82	99.78	99.76	99.78	99.72
Ba	120	2703	736	732	78	86	383	102	116	91	171	163
Ni	59	385	29	<20	330	101	48	105	55	109	40	62
Sc	25	16	15	16	20	41	27	20	33	36	17	39
Be	<1	2	1	4	<1	<1	<1	2	1	<1	<1	1
Co	34.7	42.6	13.9	14.4	58.7	49.5	29.9	28.8	35.8	37.4	23.3	39.7
Cs	0.3	11.6	6.1	5.1	4.7	0.8	4.1	0.5	0.8	2.2	0.5	3.2
Ga	22	16.1	18.4	20.1	24	24.9	19.6	15.2	17	17.8	18	16.2
Hf	2.3	5	6.4	6.1	3.5	5.6	3.4	1.7	4	2.4	3.7	4.6
Nb	9.9	11.5	18.1	17	22.4	7	8	2.3	5.5	2.5	4.1	7.7
Rb	4.9	86.9	61.4	61.3	8.5	3.5	17.8	7.3	13.2	13.7	5.4	25.7
Sn	<1	2	2	2	4	2	<1	<1	5	1	<1	2
Sr	544.7	311.9	444.1	446.7	64.8	86.3	714.2	253.1	265.3	218.7	675.3	379.7
Ta	0.5	0.6	1	0.9	1.3	0.2	0.4	0.2	0.3	0.2	0.3	0.5
Th	0.8	15.4	5.5	5.3	<0.2	0.6	1.1	0.7	2.5	0.4	2.1	6.7
U	0.3	4.1	2.4	2.3	<0.1	0.1	0.3	0.1	1.2	0.2	0.3	2.4
V	233	140	113	114	227	343	195	132	252	279	162	299
W	1.2	3.2	3.1	2.4	3.8	1.7	0.7	2	5.8	2.1	5.4	1.3
Zr	68	193.9	256.9	255.1	140.2	228.2	132.3	59.5	149.6	84.2	151	156.7
Y	19.7	19.6	30.8	31.3	22.3	31.8	25.7	18.5	35.4	30.4	17.4	34.7
La	9.8	35.3	34.6	33.3	2.7	16.9	18.3	4.7	11.5	8.2	13.7	17.6
Ce	23.5	72.2	74.9	70.7	13.6	43	40.1	11.7	29.2	17.2	31.9	37.7
Pr	3.53	8.55	9.29	9.01	3.32	6.33	5.46	1.69	4.08	2.78	4.16	4.6
Nd	17.9	32.7	37.2	37	19.6	30.7	24.2	7.5	19.1	14.3	18.4	18.8
Sm	4.36	5.81	7.2	7.03	5.83	7.29	5.02	2.09	4.89	3.68	4.11	4.6
Eu	1.6	1.37	1.86	1.89	1.81	2.21	1.46	0.76	1.61	1.09	1.38	1.57
Gd	4.38	4.9	6.51	6.7	5.47	6.91	5.31	2.73	5.84	5.02	3.98	5.81
Tb	0.67	0.65	0.99	0.99	0.82	1.09	0.84	0.47	0.99	0.83	0.58	0.95
Dy	3.82	3.7	5.64	5.56	4.39	6.34	4.88	3.13	6.13	5.42	3.24	6.13
Ho	0.75	0.67	1.15	1.14	0.87	1.17	1.01	0.65	1.35	1.13	0.66	1.32
Er	2.07	1.91	3.26	3.22	2.36	3.27	2.83	2.03	3.92	3.38	1.82	4
Tm	0.28	0.27	0.47	0.43	0.29	0.44	0.38	0.27	0.54	0.46	0.25	0.56
Yb	1.97	1.8	2.92	2.86	1.97	2.77	2.52	2.03	3.6	3.03	1.63	3.43
Lu	0.3	0.27	0.46	0.46	0.3	0.4	0.35	0.3	0.53	0.46	0.25	0.52
Mo	0.2	1.1	3.6	1.9	0.7	0.2	0.3	1.7	0.7	0.4	1.6	7.9
Cu	6.7	45.1	14.4	12.8	28.5	12.2	17.9	9.5	44.7	12.4	24.7	164.9
Pb	1	2.9	2.3	2.6	0.8	1.5	1.4	1.2	1.2	0.8	0.8	1.1
Zn	23	48	82	79	39	36	26	12	18	16	22	21
Ni	11.6	217.5	14.8	15	90.3	22.4	13.3	21.7	22.7	24.2	13.6	30.6
As	<0.5	<0.5	0.5	<0.5	<0.5	<0.5	<0.5	0.6	0.5	1.2	0.6	0.6
Cd	<0.1	<0.1	<0.1	<0.1	<0.1	<0.1	<0.1	<0.1	<0.1	<0.1	<0.1	<0.1
Sb	<0.1	<0.1	<0.1	<0.1	<0.1	<0.1	<0.1	<0.1	<0.1	<0.1	<0.1	<0.1
Bi	<0.1	<0.1	<0.1	<0.1	<0.1	<0.1	<0.1	<0.1	<0.1	<0.1	<0.1	<0.1
Ag	<0.1	<0.1	<0.1	<0.1	<0.1	<0.1	<0.1	<0.1	<0.1	<0.1	<0.1	<0.1
Au	<0.5	<0.5	<0.5	<0.5	<0.5	<0.5	<0.5	<0.5	<0.5	<0.5	<0.5	0.6
Hg	<0.01	<0.01	<0.01	<0.01	<0.01	<0.01	<0.01	<0.01	<0.01	<0.01	<0.01	<0.01
Tl	<0.1	0.6	0.3	0.3	<0.1	<0.1	0.2	<0.1	<0.1	<0.1	<0.1	0.2
Se	<0.5	<0.5	<0.5	<0.5	<0.5	<0.5	<0.5	<0.5	<0.5	<0.5	<0.5	<0.5

Basal Amphibolite (hornblende-biotite schist and hornblende schist)							Hornblende-biotite gneiss		
Analyte	**06-21**	**07-02**	**07-03**	**07-04**	**07-13**	**07-17**	**03-10**	**03-11**	**06-13**
SiO2	56.00	52.09	56.63	54.68	53.66	51.18	59.28	59.15	62.01
Al2O3	18.14	16.66	18.73	21.38	18.44	19.12	16.45	16.53	18.38
Fe2O3	7.17	11.08	4.99	8.8	7.68	7.24	7.24	7.32	4.87
MgO	3.75	4.1	4.25	3.28	4.43	6.33	3.13	3.17	2.02
CaO	5.9	7.1	5.75	1.68	7.43	7.26	5.65	5.63	5.73
Na2O	4.52	2.64	5.34	1.07	4.97	4.25	3.22	3.23	3.93
K2O	1.45	2.18	1.71	4.84	1.01	0.85	1.94	1.97	1.32
TiO2	1.31	2.01	0.73	0.93	0.93	1.17	1.11	1.11	0.56
P2O5	0.29	0.55	0.33	0.13	0.2	0.41	0.46	0.47	0.21
MnO	0.11	0.18	0.07	0.16	0.12	0.11	0.13	0.12	0.09
Cr2O3	0.005	0.043	0.016	0.023	0.008	0.017	0.014	0.01	0.006
TOT/C	<0.02	0.07	0.13	0.21	0.03	0.08	<0.02	<0.02	<0.02
TOT/S	<0.02	0.35	<0.02	0.11	0.05	<0.02	<0.02	0.03	<0.02
LOI	0.6	1.1	1.1	2.7	0.9	1.7	1.1	1	0.7
Sum	99.82	99.8	99.75	99.85	99.79	99.67	99.81	99.81	99.86
Ba	568	453	980	1386	392	360	736	732	410
Ni	<20	129	74	23	31	59	29	<20	<20
Sc	18	24	12	20	17	19	15	16	7
Be	<1	9	2	3	<1	2	1	4	4
Co	14.6	31.4	17.2	12.5	24.1	17.2	13.9	14.4	7.3
Cs	4.3	4.7	3.6	11	1.3	4.7	6.1	5.1	9.3
Ga	17.2	15.6	18.5	23.4	19.8	19	18.4	20.1	18.8
Hf	3.3	5.1	7.4	3.3	1.4	11.3	6.4	6.1	3
Nb	7.9	59.8	6	13.8	3.5	5.9	18.1	17	6.8
Rb	55.6	81.8	62.6	146.7	38	25.8	61.4	61.3	60
Sn	<1	8	<1	2	<1	5	2	2	2
Sr	490.3	183.9	818.3	135.5	735.1	762.2	444.1	446.7	613.5
Ta	0.5	3	0.3	1	0.3	0.2	1	0.9	0.5
Th	2.9	5.5	14.3	15.2	1.2	18.7	5.5	5.3	2.4
U	1.3	1.2	3.4	2.2	0.2	4	2.4	2.3	1.4
V	155	125	93	144	161	166	113	114	59
W	2.2	13.9	1.5	11.7	1.6	7.5	3.1	2.4	2.2
Zr	126.5	210.2	320.6	115.1	51.4	437.2	256.9	255.1	114.4
Y	18.2	29.3	12.2	27.9	10.3	29.6	30.8	31.3	14.7
La	15.9	40	45.2	47.3	12.1	67.8	34.6	33.3	15.2
Ce	34.3	79.8	82.5	86.8	25.7	126.2	74.9	70.7	30.6
Pr	4.4	9.06	9.18	9.74	3.19	13.83	9.29	9.01	3.95
Nd	19.8	34.7	31.2	36.8	13.2	48.6	37.2	37	16.2
Sm	4.2	6.63	4.74	6.38	2.45	7.54	7.2	7.03	3.23
Eu	1.67	1.89	1.5	1.79	1.07	1.77	1.86	1.89	1.04
Gd	4.19	6.27	3.69	6.11	2.66	6.34	6.51	6.7	3.05
Tb	0.6	0.94	0.45	0.91	0.37	0.9	0.99	0.99	0.47
Dy	3.43	5.26	2.53	5.43	2.22	5.48	5.64	5.56	2.49
Ho	0.68	1.12	0.45	0.98	0.37	1.09	1.15	1.14	0.52
Er	1.98	3.11	1.25	2.93	1.09	3.29	3.26	3.22	1.58
Tm	0.26	0.42	0.17	0.42	0.15	0.45	0.47	0.43	0.22
Yb	1.72	2.89	1.09	2.65	1.11	3.19	2.92	2.86	1.52
Lu	0.26	0.42	0.16	0.41	0.15	0.48	0.46	0.46	0.24
Mo	0.6	2.3	0.6	2.6	0.5	0.5	3.6	1.9	1.4
Cu	2.9	82.1	7.5	39.8	15.7	8.5	14.4	12.8	4.3
Pb	0.7	2.9	1	3.2	2.3	1.7	2.3	2.6	1.4
Zn	45	97	48	60	39	29	82	79	64
Ni	7	111.9	49.9	21.3	13.6	21.2	14.8	15	1.9
As	<0.5	1.4	0.6	<0.5	<0.5	<0.5	0.5	<0.5	<0.5
Cd	<0.1	<0.1	<0.1	<0.1	<0.1	<0.1	<0.1	<0.1	<0.1
Sb	<0.1	<0.1	<0.1	<0.1	<0.1	<0.1	<0.1	<0.1	<0.1
Bi	<0.1	0.1	<0.1	0.1	<0.1	<0.1	<0.1	<0.1	<0.1
Ag	<0.1	0.1	<0.1	<0.1	<0.1	<0.1	<0.1	<0.1	<0.1
Au	<0.5	0.5	<0.5	<0.5	<0.5	<0.5	<0.5	<0.5	<0.5
Hg	<0.01	<0.01	<0.01	<0.01	<0.01	<0.01	<0.01	<0.01	<0.01
Tl	0.4	0.5	0.4	0.5	0.3	0.2	0.3	0.3	0.4
Se	<0.5	0.5	<0.5	<0.5	<0.5	<0.5	<0.5	<0.5	<0.5

Messeling gneiss (Granatspitz gneiss)					
Analyte	**04-18**	**04-19**	**04-20**	**07-10**	**07-18**
SiO2	75.83	72.88	72.98	75.75	73.5
Al2O3	13.46	14.76	14.67	13.13	14.28
Fe2O3	1.31	1.7	1.69	1.21	1.54
MgO	0.33	0.56	0.48	0.43	0.39
CaO	0.63	0.64	0.52	0.48	0.99
Na2O	3.32	3.04	3.17	3.58	3.26
K2O	4.17	4.88	4.8	4.22	4.98
TiO2	0.16	0.21	0.21	0.24	0.19
P2O5	0.17	0.2	0.22	0.21	0.2
MnO	0.02	0.03	0.03	<0.01	0.03
Cr2O3	0.011	0.01	0.011	0.007	0.012
TOT/C	0.03	0.04	0.02	0.04	0.02
TOT/S	<0.02	<0.02	<0.02	<0.02	<0.02
LOI	0.6	1	1.1	0.6	0.6
Sum	99.99	99.96	99.96	99.95	99.96
Ba	135	452	396	299	349
Ni	<20	<20	<20	<20	<20
Sc	2	3	3	3	2
Be	<1	4	4	9	3
Co	1.9	3	2.6	2.1	2.7
Cs	8	8.7	6.4	8.3	17.6
Ga	14.8	17.2	16.9	13.9	15.6
Hf	2.3	3	2.9	3.8	2.7
Nb	13.2	15.1	16.9	16.4	14.9
Rb	202.8	220.1	214.5	180.6	261.8
Sn	9	15	16	6	10
Sr	60.7	86.3	98.2	56.3	77.7
Ta	1.7	1.9	2.6	1.9	2.2
Th	7	10	10.3	12.5	9.1
U	1.9	3.5	3.8	2.8	4.3
V	11	15	16	23	19
W	5.4	5.9	5.6	4.2	4
Zr	71.7	100.8	96.7	130	87.4
Y	9.6	13.2	10.9	20.2	15
La	8.9	17.2	11.1	25.2	17.3
Ce	22.4	40.5	33.3	55.6	34.5
Pr	2.32	4.4	2.83	6.23	4.12
Nd	8.3	16.2	10.5	24.1	15.1
Sm	1.79	3.32	2.15	4.56	3.12
Eu	0.21	0.48	0.31	0.48	0.48
Gd	1.93	3.05	2.04	4.24	2.96
Tb	0.31	0.49	0.31	0.67	0.5
Dy	1.77	2.63	1.92	4.13	2.93
Ho	0.32	0.47	0.4	0.7	0.5
Er	1.05	1.42	1.12	1.79	1.36
Tm	0.14	0.18	0.18	0.28	0.2
Yb	1.05	1.19	1.17	1.75	1.28
Lu	0.12	0.18	0.16	0.25	0.19
Mo	4	2.8	2.6	1.4	2.9
Cu	2.4	2.9	3.7	5	3.4
Pb	4.9	6.7	7.3	4.6	3.8
Zn	20	34	24	21	30
Ni	3.1	2.4	2.7	2.8	2.8
As	<0.5	<0.5	<0.5	<0.5	<0.5
Cd	<0.1	<0.1	<0.1	<0.1	<0.1
Sb	<0.1	<0.1	<0.1	<0.1	<0.1
Bi	0.2	1.2	1	0.1	0.1
Ag	<0.1	<0.1	<0.1	<0.1	<0.1
Au	<0.5	<0.5	<0.5	<0.5	<0.5
Hg	<0.01	<0.01	<0.01	<0.01	<0.01
Tl	<0.1	0.2	0.1	0.2	0.4
Se	<0.5	<0.5	<0.5	<0.5	<0.5

Calc-silicate rocks (Felbertal tungsten mine)			Clinozoisite-plagioclas-calc-silicate fels (Messelingscharte)					
Analyte	**08-01**	**08-01**	**03-17**	**04-12**	**04-17**	**04-22**	**06-02**	**06-03**
SiO2	43.9	48.38	45.51	51.93	40.32	51.68	55.77	46.7
Al2O3	22.16	17.77	17.47	19.03	18.87	20.3	19.32	20.9
Fe2O3	9.26	8.2	8.09	4.79	8.56	4.46	6.15	7.84
MgO	2.03	3.82	2.65	0.25	2.59	0.39	1.45	0.64
CaO	18.21	15.52	15.85	14.67	18.58	13.56	9.06	18.44
Na2O	1.25	1.5	0.65	2.1	0.34	2.88	3.76	0.4
K2O	0.26	0.86	0.18	0.49	0.19	0.7	1.03	0.66
TiO2	0.56	0.82	0.25	0.04	0.56	0.06	0.33	0.29
P2O5	0.08	0.3	0.12	0.75	0.29	0.52	0.24	0.1
MnO	0.14	0.18	0.15	0.08	0.17	0.07	0.07	0.11
Cr2O3	0.041	0.023	0.021	0.022	0.021	0.012	0.012	0.013
TOT/C	0.29	0.35	0.16	<0.02	0.11	<0.02	0.06	0.06
TOT/S	1.53	0.11	0.18	<0.02	0.09	<0.02	0.79	0.78
LOI	1.8	2.1	2.5	1.3	2.4	1.4	2.1	2.1
Sum	99.71	99.46	93.45	95.47	92.95	96.09	99.39	98.27
Ba	239	205	65	297	81	428	475	303
Ni	64	40	50	<20	37	<20	67	<20
Sc	22	32	39	22	38	22	10	15
Be	1	9	18	29	11	40	41	7
Co	26.4	26.2	20.8	2.2	18.1	2.8	108.9	3.6
Cs	1.2	8.2	2.7	2.2	5.4	3.3	4.9	12
Ga	33.9	34.6	40.8	39.1	44.5	36.1	27.2	64.2
Hf	0.9	1.2	1	0.1	1.5	0.4	0.6	0.8
Nb	1	2.2	2.4	1.3	8.4	0.8	3.9	2.7
Rb	35.9	99.1	7.2	22.8	7.9	35	57.2	27.5
Sn	86	56	760	303	640	314	259	1580
Sr	704.2	490.5	786.4	1088.5	1048.5	1040.2	975.2	944.4
Ta	<0.1	<0.1	0.1	<0.1	0.4	<0.1	0.1	0.1
Th	<0.2	<0.2	2.2	<0.2	3.8	0.5	0.3	<0.2
U	0.1	1.1	2.5	1.8	2.9	1.9	1.5	1.8
V	204	258	237	131	227	112	131	346
W	391.6	2645.9	>10000.0	>10000.0	>10000.0	>10000.0	585.1	>10000.0
Zr	29.7	45.3	29.9	4.5	58.5	7.3	21	27.6
Y	12.7	19	29.4	48.9	23.1	31.5	10.9	16.5
La	1.4	1.4	3.9	1.7	10.7	1.2	3.3	2.9
Ce	3.2	5.1	8.4	3.8	23.1	3.5	8.3	6.6
Pr	0.53	0.74	1.19	0.73	2.93	0.55	1.15	0.89
Nd	2.9	4.4	5.1	4.7	13.1	2.8	5	3.9
Sm	0.91	1.49	1.39	1.96	2.39	1.2	1.14	0.71
Eu	0.91	0.77	1.01	4.26	1.32	2.24	0.8	0.62
Gd	1.66	2.61	1.74	3.86	2.33	2.2	1.3	1.27
Tb	0.32	0.47	0.45	0.85	0.45	0.53	0.22	0.26
Dy	2.11	3.08	3.38	5.91	2.84	3.75	1.41	1.81
Ho	0.51	0.69	1.03	1.56	0.82	1	0.34	0.53
Er	1.51	2.23	3.23	4.82	2.89	3.49	1.19	1.86
Tm	0.23	0.34	0.53	0.68	0.42	0.52	0.19	0.29
Yb	1.38	2.32	4	4.55	2.9	3.61	1.04	2.14
Lu	0.23	0.35	0.57	0.7	0.43	0.55	0.18	0.36
Mo	8.6	64.1	100	10.4	35.5	13.9	4.4	9.4
Cu	453.2	86.7	831.1	37.1	588.3	96.6	2437.8	122
Pb	2.1	8.7	23.1	4	8.5	5.9	19.5	4.9
Zn	10	30	73	8	65	13	94	15
Ni	70.6	24.8	64.3	6.7	49	9.3	77.2	15.5
As	115.2	4.1	1.7	<0.5	3.1	9.7	9.6	<0.5
Cd	<0.1	0.2	1.2	<0.1	1	<0.1	1.3	0.1
Sb	0.4	0.2	<0.1	<0.1	<0.1	<0.1	<0.1	<0.1
Bi	2.6	3.2	1.5	0.3	0.5	0.4	0.6	0.5
Ag	0.4	<0.1	2	<0.1	1.5	0.3	4.4	0.2
Au	12.2	2.3	3	<0.5	2.8	5.8	5.2	<0.5
Hg	*	*	*	*	*	*	*	*
Tl	0.3	0.9	<0.1	<0.1	<0.1	<0.1	0.2	<0.1
Se	0.6	<0.5	<0.5	<0.5	<0.5	<0.5	0.8	<0.5

A.4 XRD bulk rock composition

Table 43: Quantitative XRD phase analysis. Values in mass%.

Mineral	03-17	04-12	04-17	04-22	06-03	08-01	08-02
Quartz	21.66	15.75	7.62	12.81	27.49	9.06	15.63
Clinozoisite	37.33	31.25	51.44	24.59	53.91	55.24	39.76
Albite	10.98	45.87	8.06	21.2	4.68	14.05	13.25
Anorthite	0	0	0	33.61	3.98	0	0
Scheelite	8.25	4.73	7.96	3.05	1.92	0.87	1.46
Hornblende	8.64	0	9.66	0	0	0	0
Calcite	1.62	0.23	1.23	0.75	2.43	4.58	4.59
Chlorite	10.23	1.11	12.19	2.17	3.36	1.66	3.77
Phlogopite	1.29	0.52	0.54	0.76	1.25	0	0
Almandine	0	0.54	0	1.06	0.99	0	0
Muscovite	0	0	1.3	0	0	0	0
Biotite	0	0	0	0	0	1.81	5.3
Actinolite	0	0	0	0	0	12.73	16.22

A.5 Electron probe micronalyzer (EMPA)

A.5.1 Scheelite in clinozoisite-plagioclase-calc-silicate rocks (Messelingscharte)

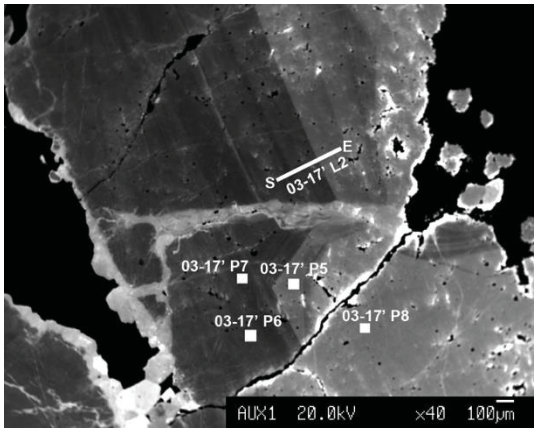

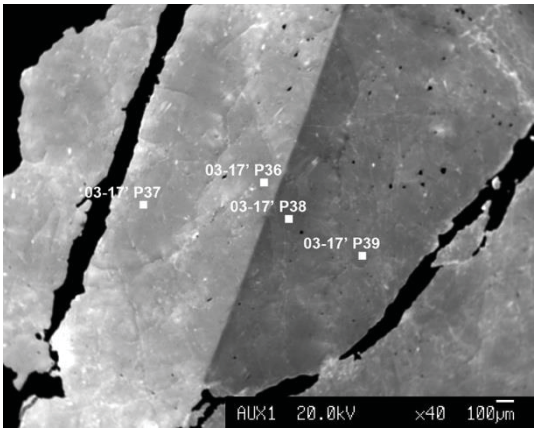

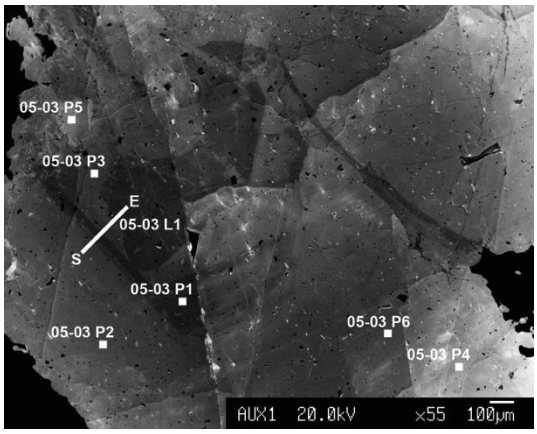

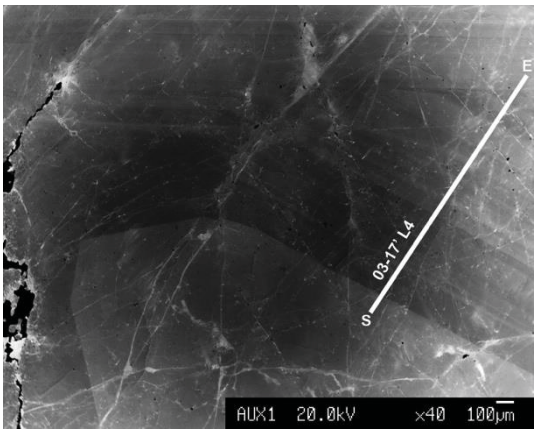

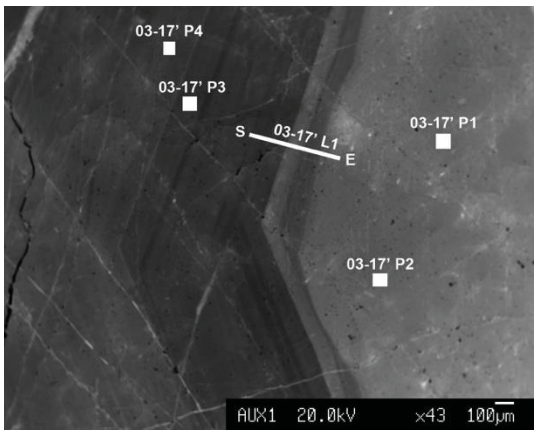

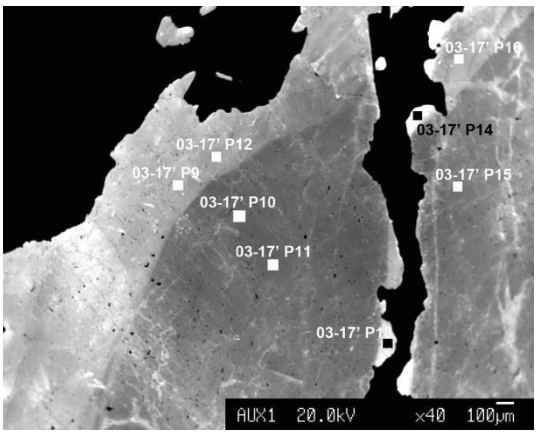

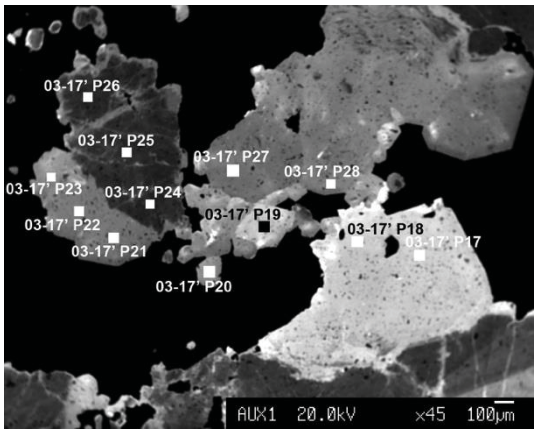

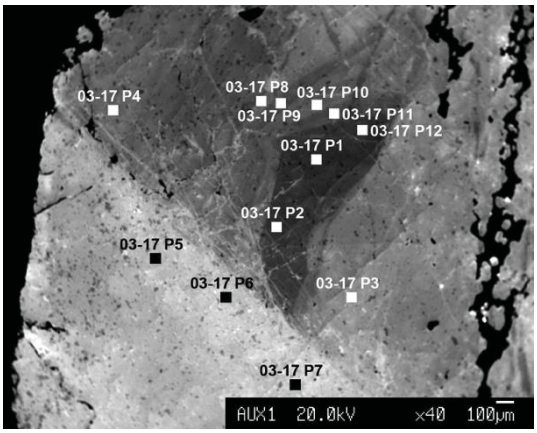

Name	CaO	WO3	MoO3	Total	Name	CaO	WO3	MoO3	Total
1 03-17' L4	20.102	79.649	1.132	100.883	4 03-17' L2	20.252	77.345	1.383	98.98
2 03-17' L4	20.149	79.254	1.061	100.464	5 03-17' L2	19.977	76.901	1.266	98.144
3 03-17' L4	20.174	79.175	1.151	100.5	6 03-17' L2	20.433	76.629	1.226	98.288
4 03-17' L4	20.12	79.534	1.111	100.765	7 03-17' L2	20.233	77.746	1.455	99.434
5 03-17' L4	20.123	78.765	1.083	99.971	8 03-17' L2	20.14	77.797	1.212	99.149
6 03-17' L4	20.049	79.014	1.02	100.083	9 03-17' L2	20.198	77.37	1.096	98.664
7 03-17' L4	20.352	79.621	1.044	101.017	10 03-17' L2	20.031	77.391	1.111	98.533
8 03-17' L4	20.087	77.532	1.553	99.172	11 03-17' L2	20.172	77.986	1.137	99.295
9 03-17' L4	20.306	79.384	1.233	100.923	12 03-17' L2	20.087	77.614	1.19	98.891
10 03-17' L4	20.298	78.798	1.725	100.821	13 03-17' L2	20.153	77.254	1.215	98.622
11 03-17' L4	20.585	78.461	1.675	100.721	14 03-17' L2	20.415	76.917	1.187	98.519
12 03-17' L4	20.391	78.64	1.617	100.648	15 03-17' L2	20.092	77.741	1.194	99.027
13 03-17' L4	20.226	78.696	1.435	100.357	16 03-17' L2	20.225	76.456	1.178	97.859
14 03-17' L4	20.461	78.545	1.514	100.52	17 03-17' L2	20.144	79.071	0.441	99.656
15 03-17' L4	20.417	78.48	1.522	100.419	18 03-17' L2	20.029	78.172	0.411	98.612
16 03-17' L4	20.43	78.285	1.394	100.109	19 03-17' L2	19.943	78.053	0.458	98.454
18 03-17' L4	20.264	78.893	1.483	100.64	20 03-17' L2	19.857	77.85	0.485	98.192
19 03-17' L4	20.116	78.211	1.487	99.814	21 03-17' L2	19.9	78.229	0.487	98.616
20 03-17' L4	20.215	78.761	1.358	100.334	22 03-17' L2	19.969	78.276	0.409	98.654
21 03-17' L4	20.176	79.29	1.464	100.93	23 03-17' L2	20.017	78.477	0.449	98.943
22 03-17' L4	20.131	78.204	1.404	99.739	24 03-17' L2	20.252	78.373	0.493	99.118
23 03-17' L4	20.241	79.451	1.448	101.14	25 03-17' L2	20.198	78.576	0.587	99.361
24 03-17' L4	20.288	78.565	1.393	100.246	26 03-17' L2	20.01	78.886	0.42	99.316
25 03-17' L4	20.142	78.586	1.509	100.237	1 03-17' L1	20.405	79.148	1.072	100.625
26 03-17' L4	20.294	78.552	1.301	100.147	2 03-17' L1	20.142	78.946	1.099	100.187
27 03-17' L4	20.128	79.299	1.2	100.627	3 03-17' L1	20.245	79.247	1.093	100.585
28 03-17' L4	20.486	78.878	1.217	100.581	4 03-17' L1	20.029	77.899	1.074	99.002
29 03-17' L4	20.311	79.385	1.06	100.756	5 03-17' L1	19.992	78.616	1.158	99.766
30 03-17' L4	20.358	78.416	1.07	99.844	6 03-17' L1	20.353	78.297	1.273	99.923
31 03-17' L4	20.213	78.989	1.281	100.483	7 03-17' L1	20.48	78.898	1.434	100.812
32 03-17' L4	20.078	78.212	1.262	99.552	8 03-17' L1	20.051	79.662	0.978	100.691
33 03-17' L4	20.2	78.494	1.495	100.189	9 03-17' L1	19.28	77.407	1.007	97.694
34 03-17' L4	20.329	78.874	1.126	100.329	10 03-17' L1	19.992	78.751	0.96	99.703
35 03-17' L4	19.931	78.354	1.164	99.449	11 03-17' L1	20.164	79.562	0.6	100.326
36 03-17' L4	20.084	79.255	0.822	100.161	12 03-17' L1	20.108	79.916	0.453	100.477
37 03-17' L4	20.044	79.105	1.029	100.178	13 03-17' L1	20	80.333	0.565	100.898
38 03-17' L4	20.007	79.158	1.028	100.193	14 03-17' L1	19.127	77.338	0.961	97.426
39 03-17' L4	20.256	79.233	1.079	100.568	15 03-17' L1	20.168	80.019	0.706	100.893
40 03-17' L4	20.256	78.456	1.088	99.8	16 03-17' L1	20.433	79.226	0.641	100.3
41 03-17' L4	19.994	79.315	0.906	100.215	17 03-17' L1	20.126	79.496	0.385	100.007
42 03-17' L4	19.998	77.752	0.905	98.655	18 03-17' L1	20.124	80.159	0.318	100.601
43 03-17' L4	20.306	79.592	1.034	100.932	19 03-17' L1	19.836	80.233	0.259	100.328
44 03-17' L4	20.37	79.367	1.114	100.851	20 03-17' L1	20.004	80.191	0.229	100.424
45 03-17' L4	19.982	78.888	1.02	99.89	21 03-17' L1	20.068	80.216	0.241	100.525
46 03-17' L4	20.193	78.066	1.225	99.484	22 03-17' L1	20.223	80.82	0.304	101.347
47 03-17' L4	20.311	78.805	1.618	100.734	23 03-17' L1	20.045	80.331	0.253	100.629
48 03-17' L4	20.235	78.85	1.427	100.512	24 03-17' L1	20.295	80.224	0.289	100.808
49 03-17' L4	20.217	79.116	1.217	100.55	25 03-17' L1	20.223	81.039	0.282	101.544
50 03-17' L4	20.205	79.664	1.075	100.944	26 03-17' L1	20.275	80.546	0.307	101.128
51 03-17' L4	20.271	79.552	0.973	100.796	1 05-03 L1	19.949	79.838	0.172	99.959
52 03-17' L4	20.351	79.377	1.023	100.751	2 05-03 L1	20.199	79.799	0.172	100.17
53 03-17' L4	20.25	79.379	1.175	100.804	3 05-03 L1	20.053	80.31	0.213	100.576
54 03-17' L4	20.222	78.228	1.251	99.701	4 05-03 L1	20.014	80.016	0.261	100.291
55 03-17' L4	20.207	78.512	1.076	99.795	5 05-03 L1	20.161	79.797	0.42	100.378
56 03-17' L4	20.182	78.69	1.099	99.971	6 05-03 L1	19.896	79.341	0.606	99.843
57 03-17' L4	19.714	76.644	1.196	97.554	7 05-03 L1	20.092	79.578	0.339	100.009
58 03-17' L4	19.997	78.145	1.222	99.364	8 05-03 L1	19.955	79.624	0.356	99.935
59 03-17' L4	20.03	78.187	1.178	99.395	9 05-03 L1	20.055	80.093	0.139	100.287
60 03-17' L4	20.106	77.829	1.075	99.01	10 05-03 L1	20.223	79.411	0.451	100.085
61 03-17' L4	20.122	79.609	1.056	100.787	11 05-03 L1	20.295	80.241	0.487	101.023
62 03-17' L4	20.275	79.181	1.072	100.528	12 05-03 L1	20.089	79.27	0.613	99.972
2 03-17' L2	20.092	77.832	1.043	98.967	13 05-03 L1	19.958	80.143	0.618	100.719
3 03-17' L2	19.75	76.968	1.22	97.938	14 05-03 L1	20.181	79.865	0.569	100.615
4 03-17' L2	20.252	77.345	1.383	98.98					

Name	CaO	WO3	MoO3	Total
03-17' P1	20.22	79.755	0.279	100.254
03-17' P2	19.951	79.548	0.304	99.803
03-17' P3	19.898	79.441	0.949	100.288
03-17' P4	20.406	78.613	0.964	99.983
03-17' P5	20.043	78.699	0.378	99.12
03-17' P6	20.183	78.138	1.323	99.644
03-17' P7	20.29	77.087	1.415	98.792
03-17' P8	20.144	78.875	0.367	99.386
03-17' P9	19.908	80.6	0.032	100.54
03-17' P10	19.883	79.804	0.231	99.918
03-17' P11	20.005	79.725	0.534	100.264
03-17' P12	19.901	79.738	0.495	100.134
03-17' P13	19.454	80.311	0.056	99.821
03-17' P14	20.334	80.911		101.245
03-17' P15	19.652	79.514	0.488	99.654
03-17' P16	19.694	80.668	0.131	100.493
03-17' P17	19.987	79.141	0.995	100.123
03-17' P18	20.068	79.645	0.093	99.806
03-17' P19	20.075	80.143	0.113	100.331
03-17' P20	19.88	80.095	0.07	100.045
03-17' P21	20.05	80.93		100.98
03-17' P22	19.927	80.246	0.042	100.215
03-17' P23	19.793	80.609	0.064	100.466
03-17' P24	20	79.143	0.928	100.071
03-17' P25	20.152	78.275	1.303	99.73
03-17' P26	20.046	78.248	1.277	99.571
03-17' P27	20.021	80.371		100.401
03-17' P28	20.234	79.278	0.078	99.59
03-17' P29	20.36	80.835	0.066	101.261
03-17' P30	20.497	78.22	1.591	100.308
03-17' P31	20.162	79.596	0.291	100.049
03-17' P32	20.303	80.768	0.044	101.115
03-17' P33	20.137	79.629	1.425	101.191
03-17' P34	20.228	80.758	0.116	101.102
03-17' P35	19.913	80.69	0.094	100.697
03-17' P36	19.889	79.543		99.432
03-17' P37	20.063	80.497		100.57
03-17' P38	19.985	79.716	0.609	100.31
03-17' P39	20.293	79.113	0.573	99.979
03-17 P1	20.568	78.116	1.484	100.168
03-17 P2	20.396	78.281	1.583	100.26
03-17 P3	19.99	79.477	0.311	99.778
03-17 P4	20.264	80.855	0.647	101.766
03-17 P5	19.998	79.793	0.056	99.847
03-17 P6	20.088	79.947	0.03	100.065
03-17 P7	19.7	79.688	0.087	99.475
03-17 P8	20.235	79.757	0.362	100.354
03-17 P9	20.026	79.721	0.69	100.437
03-17 P10	20.024	80.468	0.425	100.917
03-17 P11	20.269	79.304	0.874	100.447
03-17 P12	19.956	79.008	1.175	100.139
05-03 P1	19.992	79.599	0.553	100.144
05-03 P2	20.137	80.431	0.084	100.652
05-03 P3	20.186	79.262	0.208	99.656
05-03 P4	19.913	80.29	0.136	100.339
05-03 P5	19.965	80.573	0.155	100.693
05-03 P6	20.144	80.649	0.168	100.961

A.5.2. Clinozoisite in clinozoisite-plagioclase-calc-silicate rocks (Messelingscharte)

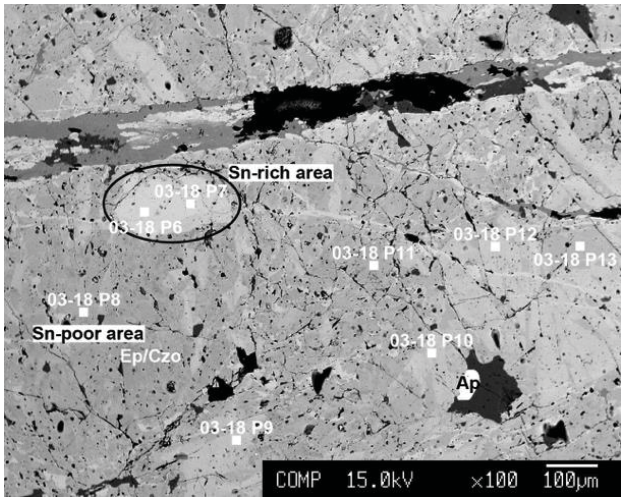

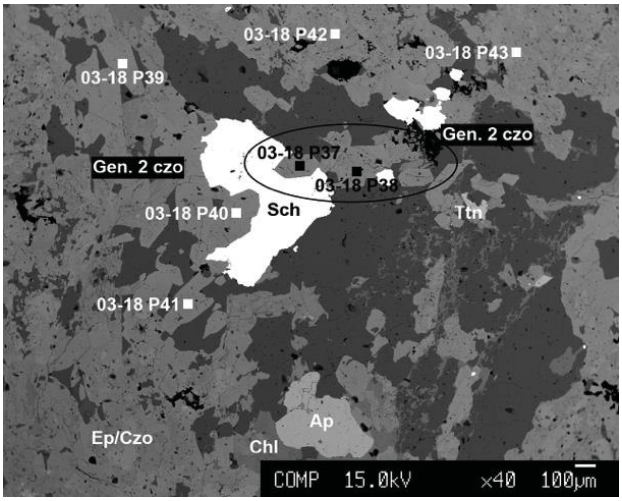

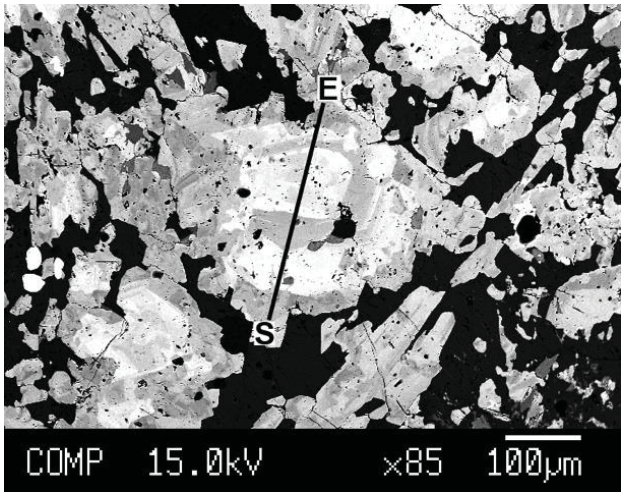

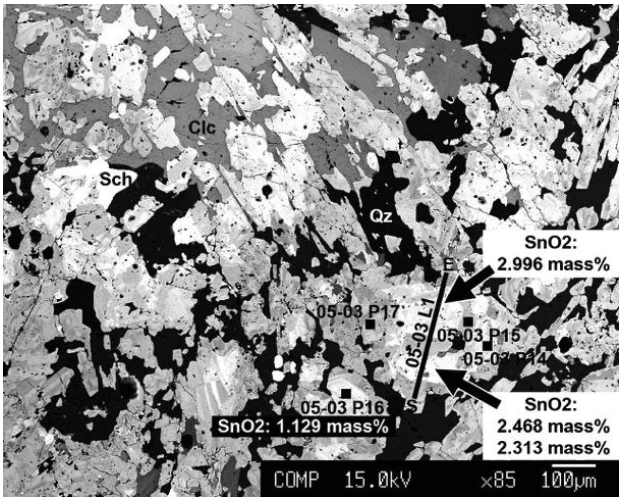

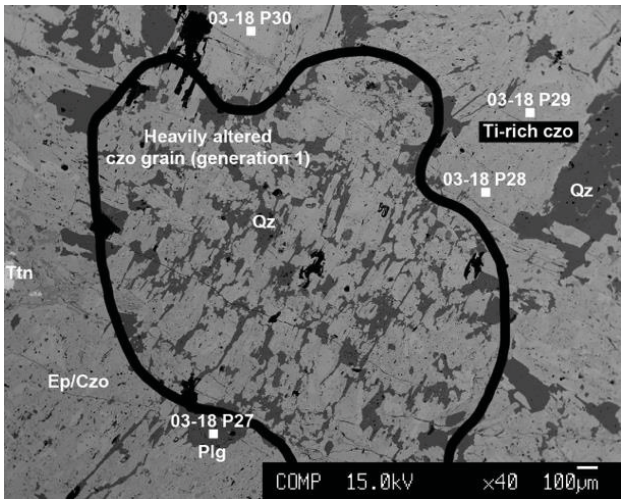

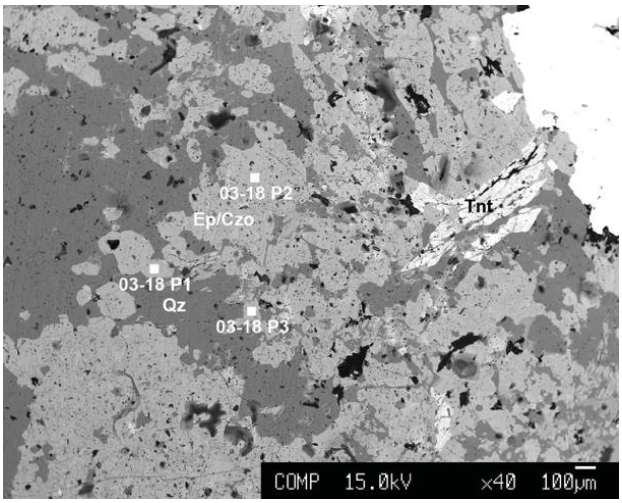

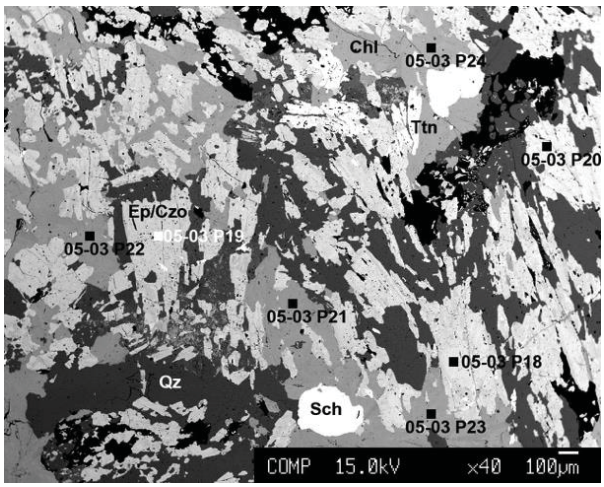
Chl
05-03 P24
Ttn
05-03 P20
Ep/Czo
05-03 P19
05-03 P22
05-03 P21
05-03 P18
Qz
Sch
05-03 P23
COMP 15.0kV ×40 100µm

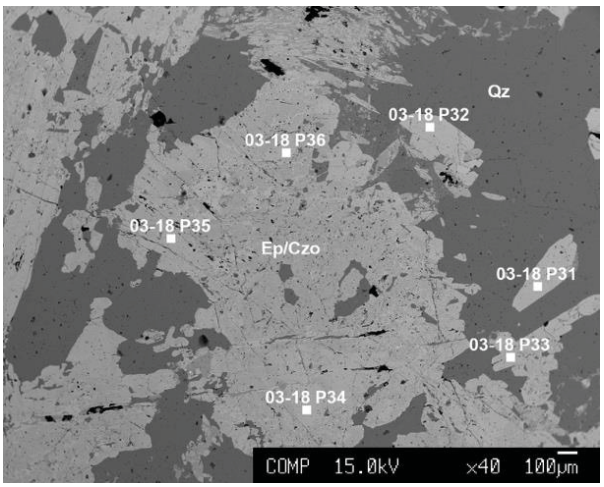
Qz
03-18 P32
03-18 P36
03-18 P35
Ep/Czo
03-18 P31
03-18 P33
03-18 P34
COMP 15.0kV ×40 100µm

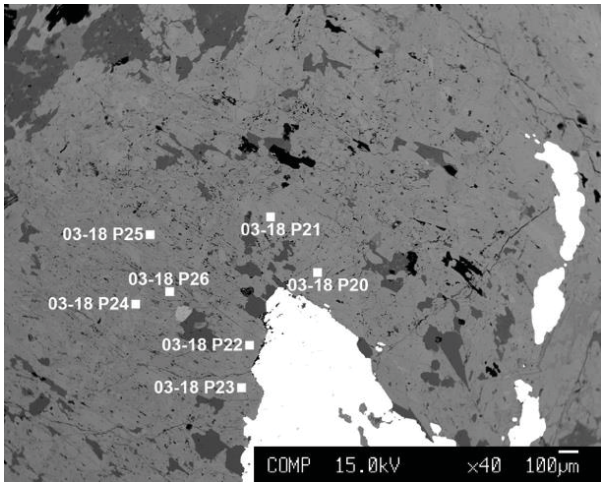
03-18 P25
03-18 P21
03-18 P26
03-18 P20
03-18 P24
03-18 P22
03-18 P23
COMP 15.0kV ×40 100µm

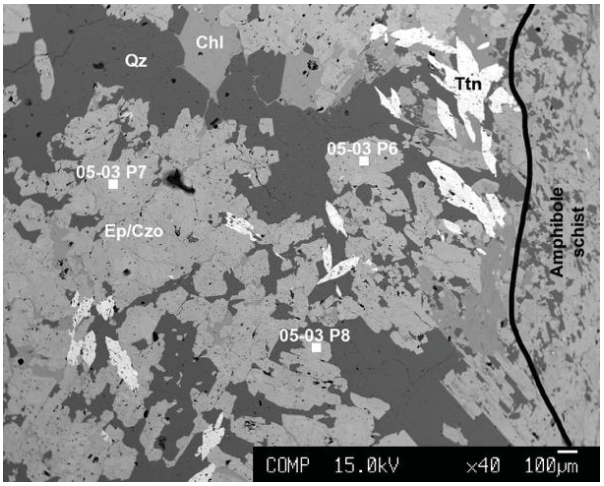
Qz
Chl
Ttn
05-03 P6
05-03 P7
Ep/Czo
Amphibole schist
05-03 P8
COMP 15.0kV ×40 100µm

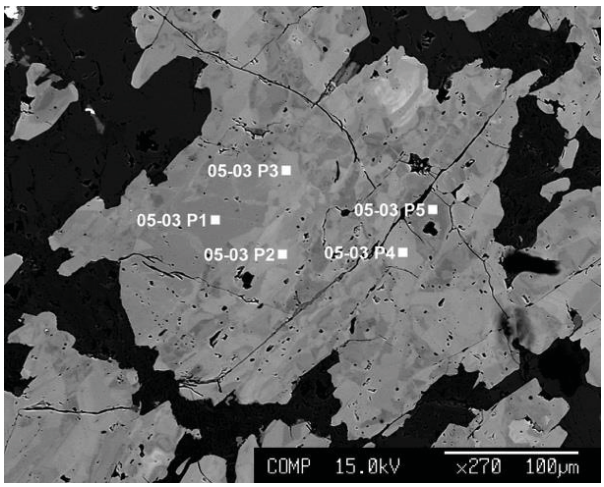
05-03 P3
05-03 P1
05-03 P5
05-03 P2
05-03 P4
COMP 15.0kV ×270 100µm

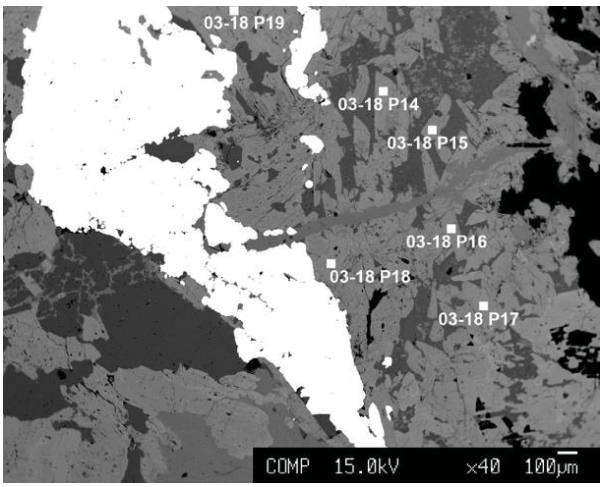
03-18 P19
03-18 P14
03-18 P15
03-18 P16
03-18 P18
03-18 P17
COMP 15.0kV ×40 100µm

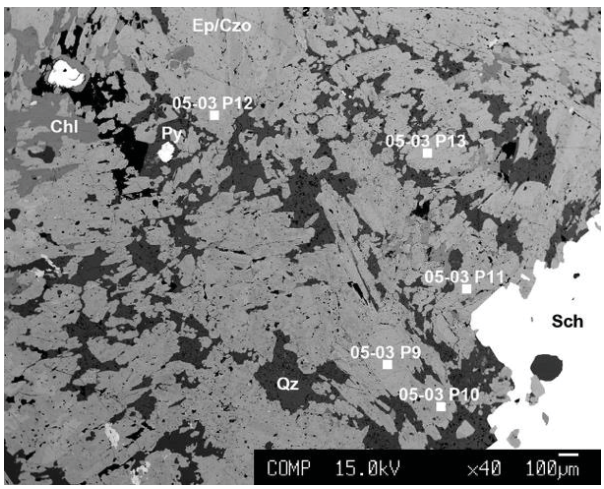
Ep/Czo
05-03 P12
Chl
Py
05-03 P13
05-03 P11
Sch
05-03 P9
Qz
05-03 P10
COMP 15.0kV ×40 100µm

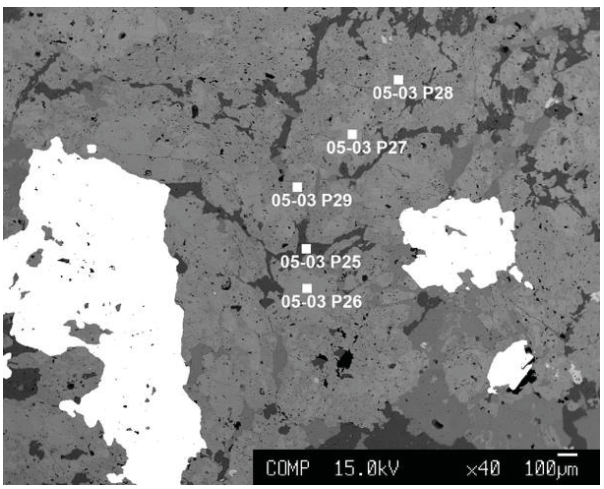
05-03 P28
05-03 P27
05-03 P29
05-03 P25
05-03 P26
COMP 15.0kV ×40 100µm

Analyte	03-18 P1	03-18 P2	03-18 P3	03-18 P6	03-18 P7	03-18 P8	03-18 P10	03-18 P11	03-18 P12
Na2O	0.02	bdl	0.01	bdl	0.02	bdl	bdl	bdl	bdl
SiO2	38.97	40.41	38.51	38.36	39.25	40.20	39.26	39.63	38.93
MnO	0.27	0.03	0.13	0.08	0.10	0.07	0.08	0.42	0.45
CaO	22.40	23.21	22.35	22.52	22.47	23.12	22.87	22.81	22.24
F	<0.00	<0.00	bdl	bdl	<0.00	<0.00	<0.00	<0.00	<0.00
MgO	0.03	0.06	bdl	bdl	bdl	bdl	0.04	0.03	bdl
FeO_{tot}	8.48	6.01	7.63	10.81	11.23	7.26	8.39	6.15	9.28
$Fe2O3_{calc}$	9.42	6.68	8.48	12.00	12.47	8.06	9.32	6.83	10.31
K2O	bdl	bdl	bdl	bdl	bdl	bdl	bdl	bdl	bdl
Al2O3	26.37	28.73	26.78	24.04	23.91	27.94	26.66	28.61	26.51
SnO2	0.17	0.05	0.06	0.71	0.46	bdl	bdl	bdl	0.04
TiO2	bdl	bdl	bdl	bdl	bdl	bdl	bdl	bdl	bdl
Total	96.70	98.59	95.47	96.53	97.73	98.59	98.10	98.21	97.48
H2O	1.91	1.97	1.90	1.89	1.91	1.96	1.93	1.95	1.93
Generation	2	1	2	1	1	1	1	1	1
Number of ions based on 12.5 oxygen atoms									
Na	<0.00	<0.00	<0.00	<0.00	<0.00	<0.00	<0.00	<0.00	<0.00
Si	3.05	3.08	3.05	3.04	3.08	3.07	3.05	3.05	3.03
Mn	0.02	<0.00	0.01	0.01	0.01	<0.00	0.01	0.03	0.03
Ca	1.88	1.89	1.89	1.91	1.89	1.89	1.90	1.88	1.85
Mg	<0.00	0.01	<0.00	<0.00	<0.00	<0.00	<0.00	<0.00	<0.00
Fe	0.56	0.38	0.50	0.72	0.74	0.46	0.55	0.40	0.60
K	<0.00	<0.00	<0.00	<0.00	<0.00	<0.00	<0.00	<0.00	<0.00
Al	2.43	2.58	2.50	2.25	2.21	2.51	2.44	2.60	2.43
Sn	0.01	<0.00	<0.00	0.02	0.01	<0.00	<0.00	<0.00	<0.00
Ti	<0.00	<0.00	<0.00	<0.00	<0.00	<0.00	<0.00	<0.00	<0.00
Sum	7.95	7.94	7.95	7.95	7.94	7.94	7.95	7.95	7.95
Al/Fe3+	4.39	6.73	4.99	3.18	3.00	5.43	4.48	6.55	4.30
Fe2+	<0.00	<0.00	<0.00	0.01	<0.00	<0.00	<0.00	<0.00	0.04
Fe3+	0.56	0.38	0.50	0.71	0.74	0.46	0.55	0.40	0.57

Analyte	03-18 P13	03-18 P20	03-18 P22	03-18 P23	03-18 P24	03-18 P25	03-18 P26	03-18 P28
Na2O	bdl	bdl	bdl	bdl	bdl	0.02	0.03	bdl
SiO2	38.54	39.04	39.58	38.90	38.29	38.44	39.68	40.39
MnO	0.23	0.32	0.07	0.39	0.30	0.08	0.13	0.26
CaO	23.04	22.08	22.80	22.35	22.39	22.87	22.75	22.57
F	bdl	bdl	bdl	bdl	bdl	bdl	bdl	bdl
MgO	bdl	0.06	bdl	0.04	0.03	0.04	0.03	bdl
FeO_{tot}	6.58	8.97	5.46	9.41	9.94	10.72	9.42	6.66
$Fe2O3_{calc}$	7.31	9.97	6.07	10.45	11.04	11.91	10.46	7.40
K2O	bdl	bdl	bdl	bdl	bdl	bdl	bdl	bdl
Al2O3	28.86	26.87	28.75	26.54	25.67	24.91	26.27	27.99
SnO2	bdl	0.12	bdl	0.04	bdl	bdl	0.07	0.08
TiO2	bdl	0.97	1.23	bdl	bdl	bdl	bdl	bdl
Total	97.62	98.43	97.92	98.00	97.01	97.10	98.52	98.44
H2O	1.93	1.95	1.96	1.93	1.90	1.91	1.95	1.96
Generation	1	1	1	1	1	1	1	1
Number of ions based on 12.5 oxygen atoms								
Na	<0.00	<0.00	<0.00	<0.00	<0.00	<0.00	<0.00	<0.00
Si	2.99	3.00	3.03	3.02	3.02	3.02	3.06	3.10
Mn	0.02	0.02	<0.00	0.03	0.02	0.01	0.01	0.02
Ca	1.91	1.82	1.87	1.86	1.89	1.93	1.88	1.85
Mg	<0.00	0.01	<0.00	<0.00	<0.00	0.01	<0.00	<0.00
Fe	0.43	0.58	0.35	0.61	0.65	0.70	0.61	0.43
K	<0.00	<0.00	<0.00	<0.00	<0.00	<0.00	<0.00	<0.00
Al	2.64	2.44	2.60	2.43	2.38	2.31	2.39	2.53
Sn	<0.00	<0.00	<0.00	<0.00	<0.00	<0.00	<0.00	<0.00
Ti	<0.00	0.06	0.07	<0.00	<0.00	<0.00	<0.00	<0.00
Sum	7.98	7.93	7.92	7.96	7.97	7.97	7.95	7.92
Al/Fe3+	7.26	5.51	9.91	4.29	3.87	3.33	3.94	5.92
Fe2+	0.06	0.14	0.09	0.04	0.04	0.01	<0.00	<0.00
Fe3+	0.36	0.44	0.26	0.57	0.62	0.69	0.61	0.43

Analyte	03-18 P29	03-18 P30	03-18 P31	03-18 P32	03-18 P34	03-18 P35	03-18 P36	03-18 P37
Na2O	bdl	bdl	bdl	bdl	bdl	bdl	bdl	bdl
SiO2	39.60	41.50	40.37	40.08	39.71	39.74	39.67	39.32
MnO	0.36	0.13	0.28	0.32	0.25	0.26	0.26	0.16
CaO	22.95	22.11	22.31	22.48	22.47	22.49	22.70	22.78
F	bdl	bdl	bdl	bdl	bdl	bdl	bdl	bdl
MgO	0.04	0.03	0.08	0.08	0.03	0.06	0.05	0.05
FeO_{tot}	7.01	9.61	8.46	8.46	10.59	10.01	9.52	7.32
$Fe2O3_{calc}$	7.78	10.68	9.40	9.40	11.77	11.12	10.58	8.14
K2O	bdl	bdl	bdl	bdl	bdl	bdl	bdl	bdl
Al2O3	27.93	25.17	25.73	26.00	25.64	26.12	25.90	27.49
SnO2	0.08	bdl	0.14	0.08	bdl	bdl	bdl	0.18
TiO2	1.04	bdl	bdl	bdl	bdl	bdl	bdl	bdl
Total	99.00	98.71	97.38	97.51	99.06	98.66	98.27	97.29
H2O	1.97	1.96	1.93	1.93	1.95	1.95	1.94	1.93
Generation	1	1	2	2	1	1	1	2
Number of ions based on 12.5 oxygen atoms								
Na	<0.00	<0.00	<0.00	<0.00	<0.00	<0.00	<0.00	<0.00
Si	3.02	3.17	3.13	3.11	3.06	3.05	3.07	3.05
Mn	0.02	0.01	0.02	0.02	0.02	0.02	0.02	0.01
Ca	1.87	1.81	1.85	1.87	1.85	1.85	1.88	1.89
Mg	<0.00	<0.00	0.01	0.01	<0.00	0.01	0.01	0.01
Fe	0.45	0.61	0.55	0.55	0.68	0.64	0.62	0.47
K	<0.00	<0.00	<0.00	<0.00	<0.00	<0.00	<0.00	<0.00
Al	2.51	2.27	2.35	2.37	2.33	2.37	2.36	2.51
Sn	<0.00	<0.00	<0.00	<0.00	<0.00	<0.00	<0.00	0.01
Ti	0.06	<0.00	<0.00	<0.00	<0.00	<0.00	<0.00	<0.00
Sum	7.94	7.88	7.92	7.93	7.94	7.94	7.95	7.95
Al/Fe3+	6.84	3.69	4.28	4.33	3.45	3.73	3.84	5.29
Fe2+	0.08	<0.00	<0.00	<0.00	0.01	0.01	<0.00	<0.00
Fe3+	0.37	0.62	0.55	0.55	0.67	0.63	0.62	0.48

Analyte	03-18 P38	03-18 P39	03-18 P40	03-18 P41	03-18 P42	03-18 P43	05-03 P1	05-03 P2
Na2O	bdl	0.02	0.05	0.02	<0.00	0.06	bdl	0.03
SiO2	40.20	40.34	39.23	39.07	40.12	39.84	38.82	37.07
MnO	0.04	0.24	0.18	0.11	0.14	0.14	0.18	0.19
CaO	22.62	22.45	22.53	22.68	23.03	23.29	22.94	22.80
F	bdl	bdl	bdl	bdl	bdl	bdl	bdl	bdl
MgO	0.07	0.04	0.04	0.05	0.02	0.07	0.06	0.07
FeO_{tot}	6.58	8.56	9.12	6.61	7.18	5.44	6.43	9.34
$Fe2O3_{calc}$	7.31	9.51	10.14	7.34	7.97	6.04	7.14	10.38
K2O	bdl	bdl	0.02	bdl	bdl	0.03	bdl	bdl
Al2O3	27.84	26.53	25.60	27.97	27.62	29.29	27.45	25.94
SnO2	0.23	0.10	0.07	0.20	0.04	bdl	bdl	bdl
TiO2	bdl	bdl	bdl	bdl	bdl	bdl	bdl	bdl
Total	97.63	98.28	96.84	96.69	98.15	98.19	95.89	95.46
H2O	1.95	1.95	1.91	1.92	1.95	1.96	1.91	1.88
Generation	2	2	2	2	1	1	1	1
Number of ions based on 12.5 oxygen atoms								
Na	<0.00	<0.00	0.01	<0.00	<0.00	0.01	<0.00	0.01
Si	3.09	3.10	3.07	3.04	3.08	3.05	3.05	2.96
Mn	<0.00	0.02	0.01	0.01	0.01	0.01	0.01	0.01
Ca	1.87	1.85	1.89	1.89	1.89	1.91	1.93	1.95
Mg	0.01	<0.00	<0.00	0.01	<0.00	0.01	0.01	0.01
Fe	0.42	0.55	0.60	0.43	0.46	0.35	0.42	0.62
K	<0.00	<0.00	<0.00	<0.00	<0.00	<0.00	<0.00	<0.00
Al	2.52	2.40	2.36	2.57	2.50	2.64	2.54	2.44
Sn	0.01	<0.00	<0.00	0.01	<0.00	<0.00	<0.00	<0.00
Ti	<0.00	<0.00	<0.00	<0.00	<0.00	<0.00	<0.00	<0.00
Sum	7.93	7.92	7.95	7.95	7.94	7.97	7.97	8.01
Al/Fe3+	5.97	4.37	3.96	6.11	5.43	7.58	6.03	4.39
Fe2+	<0.00	<0.00	<0.00	0.01	<0.00	<0.00	<0.00	0.07
Fe3+	0.42	0.55	0.60	0.42	0.46	0.35	0.42	0.56

Analyte	05-03 P3	05-03 P5	05-03 P6	05-03 P7	05-03 P8	05-03 P9	05-03 P10	05-03 P11
Na2O	0.01	0.02	bdl	bdl	bdl	bdl	bdl	bdl
SiO2	38.68	41.08	39.20	39.83	39.68	39.86	39.17	39.74
MnO	0.18	0.30	0.10	0.26	0.05	0.19	0.02	0.67
CaO	22.66	22.85	22.90	22.84	22.83	22.68	22.92	22.17
F	bdl	bdl	bdl	bdl	bdl	bdl	bdl	bdl
MgO	0.07	0.04	bdl	0.07	bdl	0.03	0.04	0.07
FeO_{tot}	10.06	6.24	9.52	8.49	8.67	10.10	8.39	9.57
$Fe2O3_{calc}$	11.18	6.93	10.57	9.43	9.63	11.22	9.32	10.63
K2O	bdl	bdl	bdl	bdl	bdl	bdl	bdl	bdl
Al2O3	25.60	28.53	26.16	26.45	25.81	25.42	26.63	25.69
SnO2	0.07	bdl	0.31	0.34	0.37	bdl	0.05	bdl
TiO2	0.89	bdl	bdl	bdl	bdl	bdl	bdl	bdl
Total	98.23	99.06	98.20	98.27	97.43	98.29	97.22	97.94
H2O	1.93	1.98	1.94	1.94	1.93	1.94	1.93	1.93
Generation	1	1	1	1	2	2	2	1
Number of ions based on 12.5 oxygen atoms								
Na	<0.00	<0.00	<0.00	<0.00	<0.00	<0.00	<0.00	<0.00
Si	3.00	3.11	3.03	3.07	3.09	3.08	3.05	3.08
Mn	0.01	0.02	0.01	0.02	<0.00	0.01	<0.00	0.04
Ca	1.88	1.85	1.90	1.89	1.90	1.88	1.91	1.84
Mg	0.01	<0.00	<0.00	0.01	<0.00	<0.00	<0.00	0.01
Fe	0.65	0.39	0.62	0.55	0.56	0.65	0.55	0.62
K	<0.00	<0.00	<0.00	<0.00	<0.00	<0.00	<0.00	<0.00
Al	2.34	2.54	2.39	2.40	2.37	2.31	2.44	2.35
Sn	<0.00	<0.00	0.01	0.01	0.01	<0.00	<0.00	<0.00
Ti	0.05	<0.00	<0.00	<0.00	<0.00	<0.00	<0.00	<0.00
Sum	7.95	7.92	7.95	7.94	7.94	7.94	7.96	7.94
Al/Fe3+	4.25	6.44	4.02	4.39	4.20	3.55	4.47	3.78
Fe2+	0.10	<0.00	0.02	<0.00	<0.00	<0.00	<0.00	<0.00
Fe3+	0.55	0.40	0.59	0.55	0.56	0.65	0.55	0.62

Analyte	05-03 P12	05-03 P14	05-03 P15	05-03 P16	05-03 P17	05-03 P18	05-03 P19	05-03 P20
Na2O	bdl	bdl	0.02	bdl	bdl	bdl	0.01	bdl
SiO2	39.26	37.23	39.78	39.42	40.18	39.30	39.61	38.63
MnO	0.03	0.06	0.14	0.03	0.28	0.12	0.15	0.06
CaO	22.97	22.46	22.82	22.61	23.00	22.48	22.98	22.76
F	bdl	bdl	bdl	bdl	bdl	bdl	bdl	bdl
MgO	0.03	bdl	0.03	0.05	0.04	0.03	0.02	bdl
FeO_{tot}	8.83	9.57	8.12	8.35	7.97	10.24	8.58	8.10
$Fe2O3_{calc}$	9.81	10.64	9.03	9.28	8.86	11.38	9.53	9.00
K2O	bdl	bdl	bdl	bdl	bdl	bdl	bdl	bdl
Al2O3	26.03	25.41	26.80	25.75	27.09	25.22	26.05	27.02
SnO2	0.08	1.06	0.09	1.13	0.03	0.04	0.04	0.03
TiO2	bdl	0.95	bdl	bdl	bdl	1.17	bdl	bdl
Total	97.58	96.76	97.85	97.88	98.69	98.60	98.12	96.94
H2O	1.92	1.89	1.94	1.92	1.96	1.94	1.93	1.91
Generation	1	1	1	1	1	2	2	2
Number of ions based on 12.5 oxygen atoms								
Na	<0.00	<0.00	<0.00	<0.00	<0.00	<0.00	<0.00	<0.00
Si	3.06	2.95	3.07	3.08	3.08	3.03	3.08	3.02
Mn	<0.00	<0.00	0.01	<0.00	0.02	0.01	0.01	<0.00
Ca	1.92	1.91	1.89	1.89	1.89	1.86	1.91	1.91
Mg	<0.00	<0.00	<0.00	0.01	<0.00	<0.00	<0.00	<0.00
Fe	0.58	0.63	0.52	0.55	0.51	0.66	0.56	0.53
K	<0.00	<0.00	<0.00	<0.00	<0.00	<0.00	<0.00	<0.00
Al	2.39	2.37	2.44	2.37	2.45	2.29	2.39	2.49
Sn	<0.00	0.03	<0.00	0.04	<0.00	<0.00	<0.00	<0.00
Ti	<0.00	0.06	<0.00	<0.00	<0.00	0.07	<0.00	<0.00
Sum	7.96	7.96	7.94	7.93	7.94	7.92	7.95	7.96
Al/Fe3+	4.15	5.31	4.65	4.35	4.79	4.03	4.28	4.94
Fe2+	<0.00	0.19	<0.00	<0.00	<0.00	0.09	<0.00	0.03
Fe3+	0.58	0.45	0.53	0.55	0.51	0.57	0.56	0.51

Analyte	05-03 P26	05-03 P27	05-03 P28	05-03 P29
Na2O	0.01	bdl	0.02	0.05
SiO2	38.84	38.64	37.81	40.17
MnO	0.08	0.02	0.23	0.09
CaO	22.76	22.45	22.67	23.18
F	bdl	bdl	bdl	bdl
MgO	0.03	bdl	0.03	0.02
FeO_{tot}	10.06	8.96	8.03	4.20
$Fe2O3_{calc}$	11.18	9.96	8.92	4.66
K2O	bdl	bdl	bdl	bdl
Al2O3	24.72	25.23	26.68	29.22
SnO2	0.30	1.36	0.10	0.06
TiO2	bdl	bdl	bdl	bdl
Total	97.20	96.92	95.56	96.98
H2O	1.90	1.90	1.89	1.95
Generation	1	1	1	1
Number of ions based on 12.5 oxygen atoms				
Na	<0.00	<0.00	<0.00	0.01
Si	3.06	3.05	3.00	3.09
Mn	0.01	<0.00	0.02	0.01
Ca	1.92	1.90	1.93	1.91
Mg	<0.00	<0.00	<0.00	<0.00
Fe	0.66	0.59	0.53	0.27
K	<0.00	<0.00	<0.00	<0.00
Al	2.29	2.35	2.50	2.65
Sn	0.01	0.04	<0.00	<0.00
Ti	<0.00	<0.00	<0.00	<0.00
Sum	7.95	7.94	7.98	7.95
Al/Fe3+	3.46	4.15	5.01	9.82
Fe2+	<0.00	0.03	0.04	<0.00
Fe3+	0.66	0.57	0.50	0.27

Analyte	Line 1	Line 2	Line 3	Line 4	Line 5	Line 6	Line 7	Line 8	Line 9	Line 10	Line 11
Na2O	bdl	0.02	0.01	bdl	0.01	bdl	bdl	bdl	bdl	bdl	0.02
SiO2	38.46	39.63	39.27	39.67	38.61	39.47	39.62	40.29	39.62	40.43	39.35
MnO	0.17	0.15	0.17	0.10	0.07	0.05	0.07	0.06	0.06	0.04	0.14
CaO	22.77	22.67	23.03	22.45	22.66	22.56	22.58	22.91	23.09	23.13	22.95
F	bdl	bdl	bdl	bdl	bdl	bdl	bdl	bdl	bdl	bdl	bdl
MgO	0.03	bdl	0.02	0.03	bdl	bdl	bdl	bdl	0.02	bdl	bdl
FeO_{tot}	8.02	7.86	8.00	8.88	9.22	9.23	8.79	7.80	8.14	7.42	7.23
$Fe2O3_{calc}$	8.90	8.73	8.89	9.86	10.24	10.26	9.77	8.67	9.04	8.24	8.03
K2O	bdl	bdl	bdl	bdl	bdl	bdl	bdl	bdl	bdl	bdl	bdl
Al2O3	27.10	27.05	27.34	25.69	24.97	24.84	25.57	26.76	27.12	27.64	27.06
SnO2	0.28	0.31	0.08	2.06	2.47	2.31	1.83	0.29	0.33	0.14	0.53
TiO2	bdl	bdl	bdl	bdl	bdl	bdl	bdl	bdl	bdl	bdl	bdl
Total	96.82	97.69	98.10	98.88	98.62	98.76	98.47	98.12	98.40	98.81	97.48
H2O	1.92	1.94	1.94	1.94	1.91	1.92	1.93	1.95	1.95	1.97	1.93
Number of ions based on 12.5 oxygen atoms											
Na	<0.00	<0.00	<0.00	<0.00	<0.00	<0.00	<0.00	<0.00	<0.00	<0.00	<0.00
Si	3.01	3.07	3.03	3.07	3.03	3.07	3.07	3.10	3.05	3.08	3.06
Mn	0.01	0.01	0.01	0.01	<0.00	<0.00	<0.00	<0.00	<0.00	<0.00	0.01
Ca	1.91	1.88	1.91	1.86	1.91	1.88	1.88	1.89	1.90	1.89	1.91
Mg	<0.00	<0.00	<0.00	<0.00	<0.00	<0.00	<0.00	<0.00	<0.00	<0.00	<0.00
Fe	0.52	0.51	0.52	0.57	0.61	0.60	0.57	0.50	0.52	0.47	0.47
K	<0.00	<0.00	<0.00	<0.00	<0.00	<0.00	<0.00	<0.00	<0.00	<0.00	<0.00
Al	2.50	2.47	2.49	2.34	2.31	2.28	2.34	2.43	2.46	2.48	2.48
Sn	0.01	0.01	<0.00	0.06	0.08	0.07	0.06	0.01	0.01	<0.00	0.02
Ti	<0.00	<0.00	<0.00	<0.00	<0.00	<0.00	<0.00	<0.00	<0.00	<0.00	<0.00
Sum	7.97	7.94	7.96	7.91	7.93	7.91	7.92	7.93	7.95	7.94	7.95
Al/Fe3+	5.18	4.85	4.91	4.39	4.32	3.96	4.25	4.83	4.73	5.25	5.28
Fe2+	1.92	1.94	1.94	1.94	1.91	1.92	1.93	1.95	1.95	1.97	1.93
Fe3+	0.04	<0.00	0.01	0.04	0.07	0.03	0.02	<0.00	<0.00	<0.00	<0.00

Analyte	Line 12	Line 13	Line 14	Line 15	Line 16	Line 17	Line 18	Line 19	Line 20	Line 21	Line 22
Na2O	bdl	bdl	bdl	0.02	bdl	bdl	bdl	0.05	0.01	0.03	0.01
SiO2	39.86	37.70	39.15	39.22	39.57	38.50	39.74	39.74	39.84	39.16	40.49
MnO	0.23	0.20	0.16	0.14	0.11	0.30	0.15	0.10	0.05	0.03	0.13
CaO	22.73	22.92	22.75	22.85	22.93	22.37	22.76	22.72	23.17	22.77	22.95
F	bdl	bdl	bdl	bdl	bdl	bdl	bdl	bdl	bdl	bdl	bdl
MgO	bdl	0.05	bdl	0.04	bdl	0.03	bdl	0.05	0.03	bdl	0.04
FeO_{tot}	6.72	8.84	7.19	6.60	6.89	8.57	8.02	6.90	6.04	9.73	7.96
$Fe2O3_{calc}$	7.46	9.82	7.99	7.33	7.65	9.52	8.91	7.67	6.71	10.81	8.85
K2O	bdl	bdl	bdl	bdl	bdl	bdl	bdl	bdl	bdl	bdl	bdl
Al2O3	27.16	25.70	26.74	27.11	26.90	25.04	26.32	27.56	28.29	25.56	26.90
SnO2	1.45	0.96	1.42	1.19	1.34	3.00	1.33	0.08	bdl	0.09	0.15
TiO2	bdl	bdl	1.60	bdl	bdl	bdl	bdl	bdl	bdl	bdl	bdl
Total	98.73	96.50	99.02	97.45	97.81	97.81	98.32	97.19	97.43	97.45	98.62
H2O	1.94	1.89	1.95	1.92	1.93	1.90	1.94	1.94	1.95	1.92	1.96
Number of ions based on 12.5 oxygen atoms											
Na	<0.00	<0.00	<0.00	<0.00	<0.00	<0.00	<0.00	0.01	<0.00	<0.00	<0.00
Si	3.08	2.99	3.01	3.06	3.07	3.03	3.07	3.08	3.07	3.05	3.10
Mn	0.02	0.01	0.01	0.01	0.01	0.02	0.01	0.01	<0.00	<0.00	0.01
Ca	1.88	1.95	1.87	1.91	1.91	1.89	1.89	1.88	1.91	1.90	1.88
Mg	<0.00	0.01	<0.00	<0.00	<0.00	<0.00	<0.00	0.01	<0.00	<0.00	<0.00
Fe	0.43	0.59	0.46	0.43	0.45	0.56	0.52	0.45	0.39	0.63	0.51
K	<0.00	<0.00	<0.00	<0.00	<0.00	<0.00	<0.00	<0.00	<0.00	<0.00	<0.00
Al	2.47	2.40	2.42	2.49	2.46	2.32	2.40	2.51	2.57	2.35	2.43
Sn	0.04	0.03	0.04	0.04	0.04	0.09	0.04	<0.00	<0.00	<0.00	<0.00
Ti	<0.00	<0.00	0.09	<0.00	<0.00	<0.00	<0.00	<0.00	<0.00	<0.00	<0.00
Sum	7.92	7.98	7.91	7.94	7.93	7.93	7.93	7.94	7.95	7.95	7.93
Al/Fe3+	5.70	4.48	7.91	5.79	5.50	4.76	4.62	5.63	6.61	3.70	4.77
Fe2+	1.94	1.89	1.95	1.92	1.93	1.90	1.94	1.94	1.95	1.92	1.96
Fe3+	<0.00	0.05	0.16	<0.00	<0.00	0.08	<0.00	<0.00	<0.00	<0.00	<0.00

A.5.3. Clinozoisite in calc-silicate rocks (Felbertal tungsten mine)

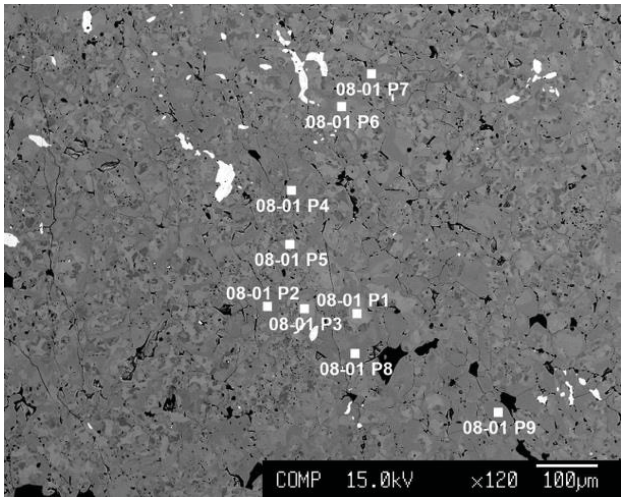

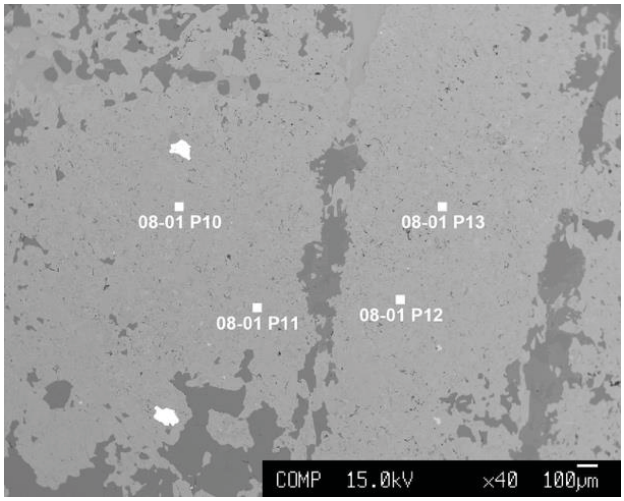

Analyte	08-01 P2	08-01 P3	08-01 P4	08-01 P5	08-01 P6	08-01 P7	08-01 P8	08-01 P10	08-01 P11
Na2O	bdl	0.01	0.01	0.01	bdl	bdl	0.01	bdl	<0.00
SiO2	40.65	39.39	40.75	39.33	39.89	41.44	40.24	39.55	40.47
MnO	0.06	0.30	0.07	0.11	0.14	0.06	0.07	0.08	bdl
CaO	22.94	22.49	23.10	22.76	22.93	23.30	23.08	23.37	23.42
F	bdl	bdl	bdl	bdl	bdl	bdl	bdl	bdl	bdl
MgO	0.04	0.02	0.04	0.06	0.05	0.06	0.05	bdl	bdl
FeO_{tot}	5.90	9.69	5.94	9.09	7.80	5.96	6.26	4.29	5.83
$Fe2O3_{calc}$	6.56	10.77	6.60	10.10	8.67	6.62	6.96	4.76	6.48
K2O	bdl	bdl	bdl	bdl	bdl	bdl	bdl	bdl	bdl
Al2O3	28.74	25.59	29.07	25.55	26.99	28.09	28.40	29.84	29.38
SnO2	0.02	0.07	bdl	0.15	bdl	0.02	0.02	bdl	bdl
TiO2	bdl	bdl	bdl	bdl	bdl	bdl	bdl	bdl	bdl
Total	99.16	97.77	99.35	97.05	97.80	98.93	98.22	97.18	99.22
H2O	1.97	1.93	1.98	1.92	1.94	1.98	1.96	1.95	1.98
Number of ions based on 12.5 oxygen atoms									
Si	3.09	3.07	3.08	3.07	3.08	3.14	3.08	3.05	3.06
Al	2.58	2.35	2.59	2.35	2.45	2.51	2.56	2.71	2.62
Mn	<0.00	0.02	<0.00	0.01	0.01	<0.00	<0.00	0.01	<0.00
Ca	1.87	1.88	1.87	1.91	1.90	1.89	1.89	1.93	1.90
Mg	0.03	0.02	0.03	0.05	0.04	0.05	0.04	<0.00	<0.00
Fe	0.38	0.63	0.38	0.59	0.50	0.38	0.40	0.28	0.37
Na	<0.00	<0.00	<0.00	<0.00	<0.00	<0.00	<0.00	<0.00	<0.00
Sn	<0.00	<0.00	<0.00	0.01	<0.00	<0.00	<0.00	<0.00	<0.00
Ti	<0.00	<0.00	<0.00	<0.00	<0.00	<0.00	<0.00	<0.00	<0.00
Sum	7.95	7.96	7.96	8.00	7.98	7.96	7.98	7.96	7.95
Fe2+	<0.00	<0.00	<0.00	<0.00	<0.00	<0.00	<0.00	<0.00	<0.00
Fe3+	0.38	0.63	0.38	0.59	0.50	0.38	0.40	0.28	0.37
Al/Fe3+	6.86	3.72	6.90	3.96	4.88	6.65	6.39	9.81	7.10

Analyte	08-01 P12	08-01 P13
Na2O	0.02	bdl
SiO2	39.36	40.19
MnO	0.09	0.05
CaO	22.98	23.24
F	bdl	bdl
MgO	bdl	0.03
FeO_{tot}	6.59	7.43
$Fe2O3_{calc}$	7.32	8.25
K2O	bdl	bdl
Al2O3	27.92	27.44
SnO2	bdl	bdl
TiO2	0.85	bdl
Total	97.82	98.37
H2O	1.95	1.96
Number of ions based on 12.5 oxygen atoms		
Si	3.03	3.08
Al	2.53	2.48
Mn	0.01	<0.00
Ca	1.90	1.91
Mg	<0.00	0.02
Fe	0.42	0.48
Na	<0.00	<0.00
Sn	<0.00	<0.00
Ti	0.05	<0.00
Sum	7.94	7.97
Fe2+	0.06	<0.00
Fe3+	0.37	0.48
Al/Fe3+	6.91	5.21

A.5.4. Titanite in clinozoisite-plagioclase-calc-silicate rocks (Messelingscharte)

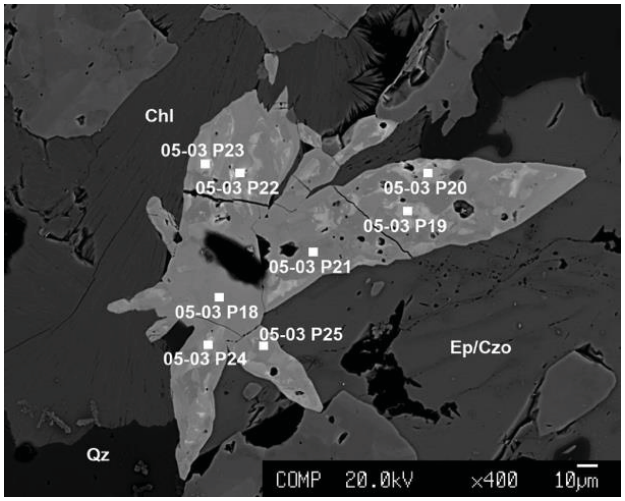

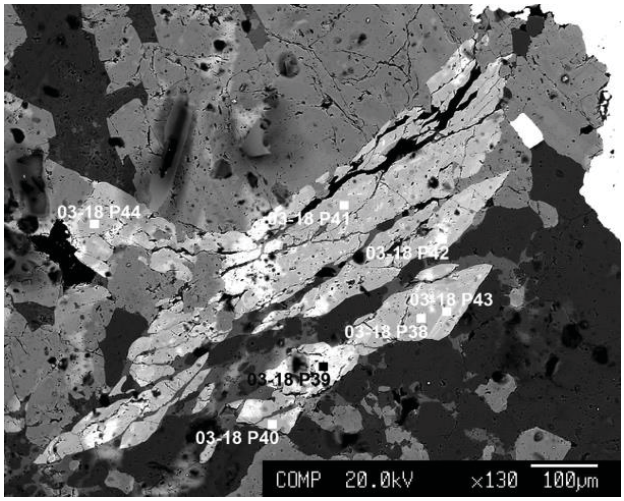

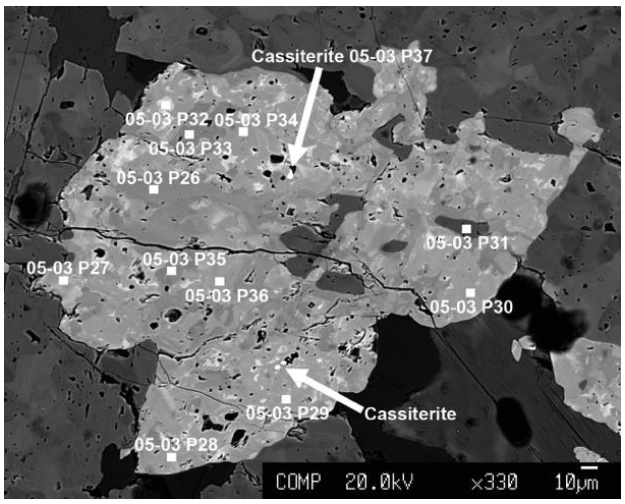

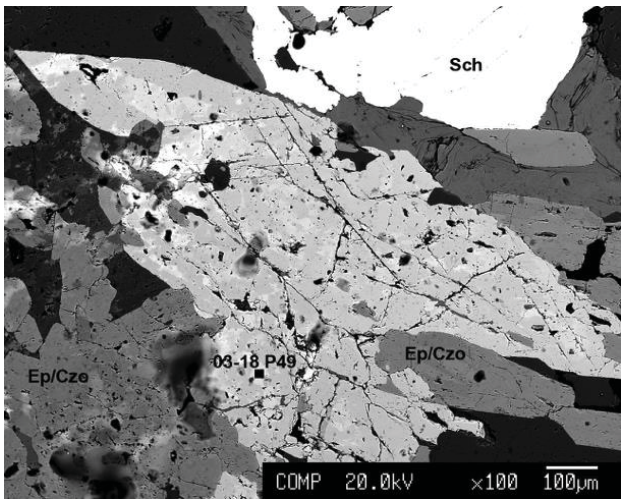

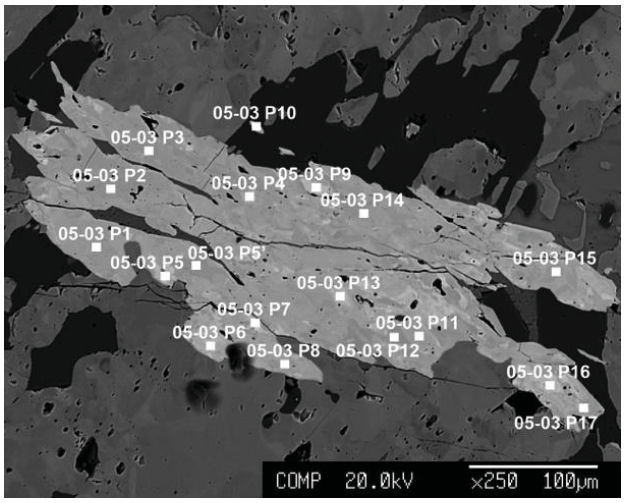

Analyte	05-03ttnP1	05-03ttnP2	05-03ttnP3	05-03ttnP4	05-03ttnP5	05-03ttnP6	05-03ttnP7
F	1.02	1.49	0.69	0.83	0.83	1.19	1.18
Al2O3	3.01	4.51	2.21	2.95	2.58	3.61	3.39
FeO_{tot}	0.87	1.14	0.43	0.48	1.65	1.42	0.89
$Fe2O3_{calc}$	0.97	1.26	0.48	0.53	1.83	1.58	0.98
SiO2	29.93	30.13	29.44	29.39	28.99	29.53	28.36
TiO2	34.27	32.32	37.06	35.56	33.85	31.75	33.01
CaO	26.63	27.08	26.67	26.98	26.20	26.44	27.42
SnO2	1.91	1.26	0.80	1.54	5.51	5.04	2.21
Total	97.73	98.05	97.34	97.78	99.78	99.13	96.56
H2O	0.16	0.24	0.12	0.19	0.27	0.25	0.15
-F=O	0.43	0.63	0.29	0.35	0.35	0.50	0.50
Sum (no H2O)	98.15	98.67	97.63	98.12	100.13	99.63	97.05
Brightness	medium	medium	medium	bright	bright	bright	bright
Number of ions based on 1 Si atom							
Si	1.00	1.00	1.00	1.00	1.00	1.00	1.00
Ti	0.86	0.81	0.95	0.91	0.85	0.81	0.88
Al	0.12	0.18	0.09	0.12	0.10	0.14	0.14
Sn	0.03	0.02	0.01	0.02	0.07	0.07	0.03
Fe	0.02	0.03	0.01	0.01	0.05	0.04	0.03
Ca	0.95	0.96	0.97	0.98	0.94	0.96	1.04
F	0.11	0.16	0.07	0.09	0.09	0.13	0.13
OH	0.04	0.05	0.03	0.04	0.06	0.06	0.04
O	0.86	0.79	0.90	0.87	0.85	0.82	0.83

Analyte	05-03ttnP9	05-03ttnP11	05-03ttnP12	05-03ttnP13	05-03ttnP14	05-03ttnP15	05-03ttnP16
F	0.94	1.46	1.57	1.37	1.27	0.67	1.20
Al2O3	2.87	4.23	4.95	4.06	3.66	2.09	3.39
FeO_{tot}	0.34	0.78	0.86	0.68	1.17	0.50	1.26
$Fe2O3_{calc}$	0.37	0.86	0.96	0.75	1.30	0.56	1.40
SiO2	29.72	29.50	29.68	29.64	29.49	29.80	28.91
TiO2	35.87	30.79	32.40	33.63	33.14	39.00	31.57
CaO	26.75	26.42	26.94	27.01	26.77	26.94	26.19
SnO2	1.30	3.43	2.21	2.29	1.66	1.18	6.48
Total	97.82	96.68	98.71	98.76	97.28	100.23	99.16
H2O	0.11	0.15	0.24	0.15	0.19	0.11	0.19
-F=O	0.39	0.61	0.66	0.58	0.53	0.28	0.50
Sum (no H2O)	98.22	97.30	99.37	99.34	97.81	100.51	99.66
Brigthness	bright	bright	medium	bright	medium	medium	bright
Number of ions based on 1 Si atom							
Si	1.00	1.00	1.00	1.00	1.00	1.00	1.00
Ti	0.91	0.79	0.82	0.85	0.85	0.98	0.82
Al	0.11	0.17	0.20	0.16	0.15	0.08	0.14
Sn	0.02	0.05	0.03	0.03	0.02	0.02	0.09
Fe	0.01	0.02	0.02	0.02	0.03	0.01	0.04
Ca	0.96	0.96	0.97	0.98	0.97	0.97	0.97
F	0.10	0.16	0.17	0.15	0.14	0.07	0.13
OH	0.02	0.04	0.05	0.03	0.04	0.03	0.04
O	0.88	0.81	0.78	0.82	0.82	0.90	0.83

Analyte	05-03ttnP17	05-03ttnP18	05-03ttnP19	05-03ttnP20	05-03ttnP21	05-03ttnP22	05-03ttnP23
F	0.98	1.05	1.52	1.18	1.04	1.02	1.11
Al2O3	3.11	2.61	5.43	4.17	3.95	2.77	3.31
FeO_{tot}	0.33	0.32	0.53	0.88	0.88	0.82	0.84
$Fe2O3_{calc}$	0.37	0.36	0.59	0.97	0.97	0.91	0.94
SiO2	29.51	30.15	29.38	29.01	29.38	30.24	29.10
TiO2	37.83	36.35	28.75	31.62	34.62	33.69	32.00
CaO	26.71	26.78	26.58	26.23	26.96	26.46	26.25
SnO2	1.12	1.36	5.46	4.85	0.07	3.72	5.44
Total	99.63	98.65	97.72	98.03	96.98	98.80	98.15
H2O	0.13	0.00	0.30	0.28	0.31	0.11	0.16
-F=O	0.41	0.44	0.64	0.50	0.44	0.43	0.47
Sum (no H2O)	100.04	99.09	98.36	98.53	97.42	99.23	98.62

Brigthness	bright	medium	bright	bright	medium	bright	bright
Number of ions based on 1 Si atom							
Si	1.00	1.00	1.00	1.00	1.00	1.00	1.00
Ti	0.96	0.91	0.74	0.82	0.89	0.84	0.83
Al	0.12	0.10	0.22	0.17	0.16	0.11	0.13
Sn	0.02	0.02	0.07	0.07	0.00	0.05	0.08
Fe	0.01	0.01	0.02	0.03	0.03	0.02	0.02
Ca	0.97	0.95	0.97	0.97	0.98	0.94	0.97
F	0.11	0.11	0.16	0.13	0.11	0.11	0.12
OH	0.03	0.00	0.07	0.07	0.07	0.02	0.04
O	0.87	0.89	0.77	0.81	0.82	0.87	0.84

Analyte	**05-03ttnP24**	**05-03ttnP25**	**05-03ttnP26**	**05-03ttnP28**	**05-03ttnP29**	**05-03ttnP30**	**05-03ttnP31**
F	1.00	1.10	1.00	1.26	0.91	1.06	1.44
Al2O3	3.30	3.87	3.10	3.13	2.52	2.90	4.30
FeO_{tot}	0.94	0.27	0.57	0.94	0.98	0.99	0.65
$Fe2O3_{calc}$	1.04	0.30	0.64	1.05	1.09	1.10	0.73
SiO2	29.24	29.33	29.88	29.26	28.96	29.58	29.26
TiO2	32.73	35.30	36.10	33.07	35.77	33.20	35.08
CaO	26.46	26.83	26.89	26.28	26.21	26.56	26.52
SnO2	3.03	1.08	3.76	4.51	2.83	2.48	2.03
Total	96.80	97.81	101.36	98.57	98.28	96.87	99.36
H2O	0.23	0.19	0.14	0.07	0.14	0.13	0.16
-F=O	0.42	0.46	0.42	0.53	0.38	0.45	0.61
Sum (no H2O)	97.22	98.27	101.78	99.10	98.66	97.32	99.97
Brigthness	bright	medium	medium	bright	medium	medium	dark
Number of ions based on 1 Si atom							
Si	1.00	1.00	1.00	1.00	1.00	1.00	1.00
Ti	0.84	0.91	0.91	0.85	0.93	0.84	0.90
Al	0.13	0.16	0.12	0.13	0.10	0.12	0.17
Sn	0.04	0.02	0.05	0.06	0.04	0.03	0.03
Fe	0.03	0.01	0.02	0.03	0.03	0.03	0.02
Ca	0.97	0.98	0.96	0.96	0.97	0.96	0.97
F	0.11	0.12	0.11	0.14	0.10	0.11	0.16
OH	0.05	0.04	0.03	0.02	0.03	0.03	0.04
O	0.84	0.84	0.86	0.85	0.87	0.86	0.81

Analyte	**05-03ttnP32**	**05-03ttnP33**	**05-03ttnP34**	**05-03ttnP36**	**03-18ttnP38**	**03-18ttnP40**	**03-18ttnP41**
F	0.92	0.93	1.06	1.13	1.37	0.65	0.50
Al2O3	2.76	3.07	3.13	3.26	4.41	2.43	2.26
FeO_{tot}	1.06	0.91	0.84	0.70	1.27	0.39	0.36
$Fe2O3_{calc}$	1.18	1.01	0.94	0.78	1.42	0.44	0.40
SiO2	29.26	29.38	30.31	28.84	29.69	29.89	29.59
TiO2	32.61	34.61	35.72	33.42	33.42	38.30	40.53
CaO	26.53	26.85	27.02	26.08	27.03	27.16	26.91
SnO2	3.65	2.38	2.02	2.94	0.53	0.32	0.10
Total	96.91	98.24	100.20	96.44	97.87	99.17	100.29
H2O	0.19	0.21	0.16	0.13	0.29	0.17	0.21
-F=O	0.39	0.39	0.45	0.48	0.58	0.27	0.21
Sum (no H2O)	97.30	98.63	100.65	96.92	98.45	99.45	100.50
Brigthness	bright	medium	bright	bright	medium	medium	medium
Number of ions based on 1 Si atom							
Si	1.00	1.00	1.00	1.00	1.00	1.00	1.00
Ti	0.84	0.89	0.89	0.87	0.85	0.96	1.03
Al	0.11	0.12	0.12	0.13	0.18	0.10	0.09
Sn	0.05	0.03	0.03	0.04	0.01	0.00	0.00
Fe	0.03	0.03	0.02	0.02	0.04	0.01	0.01
Ca	0.97	0.98	0.96	0.97	0.98	0.97	0.97
F	0.10	0.10	0.11	0.12	0.15	0.07	0.05
OH	0.04	0.05	0.03	0.03	0.07	0.04	0.05
O	0.86	0.85	0.86	0.85	0.79	0.89	0.90

Analyte	03-18ttnP43	03-18ttnP44	03-18ttnP49
F	1.39	0.72	1.40
Al2O3	4.83	2.45	3.79
FeO_{tot}	0.85	0.37	1.47
$Fe2O3_{calc}$	0.95	0.41	1.64
SiO2	29.71	29.57	29.40
TiO2	32.11	39.20	30.95
CaO	26.80	27.06	25.64
SnO2	4.84	0.25	3.32
Total	100.60	99.66	96.14
H2O	0.30	0.14	0.19
-F=O	0.58	0.30	0.59
Sum (no H2O)	101.19	99.96	96.73
Brigthness	bright	medium	bright
Number of ions based on 1 Si atom			
Si	1.00	1.00	1.00
Ti	0.81	1.00	0.79
Al	0.19	0.10	0.15
Sn	0.07	0.00	0.05
Fe	0.02	0.01	0.04
Ca	0.97	0.98	0.94
F	0.15	0.08	0.15
OH	0.07	0.03	0.04
O	0.78	0.89	0.81

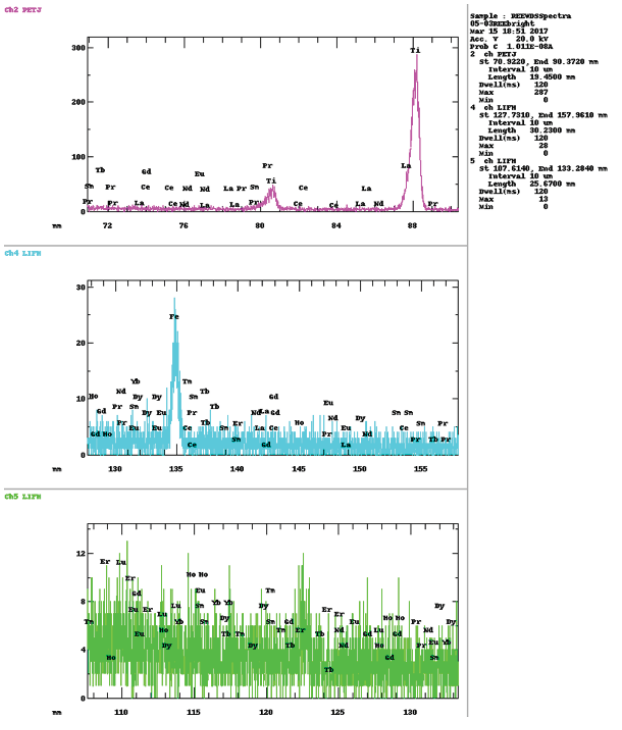

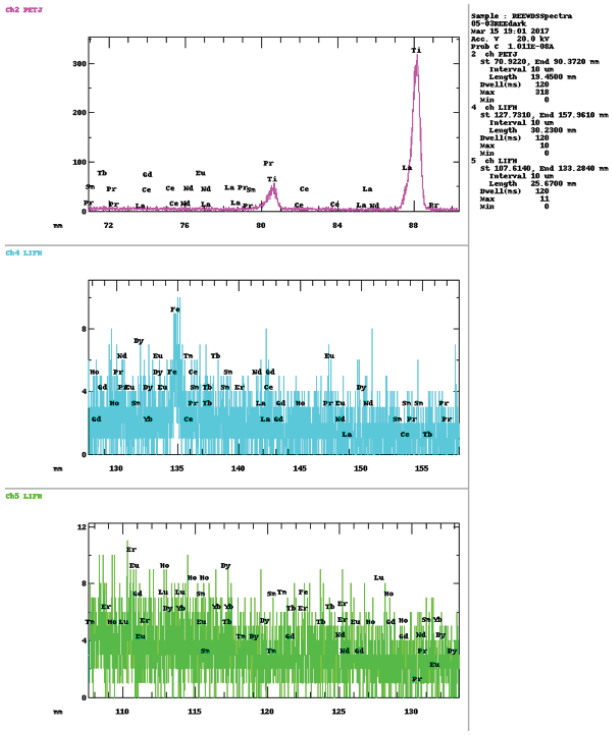

A.6 Core logs

Bohrprofil B1

Bohrteufe	Geologische Beschreibung
0,6	Boden, humos, stark mit verwittertem Gestein durchsetzt
1,05	Biotit-Hornblende Schiefer, feinkörnig, dicht, grau-grün, Einfallen 20°
2,4	Amphibolit, mittelkörnig, graugrün
2,5	Biotit-Prasinit, dicht, dunkelgrün, Einfallen 26°
3,35	Amphibolit, mittelkörnig, grau-grün, in Schnüren Sulfide und Quarzzwischenlagen, Einfallen 20°
3,4	Sulfide und Scheelit in Flittern
4,9	Amphibolit, mittelkörnig, grau-grün, mit Sufliden und Quarzzwischenlagen
6,3	Biotit-Prasinit, dunkelgrün, starke Fließfaltung durch Magmatisierung
9,2	Amphibolit, lagig, feinkörnig und mittelkörnig, Quarz in Schnüren und Knauern, z.T. Fließfaltung, vereinzelt dünne Lage Biotit und Sulfide, Einfallen 28°
9,45	Quarzit mit Pyrit und Kupferkies
10,05	Hornblendeschiefer, feinkörnig, graugrün, lagig Albit, Einfallen 30°
12,6	Biotit-Prasinit, dicht, graugrün, <1 cm Quarzit Zwischenlagen, lagig, chloritisiert, Kleinfältelung
12,65	Scheelit Flitter im Biotit-Prasinit
16,6	Amphibolit, mittel-grobkörnig, graugrün, lagig Biotit, lagig Epidotisierung und Suflide, Einfallen 18°
17,0	Biotit-Prasinit, stark epidotisiert
18,3	Biotit-Prasinit, grob-mittelkörnig, viele Sulfide in bis 1 cm starken Lagen, Einfallen 22°
19,0	Störung mit Quarz, Periklin und Klinochlor verheilt, Einfallen 50°
19,4	Prasinit, feinkörnig, grün, stark epidotisiert
20,4	Hornblende-Prasinit, grob-mittelkörnig, grün
23,3	Hornblende-Prasinit mit vielen Sulfiden, Quarzknauern und Schliefern, grün, Einfallen 16°
23,4	Prasinit, mittelkörnig mit Scheelitflittern und Sulfiden
23,95	Amphibolit, mittelkörnig, grün
24,05	Störung mit Quarz verheilt, viele Sulfide
26,0	Amphibolit, mittel- bis grobkörnig, lagig Quarzit, Biotit, z.T. gefaltet
30,6	Amphibolit, fein- bis mittelkörnig, dicht, graugrün mit lagig Quarzit und Biotit, Einfallen 8°
32,6	Biotit-Prasinit, lagig epidotisiert, einzelne Quarzschlieren, grau
35,5	Hornblende-Prasinit, mittelkörnig, lagig Biotit, Quarzknauern, epidotisiert, Einfallen 5°
35,8	Hornblendefels, grün, dicht mit großen Hornblende-kristallen, kaum Plagioklas
36,5	Amphibolit, mittelkörnig, dicht, graugrün
36,9	Hornblendefels, schlierig, dicht, mittelkörnig, grün
40,5	Amphibolit, mittelkörnig, dicht, graugrün
43,9	Hornblende-Prasinit, grün, lagig Biotit, Quarz, Sulfide, Einfallen 20°
44,2	Quarzknauer mit Scheelitidioblasten, in Begleitung der Quarz Biotitblastese
49,0	Amphibolit, mittelkörnig, dicht, graugrün, lagig Suflide, reine Hornblende, Einfallen 32°
52,0	Amphibolit, feinkörnig, dicht, graugrün, migmatisiert
55,9	Biotit-Prasinit, feinkörnig, mit lagenweise mittelkörnigen Hornblenditen, grün, von 54,5 - 54,8 stark epidotisiert, Einfallen 20°
57,9	Biotit-Schiefer mit Albitsprossung, z.T. schlierig, Einfallen 28°
64,0	Biotit-Prasinit, dicht, sehr hell mit viel Quarz, lagenweise Hornblendefels, grün, sonst grau, Migmatisierung, Einfallen 15°
66,4	Hornblendefels, mittelkörnig, dicht, grün, kaum Plagioklas
66,55	Quarz mit Pyritkristallen, 1 cm Kantenlänge, auch Kupferkies, Einfallen 33°
70,9	Biotit-Prasinit, magmatisiert, grau-grün, dicht, lagig Hornblendefels, grün, und Quarz

Farben korrespondieren zu Farben in digitalisierter geologischer Karte von Otto Gold Consulants.

Bohrprofil B2

Bohrteufe	Geologische Beschreibung
0,2	Boden, schwach humos, moosig, viel Gesteinsbrocken
0,7	Biotit-Chlorit-Prasinit in Gesteinstrümmern, grau-braun, viel Eisenoxide, Scheelitflitter
4,8	Biotit-Chlorit-Prasinit, dicht, lagig Sulfide, Plagioklas, bei 2,3 m Kluftfüllung mit Quarz, Einfallen 35°
5,75	Amphibolit, grobkörnig, grün, lagig Sulfide, Einfallen 40°
6,1	Gneis, feinkörnig, grau-weiß
6,7	Amphibolit, fein-mittelkörnig, klüftig, grau-grün
6,8	Störung, Einfallen 50°
7,0	Amphibolit, mittelkörnig, dicht
8,1	Biotit-Prasinit, dicht, z.T. schlierig, mit Quarzbändern, grau-grün bis grauweiß, Einfallen 50°
11,1	Hornblende-Prasinit, dicht, grau-grün, lagenweise Epidotisierung und Sulfide, Einfallen 30°
14,7	Amphibolit, mittel-feinkörnig, lagig Quarz, schlierige Epidotisierung, grau-grün, lagig Sulfide, Einfallen 25°
18,0	Biotit-Prasinit in Wechsellagerung mit Hornblende-Prasinit, lagig Quarz, Sulfide, schlierige Epidotisierung, grau-braun-grau-grün, Einfallen 32°
18,2	Gneis, feinkörnig, grau-weiß, Einfallen 25°
18,6	Hornblende-Biotit-Prasninit, dicht, grau-grün ,mit Quarz-bändern und viel Sufliden, Scheelit
19,6	Quarz, schlierig eingelagert Hornblende
21,5	Amphibolit, fein-mittelkörnig, dicht, grün, lagig epidotisiert, Einfallen 28° bei 20,7 und 21,0 Störungen mit Quarz, Clinozoisit und Sufliden verheilt
31,4	Biotit-Prasninit, dicht, grau, lagig Quarz und grüne Hornblende, Epidotisierung, Einfallen 25°
31,6	Quarzit, stellenweise epidotisiert, dicht
35,4	Hornblende-Prasinit, feinkörnig, dicht, lagig Quarz, schlierige Epidotisierung von 34,3 - 35,4 Störung, Einfallen 10°
43,0	Hornblende-Biotit-Prasinit, dicht, teilweise schlierig, lagig Quarz, Suflide, grau-grün, Einfallen 15°
43,7	Horblendefels, grobkörnig, dicht, grün
47,7	Hornblende-Biotit-Prasinit, mittelkörnig, dicht, schlierig grau-grün
59,6	Chlorit-Prasinit in Wechsellagerung mit Hornblendefels, dicht, grau-grün, Einfallen 15°
59,6	Hornblende-Prasinit, feinkörnig, z.T. epidotisiert, weiß-grau, Einfallen 25°
59,68	Störung mit Quarz verheilt, Einfallen 12°
61,5	Hornblende-Biotit-Prasinit, dicht, schlierig, grau-grün
62,3	Augengneis, dicht, grau, Einfallen 10°
63,0	Gneis, dicht, graugrün mit Quarzknauer, Knitterung
65,4	Gneis, grau, schlierig zum Liegenden mit Hornblende-Einschaltungen
65,9	Hornblende-Prasinit, grau-grün mit Quarzschlieren, epidotisiert, Einfallen 15°
70,0	Gneis, grau-weiß, schlierig, mit Hornblendefels Zwischen-lagen

Farben korrespondieren zu Farben in digitalisierter geologischer Karte von Otto Gold Consulants.

A.7 Geological map

Geological map of Messelingscharte, East Tyrol

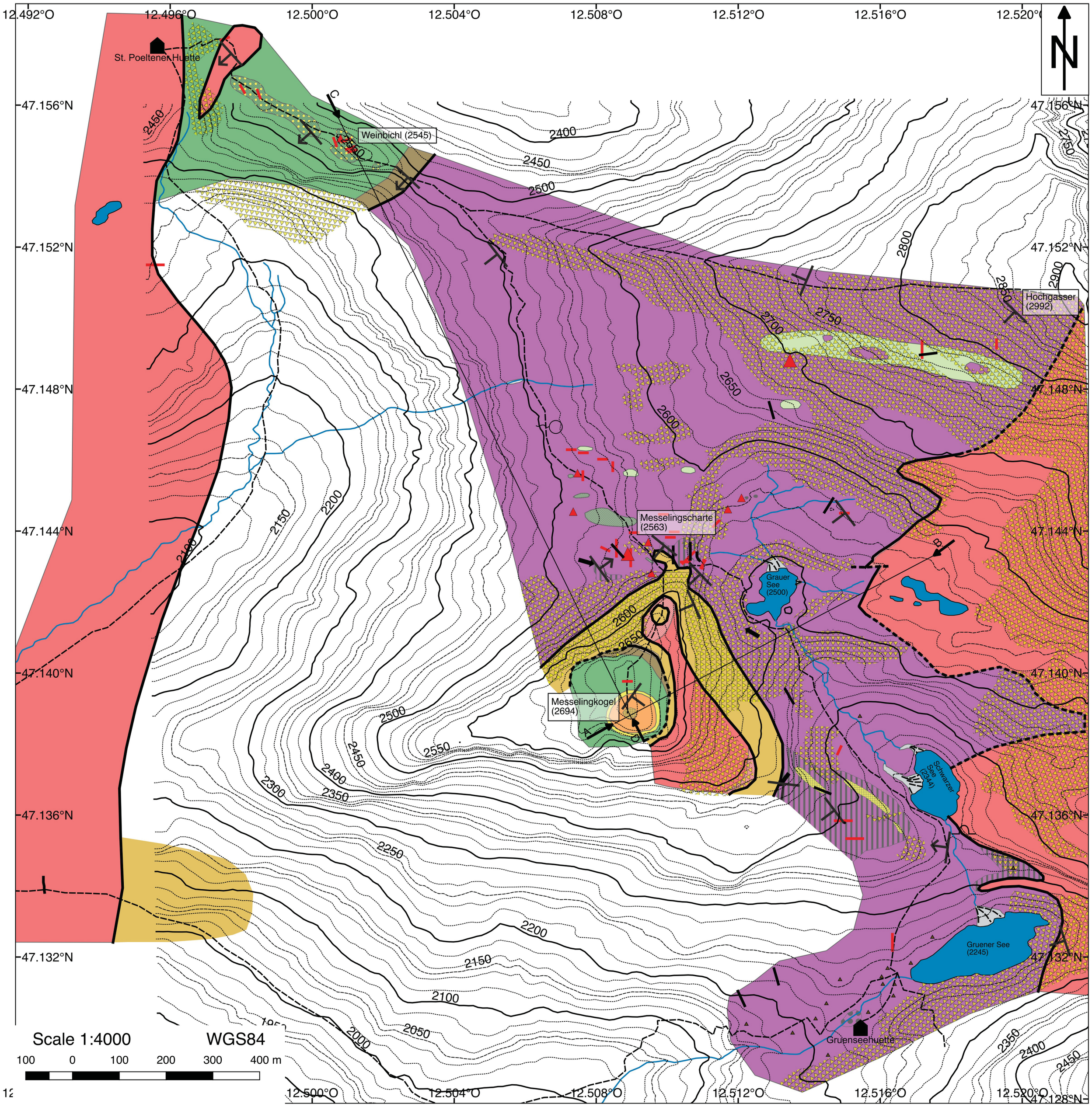

Legend

- Sand and gravel
- Metasediments associated with Weinbühl Amphibolite
- Weinbühl Amphibolite
- Metasediments
- Cataclasite
- Mica schist
- Amphibolite with orthogneiss
- Actinolite-rich schist
- Hornblende-biotite gneiss
- Hornblende-biotite schist
- Hornblende fels
- Amphibolite
- Quartzite, marble and mica schist
- Quarzite
- Garnet amphibolite
- Garnet-bearing orthogneiss
- Weissschiefer
- Orthogneiss

Formation

- Alluvium
- Habach Complex
- Basal Schist
- Basal Amphibolite
- Quartzites with marbles and mica schist
- Central Gneisses

Quartz veins and sheets

- Large sheet with unclear orientation
- Small sheet with unclear orientation
- Large quartz vein
- Small quartz vein

Faults/Thrusts

- Measured
- Indicated

Lineations

- Flat dipping lineations (< 20°)
- Steep dipping lineations (> 20°)

Strike and dip of foliation

- 0-5°
- 6-30°
- 31-60°
- 61-85°
- 86-90°

Quartary

- Blocks and boulders
- Hillside debris
- Stream
- Lake

Special signs

- Hiking path
- Overhang shelter
- Spring
- Lodge

Ordosch Alexander, Montanuniversität Leoben 2017
Field work summer 2016
Wolfram Bergbau und Hütten AG